
# CREEP OF HI-NICALON™ S CERAMIC FIBER TOWS AT 700°C IN AIR AND IN SILICIC ACID-SATURATED STEAM

THESIS

Matthew W. Piper, Captain, USAF

AFIT-ENY-MS-16-M-234

**DEPARTMENT OF THE AIR FORCE**
**AIR UNIVERSITY**

**AIR FORCE INSTITUTE OF TECHNOLOGY**

**Wright-Patterson Air Force Base, Ohio**

AFIT-ENY-16-M-234

# CREEP OF HI-NICALON™ S CERAMIC FIBER TOWS AT 700°C IN AIR AND IN SILICIC ACID-SATURATED STEAM

THESIS

Presented to the Faculty

Department of Aeronautics and Astronautics

Graduate School of Engineering and Management

Air Force Institute of Technology

Air University

Air Education and Training Command

In Partial Fulfillment of the Requirements for the

Degree of Master of Science in Astronautical Engineering

Matthew W. Piper, BS

Captain, USAF

March 2016

AFIT-ENY-16-M-234

# CREEP OF HI-NICALON™ S CERAMIC FIBER TOWS AT 700°C IN AIR AND IN SILICIC ACID-SATURATED STEAM

Matthew W. Piper, BS

Captain, USAF

Committee Membership:

Dr. Marina B. Ruggles-Wrenn
Chair

Dr. Randall S. Hay
Member

Dr. Thomas G. Eason III
Member

## Abstract

Aircraft structural and engine components are subjected to elevated temperature and steam environments during operation. Turbine blades experience particularly harsh conditions that are approaching the operating temperature limits of current Nickel-based superalloys even with active cooling. Ceramic matrix composites (CMCs), which demonstrate high specific strength and specific stiffness and maintain these properties at elevated temperatures such that active cooling is not required, are prime candidates to replace superalloys as the materials for turbine blades. Ceramic matrix composites are composite materials that consist of a ceramic matrix with fiber reinforcement. This research investigated a silicon carbide (SiC) fiber, Hi-Nicalon™ S, which is a candidate for reinforcement of CMCs with SiC-based matrices. Hi-Nicalon™ S fiber tows, consisting of approximately 500 filaments, were creep tested at 700°C in air and in silicic acid-saturated steam. The steam was saturated with silicic acid in order to simulate the interaction that would occur in a SiC-SiC CMC as the steam environment enters through matrix cracks and leaches Si from the matrix while moving towards the fibers. Creep stresses ranged from 2.96 to 1256 MPa in air and from 2.96 to 798 MPa in silicic acid-saturated steam. Creep run-out was defined as 100 h at creep stress. Creep strains were measured and steady-state creep rates were determined in all tests. In air creep runout was achieved at stresses as high as 1023 MPa, while in saturated steam creep runout was achieved only at 750 MPa. Creep rates were approximately an order of magnitude greater in saturated steam than in air. Post-test fiber microstructure was examined using a scanning electron microscope (SEM). Microscopy revealed the presence of a passive

oxidation layer on the fibers tested both in saturated steam and in air but no evidence of active oxidation.

**Acknowledgments**

I would first like to thank my advisor, Dr. Marina Ruggles-Wrenn. She provided technical advice and guidance throughout the thesis process and, most importantly, was always willing to make time to fully answer any questions I had along the way. I could not have completed data collection without the help, patience, and expertise of J.S., K.L, J.D, who were always eager to help with any issue I encountered in the laboratory. J.K. provided many hours of training and support with the SEM equipment, and Dr. R.H. provided helpful analysis of microscopy images. Finally, I'd like to acknowledge the support and patience of my parents and my wife over the last 18 months. I am eternally grateful to God for being given this opportunity.

Matthew W. Piper

## Table of Contents

Page

## List of Figures

Page

## List of Tables

Page

# CREEP OF HI-NICALON™ S CERAMIC FIBER TOWS AT 700°C IN AIR AND IN SILICIC ACID-SATURATED STEAM

## I. Introduction

Engineering and manufacturing advancements have long been brought about through access to and understanding of improved materials. This is particularly true in aerospace applications, where the quest for greater efficiency has driven a desire for materials with greater strength, higher temperature tolerance, and increased longevity as well as the ability to withstand harsh environments and frequent cycling. In order to produce lighter and stronger structural components for aircraft and spacecraft, research has been focused into the design and use of composite materials. Composites have numerous advantages over monolithic materials, including high specific strength (ratio of strength to density), high specific stiffness (ratio of stiffness to density), anisotropic properties, and heterogeneous character [1].

The first composite materials were clay bricks reinforced with straw in ancient Egypt, creating a heterogeneous material with greater toughness than bricks made from monolithic clay. Modern engineering development and use of composite materials began in the first half of the 20$^{th}$ century. Fiber-reinforced composites became possible with the first commercial production of continuous glass fibers in 1939 [2] followed by the development of boron and carbon fibers during the 1950s and 1960s [3]. United States Air Force (USAF) interest in composites began in the 1960s when the USAF began funding research and development for the use of composites in aircraft electronic control surfaces. US Air Force interest and investment in composites has only increased in the intervening decades, placing the service among the leaders in adapting high performance fiber composites to engineering applications [4, 5].

Composite materials were first used in commercial aircraft in the 1950s when the Boeing 707 was built using fiberglass composites that made up about two percent of its structure by weight. In military aircraft, the F-15 and F-16 were developed in the 1970s with similar two percent by weight composites constituents. Modern military and commercial aircraft are built using much higher percentages of composites; the F-22A and F/A-18E/F contain approximately 25% composites (by weight) [6], while the newer F-35A consists of 42% by weight composite materials [7]. In 2011, Boeing introduced the 787 Dreamliner consisting of over 50% composites by weight, with the fuselage and wings largely made of composites [8].

Ceramic matrix composites (CMCs) are a particular form of fiber-reinforced composites of interest to the aerospace industry. Monolithic ceramics generally exhibit several attributes that are useful in aerospace design, including higher hardness, elastic modulus, and strength combined with lower thermal conductivity, thermal expansion coefficient, and density, when compared to properties of most metals or polymers [9]. However, monolithic ceramics have very limited dislocation mobility; as a result, these materials are unable to absorb energy through plastic deformation. Ceramics can fail catastrophically under mechanical loading, particularly in tensile or impact loading. CMCs overcome this behavior through the incorporation of a physically distinct phase such as fibers or particles distributed throughout the ceramic matrix in order to dissipate energy as a crack progresses through the matrix [9].

In addition to the utility of composites for aircraft fuselages and wings, ceramic matrix composites generally exhibit improved material properties relative to metals at high temperatures, making CMCs desirable materials for internal engine components.

Early stage turbine blades are the most temperature-critical components of modern engines and are generally made of Nickel-based superalloys that require active cooling, as seen in **Figure 1**. Thus, the CMCs, which retain their strength to weight ratio at significantly higher service temperatures than alloys or superalloys (see **Figure 2**), are candidate materials to replace alloys in turbine blades [9].

**Figure 1: Turbine blade built from super-alloy with vanes for cooling, reproduced from Shillig [10]**

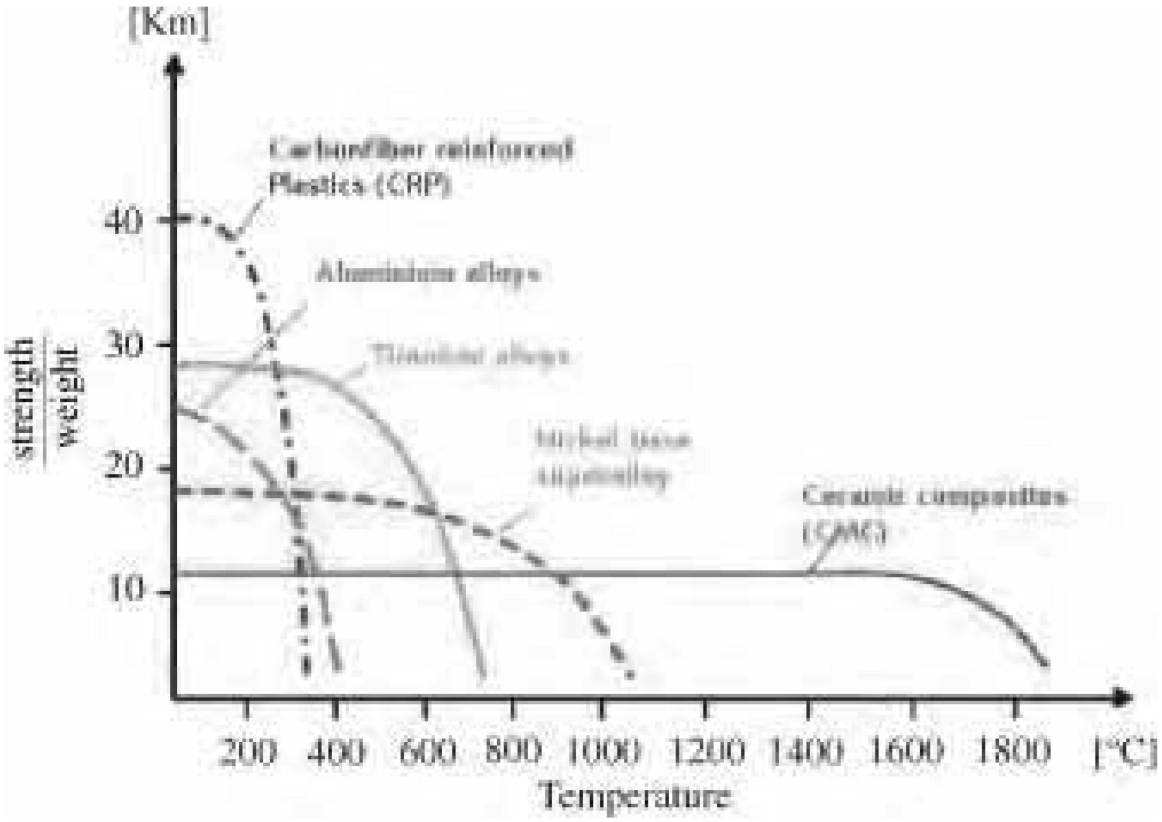


**Figure 2: Strength to weight ratios as a function of temperature for various materials. Note that CMCs maintain their strength to weight ratio at higher temperatures than conventional alloys or superalloys. Reproduced from Schmidt [11] with permission from Elsevier Ltd.**

# II. Background

## 2.1 Ceramic Matrix Composites

Ceramic matrix composites (CMCs) are designed to exhibit energy-dissipating phenomena such as fiber/matrix debonding and crack deflection, creating a material that shows damage-tolerant behavior. In continuous-fiber ceramic composites, the matrix consists of a strong but brittle ceramic, while the reinforcing fibers provide high strength and elastic modulus and serve to increase the fracture toughness of the resulting CMC by arresting crack growth[9]. The brittle nature of ceramics is due to the ionic and covalent bonding present in the matrix; this bonding causes the ceramic to resist large-scale plastic deformation at low and medium temperatures [9]. A number of methods have been attempted to increase the fracture toughness of ceramics, with the addition of continuous fibers being one of the most successful methods [9].

The matrix serves a dual-fold purpose of holding together the CMC as well as transferring the load applied to the CMC to the fibers [9]. Damage in CMCs, which are classified as brittle-matrix composites, generally occurs in the form of multiple cracks in the matrix material. The cracks produce high shear stresses in the fiber-matrix interface, which cause an increase of the tensile stress in the fibers, resulting in either fiber breaks or debonding between the fiber and the matrix [1].

Failure of individual fibers through fiber breaks, pullouts, or debonding behaviors is used in the design of CMCs. Each of these failure mechanisms results in high energy dissipation, leading to graceful failure and increasing the strength of the composite, assuming that the broken fibers are sufficiently isolated from one another[9, 12]. After fiber failure, inelastic deformation of the matrix and its ability to transfer the stress the

surrounding fibers is responsible for the behavior of the CMC [12], resulting in greater strength and allowing graceful failure. A schematic of fiber pullout and debonding is shown in **Figure 3a**.

There are generally three design methodologies used to enable graceful failure of CMCs. **Figure 3b** shows one method which uses fiber coatings to create a weak interface between the fibers and the matrix. The fiber and matrix both exhibit rough surfaces at the interface, enabling the transfer of the load through sliding along the interface [13]. This frictional sliding contributes to crack deflection back into the matrix. Thus, multiple cracks can develop in the matrix while the fibers remain decoupled and fail individually [12]. The second method uses uncoated fibers and also relies on a weak fiber-matrix interface to deflect cracks. In this case, seen in  failure occurs in the interface itself rather than in a fiber coating [14]. A third method, seen in **Figure 3c**, utilizes a porous matrix to stimulate crack deflection around the fibers, allowing load transfer to the fibers themselves and progressing towards graceful failure [12]. In the method shown in **Figure 3d**, a coating is applied to the fiber but is removed through oxidation during the production process. This leaves a gap between the fiber and matrix, offering load transfer between the fiber and matrix in a manner similar to that used in the weak interface approach [15].

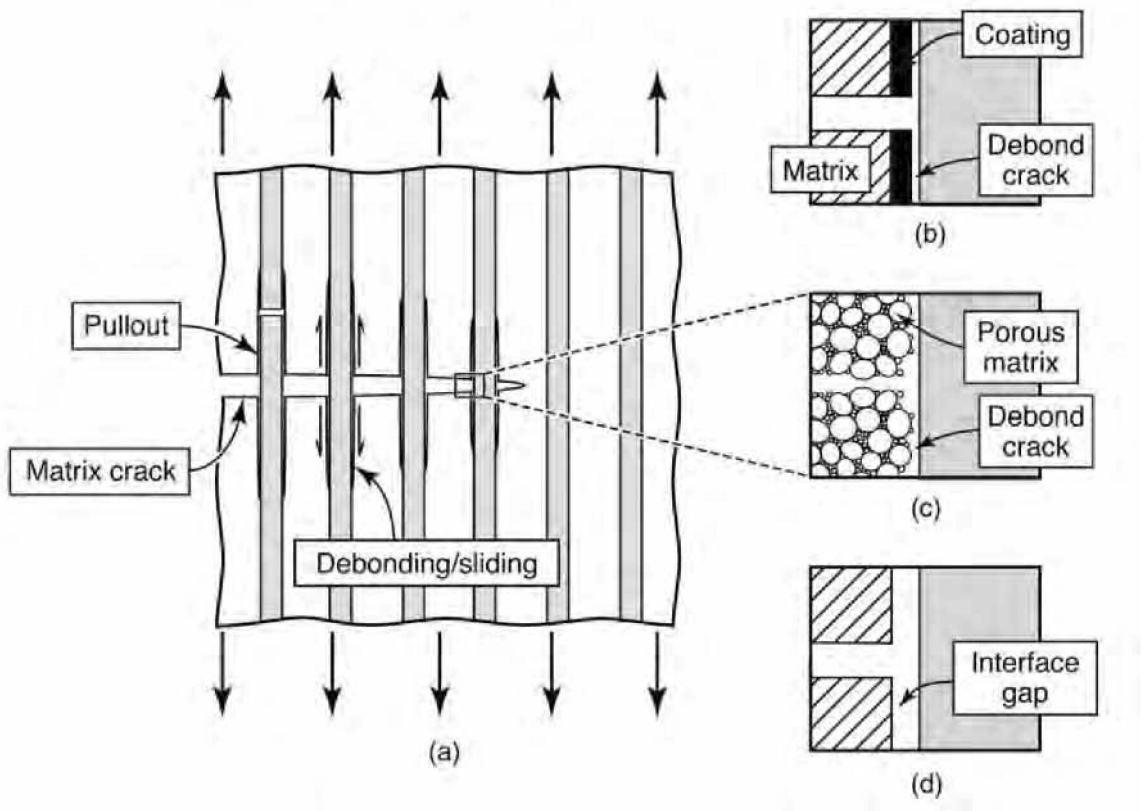


**Figure 3. CMC Design Philosophies. Reproduced from Zok** [16] **with permission from Wiley & Sons.**

## 2.2 Creep in Ceramics

Creep occurs when a material undergoes a continuing inelastic deformation (strain) under a constant stress [17, 18]. In ceramics and CMCs, creep is normally seen under low strain-rate, intermediate-stress loading conditions [18]. The ability to resist creep is especially important in CMCs used in aerospace applications, which are subjected to high-stress, high-temperature conditions for both long durations and many

cycles. In particular, creep resistance is vital in proposed applications of CMCs such as turbine blades, in which creep deformation of the blade could lead to catastrophic engine failure during operation.

Creep curves are generated by plotting strain against time for a constant applied stress and are traditionally divided into three regions: primary, secondary, and tertiary. A typical creep curve is shown schematically in **Figure 4**.

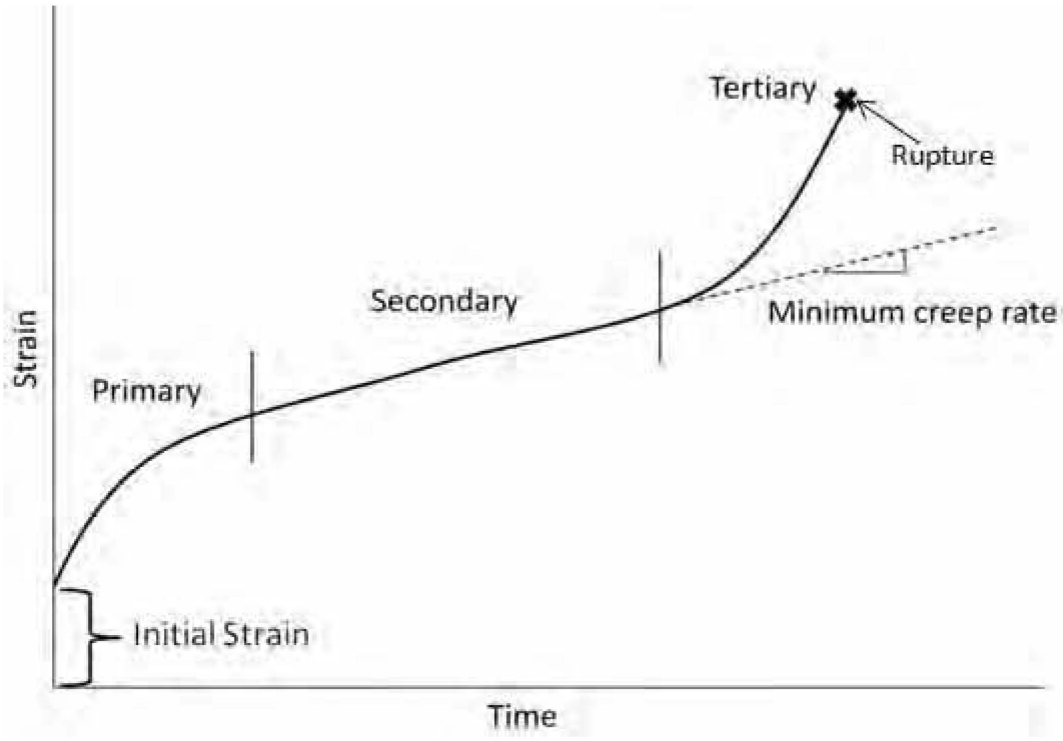


**Figure 4. Three stages of creep deformation. Reproduced from Robertson** [13]**.**

Primary creep is characterized by a decreasing strain rate, associated with changes in the structure of the material such as grain size or dislocation density. Secondary creep is defined as the region on the strain-time curve during which the strain rate is constant. This is generally the portion of the curve that covers the greatest period of time, and it is

associated with microstructural deformation. The final creep stage, tertiary creep, is the region of the creep curve with an increasing strain rate. This stage is characterized by initiation of failure of the material, generally through the formation of cracks and voids. Due to their brittle nature, tertiary creep is either non-existent or very short in ceramics [1, 3, 4].

Study of creep in ceramics is focused on secondary or steady-state creep. In CMCs, which consist mostly of fine polycrystalline constituents, steady-state creep at high temperatures proceeds by two mechanisms: diffusional creep and grain-boundary sliding (GBS) [13, 19, 20]. While these mechanisms are always present and are coupled, creep behavior can generally be defined by one mechanism which dominates. However, while one creep mechanism is considered dominant, it is important to note, as Poirier states, that "diffusion creep creates the driving force for GBS and vice versa. These processes are therefore strongly coupled and mutually accommodating; one cannot exist without the other" [21].

Diffusional creep occurs due to mass transport and is classified as Nabarro-Herring creep or Coble creep depending on the transport mechanism present. Nabarro-Herring creep is also known as lattice diffusion and refers to transport through the grain boundaries. Diffusion along the grain boundary is referred to as Coble creep [19]. Coble creep is seen more often than Nabarro-Herring creep at lower temperatures due to the lower activation energy required for diffusion along the grain boundary relative to diffusion through the grain [18]. For either form of diffusional creep, grain elongation occurs in the direction of the applied load [20]. Grain boundary sliding differs from diffusional creep in that it involves movement of whole grains with respect to one

another. This movement, which relieves local stresses in the material, causes elongation of the material as a whole in the direction of load application[13].

It is widely recognized that steady state creep can be modeled by the Arrhenius rate equation [18]:

$$\dot{\varepsilon} = B\frac{D\mu b}{kT}\left(\frac{b}{d}\right)^{p}\left(\frac{\sigma}{\mu}\right)^{n} \quad \textbf{(1)}$$

where $\dot{\varepsilon}$ is the strain rate, B is a constant, D is the diffusion coefficient, $\mu$ is the shear modulus, b is magnitude of the Burgers vector, k is the Boltzmann constant, T is the absolute temperature, d is the grain size diameter, $\sigma$ is the applied tensile stress, p is the grain size power law exponent (p=2 for Nabarro-Herring creep, p=3 for Coble creep), and n is the stress power law exponent [18, 19]. The diffusion coefficient, D, is given by [19]:

$$D = D_o \exp\left(\frac{-Q}{RT}\right) \quad \textbf{(2)}$$

where Do is a frequency factor, Q is the creep activation energy, and R is the universal gas constant.

The exponents, p and n, in **Equation 1** correspond to different creep mechanisms and can be determined from the experimental creep data. Thus, identification of the primary creep mechanism is possible using the creep data. **Table 1** shows the relation of the predominant creep mechanisms to the power law exponents.

**Table 1. Creep mechanisms in fine-grained polycrystalline ceramics. Reproduced from Armani [19].**

| ***n*** **stress exponent** | ***p*** **grain size exponent** | **Mechanism** |
|---|---|---|
| 1 | 2 | Diffusional creep through lattice (Nabarro-Herring creep) |
| 1 | 3 | Diffusional creep along grain boundaries (Coble creep) |
| 2 | 1 | Grain boundary sliding and interface-reaction controlled creep |
| 4 | 3 | Grain boundary sliding and cavity growth |
| 3-5 | 0 | Dislocation creep: 3 –glide controlled, 5 –climb controlled |
| >5 | | Cavity growth controlled creep |

### 2.3 Silicon Carbide Fibers

Si-C–based fibers were first developed in Japan in the 1970s and have mainly been commercially manufactured by two Japanese companies, Nippon Carbon Co. and Ube Industries, beginning in 1982 [22, 23]. Each company has manufactured three generations of fibers, and the fibers made by each company differ due to their components and the manufacturing processes used [22]. Nippon developed the Nicalon™ series of fibers, which now includes Hi-Nicalon™ and Hi-Nicalon™ S fibers, while the

Ube fibers fall under the Tyranno family. Properties and specifications for the three generations of fibers are shown in **Table 2**.

**Table 2. Specifications and Material Properties of SiC fiber tows. Reproduced from Ishikawa** [24] **with kind permission from Springer Science & Business Media B.V., pg.117, Table 3. Copyright ©2005 by Springer-Verlag Berlin Heidelberg.**

: Nearly stoichiometric SiC fiber

| | SiC Fibers | | | | | | | |
|---|---|---|---|---|---|---|---|---|
| | Nicalon | | | Tyranno | | | | Sylramic |
| | NL-200 | Hi-Nicalon | Hi-Nicalon-s | Lox M | ZMI | ZE | SA* | |
| Atomic Composition | $SiC_{1.34}O_{0.36}$ | $SiC_{1.39}O_{0.01}$ | $SiC_{1.05}$ | $SiTi_{0.02}C_{1.37}O_{0.32}$ | $SiZr_{<0.01}C_{1.44}O_{0.24}$ | $SiZr_{<0.01}C_{1.52}O_{0.05}$ | $SiC,O,Al_{<0.008}$ | $SiCTi_{0.02}B_{0.09}O_{0.02}$ |
| Tensile Strength (GPa) | 3.0 | 2.8 | 2.6 | 3.3 | 3.4 | 3.5 | 2.8 | 3.0 |
| Tensile Modulu (GPa) | 220 | 270 | 410 | 187 | 200 | 233 | 410 | 420 |
| Elongation (%) | 1.4 | 1.0 | 0.6 | 1.8 | 1.7 | 1.5 | 0.7 | 0.7 |
| Density ($g \cdot cm^{-3}$) | 2.55 | 2.74 | 3.10 | 2.48 | 2.48 | 2.55 | 3.02 | >3.1 |
| Diameter (μm) | 14 | 14 | 12 | 8 & 11 | 8 & 11 | 11 | 8 & 10 | 10 |
| Specific Resistivity ($\Omega \cdot cm$) | $10^3$-$10^4$ | 1.4 | 0.1 | 30 | 2.0 | 0.3 | — | — |
| Thermal Expansion coeff. ($10^{-6}$/K) | 3.2 (25-500℃) | 3.5 (25-500℃) | — | 3.1 | 4.0 | — | 4.5 (20-1320℃) | — |
| Thermal Conductivity (W/mK) | 2.97(25℃)<br>2.20(500℃) | 7.77(25℃)<br>10.1(500℃) | 18.4 (25℃)<br>16.3 (500℃) | — | 2.52 | — | 64.6 | 40-45 |

The first generation of Si-C-based fibers included the Nicalon™ (NL-200) fibers produced by Nippon Carbon and the Tyranno fibers developed by Ube [22]. Both types of fibers had high oxygen content in the form of silicon oxycarbide phases. These phases decompose at temperatures above 1100°C, which causes the fiber strength to degrade at

high temperatures [22]. Additionally, the first generation of fibers were susceptible to creep from around 1000°C [23]. The strength degradation and reduced creep performance limited the fibers to use in relatively low temperature applications.

In order to reduce the high temperature degradation, Nippon Carbon, in 1999, developed a second generation fiber (Hi-Nicalon™) which is nearly oxygen-free [22]. This was achieved by eliminating oxygen induced cross-linking from the manufacturing process [23]. While reducing the thermal instability seen in Nicalon™, the Hi-Nicalon fiber displayed a reduced ability to resist oxidation and creep as a result of an excess of turbostratic carbon [22]. Ube used a different method of improving high temperature performance by producing Tyranno fibers containing metal additives which pushed the degradation temperature to 1300°C [22].

Nippon Carbon then followed Hi-Nicalon™ with a third generation fiber known as Hi-Nicalon™ S. This fiber was designed to be near pure SiC in order to reduce the free carbon content while improving performance at high temperatures [22]. This reduction in free carbon resulting in properties more closely approximating those of bulk SiC than was seen in the first two generations of fibers [23]. Hi-Nicalon™ S has a higher Young's modulus and higher creep and oxidation resistance relative to Hi-Nicalon™; it also exhibits thermal stability, or resistance to degradation, at temperatures up to 1600°C [22]. **Figure 5** shows the microstructures of the three generations of the Nicalon™ family of fibers produced by Nippon Carbon.

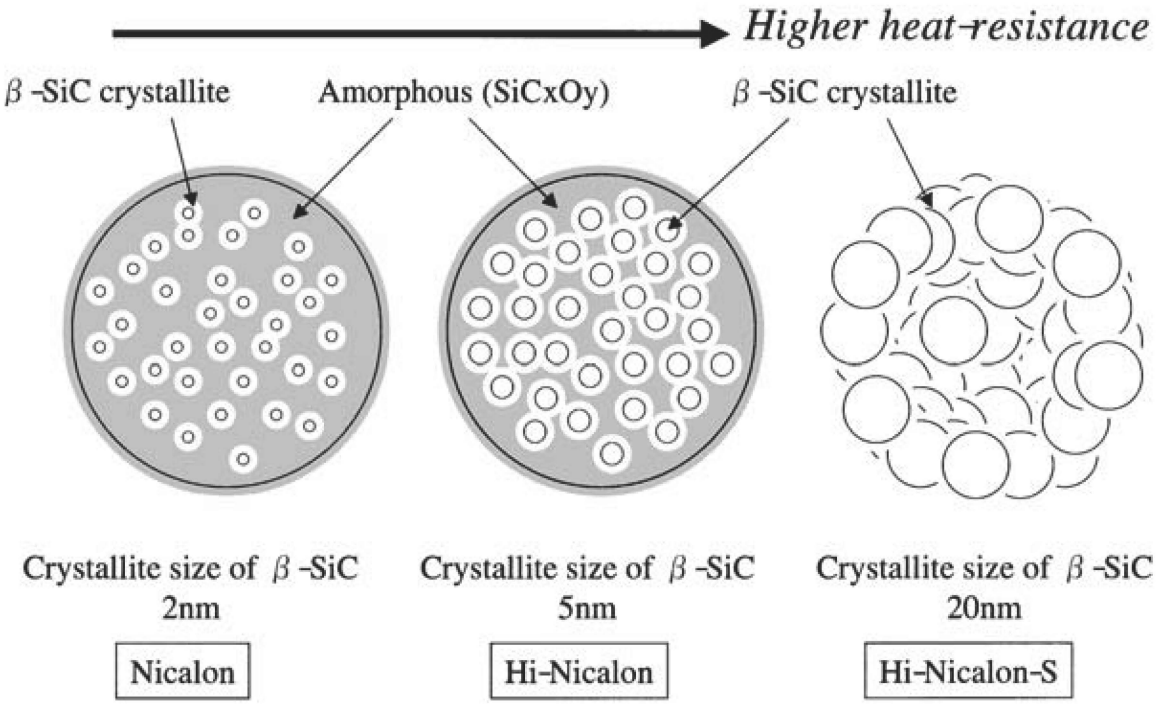


**Figure 5. Microstructures of 1st, 2nd, and 3rd generation Nicalon™ fibers. Reproduced from Ishikawa [24] with kind permission from Springer Science & Business Media B.V., pg.118, Figure 9. Copyright ©2005 by Springer-Verlag Berlin Heidelberg.**

Due to their relatively recent development, the creep behavior of third generation SiC fibers has not been studied extensively. Despite the shorter time period for study compared to the first and second generation fibers, several researchers have recently undertaken studies on these fibers at elevated temperatures.

Sha et al. [25, 26] conducted tests on three types of fibers – Hi-Nicalon™, Hi-Nicalon™ S, and Tyranno™ SA to study the effects of heat treatment on their creep resistance. The fibers were heat-treated in argon for one hour at temperatures of 1300-1900°C, in order to simulate the effects of CMC processing at temperatures above the sintering temperatures of the fibers. It was shown that the heat treatment increased both

the creep resistance and the creep activation energy of the fibers. The influence of heat treatment on creep resistance was seen in all fibers; however, only the Hi-Nicalon™ and Hi-Nicalon™ S fibers exhibited higher creep activation energies after heat treatment. It was also found that the creep resistance depends on the grain size and the composition within and adjacent to the grain boundaries [25, 26].

Sauder and Lamon [27] also studied Hi-Nicalon™, Hi-Nicalon™ S, and Tyranno™ SA3 fibers, investigating the effects of temperature on creep of the fibers in vacuum. All three stages of creep were observed, with a longer than expected primary creep duration. Primary creep in all fibers was attributed to deformation of carbon (C) along with SiC grain boundaries. Secondary creep was found to proceed with a stress exponent, n, of approximately 2.5, corresponding to Rauchinger creep. The Rauchinger creep mechanism refers to grain-boundary sliding without grain elongation and glassy phase, which Sauder and Lamon posit involves carbon deformation based on analysis of activation energies. The steady state creep rates as functions of temperature at a constant stress of 850 MPa for Hi-Nicalon™ S, and Tyranno™ SA3 are shown in **Figure 6**. Tertiary creep, caused by silicon volitization starting at the surface and moving inward to the core of the fiber,  was observed in tests at temperatures near 1400°C [27].

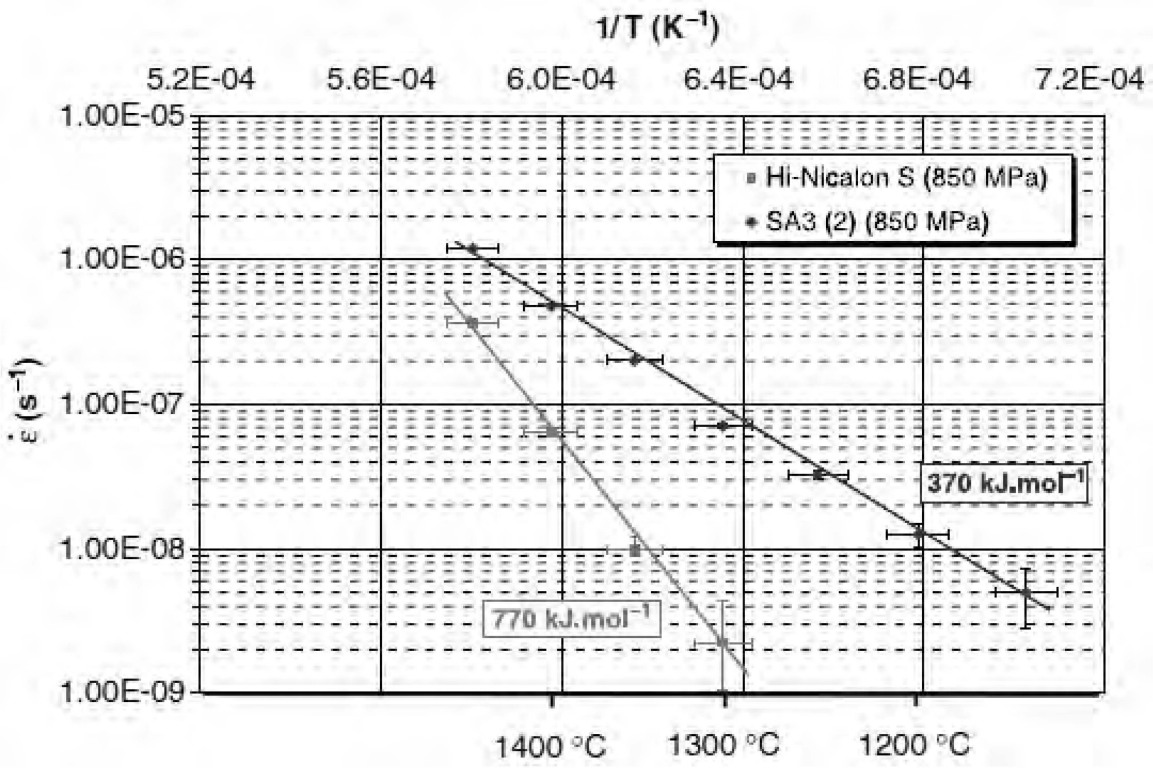


**Figure 6. Steady state creep rate vs temperature for Tyranno™ SA3 and Hi-Nicalon™ S fibers under a stress of 850 MPa, reproduced from Sauder and Lamon [27] with permission from Wiley & Sons.**

Yun and DiCarlo [28] conducted tests on six types of stoichiometric SiC fibers: Hi-Nicalon™ S, Tyranno™ SA1 and SA2, standard Sylramic fibers, and two types of developmental Sylramic fibers referred to as Syl(1) and Syl(2). (The developmental Sylramic fibers are now known as Sylramic-iBN [20].) Yun and DiCarlo conducted constant displacement rate tensile tests at room temperature as well as creep rupture tests at 1400°C. **Figure 7** and **Figure 8** show typical creep curves and rupture strengths, respectively, obtained by Yun and DiCarlo [28] for the six fibers in air at 1400°C. These tests showed increased creep and rupture resistance at high temperatures in Hi-Nicalon™ S and other third-generation SiC fibers relative to their predecessors. However, a

significant decrease in fast fracture tensile strengths was also observed. The authors concluded that no single stoichiometric SiC fiber will perform best under all possible applications of CMCs.

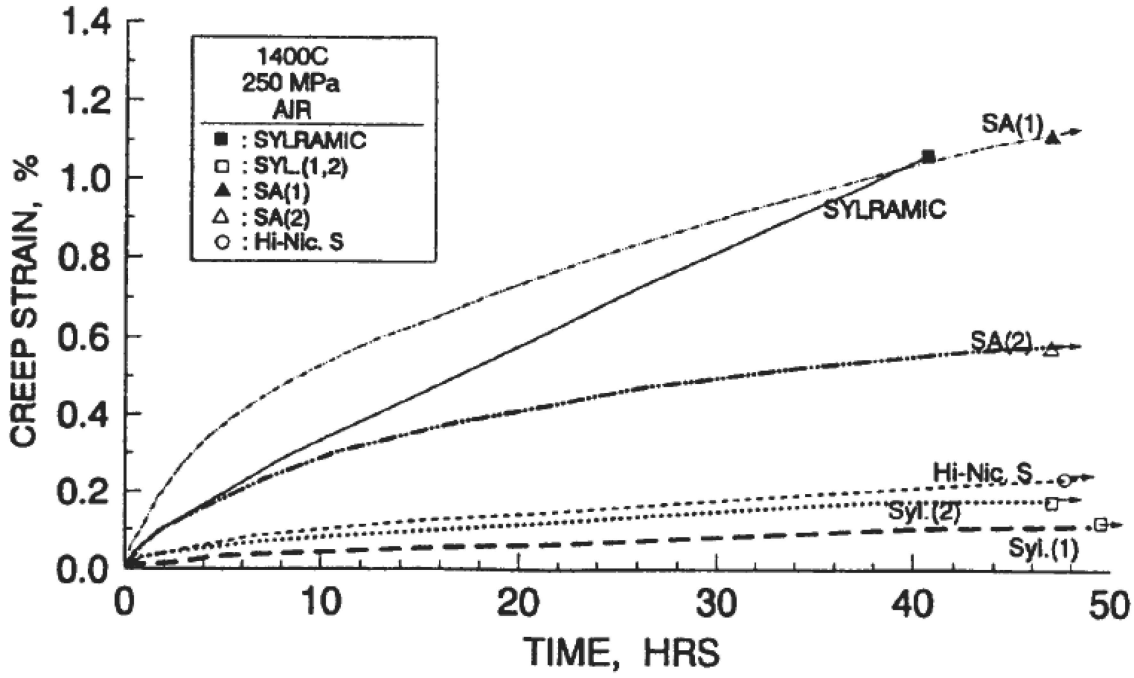


**Figure 7. Typical creep-rupture curves of SiC fibers at 1400°C in air. Reproduced from Yun and DiCarlo [28]**

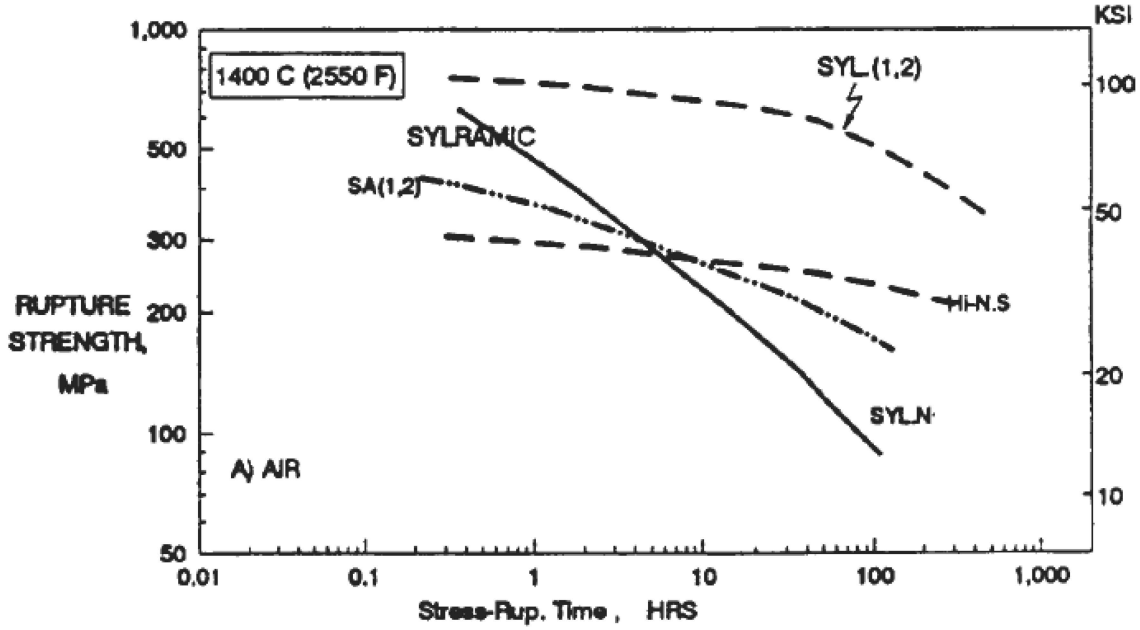


**Figure 8. Rupture strengths of SiC fibers at 1400°C in air. Reproduced from Yun and DiCarlo [28]**

Steffens [29] conducted creep tests of Hi Nicalon™ S fiber tows in air and in steam at 800°C and 1100°C. Steady state creep data was collected in all tests and was fitted with the Norton-Bailey power law:

$$\dot{\varepsilon} = A\sigma^n \tag{3}$$

where $\dot{\varepsilon}$ is the minimum creep rate, A is a temperature-dependent coefficient that accounts for the activation energy, grain size and other variables in the full form of the power law, and σ is the applied stress. Observed creep rates in air at 1100°C at a stress of 850 MPa were an order of magnitude higher than the rates predicted by extrapolating the creep rates calculated by Sauder and Lamon [27] and shown in **Figure 6**. Steffens determined stress exponent values of n=4.8 in air and n=3.8 in steam, which led to a

conclusion that the primary creep methods were climb-controlled dislocation creep in air and GBS with cavity growth in steam [29]. These conclusions were not confirmed with microstructural analysis [13]. **Figure 9** shows the creep rate data obtained by Steffens [29] and used to determine the stress exponents. Steffens [29] also found that creep lifetimes in air, as expected, decreased with both increased temperature and increased load, and rupture time data closely matched those reported by Gauthier and Lamon [30]. An even greater effect on creep lifetime was seen when the fibers tows were tested in a steam environment. However, the effect of steam was more pronounced at 800°C than at 1100°C, leading to the conclusion that a protective silica scale forms on the fiber surface at higher temperatures, improving the performance in creep [29]. Rupture data obtained by Steffens [29] is reproduced in **Figure 10**.

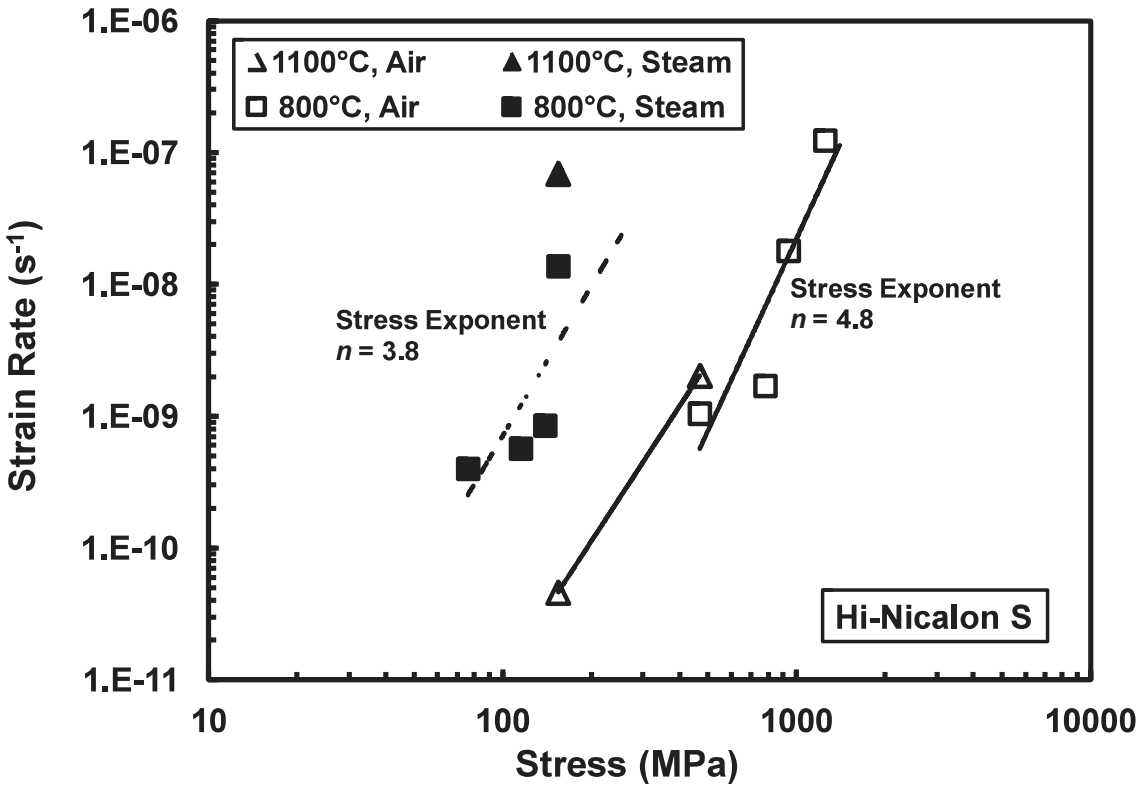


**Figure 9. Steady-state creep rate vs applied stress for Hi-Nicalon™ S fiber tows at 800°C and 1100°C in laboratory air and in steam. Reproduced from Steffens [29].**

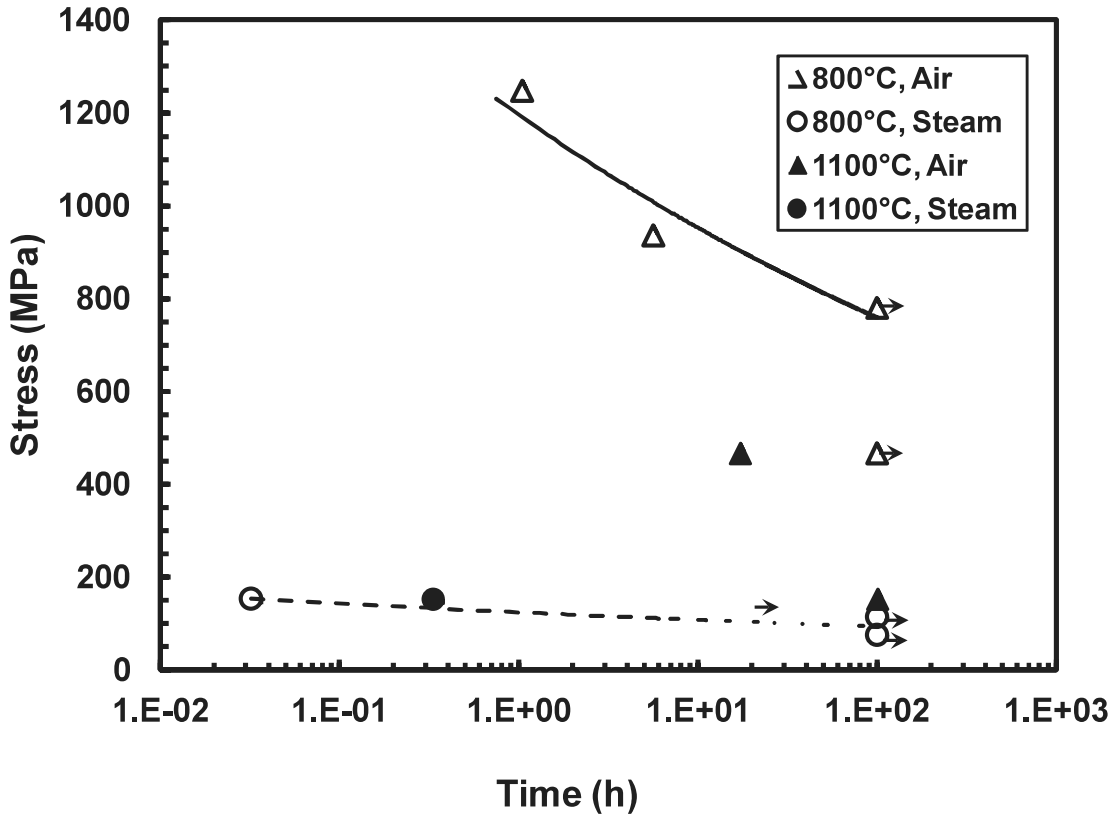


**Figure 10. Creep stress vs. time to rupture for Hi-Nicalon™ S fiber tows at 800°C and 1100°C in laboratory air and in steam. Arrow indicates that failure of specimen did not occur when the test was terminated. Reproduced from Steffens [29].**

Shillig [10] conducted creep-rupture tests of the Hi-Nicalon™ S fiber tows in air and in steam at temperatures 800°C, 900°C, 1000°C, and 1100°C. Creep performance in air was found to be somewhat temperature-dependent at 800-1000°C, with a drastic decrease in creep performance seen at 1100°C. The steam environment also caused a substantial decrease in creep performance at temperatures of 800-1000°C, but this effect was considerably less pronounced at 1100°C. Like Steffens, Shillig concluded that this improved creep resistance was a result of a protective silica scale forming on the surface of the fiber at 1100°C. Shillig attempted to determine the stress exponent in air and in

steam but was unable to do so because of the considerable scatter in the data, as shown in **Figure 11**. Creep rupture data is shown in **Figure 12**.

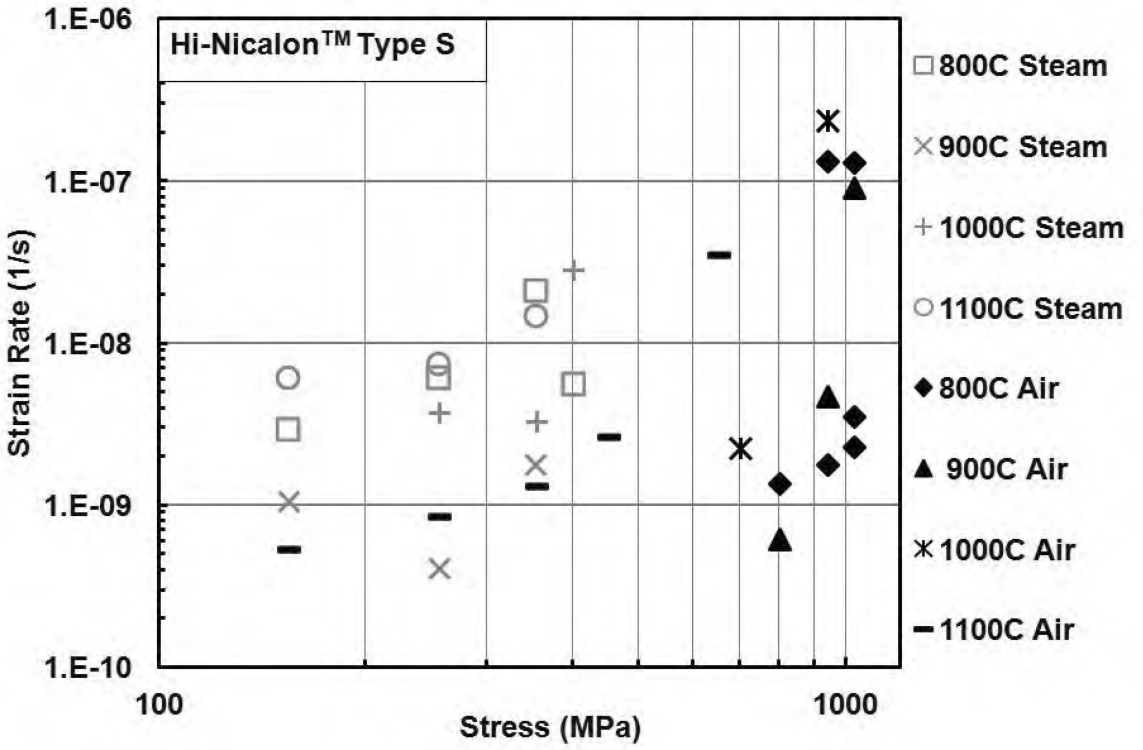


**Figure 11. Steady-state creep rate vs applied stress for Hi-Nicalon™ S fiber tows at 800°C, 900°C, 1000°C, and 1100°C in air and in steam. Reproduced from Shillig [10].**

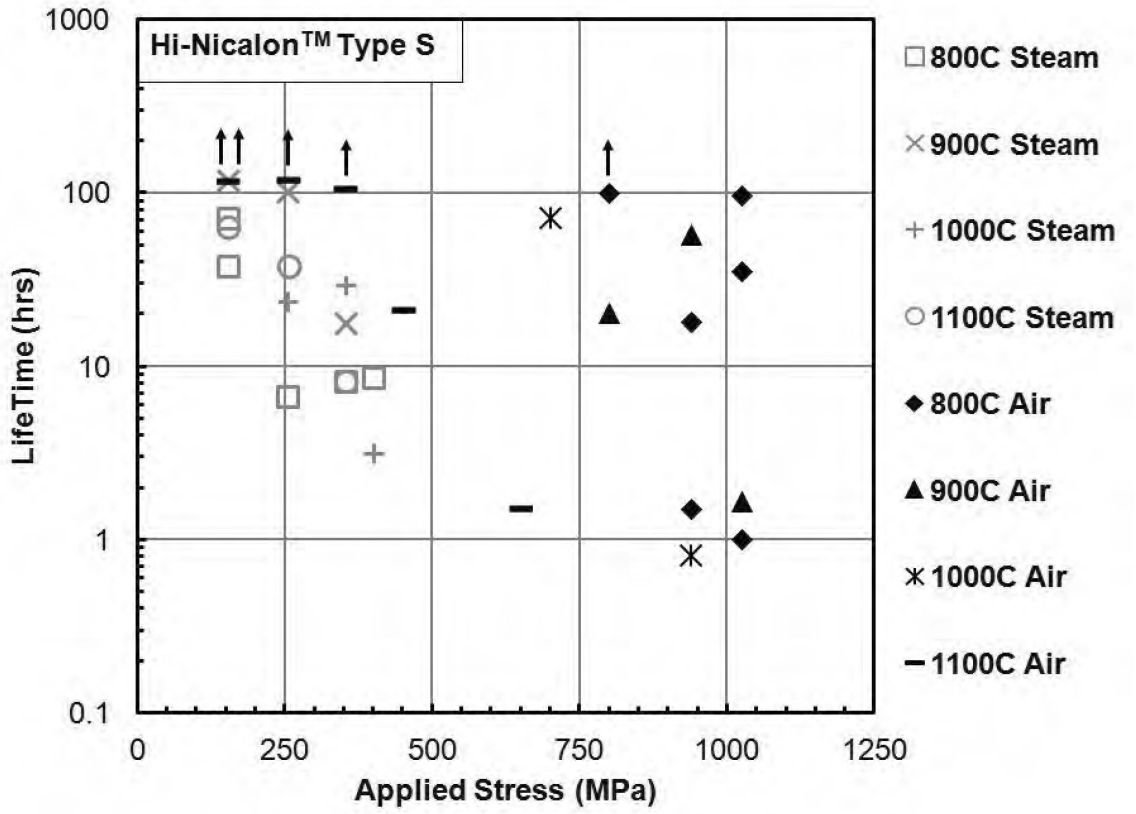


**Figure 12. Stress Rupture data for Hi-Nicalon™ S fiber tows tested at 800°C, 900°C, 1000°C, and 1100°C in air and in steam. Reproduced from Shillig [10].**

Robertson [13] investigated the effects of silicic acid-saturated steam on the tensile and creep-rupture performance of Hi-Nicalon™ S fibers at 800°C. The tests were conducted in silicic acid-saturated steam in order to prevent active oxidation of the fibers. Robertson performed tensile tests at stress rates ranging from 0.1 MPa/s to 100.0 MPa/s. The tensile tests results showed degradation of tensile strength in steam relative to air but very little dependence of tensile strength on loading rate, even at the lowest loading rate. Robertson noted that this lack of rate dependence of tensile strength contrasted with the strong rate

dependence of tensile strength observed by Armani [19] for oxide fibers. The trend lines in **Figure 13** and **Figure 14** indicate the lack of rate dependence.

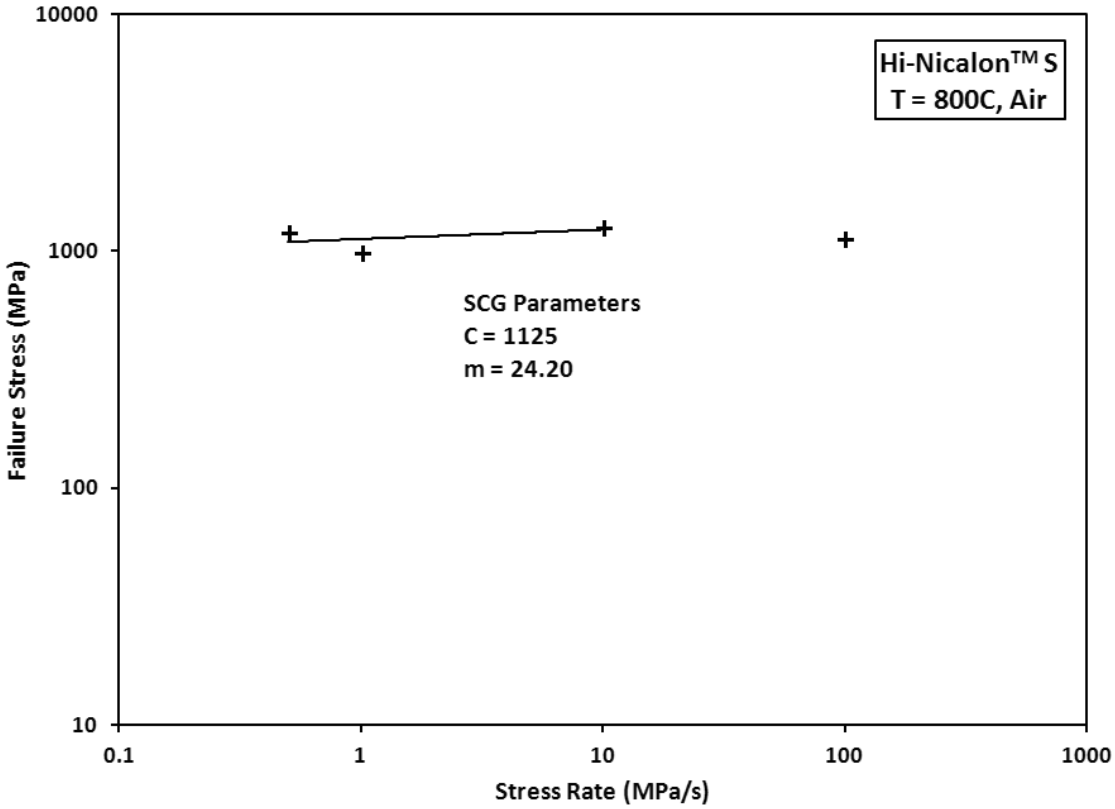


**Figure 13. Failure stress of Hi-Nicalon™ S fibers at 800°C in air as a function of stress rate. Note the lack of stress rate dependence. Reproduced from Robertson [13]**

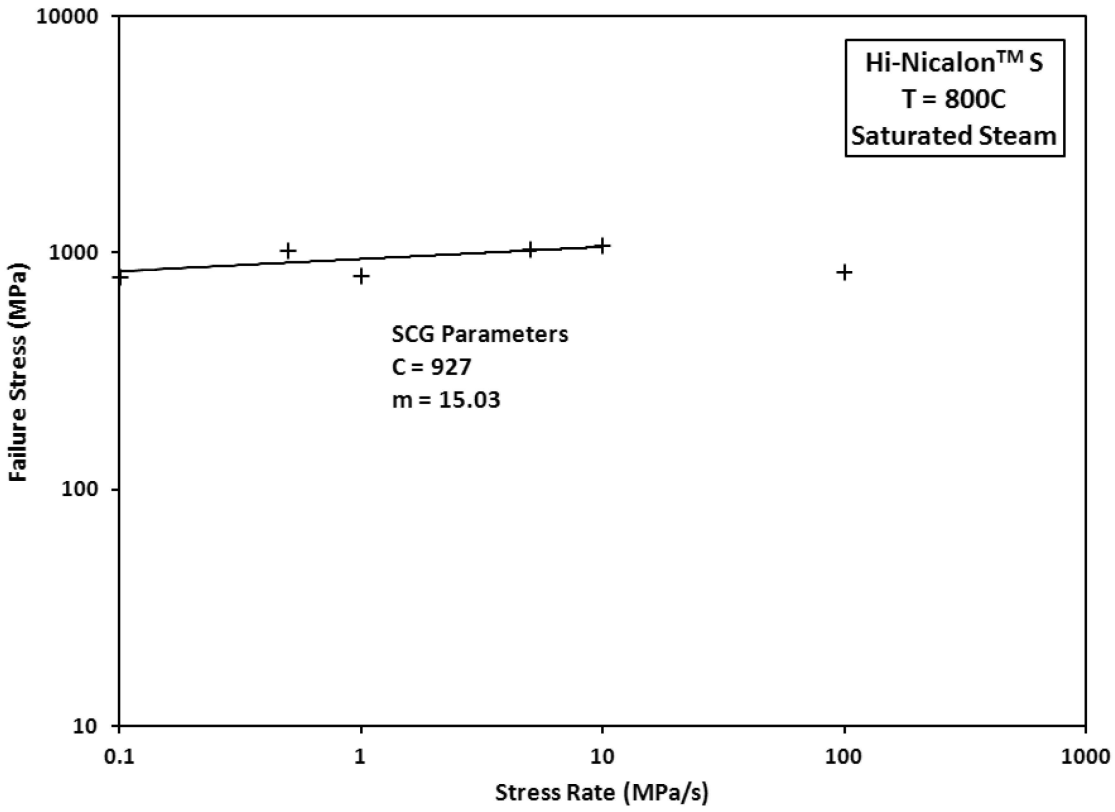


**Figure 14. Failure stress of Hi-Nicalon™ S fibers at 800 °C in silicic acid-saturated steam as a function of stress rate. Note the lack of stress rate dependence. Reproduced from Robertson [13]**

The creep-rupture tests conducted by Robertson [13] were used to determine the stress exponent, n, of 5.0 in air and 4.1 in silicic-acid saturated steam (**Figure 15**). Note that the stress exponent values reported by Steffens [29] are n=4.8 in air and n=3.8 in unsaturated steam. The values of the stress exponent determined by Robertson were consistent with climb-controlled dislocation creep in air and grain boundary sliding with cavity nucleation and growth in steam. However, Robertson found that the fiber tows were capable of maintaining stresses up to five times as high as those reported by Steffens [5, 12]. This difference is attributed to the tests being conducted in silicic acid-saturated

steam as opposed to unsaturated steam. Notably, testing in unsaturated steam cause active oxidation of the fibers [13]. **Figure 16** shows creep rupture data in air and in saturated steam obtained by Robertson [13].

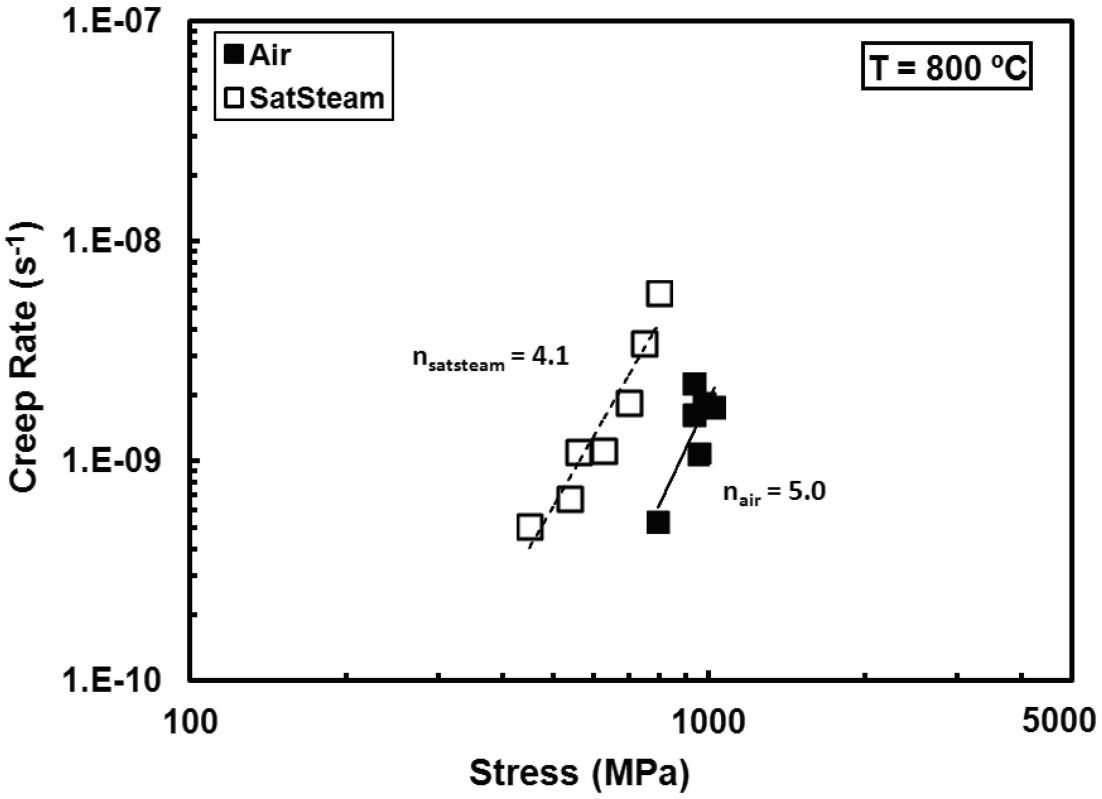


**Figure 15. Creep strain rate vs. applied stress of Hi-Nicalon™ S fibers at 800 °C in air and in silicic acid-saturated steam. Reproduced from Robertson [13]**

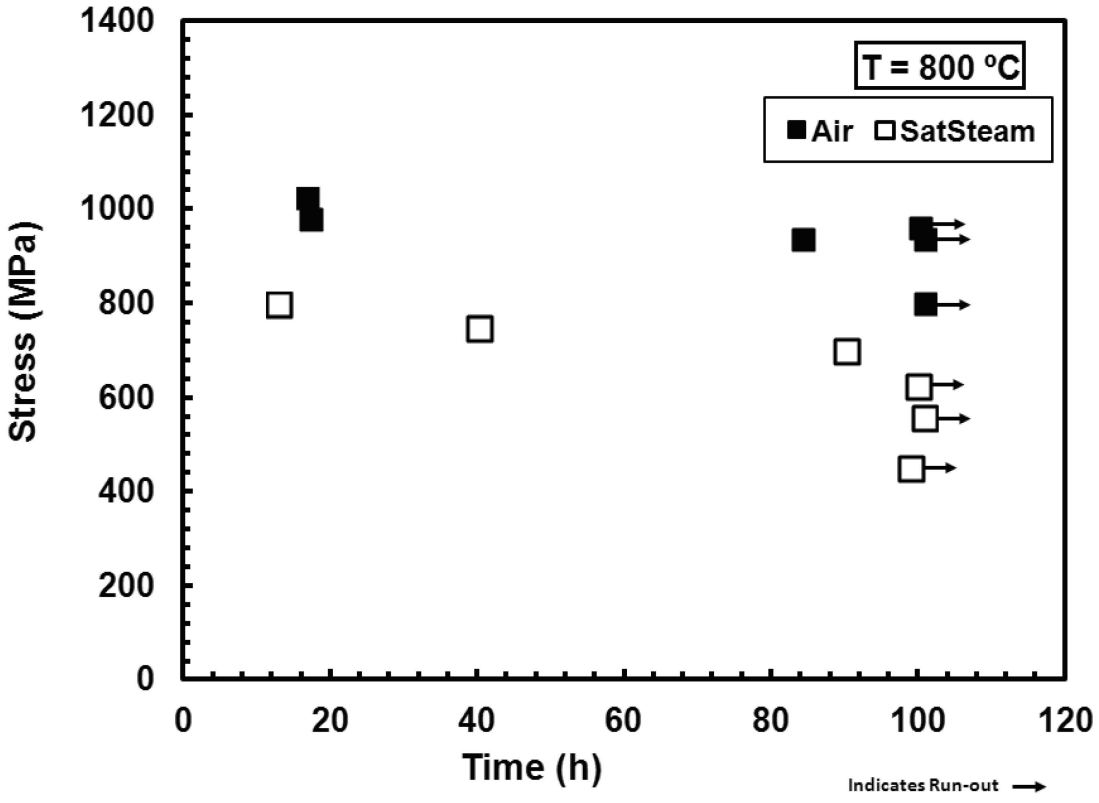


**Figure 16. Creep lifetimes of Hi-Nicalon™ S fibers at 800 °C in air and in silicic acid-saturated steam. Reproduced from Robertson [13]**

## 2.4 Environmental Effects

One of the drivers of research into SiC fiber-reinforced CMCs is their use in hot-section components of aircraft turbine engines. This use requires prolonged exposure to combustion by-products and steam environment [8, 31, 32], making an understand of the effects of such exposure vital to the designers of engine components. Oxide fibers and oxide fiber-reinforced CMCs demonstrate less susceptibility to environmental effects;

however, SiC fibers are more desirable for high temperature applications based on their ability to retain their strength and creep resistance at higher temperatures than oxide fibers [8].

Subcritical crack growth at room temperature primarily results from the phenomenon known as stress corrosion cracking (SCC) [18], which is now generally known as environmentally assisted crack growth (EACG) [13]. In EACG, water and other environmental components interact with the material to cause a stress-assisted chemical reaction, resulting in a crack in a small component of the material [13]. In silicon-based CMCs, the water vapor and silicon interact to form silica ($SiO_2$). The tensile stress on the material holds the crack open, exposing the interior of the material (e.g., the inner portion of the matrix and the fibers) to the corrosive environment.

A process known as passive oxidation occurs when the material-environment interaction causes a protective film to form on the material. In SiC-based materials, passive oxidation causes a thin layer of silica to form on the surface, providing protection of the material from the corrosive environment. The environmental constituent must then diffuse through the silica in order to interact with the material, and this process occurs more slowly than if the silica layer was not present. At high temperatures, the primary crack growth method transitions to diffusion of the environmental species to the crack tip [18], with diffusion generally occurring faster as temperature increases. The rate of subcritical crack growth is highly sensitive to temperature, stress, and environmental species concentration [10].

Hay and his colleagues conducted numerous studies assessing the effects of the environment on SiC fibers, particularly Hi-Nicalon™ S fibers [33 – 36]. In 2010, Hay et

al. subjected Hi-Nicalon™ S fibers to oxidation in dry air at temperatures ranging from 800°C to 1200°C and found that silica scale growth up to 100 nm resulted in a fiber strength increase of approximately 10% [33]. They attributed this strength increase to the residual compressive stress in the scale from its formation and possibly to the healing of surface flaws in the fiber. For scale growth greater than 100 nm, the fiber strength decreased, likely as a result of scale crystallization which led to cracks forming in the scale and partial debonding of the scale from the fiber [33] . Further studies on silica scale growth in dry air were conducted in 2011 at a greater range of temperatures (700-1400°C) [34, 35]. A smooth amorphous silica scale was found to form initially followed by crystallization. Crystallized scale was thinner than amorphous scale and exhibited cracks and debonding. Scale crystallization and onset of loss of strength were strongly coupled, and this relationship was attributed to the tensile thermal stress within the crystallized scale [35].

Hay et. al then conducted similar experiments to assess silica scale growth in steam at temperatures ranging from 700-1300°C [36]. These fibers exhibited similar strength increases to those seen in dry air of approximately 10% for scales up to 100 nm in thickness, with decreases in strength seen in thicker scales. The fibers that exhibited degraded strength all had scales that were partially or fully crystallized [36].

SiC fibers, namely Hi-Nicalon™ S, were also studied by Steffens [29], Shillig [10], and Robertson [13]. Steffens conducted creep testing of fiber tows in air and in unsaturated steam at temperatures of 800°C and 1100°C. At 800°C, steam was shown to greatly decrease the creep performance of the fiber tows. For tests at the same stress in air and in unsaturated steam, the fiber tows tested in steam exhibited creep rates an order of

magnitude higher and creep lifetimes three orders of magnitude shorter compared to the tests in air. At 1100°C, Steffens observed similar creep rates in air and in steam to the equivalent tests at 800°C; however, creep lifetimes increased by an order of magnitude in steam while decreasing by an order of magnitude in air. The longer creep lifetimes at 1100°C were attributed to the formation of a protective silica scale on the surface of the fibers [29]. Shillig [10] tested fiber tows in air and in unsaturated steam at temperatures ranging from 800°C to 1100°C. The data collected by Shillig [10] generally substantiated Steffens' results [29] but also showed evidence of both active and passive oxidation at all temperatures. Robertson [13] redesigned the test facility used by Steffens [29] and Shillig [10] in order to saturate the steam prior to introducing it to the test chamber. These changes to the experimental facility are described in further detail in Section 3.3. Robertson [13] showed a fivefold increase in creep lifetime at 800°C while calculating similar stress exponent values from the Norton-Bailey form of the power law creep equation **(Equation 3)**. Creep rates for the tests in saturated steam were an order of magnitude lower than those reported by Steffens and Shillig [10, 26] in unsaturated steam.

This work seeks to characterize the performance of Hi-Nicalon™ S fiber tows in silicic acid-saturated steam and in air at 700°C. Displacement data will be collected and used to calculate creep strains and creep rates. Analysis will be conducted to compare the values obtained at 700°C in saturated steam and in air to the data obtained in prior research at 800-1100°C in air, in saturated steam, and in unsaturated steam.

# III. Experimental Arrangements

## 3.1 Material

This research sought to characterize creep behavior of Hi Nicalon™ Type-S fiber tows at 700°C. Hi-Nicalon™ S fibers are near-stoichiometric third-generation SiC fibers, developed by Nippon Carbon Co. of Tokyo, Japan. The fiber tows used in this work consisted of approximately 500 individual fibers with average diameter of 12 μm (12 x $10^{-6}$ m) [29]. These data were used to calculate an average cross-sectional area for the fiber tow of 5.655 x $10^{-8}$ $m^2$. Fiber tows were taken from the same spool as those used in previous research efforts by Steffens [29], Shillig [10], and Robertson [13]. Typical material characteristics for Hi-Nicalon™ S fibers, as provided by the manufacturer, are displayed in **Table 3**.

**Table 3. Typical properties of Hi-Nicalon™ S fibers; data reproduced from NGS Advanced Fibers Co., Ltd. [37]**

| | |
|---|---|
| Number of filaments | 500 |
| Filament diameter (μm) | 12 |
| Product Form | Tow |
| Sizing Agent | PVA |
| Linear density, tex (g/km) | 198 |
| Oxygen content (wt%) | 0.8 |
| Modulus of Elasticity (GPA) | 380 |

## 3.2 Test Specimen

Test specimens for dead weight creep testing were prepared using the three-tab method developed by Steffens. Steffens [29] describes the procedure for fabricating the fiberglass tabs in Appendix A4 and the procedure for preparing the test specimens in Appendix A2. This method was also used by Shillig [10], Sprinkle [20], and Robertson [13]. According

to this method, each end of the fiber tow was secured using three fiberglass tabs. The primary tab is 1.0 in. x 1.5 in. (0.0254 m x 0.0381 m); the secondary tab is 1.0 in. x 1.0 in. (0.0254 m x 0.0254 m), and the tertiary tab is 0.75 in. x 0.75 in. (0.0191 m x 0.0191 m). After the fiberglass tabs were cut to size, a hole was punched along the centerline of each primary tab in order to suspend the specimen between the hook fixtures in the test facility. The primary tabs were then laid out and secured with tape on the grid of a cutting board with a 7 in. (0.178 m) gap between the tabs and with one of the grid lines of the cutting board bisecting the hole in each tab as shown in (step 1 in **Figure 17)**. Using the same grid line that was used to place the tab to ensure alignment, a length of fiber tow was then cut from the spool and taped to the cutting board beyond the primary tab at each end (step 2 in **Figure 17)**. Since the fiber tow and the grid line along which it was aligned bisected the centerline of the tabs, the fiber tow is subjected to only axial loading during the creep test. The secondary tab was then secured to primary tab using a two part epoxy as shown in step 3 of **Figure 17**. After the epoxy dried, the excess fiber was folded over and secured using the tertiary tab and the same epoxy (step 4 in **Figure 17**). Finally, the remaining excess fiber was cut with a razor blade where it protruded from the tertiary tab as shown in step 5 of **Figure 17**. Further details and step-by-step instructions of the specimen preparation process are given in Appendix A1 of Steffens [29].

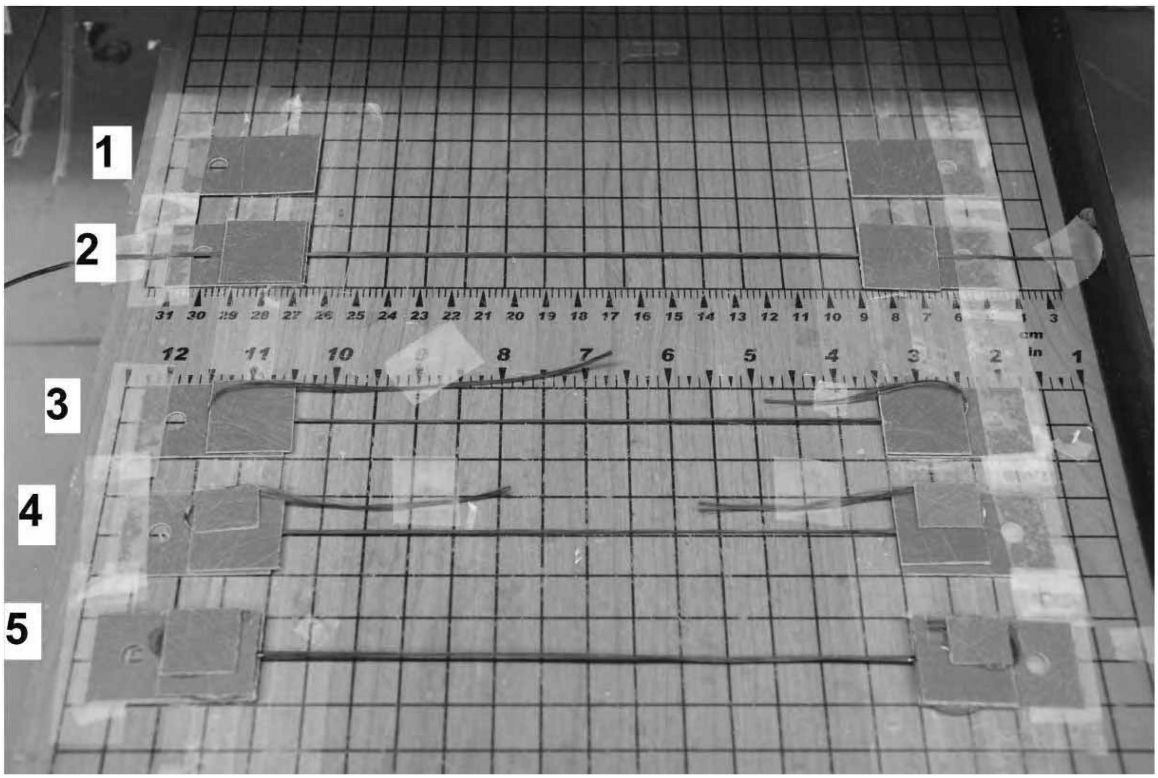


**Figure 17. Test specimen preparation process. Reproduced from Steffens [29]**

### 3.3 Experimental Facility

Tests were conducted in the Mechanics of Advanced Aerospace Materials Laboratory of the Department of Aeronautics and Astronautics at AFIT. The test facility was originally designed and built by Armani [19] to test oxide fiber tows in elevated temperature air and steam environments. This facility was modified by Steffens [29] and Shillig [10] for testing SiC fiber tows. Steffens and Shillig found that the steam environment was detrimental to SiC fibers under creep loading. Steffens noted that the fiber tows consistently failed at the point of steam entry into the test chamber, which he concluded was caused by steam impingement on the fibers. Robertson [13] later showed that the actual cause of failure was active oxidation at the point of impingement,

extracting silicon from the tow and saturating the steam with silicic acid ($Si[OH]_4$). In order to overcome the active oxidation, Robertson [13] and Sprinkle [20] collaboratively developed a facility to saturate the steam with silicic acid prior to introducing the steam to the test chamber.

The test facility augmented by Robertson and Sprinkle was used for testing Hi-Nicalon™ S fiber tows in air and in silicic acid-saturated steam at 700° C. The fiber tows were contained within an alumina susceptor that was designed to fit within the furnace. Steam is supplied to the susceptor through a feeding tube with a slight positive pressure. A detailed description of the test setup is given by Robertson [13]. To achieve a uniform temperature distribution along the gauge section of the fiber tow specimen, the susceptor was used for testing in air and in steam.

The fiber tow, contained within the susceptor, was heated by an MTS 653.03A two-zone resistive furnace. The furnace contains four silicon carbide heating elements and two non-contacting R-type thermocouples, with two heating elements and one thermocouple assigned to each the upper and lower zones of the furnace. The thermocouples provide feedback to an MTS 409.83 temperature controller. The hot zone within the furnace is nominally 90 mm (3.5 in). However, temperature profiles were taken using a K-type thermocouple at points along the length of the furnace, and the results were used to determine an effective length for strain and strain rate calculations as described in Sections 3.4 and 3.5 below.

The fiber tow specimen was attached to hooks above and below the furnace using the holes in the fiberglass tabs. The upper hook was static while the lower hook was free to move vertically. The lower hook was attached to a high resolution Schaevitz M12-30

linear variable differential transformer (LVDT) that provided displacement measurements. The load was applied using weights attached below the LVDT. The test facility is shown in **Figure 18** with a fiber tow specimen mounted in the test configuration. Temperature data from the thermocouples and displacement data from the LVDT were collected using an MTS FlexTest 40 digital controller.

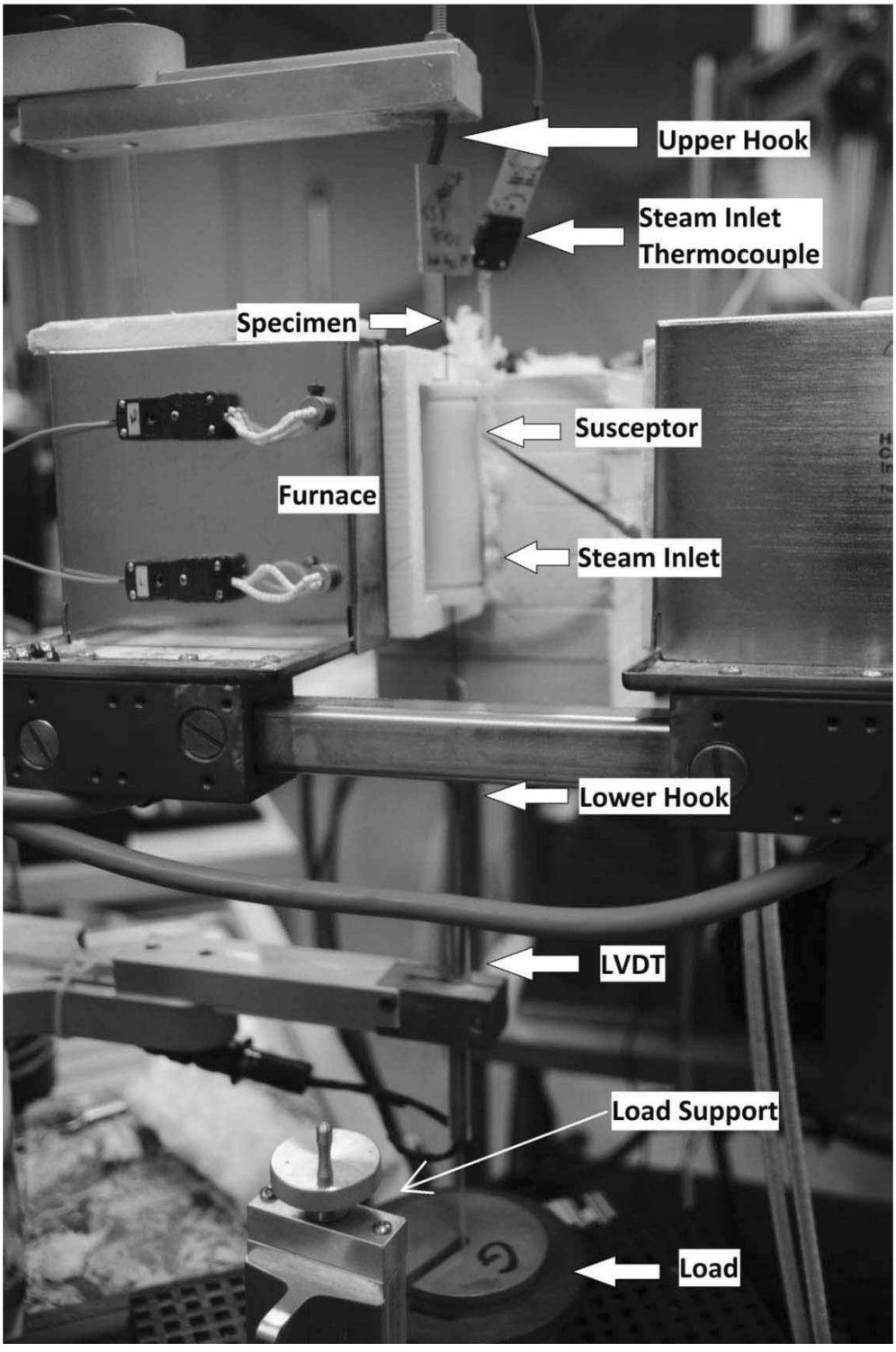


**Figure 18. Fiber tow creep test setup. Reproduced from Robertson [13]**

For tests in silicic acid-saturated steam, steam was produced using a steam generator produced by Micropyretics Heaters International (MHI), model HGA-H. The HGA-H model was also used in previous efforts by Armani [19], Steffens [29], and Shillig [10]. Robertson [13] and Sprinkle [20] made use of both steam generator models HGA-H and HGA-S. The internal components of the steam generators are identical, but the HGA-S model includes an over-temperature thermocouple to provide a fail-safe against overheating. For tests in this effort that utilized the HGA-H model, an over-temperature thermocouple was installed to monitor the steam generator temperature. For all tests in silicic acid-saturated steam, deionized water was provided to the steam generator using a Cole Parmer ® model 7518-10 peristatlic pump. Power input to the steam generator was controlled using a Variac rheostat.

After exiting the steam generator, the entered into an alumina tube that contained sacrificial silica to saturate the steam. The alumina tube passed through two MHI CX1300 heaters equipped with heating coils manufactured by I Squared R Element Company and encased in RATH KVS 174/400 insulation. As the steam moves through the alumina tube filled with silica wool, it becomes saturated with silicic acid. In addition, the steam is now heated to the desired test temperature. Finally, the saturated and heated steam enters the test chamber. The creep test facility, as configured for steam tests, is shown in **Figure 19** and **Figure 20** and is described in detail by Robertson [13].

Creep tests in air were conducted using the same setup. Since it was not necessary to saturate the air with silicic acid, the alumina tube was not filled with silica wool but still passed through the CX1300 preheaters in order to heat the air before introducing it to

the test chamber. The air supply was fed through an interface directly into the alumina tube that passed through the preheaters.

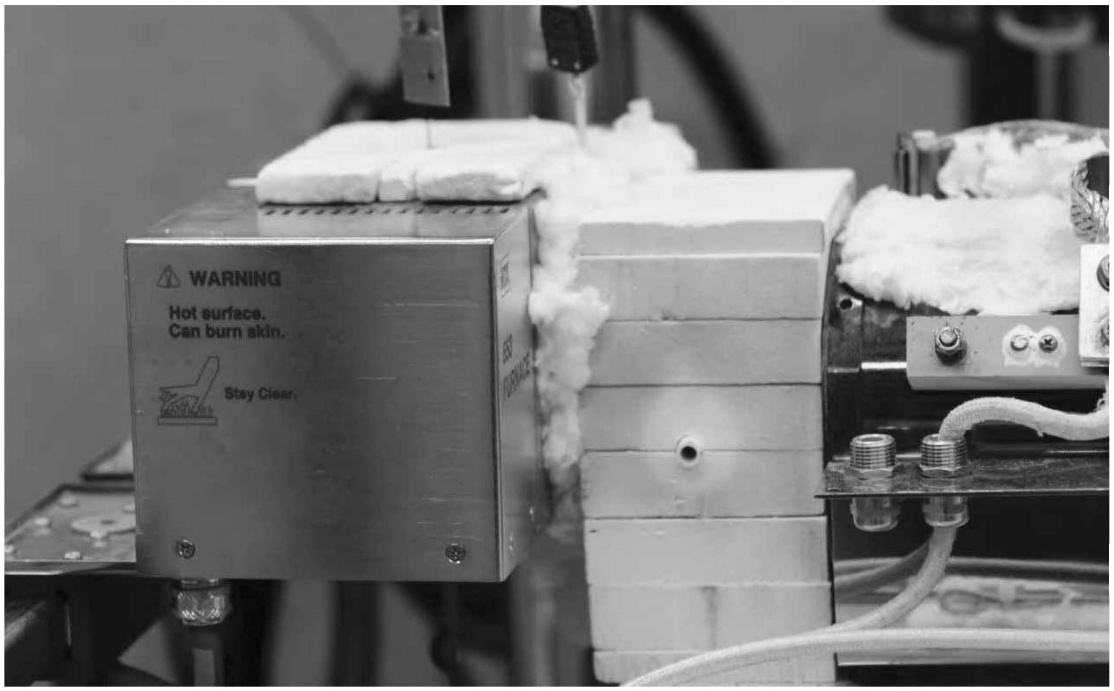


**Figure 19. Steam bleed-off tube encapsulated in layered insulation between furnace (left) and CX1300 heater (right). Reproduced from Robertson [13]**

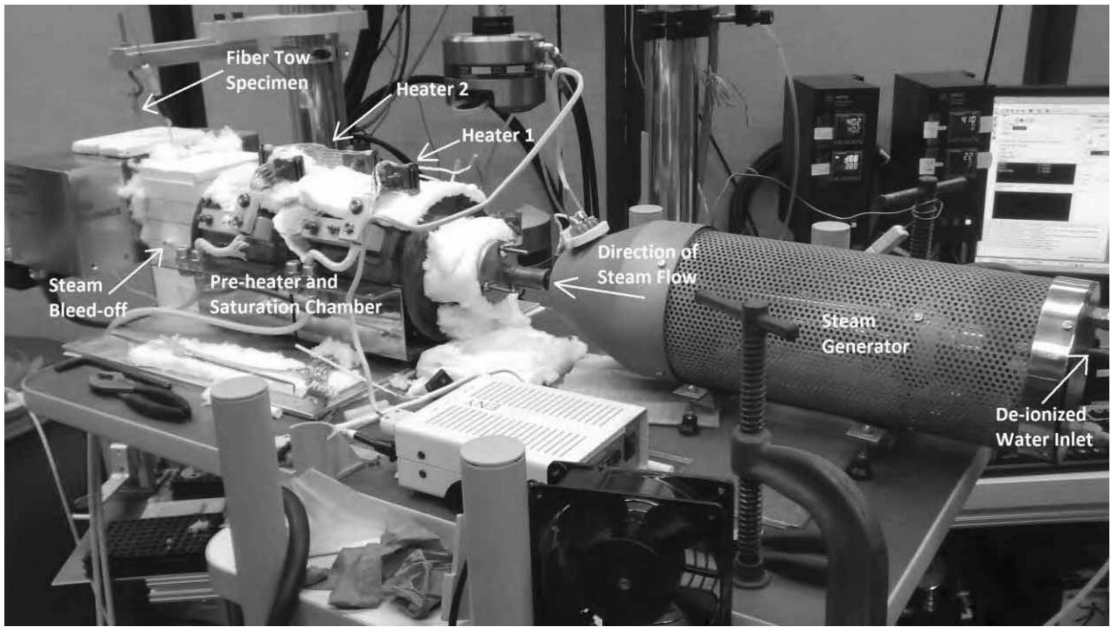


**Figure 20. Creep test facility configured for saturated steam tests. Reproduced from Robertson [13]**

### 3.4 Temperature Profiles

Prior to testing, temperature profiles of the test chamber were taken to validate the test conditions and to determine the effective length of the specimen needed to calculate the engineering strain from displacement as described in Section 3.5 below. Temperature along the furnace centerline was measured using a K-type thermocouple with an accuracy of ±3°C. A CL3515R thermometer with an accuracy of ±1.5°C was attached to the thermocouple for temperature readings within the test chamber.

Temperature measurements were taken over a 100 mm (3.94 in) length along the centerline of the furnace. The temperature profile obtained in air at 700°C is shown in **Figure 21**. Note that the zero position corresponds to the center along the axis of the furnace. Position of +60mm corresponds to the top of the furnace and position of -60mm to the bottom of the furnace.

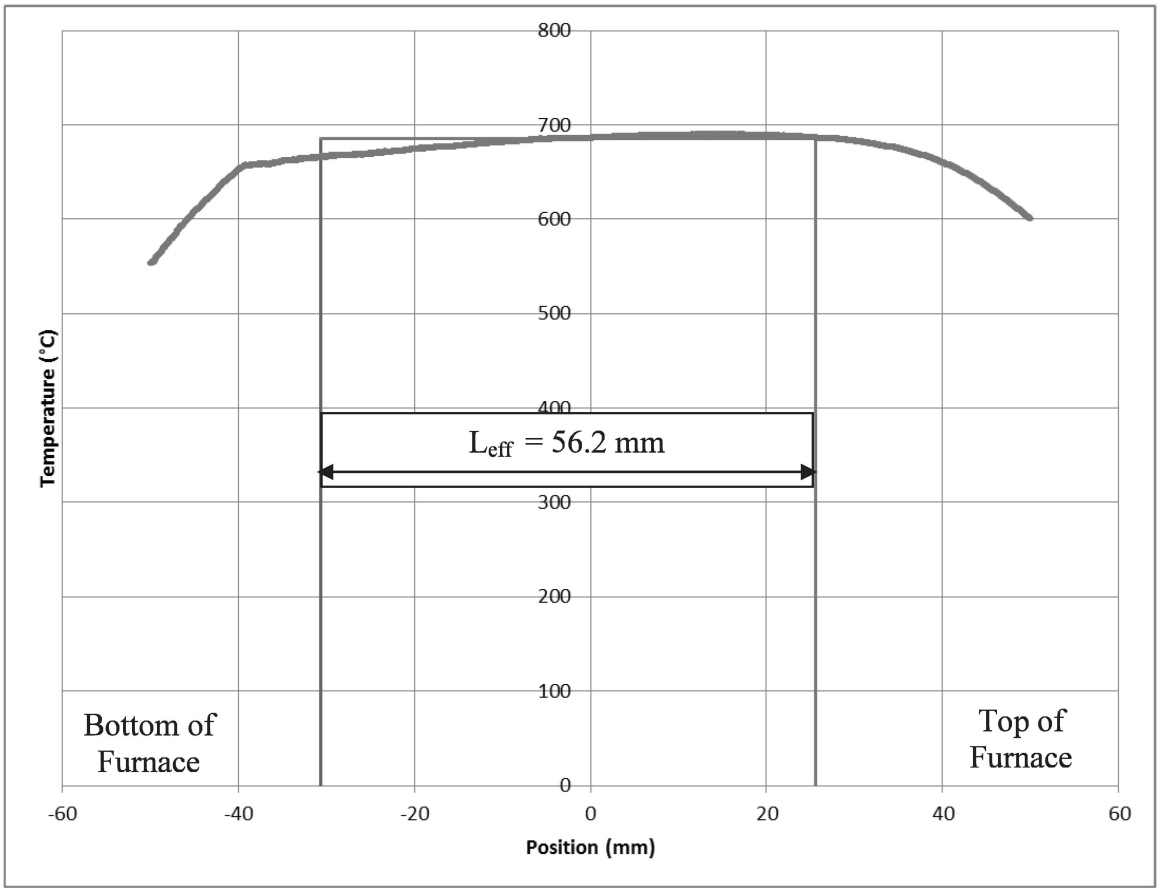


**Figure 21. Temperature profile obtained in air at 700°C**

### 3.5 Strain Measurement

The creep testing of fiber tows precludes the installation of direct strain measurement devices, such as extensometers, within the test chamber. Therefore, indirect methods must be used to determine the strain in the fiber tow specimen. The methods of strain and strain rate determination described here are discussed in detail by Armani [19].

In the dead-weight creep rig used for tensile creep testing, the bottom tab of the fiber tow specimen is connected to a Schaevitz M12-30 LVDT. The dead weights were attached to the rod on the bottom side of the LVDT core. The LVDT, located outside the

furnace and below the fiber tow, measures extension of entire fiber tow specimen. These extension data must be converted to displacement of the test section of the fiber tow in order to determine the representative strain at the test temperature. The fiber tow specimen is exposed to room temperature conditions above and below the furnace, the test temperature along the effective length, and transition temperatures within the furnace but outside gauge section as determined by the temperature profile. Therefore, a method for calculating strain and strain rate from displacement measurements, proposed by Armani [19] and used by Shillig [10], Steffens [29], Robertson [13], and Sprinkle [20], was used in this work. This method is similar to those described in literature [38 – 40]. A brief description of the method is given below.

Consider a constant cross-section test specimen of length 2L. Taking the center of the specimen gauge length as zero, creep occurs over the length –L to L. Creep is considered negligible outside these boundaries. Then, the creep strain and creep strain rate can be calculated as:

$$\varepsilon_m = \frac{\Delta l}{2L} = \int_0^t \dot{\varepsilon}_m dt \tag{4}$$

$$\dot{\varepsilon}_m = \frac{measured\ extension\ rate}{2L} = \frac{1}{2L}\int_{-L}^{L} \dot{\varepsilon} dl \tag{5}$$

Notice that the total measured strain and strain rate, calculated as shown above in **Equations 4 and 5**, account for the strain and strain rate variations that occur along the length of the fiber tow specimen based on the temperature profile. The portions of the specimen in the hottest sections of the temperature profile would experience higher strain and strain rate than those in cooler sections.

Now consider the strain and strain rate observed at the center point of the fiber length within the furnace. Let these values be denoted by subscript 0. Strain at the center of the furnace can be calculated by taking the time integral of the strain rate at that location. Engineering strain can be calculated as the change in length of a specimen over the original length of the specimen. In this treatment, the strain at center point of the furnace can be described as the overall change in length of the specimen measured by the LVDT divided by a hypothetical length called the effective gauge length, $(2L)_{eff}$. The effective length can be considered as the gauge length obtained if the temperature profile is considered as a hypothetical step function temperature profile in which all strain is treated as being accumulated at the increased temperature and no strain is accumulated at the lower temperature. The strain at the desired maximum temperature (i.e., strain at the center of the furnace) can then be described in terms of effective gauge length as shown in **Equation 6.**

$$\varepsilon_0 = \int_0^t \dot{\varepsilon}_0 dt = \frac{\Delta l}{(2L)_{eff}} \tag{6}$$

Similarly, the strain rate at desired maximum temperature (or at the center of the furnace) can be expressed in terms of effective gauge length as:

$$\dot{\varepsilon}_0 = \frac{measured\ extension\ rate}{(2L)_{eff}} = \frac{1}{(2L)_{eff}} \int_{-L}^{L} \dot{\varepsilon} dl \tag{7}$$

Then, the ratio of **Equation 5** to **Equation 7** can be written:

$$\frac{\dot{\varepsilon}_m}{\dot{\varepsilon}_0} = \frac{\Delta l}{(2L)_{eff}} \tag{8}$$

Stress is constant in dead-weight creep testing, and temperature can be considered as a function of location along the specimen according to the temperature profile. These considerations can be applied to the general power law creep equation (**Equation 3**) to obtain:

$$\dot{\varepsilon} = A\sigma^n \exp\left(\frac{-Q}{RT(l)}\right) \tag{9}$$

**Equations 5, 8, and 9** can then be combined to express the ratio of measured strain rate to actual strain rate as a function of temperature only, given as:

$$\frac{\dot{\varepsilon}_m}{\dot{\varepsilon}_0} = \frac{1}{2L}\int_{-L}^{L} \exp\left\{\frac{-Q}{R}\left(\frac{1}{T(l)} - \frac{1}{T_0}\right)\right\} dl \tag{10}$$

This ratio can then be expressed in terms of a numerical summation of increments of length h, where L=hk and k is an integer. The ratio of measured to actual strain rate then becomes:

$$\frac{\dot{\varepsilon}_m}{\dot{\varepsilon}_0} = \frac{1}{2k}\sum_{i=-k}^{k} \exp\left\{\frac{-Q}{R}\left(\frac{1}{T(l)} - \frac{1}{T_0}\right)\right\} \tag{11}$$

Now, the effective gauge length can be calculated as:

$$(2L)_{eff} = 2L\left(\frac{\dot{\varepsilon}_m}{\dot{\varepsilon}_0}\right) \tag{12}$$

The effective gauge length, once calculated, can be used to determine the strain and strain rate of the fiber tow specimen using the displacement calculations from the LVDT outside the hot zone of the furnace. This approach, along with the temperature profiles determined in Section 4.2 and creep activation energy of 177 kJ/mol of Hi-

Nicalon™ S was used to calculate effective gauge lengths in air and in steam at 700°C. The calculated effective lengths in air and in steam are shown in Table 4.

**Table 4. Effective gauge lengths of Hi-Nicalon™ S fibers at 700°C**

| | Air | Steam |
|---|---|---|
| Effective Length (mm) | 56.20 | 73.51 |

This approach differs from that used by Hammond [41] and Yun, et al. [42] in that they assumed that the majority of creep deformation occurred only within the furnace hot zone and therefore used the flat portion of the temperature profile to determine the gauge length. This approach is both subjective because it relies on human determination of the flat zone and is dependent of the flatness of the temperature profile and the sharpness at which the temperature drops off at the edges of the hot zone. Alternatively, this method is somewhat more independent of the shape of the temperature profile

### 3.6 Experimental Procedures for Creep Testing in Air and in Steam

Detailed procedures for creep testing of fiber tows are given in Appendix A2 of Steffens [29]. As discussed in Section 3.3 above, the test facility used by Steffens was redesigned in order to saturate the steam with silicic acid before introducing it into the test chamber. Procedures for generating and saturating the steam are given in Appendix A of this document.

# IV. Results and Discussion

## 4.1 Creep of Hi-Nicalon™ S Fiber Tows at 700°C

Hi-Nicalon™ S fiber tows were subjected to tensile creep through dead weight loading in dry air and in silicic acid-saturated steam environments. Creep run-out was set to 100h. Creep-rupture test results are summarized in **Table 5**.

**Table 5. Creep results obtained for Hi-Nicalon™ S SiC fiber tow specimens at 700°C in air and in silicic acid-saturated steam**

| Specimen ID | Test Environment | Creep Stress (MPa) | Creep Lifetime (h) | Steady-State Creep Rate ($s^{-1}$) | Creep Strain (%) |
|---|---|---|---|---|---|
| A13 | Air | 1257 | 0.58 | 1.82 E -07 | 0.079 |
| A12 | Air | 1223 | 1.59 | 8.42 E -08 | 0.158 |
| A11 | Air | 1156 | 26.44 | 5.03 E -09 | 0.236 |
| A16 | Air | 1123 | 1.33 | 2.76 E -08 | 0.031 |
| A15 | Air | 1123 | 2.23 | 7.09 E -08 | 0.180 |
| A10 | Air | 1089 | 85.03 | 8.71 E -09 | 0.519 |
| A3 | Air | 1023 | 2.87 | 5.28 E -08 | 0.209 |
| A8 | Air | 1023 | 100† | 4.65 E -09 | 0.431 |
| A7 | Air | 980 | 100† | 3.86 E -09 | 0.417 |
| A4 | Air | 937 | 84.45 | 1.86 E -09 | 0.280 |
| A9 | Air | 2.96 | 100† | 1.80 E -09 | 0.071 |
| S27 | Steam | 787 | .013 | ‡ | ‡ |
| S25 | Steam | 798 | 2.08 | 2.78 E -08 | .091 |
| S22 | Steam | 752 | 100† | 2.06 E -09 | 0.169 |
| S21 | Steam | 700 | 1.00 | 7.00 E -08 | 0.094 |
| S16 | Steam | 625 | 89.85 | 1.46 E -09 | 0.160 |
| S12 | Steam | 538 | 99.58 | 7.78 E -10 | 0.222 |
| S3 | Steam | 450 | 100† | 5.95 E -10 | 0.162 |
| S4 | Steam | 2.96 | 100† | 3.34 E -10 | 0.012 |

† Creep run-out defined as 100 h at creep stress. Failure did not occur when the test was terminated

‡ Insufficient data to determine creep and creep rate due to very short test duration

The experimental creep data can be used to determine the predominant creep mechanism. Fitting the experimental data in **Figure 22** with a Norton-Bailey power law

yields the stress exponents. These values of n≈5.1 in air and n≈5.3 in silicic-acid saturated steam suggest cavity growth controlled creep. However, these values are close to the value of n≈5.0 found by both Steffens [29] and Robertson [13] for Hi-Nicalon™ S fiber tows in air at 800°C, which corresponds to climb-controlled dislocation creep. Both Steffens, testing in unsaturated steam, and Robertson, testing in silicic acid-saturated steam, reported the stress exponent of n≈4.0 at 800°C which is consistent with grain boundary sliding and cavity growth. The results of this work indicate cavity growth as the primary creep mechanism in silicic acid-saturated steam at 700°C.

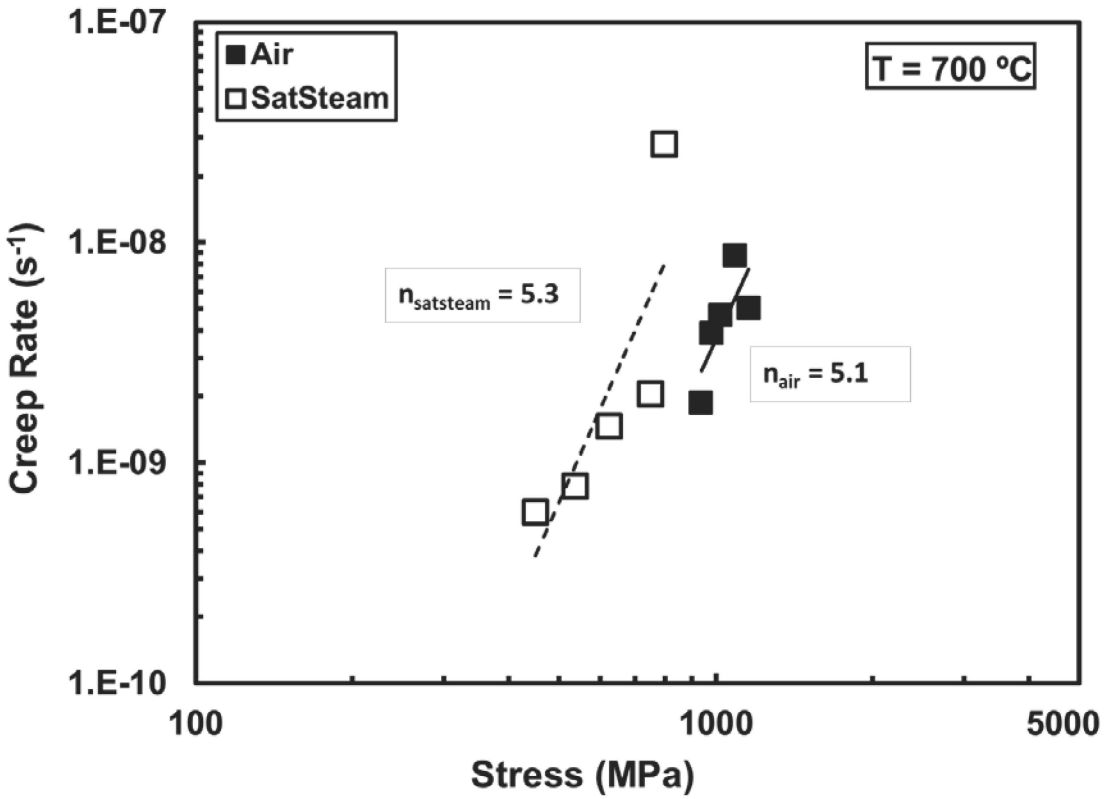


**Figure 22. Creep strain rate vs. applied creep stress for Hi-Nicalon™ S fiber tows at 700°C in air and in saturated steam. Calculated creep exponents are shown**

Steffens [29], Shilling [10], and Robertson [13] all conducted creep tests of Hi-Nicalon™ S fiber tows in air and in steam at elevated temperatures using the same general methodology and laboratory setup developed by Armani [19]. Robertson and Sprinkle [20] made significant changes to the test facility to allow for pre-saturation and pre-heating of the steam before it entered the test chamber. Robertson showed that tests conducted at 800°C in saturated steam using the modified test facility revealed much better creep performance and an order of magnitude lower creep rates than the tests performed at the same temperature in unsaturated steam by Shillig and Steffens.

Determining creep strains and creep rates for Hi-Nicalon™ S fiber tows at 700°C is not a trivial exercise for several reasons. First, the creep studied in this work may not be creep in the traditional sense but may be a result of progressive failure of the fibers within the fiber tow specimen which leads to a creep-like phenomenon due to the manner in which stress is carried by the remaining intact fibers in the tow until failure. Oxidation of the fibers also takes place, particularly in steam, which causes the fibers to become more compliant and slightly decreases the fiber cross-section, leading to increased calculated stress. A constant cross-sectional area for the fiber tow was used in calculations, but the cross-sectional area clearly does not remain unchanged through the entire duration of the test.

Creep-rupture results obtained at 700°C in air and in saturated steam are shown in **Figure 23**. The data show a fairly drastic transition from early failure (less than three hour creep lifetime) to run-out, with no lifetimes between 30 and 80 hours. This transition

is sharper for tests in saturated steam than in air at 700°C. At 800°C, Robertson reported a similarly sharp transition from early failure to run-out.

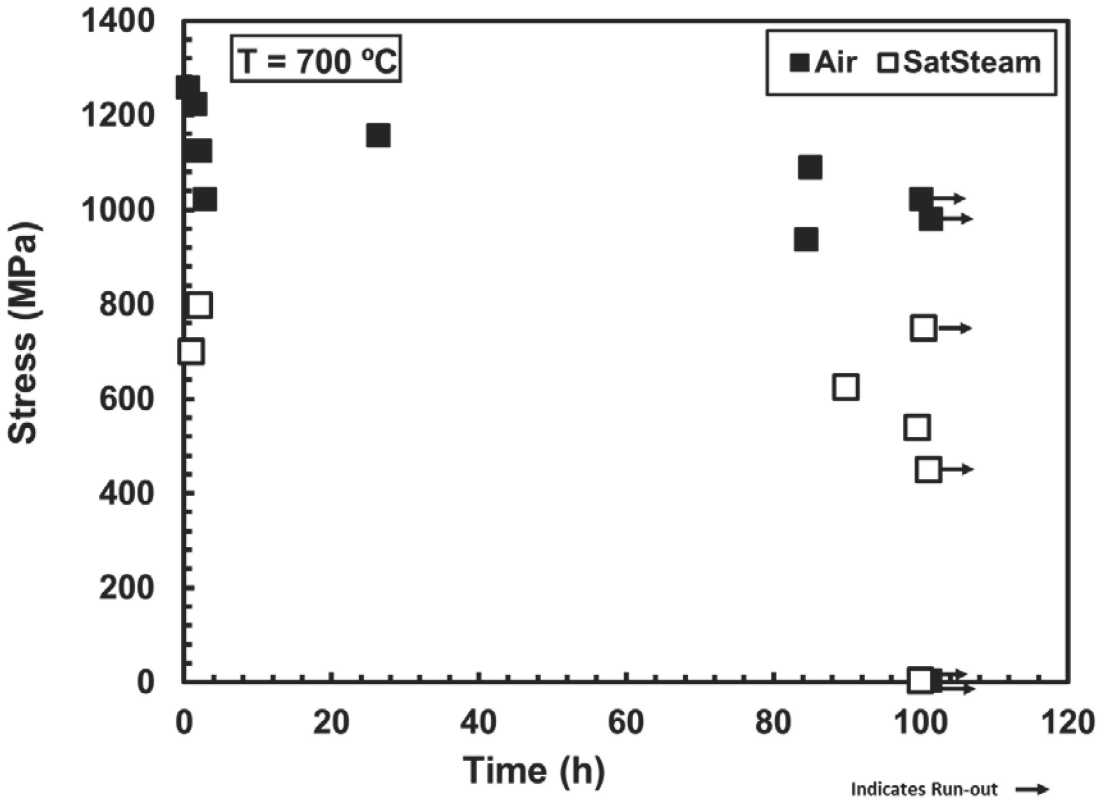


**Figure 23. Creep lifetimes of Hi-Nicalon S fibers at 700°C in air and in silicic acid-saturated steam**

Representative creep curves obtained at 700°C are shown in **Figures 24 - 27**. With the exception of the specimens tested at a creep stress of 2.96 MPa, all specimens in air and in steam show primary and secondary creep regimes. **Figure 25** and **Figure 27** present the first eight hours of test data in order to show both the primary to secondary creep transition more clearly. Some creep curves, such as the creep curve in **Figure 27** produced at 1023 MPa in air, appear to show a tertiary creep regime. However, this is

increase in strain rate is likely due to progressive failure of the fibers in the fiber tow specimen.

The time at which transition from primary to secondary creep occurred was approximately the same in all tests performed at 700°C in air. Notably, the transition from primary to secondary creep occurs earlier in saturated steam than in air. It is noteworthy that the specimens that achieved run-out in air accumulated larger strains than those that achieved run-out in steam.

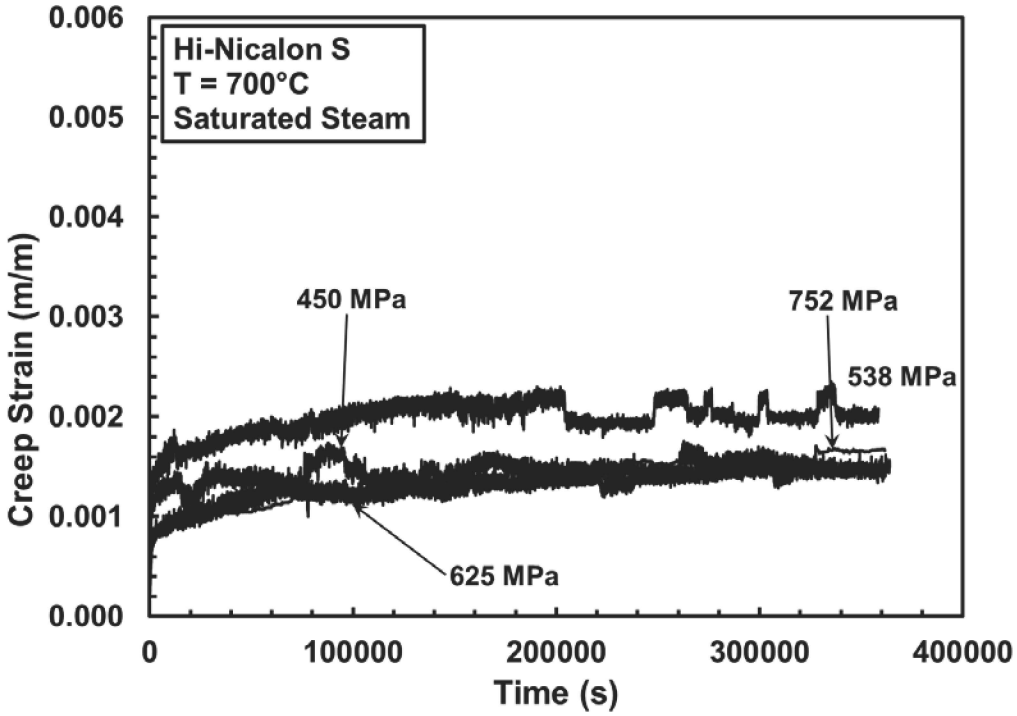


**Figure 24. Representative creep curves for Hi-Nicalon™ S fibers at 700°C in silicic acid-saturated steam**

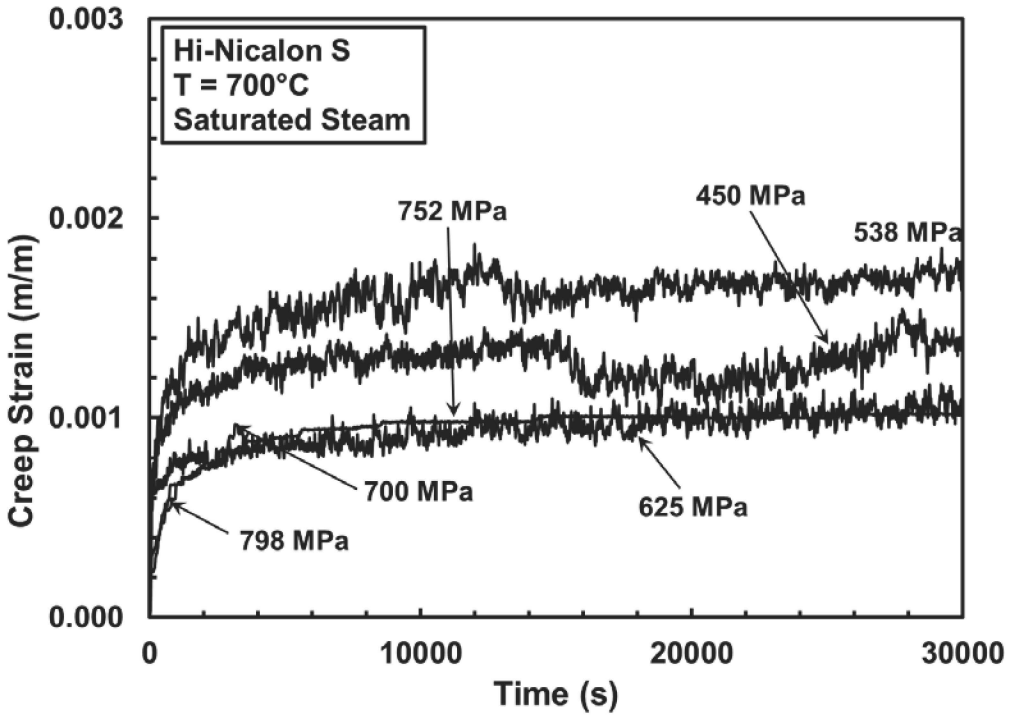


**Figure 25. Representative creep curves for early stages of creep of Hi-Nicalon™ S fibers at 700°C in silicic acid-saturated steam**

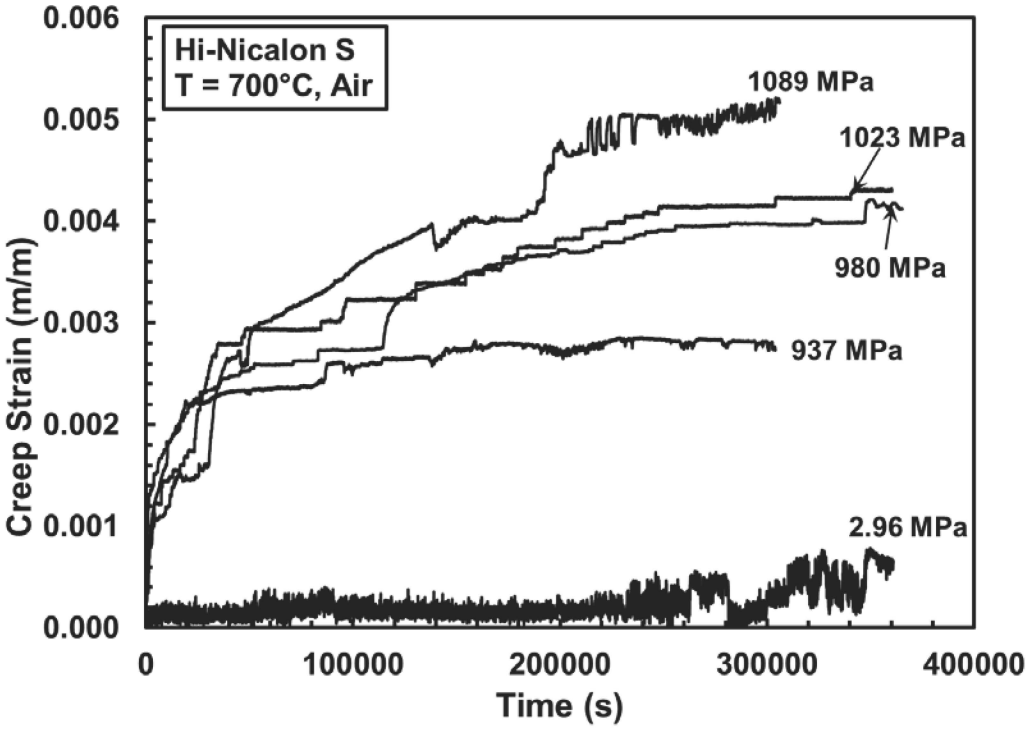


**Figure 26. Representative creep curves for Hi-Nicalon™ S fibers at 700°C in air**

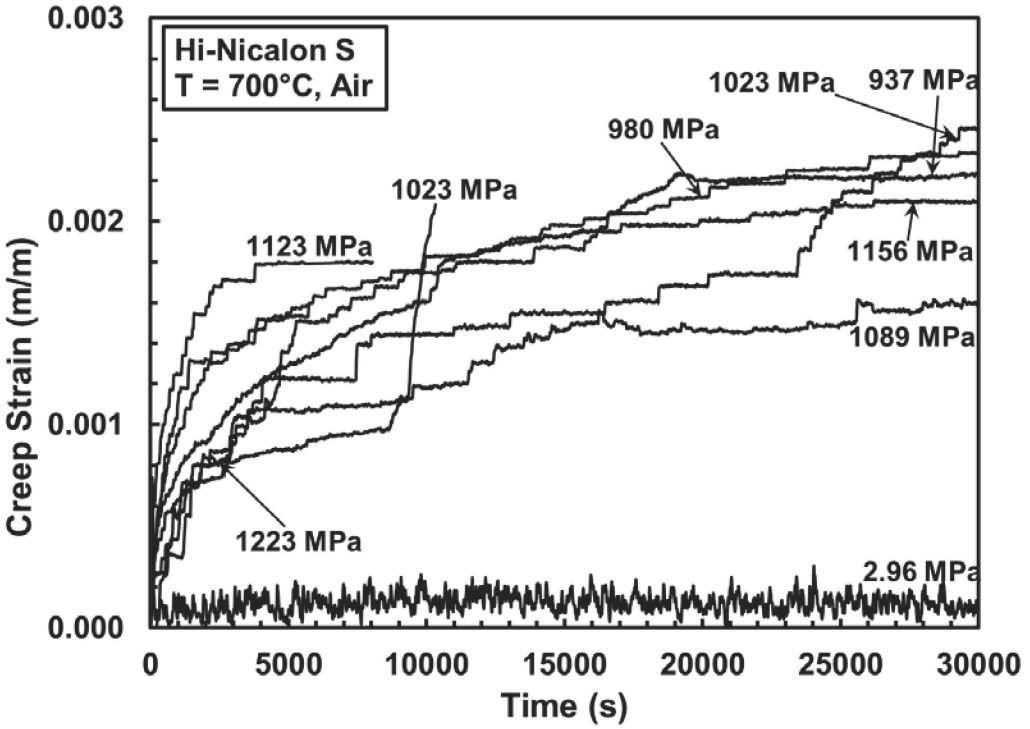


**Figure 27. Representative creep curves for early stages of creep of Hi-Nicalon™ S fibers at 700°C in air**

## 4.2 Post-Test Microstructural Analysis of Hi-Nicalon™ S Fiber Tows

Post-test microstructural analysis of the Hi-Nicalon™ S fiber tow specimens was conducted using a FEI Quanta 450 scanning electron microscope (SEM). A total of fifteen specimens taken from six fiber tows, three tested in saturated steam and three tested in air, were analyzed.

Fiber tows were prepared for microstructural analysis by mounting them on an aluminum puck with a 45° surface. First, double-sided carbon tape was applied to the angled surface of the mounting puck. The fibers were then pressed onto the carbon tape such that the portion of the fibers to be analyzed protruded 1-5 mm above the angled surface. After placing the fibers, a layer of silver paint was applied in order to secure the fibers in place. The silver paint also provides electric conductivity between the fibers and the aluminum puck, which is required for SEM imaging. After the fibers were securely fixed in place, the remainder of the fiber tow was cut at the bottom of the angled surface to separate it from the specimen to be analyzed.

The fiber tow specimens analyzed using SEM were selected to give a representative sample of the tests conducted. For both air and saturated steam, one tow that ruptured in less than two hours, one tow achieved creep run-out (100 h) with a load within 10% of the rupture specimen load, and one tow that was tested at minimal load (2.96 MPa applied stress). For all fiber tows, one specimen was created from the fiber segment near the air or steam entry in the creep test apparatus and one was taken from near the midpoint of the segment, either by cutting or by using the fracture surface. For the fiber tows tested in saturated steam, a third SEM specimen was cut from the upper section of the tow in order to compare oxidation along the effective length of the fiber

tow. The SEM specimens are listed in **Table 6**. All SEM micrographs taken as part of this work are included in Appendix B.

**Table 6. Hi-Nicalon™ S specimens analyzed using scanning electron microscope.**

| Specimen | Creep Test Load | Creep Test Duration | SEM Specimen Location |
|---|---|---|---|
| A8 | 1023 MPa | 100 h (Run-out) | Midpoint |
| | | | Lower Section |
| A9 | 2.96 MPa | 100 h (Run-out) | Midpoint |
| | | | Lower Section |
| A16 | 1123 MPa | 1.35 h | Fracture Surface |
| | | | Below Fracture |
| S4 | 2.96 MPa | 100 h (Run-out) | Upper Section |
| | | | Midpoint |
| | | | Lower Section |
| S22 | 750 MPa | 100 h (Run-out) | Upper Section |
| | | | Midpoint |
| | | | Lower Section |
| S25 | 798 MPa | 1.83 h | Above Fracture |
| | | | Fracture Surface |
| | | | Below Fracture |

Fiber tows tested by Steffens [29] and Shillig [10] had shown significant variation of chemical composition along the length of the fibers. This variation was likely due to the presence of active oxidation near the point at which the unsaturated steam entered the test chamber, leading to variations in the presence of silica scale and in pitting along the length of the fiber as the steam became saturated while traveling upward through the test chamber. Robertson [13] showed that tests conducted in saturated steam resulted in a more uniform appearance and chemical composition along the length of the fibers at 800°C, with minimal pitting or observable silica deposits. The SEM images of fiber tows tested at 700°C likewise appeared more uniform along the length of the fibers. The variation in composition along the tow resulting from tests in unsaturated steam conducted by Shillig [10] can be seen in **Figure 28** which shows SEM images typical of

those observed near the steam entry point (**Figure 28a**) and near the top of the hot zone in the test chamber (**Figure 28b**). The relatively uniform appearance of the fibers along the length of the fiber tow produced in tests at 700°C in saturated steam can be seen in **Figure 29a**, showing a fiber near the bottom of the test chamber, and **Figure 29b**, which shows a fiber portion near the top of the chamber. These images are typical of those observed in this work.

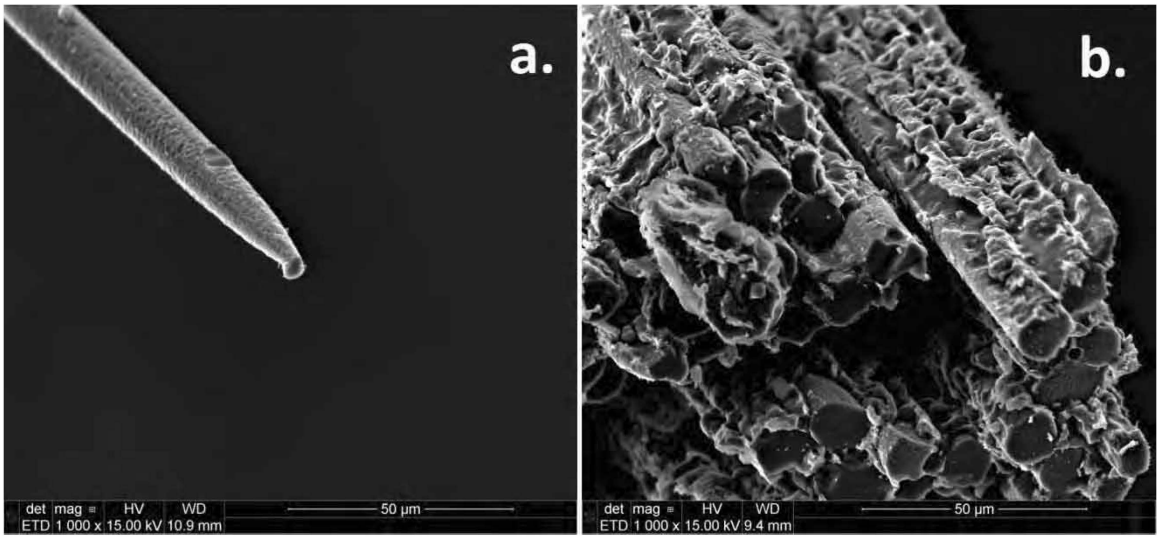


**Figure 28. SEM images showing variations along the length of the fiber tow observed for tests in unsaturated steam. a) Fiber degradation due to active oxidation. This image is typical of the oxidation seen near the steam entry point into the test chamber. b) Silica scale growth, typical of that observed near the top of the hot zone in the test chamber. Reproduced from Shillig [10]**

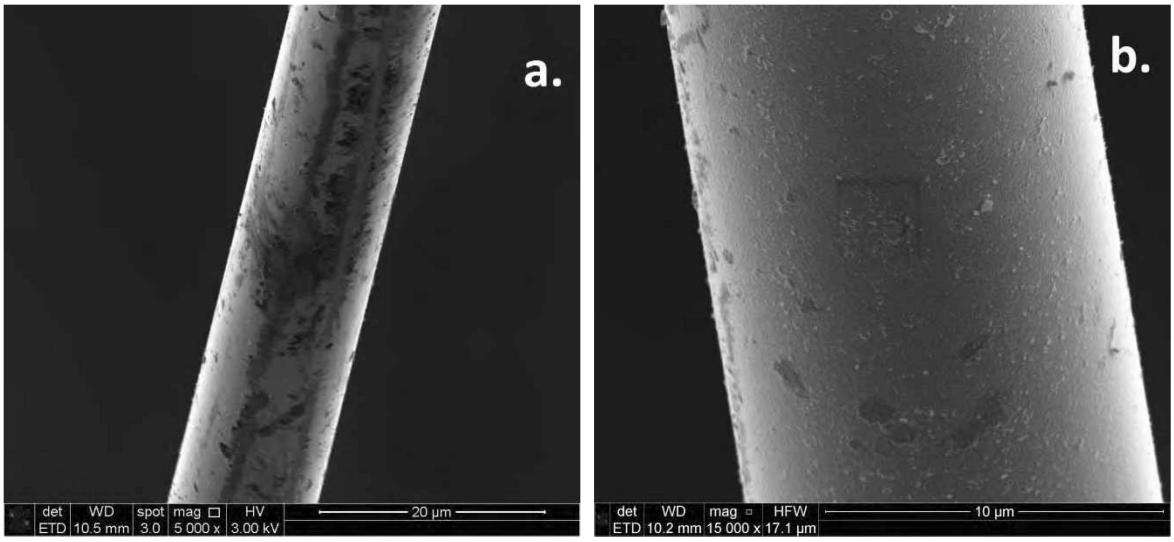


**Figure 29. SEM images showing relatively uniform appearance along the length of a fiber tow tested in saturated steam. These images are typical of those seen on all specimens tested in saturated steam and analyzed using SEM. a) Image of fiber from the "Steam 25" specimen near the steam inlet in the test chamber b) Image of fiber from the "Steam 25" specimen near the top of the hot zone in the test chamber showing little visible evidence of scale**

A common feature of fibers tested in air and in silicic acid-saturated steam was a generally smooth surface with some areas displaying a mottled appearance. A representative image for tests in air can be seen in **Figure 30**, while **Figure 31** shows a similarly representative image for tests in saturated steam. Robertson [13] had reported the mottled appearance for fibers tested in saturated steam, but its presence on fibers tested in air was not previously reported. Energy dispersive spectroscopy (EDS) was used to discern the composition of the mottled areas. EDS results were inconclusive for the fibers tested in air, but it is possible that the mottling is a result of the calcium deposits from the sizing. EDS analysis for fibers tested in saturated steam showed higher oxygen content and lower silicon content in the mottled areas than in other areas of the fibers. **Figure 32** shows a representative EDS sample of a specimen with mottling on the right

side of the specimen in the SEM micrograph **Figure 32a**. An image taken using EDS of the same area is shown in **Figure 32b**, with brighter green areas depicting higher levels of oxygen content.

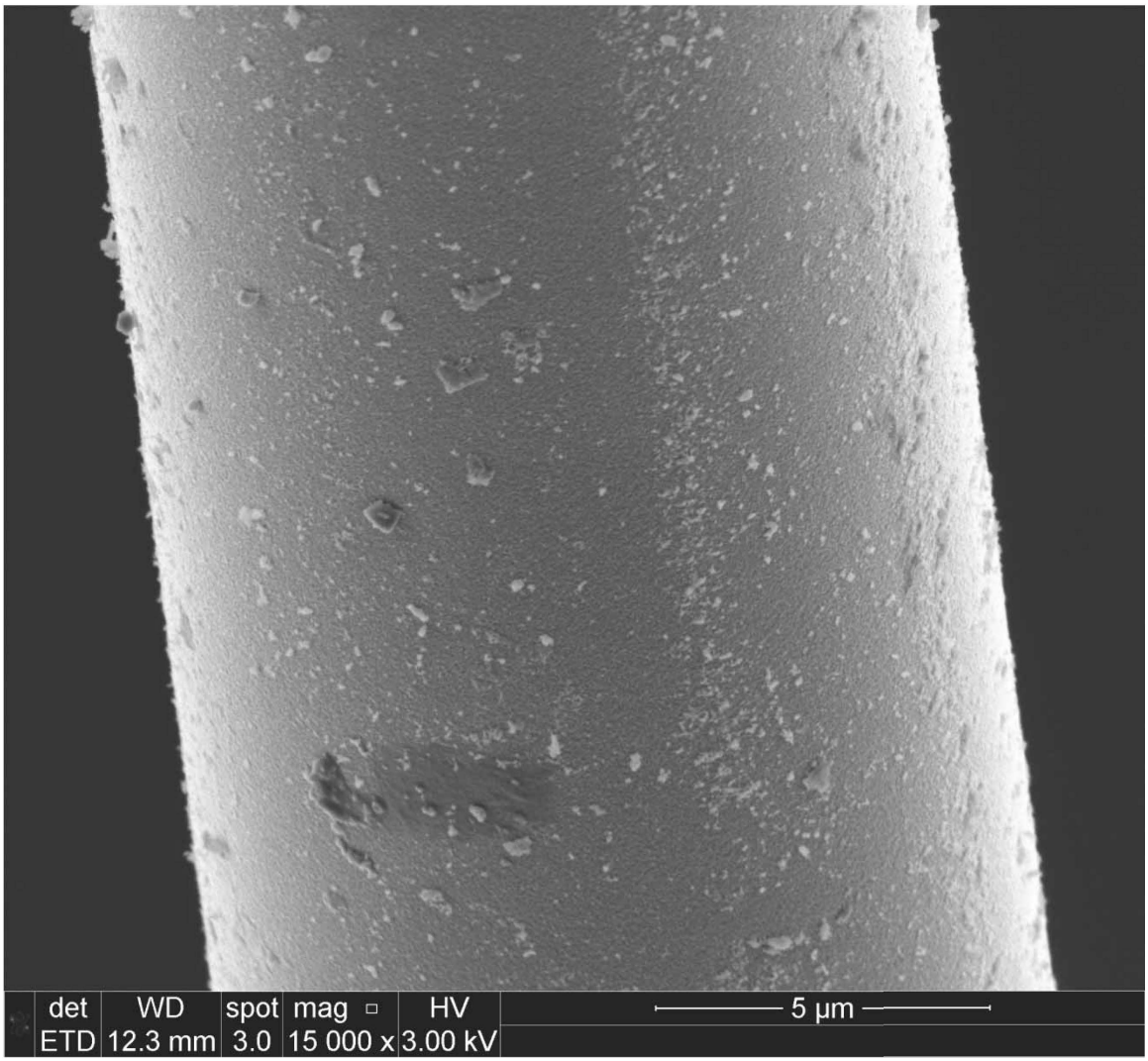


**Figure 30. SEM image of Hi-Nicalon™ S fiber from near the midpoint of the specimen "Air 8" tested in air at 700°C. The fiber surface appears generally smooth, with some areas displaying a mottled appearance ($\sigma_{cr}$ = 1023 MPa, $t_f$ > 100 h)**

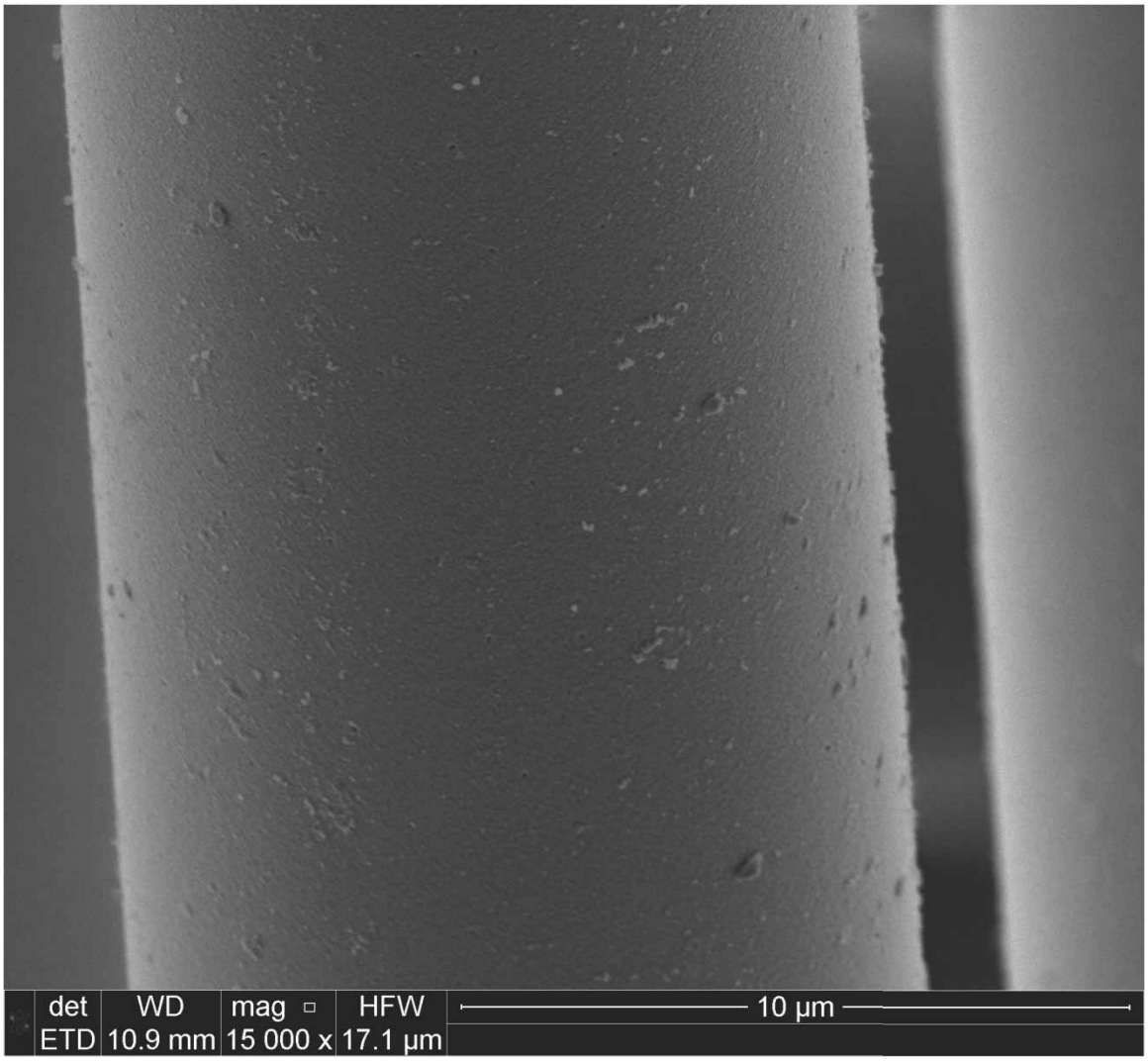


**Figure 31. SEM image of Hi-Nicalon™ S fiber from near the midpoint of the specimen "Steam 4" tested in saturated steam at 700°C. The fiber surface appears generally smooth, with some areas displaying a mottled appearance ($\sigma_{cr}$ = 2.96 MPa, $t_f$ > 100 h)**

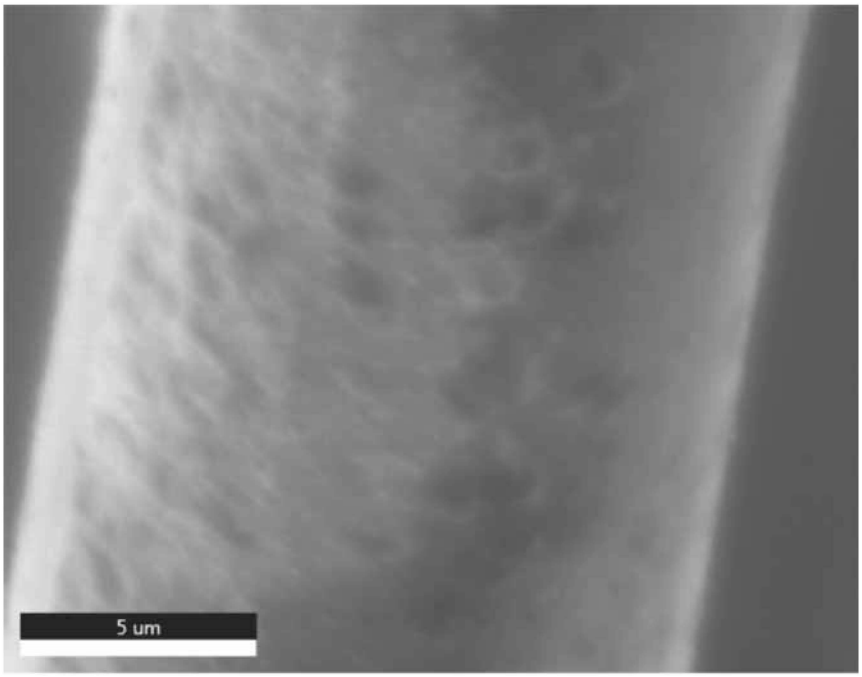


**(a)**

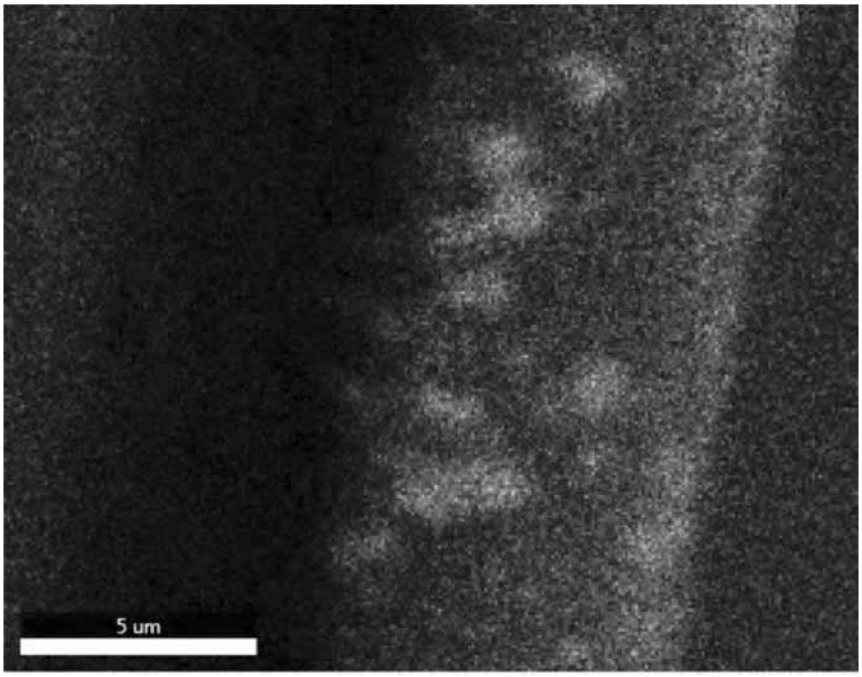


**(b)**

**Figure 32. SEM and EDS analysis of Hi-Nicalon™ S fiber near the midpoint of specimen "Steam 22" tested in saturated steam at 700°C ($\sigma_{cr}$ = 750 MPa, $t_f$ > 100 h). a) SEM image of a portion of the fiber showing mottled appearance. b) EDS analysis of oxygen content. Brighter areas show higher levels of oxygen present**

A number of fibers analyzed under SEM showed dark areas running axially along the fiber length. These dark areas occurred in relatively straight lines, indicating that they resulted from contact between fibers. As noted for the mottled areas in **Figure 32**, the lighter areas show higher oxygen content while oxygen content is lower in the darker areas. In the case of the dark axial lines, such as those seen in **Figure 33** (tested in air) and **Figure 34** (tested in saturated steam), this is indicative of areas of contact between two neighboring fibers. The contact between fibers limited the exposure of the surfaces to oxidation, resulting in lower oxygen content than neighboring areas on the fibers.

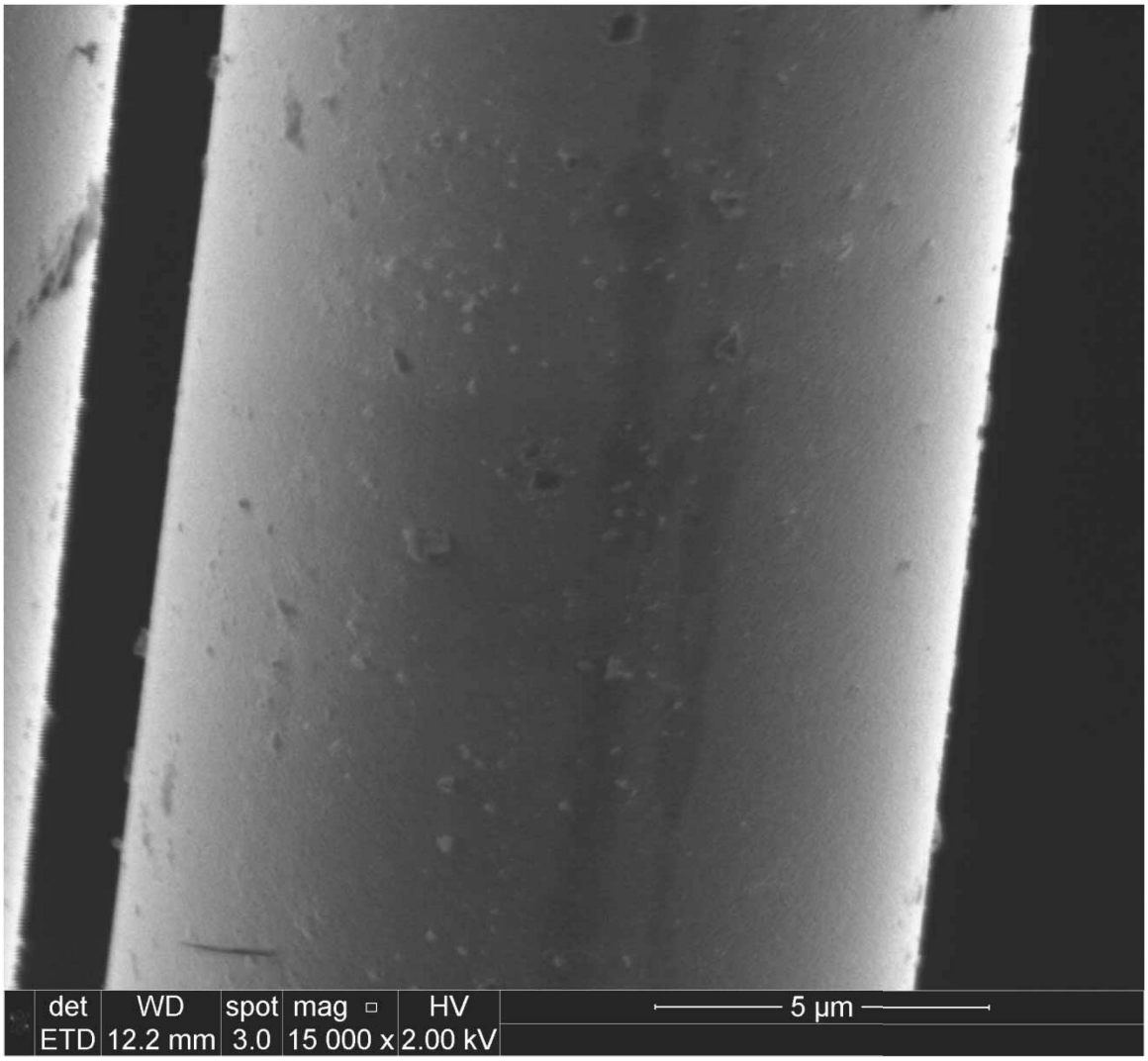


**Figure 33. SEM image of Hi-Nicalon™ S fiber from near the midpoint of the specimen "Air 16" tested in air at 700°C. The dark vertical line is indicative of contact between fibers ($\sigma_{cr}$ = 1123 MPa, $t_f$ = 1.35 h)**

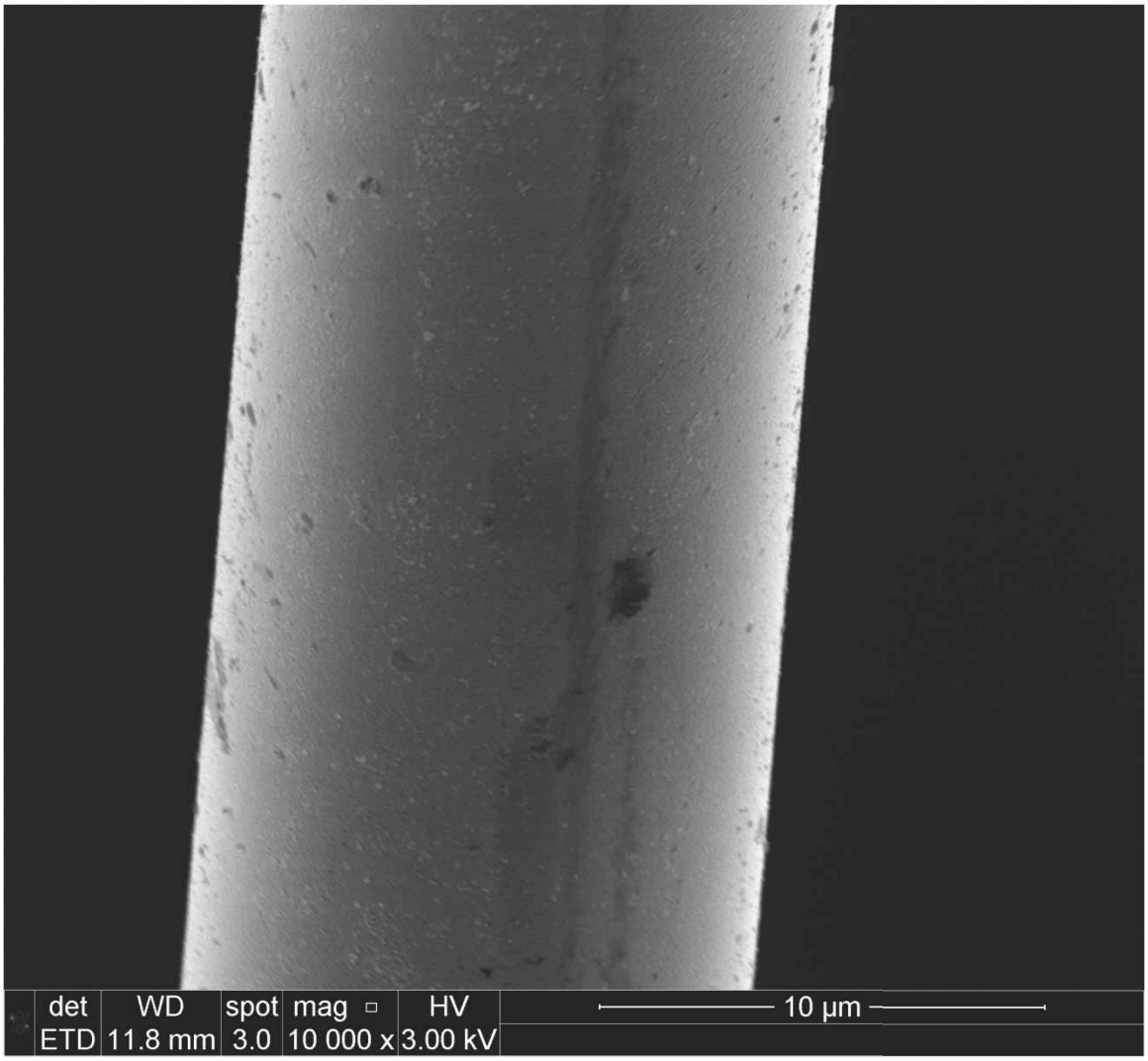


**Figure 34. SEM image of Hi-Nicalon™ S fiber from near the midpoint of the specimen "Steam 25" tested in saturated steam at 700°C. The dark vertical line is indicative of contact between fibers ($\sigma_{cr}$ = 798 MPa, $t_f$ = 1.83 h)**

Fracture surfaces of two fiber tows that experienced creep rupture, one tested in air and one tested in silicic acid-saturated steam, were analyzed using SEM. Within the fiber tow tested in air, fibers generally showed evidence of classic brittle fracture, as shown in **Figure 35a**. A clear initiation point is visible on the edge of the fracture surface, and there is evidence of radial progression of the fracture from that point. Some fibers within the tow also showed evidence of what appear to be voids within the fibers, as seen in **Figure 35b**. If these voids existed prior to testing, the fibers would have been porous and more susceptible to premature failure in creep. However, it should be noted that even the fibers that appear to have voids show some evidence of classic brittle fracture, including initiation points along the edges of the fibers and at least some evidence of progressive failure.

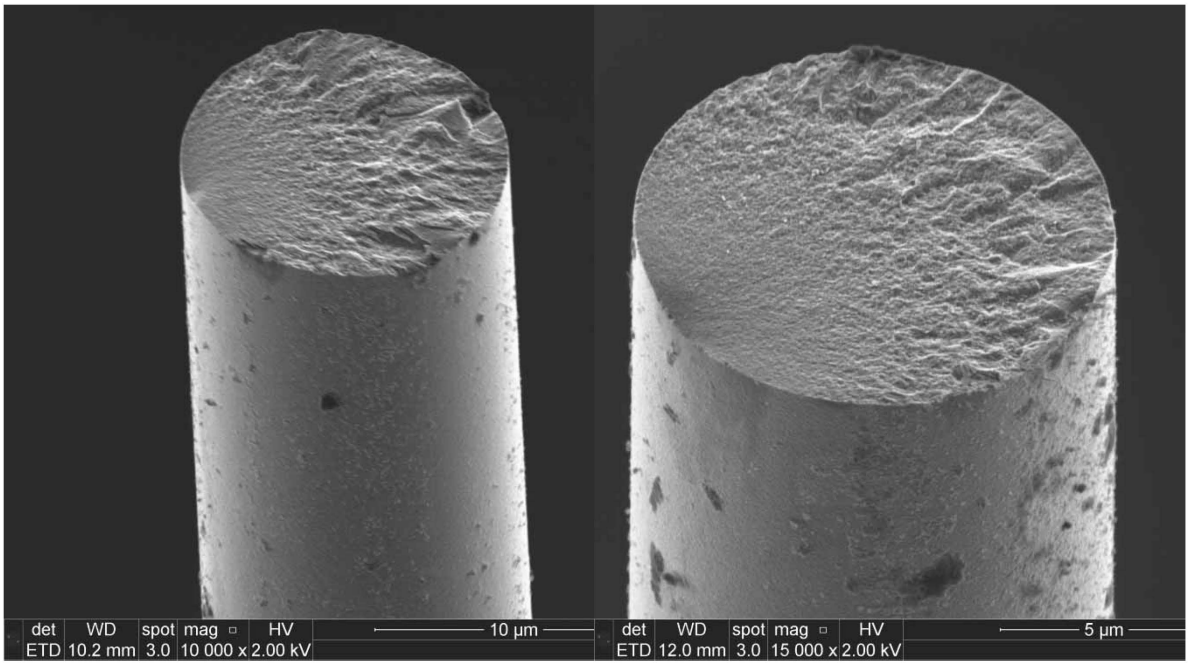


**(a)**

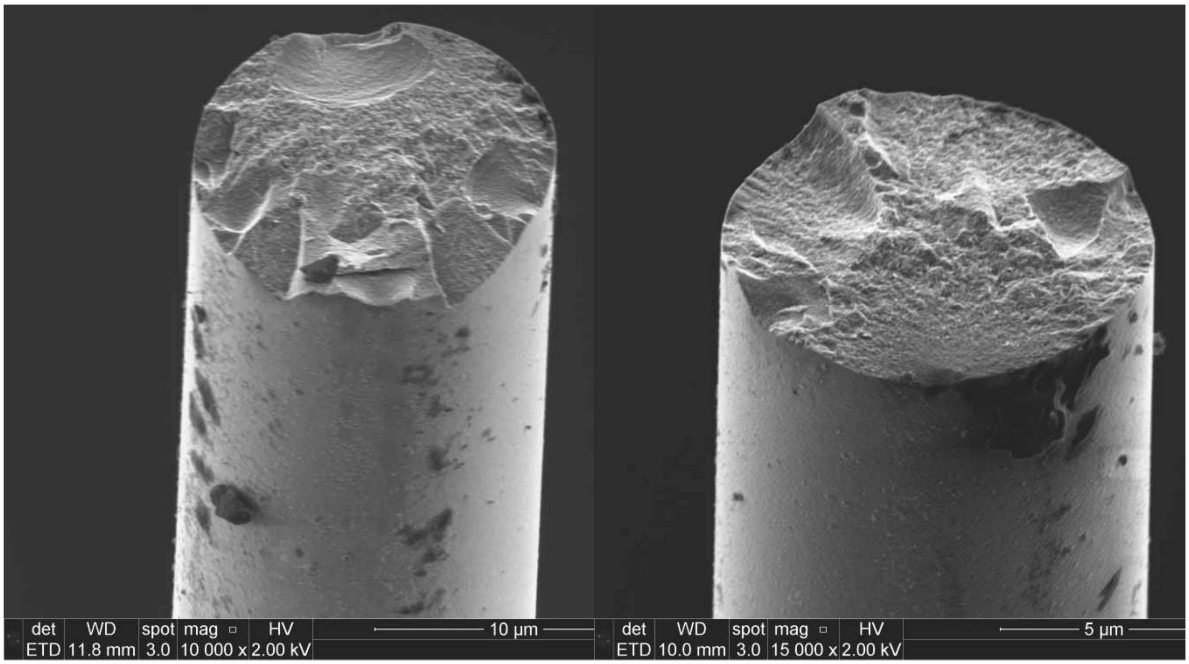


**(b)**

**Figure 35. SEM micrograph of fracture surfaces of four fibers in specimen "Air 16" showing a) classic brittle fracture and b) evidence of porous areas in the fiber at the fracture surface ($\sigma_{cr}$ = 1123 MPa, $t_f$ = 1.35 h)**

The SEM analysis of "Steam 25," a fiber tow specimen tested in saturated steam at a creep stress of 798 MPa, did not generally show evidence of classical brittle failure in the fibers examined. Additionally, areas around the edge of the fracture surface were darker in SEM microscopy, as shown in **Figure 36** and **Figure 37**. These dark areas could be evidence of slow crack growth leading to failure of the fibers. EDS analysis was conducted on several fracture surfaces that showed the dark areas contained higher levels of carbon and oxygen and lower levels of silicon compared to the fibers as a whole. **Figure 38a** shows a micrograph of a fiber fracture surface with a dark ring around the edge of the surface. In **Figure 38b** and **Figure 38c**, respectively, the increased carbon and oxygen content within the ring can be seen. **Figure 38d** shows the decreased silicon content within the dark ring relative to the remainder of the fiber and fracture surface.

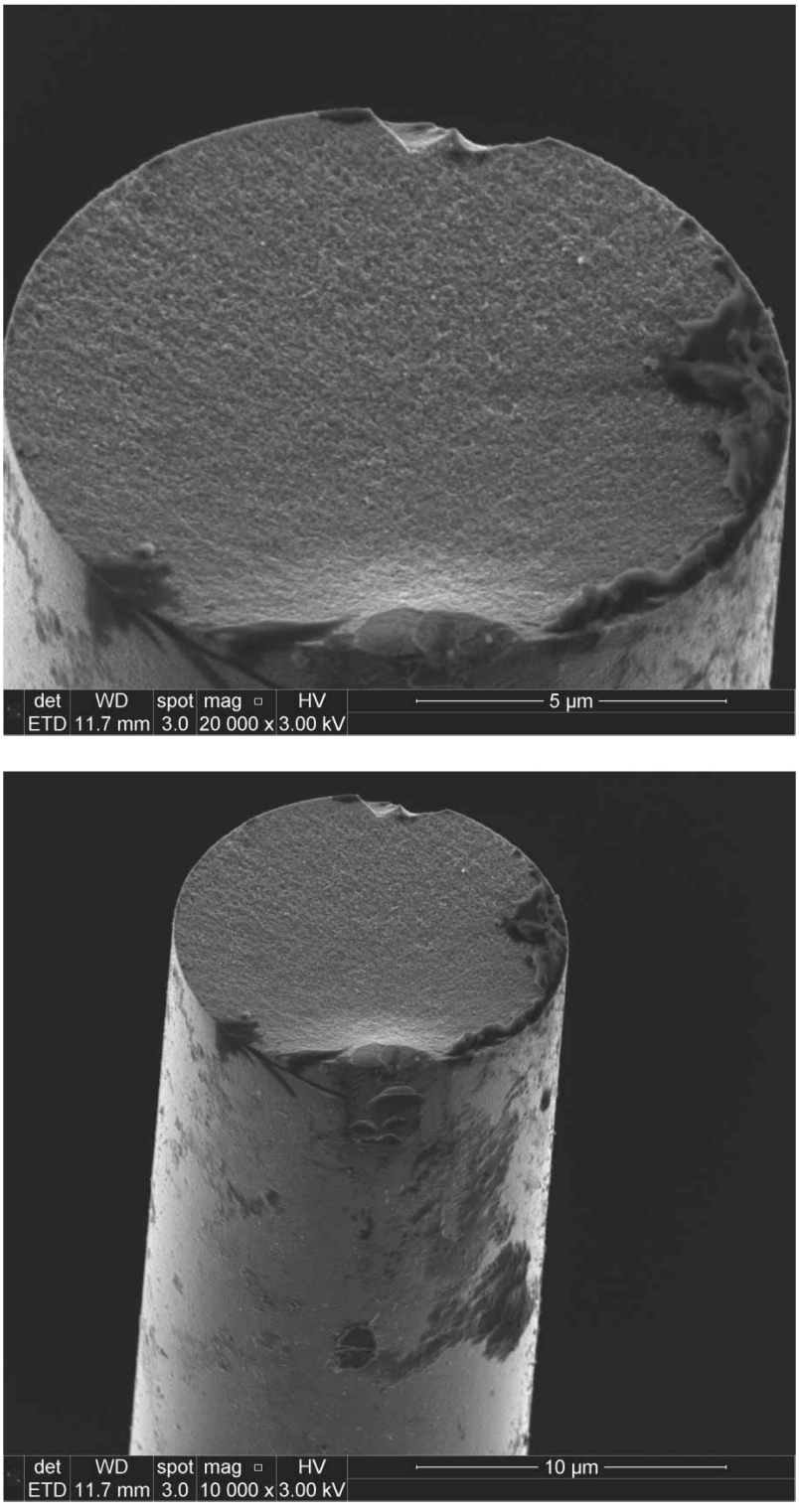


**Figure 36. SEM micrographs of the fracture surface of a fiber at two magnifications in specimen "Steam 25" showing deposits along the radial edge of the fracture surface ($\sigma_{cr}$ = 798 MPa, $t_f$ = 1.83 h)**

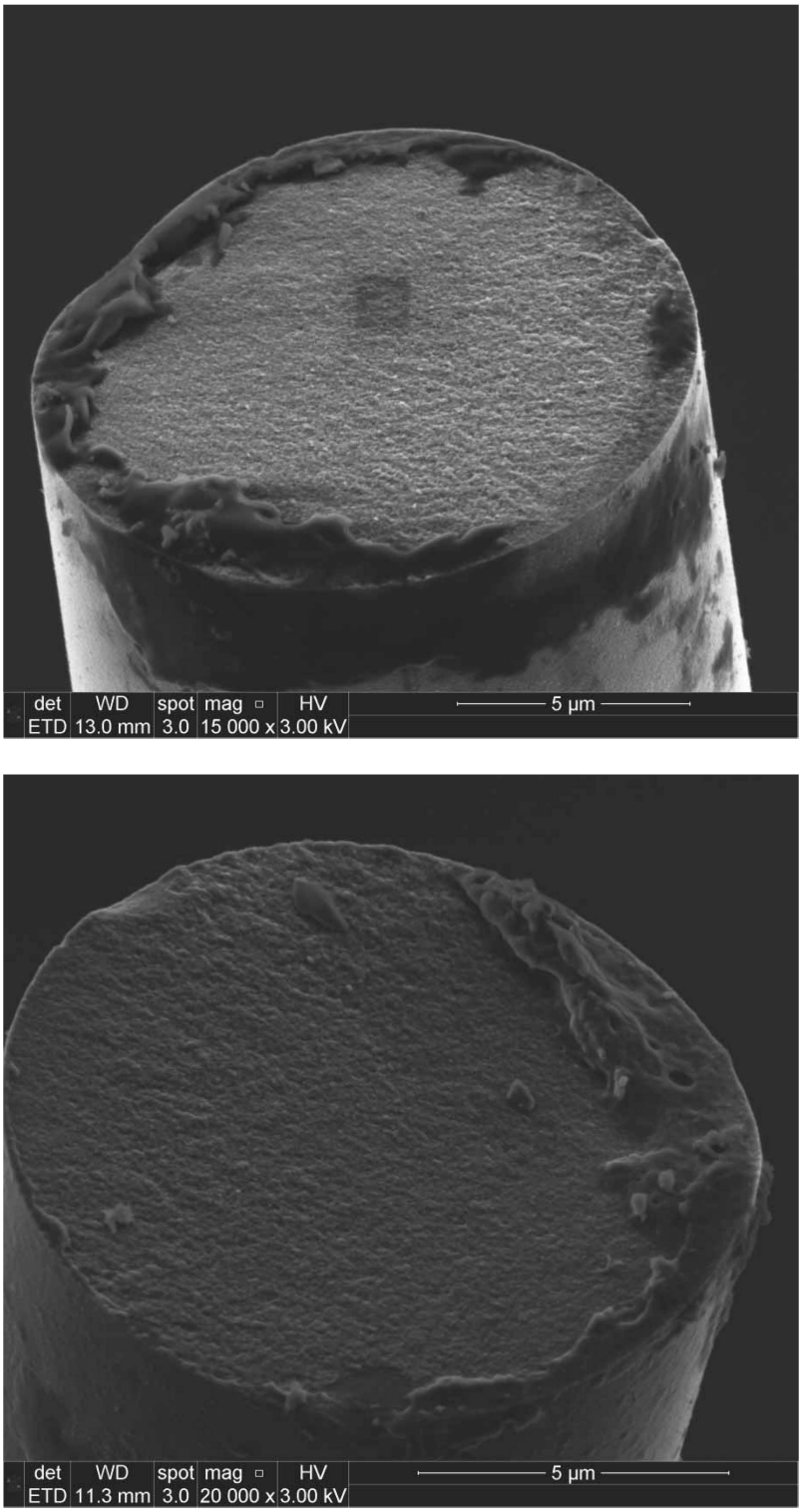


**Figure 37. SEM micrographs of fracture surfaces of two fibers in specimen "Steam 25" showing deposits along the radial edge of the fracture surface**

**($\sigma_{cr}$ = 798 MPa, $t_f$ = 1.83 h)**

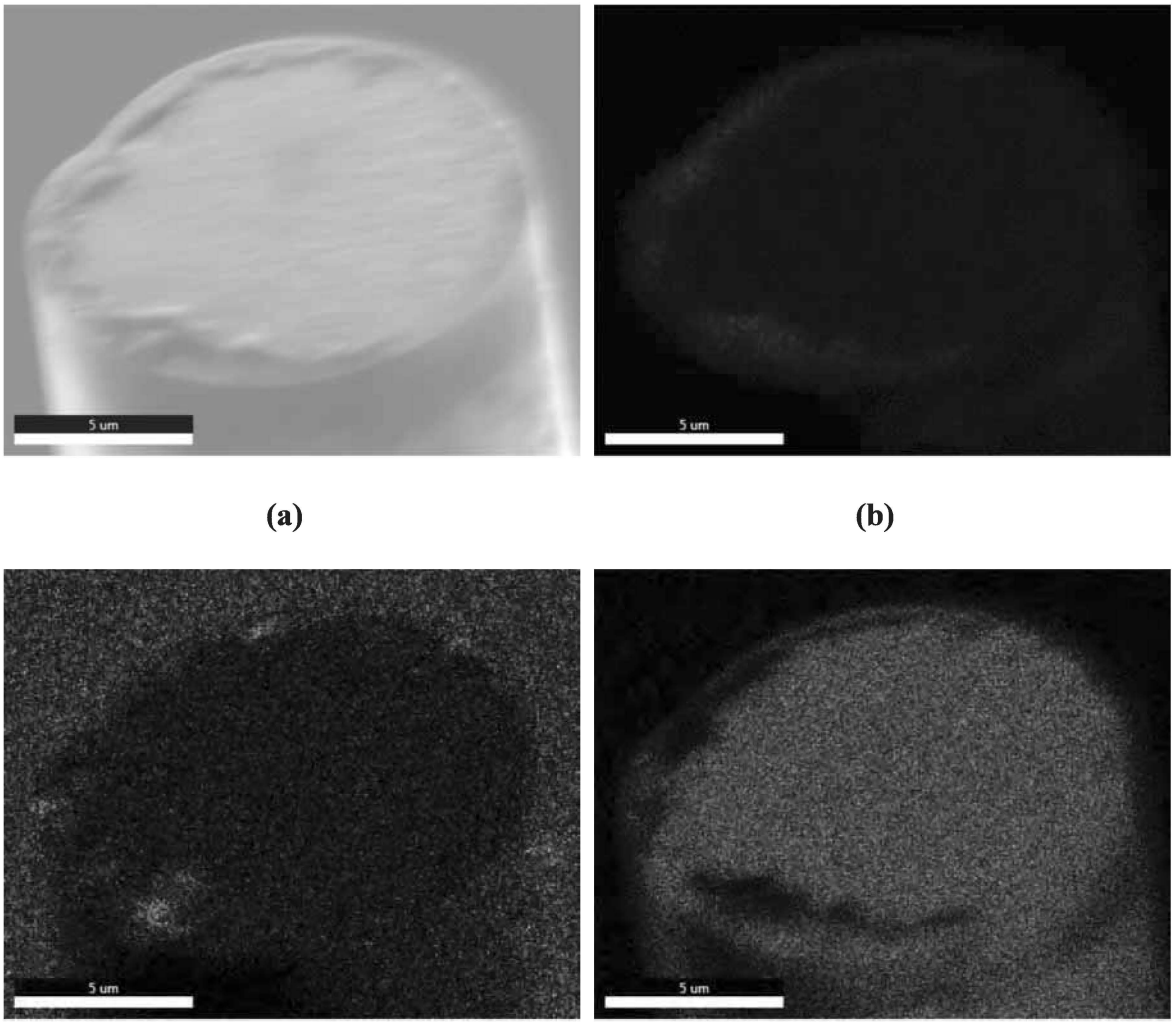


**(a)** **(b)**

**(c)** **(d)**

**Figure 38. SEM micrograph and EDS composition analysis of fracture surface of a fiber in specimen "Steam 25" showing deposits along the radial edge of the fracture surface. In the EDS images, brighter colors indicate greater presence of the component. a) SEM micrograph of the fracture surface. b) EDS imagery of carbon content on the fracture surface; carbon is present throughout the dark ring. C) EDS imagery of oxygen content on the fracture surface; note, the oxygen surrounding the fiber is mostly found on the aluminum mounting puck. d) EDS imagery of silicon content on the fracture surface; reduced levels of silicon are present within the ring.**

**($\sigma_{cr}$ = 798 MPa, tf = 1.83 h)**

When examining the fiber tow specimens using SEM, a small percentage of the fibers were observed with a thick, crystallized oxide layer. This phenomenon had been observed in previous efforts, and the fibers displaying the excessive oxidation were termed “rogue” fibers. These fibers were observed in specimens tested in saturated steam and in air. Representative SEM micrographs for saturated steam and air are shown in **Figure 39** and **Figure 40**, respectively. The reason these fibers present oxidation which differs from that seen in the vast majority of fibers in the fiber tow is not understood. Due to the limited number of “rogue” fibers observed in any specimen, it is not believed that they have an appreciable effect on the strength or creep lifetime of the fiber tows.

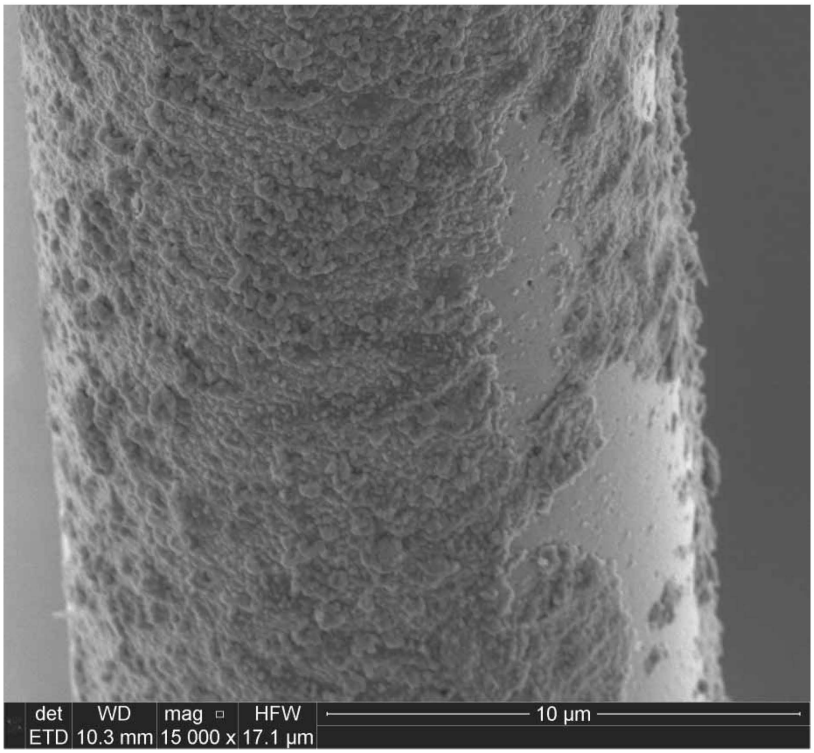


**Figure 39. SEM micrograph of a representative "rogue" fiber taken from specimen "Steam 4" showing thick, crystallized oxidation ($\sigma_{cr}$ = 2.96 MPa, $t_f$ > 100 h)**

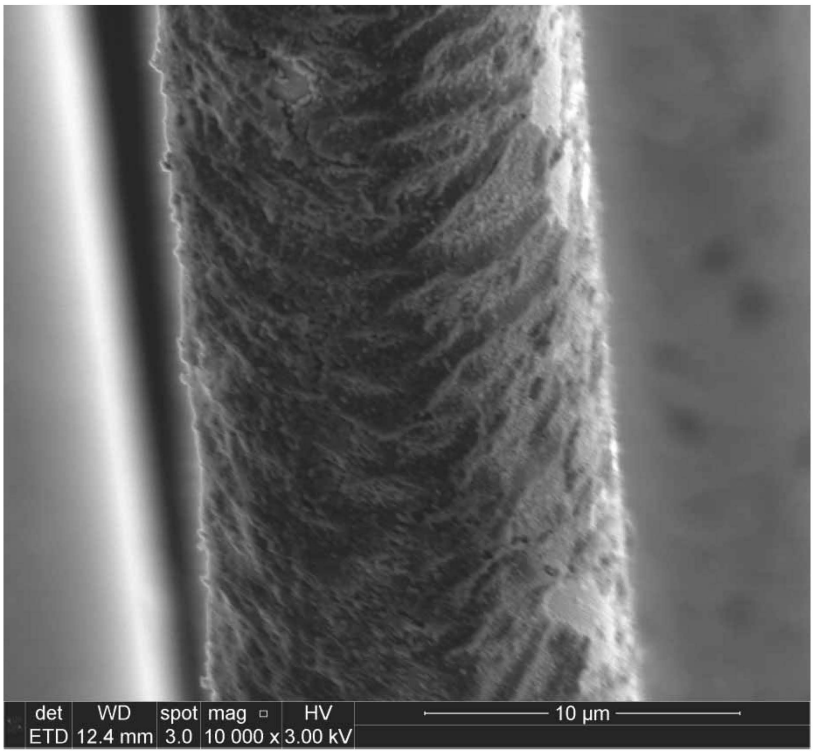


**Figure 40. SEM micrograph of a representative "rogue" fiber taken from specimen "Air 8" showing thick, crystallized oxidation ($\sigma_{cr}$ = 1023 MPa, $t_f$ > 100 h)**

# V. Conclusions and Recommendations

## 5.1 Conclusions

The effects of silicic acid-saturated steam on creep of Hi-Nicalon™ S fiber tows at 700°C were investigated. Tests were conducted in saturated steam and in air. In saturated steam, the maximum stress at which creep runout of 100 h was achieved was 750 MPa, while runout at 1023 MPa was observed in air. Exposure to silicic acid-saturated steam caused ~25% decrease in creep run-out stress. Notably, exposure to unsaturated steam degraded creep run-out stress by nearly 500%.

Following creep testing, a selection of fiber tows from tests in air and in saturated steam was analyzed using a scanning electron microscope. The fibers tested in both environments showed consistent features along the length of the fiber tow. Evidence of passive oxidation was present on the fiber tows tested in air and in steam. Mottled areas were observed on fibers from both environments but were seen more frequently on the surfaces of fibers tested in saturated steam. A small number of fibers, termed “rogue” fibers, from any given specimen tested in air or in saturated steam showed evidence of scale crystallization; the cause of these rogue fibers is not understood.

## 5.2 Recommendations for Future Research

Creep testing of Hi-Nicalon™ S fiber tows has been conducted at 700°C and 800°C in a saturated steam environment. There were no marked differences in the results at these two temperatures; however, the effects of silicic acid-saturated steam at a wider range of temperatures remain to be investigated. Previous work reported increased creep lifetimes in unsaturated steam at 1100°C and 1200°C relative to the same environment at

800°C. Testing should be carried out to determine whether this relationship holds when the steam is saturated with silicic acid.

SEM images were collected to analyze the failure mechanisms and oxidation of the fibers following the creep tests. This work should be supported by follow-on transmission electron microscopy (TEM) analysis of the fibers. TEM allows a greater level of fidelity in determining the presence of an oxide layer or other constituents on the surfaces of the fibers. Additional EDS spot analysis should be conducted in order to determine the composition of the mottled areas on the fiber surface and whether this composition varies between fibers tested in air and in saturated steam.

The tests conducted on silicon carbide fibers have provided useful data on the fiber performance in saturated steam environments. This should be further expanded by testing the properties of SiC-SiC CMCs (ceramic matrix composites with silicon carbide fibers and matrix) in a steam environment. Saturated steam is thought to degrade SiC fiber performance less than unsaturated steam because the unsaturated steam leeches silica from the fibers. Testing SiC-SiC CMCs in unsaturated steam could help determine whether the amount of silica from the matrix that saturates the steam sufficiently degrades performance over long time intervals as well.

## Appendix A. Procedures for Generating Steam

1. INSERT SILICA WOOL INTO ALUMINA TUBE

Wearing latex gloves remove silica wool from the packaging, roll it to fit into the tube, and insert the silica wool into the alumina tube. The tube is shown in **Figure 41**. Use the dental pick to push the wool towards the nose of the tube. Once the silica wool is spread throughout the length of the tube, use the dental pick to create a pathway for the steam to flow through the center of the wool axially along the tube. **Figure 42** shows the aft end of the alumina tube after the silica wool has been inserted and the opening for steam flow has been made. Silica wool should be replaced every 100 running hours.

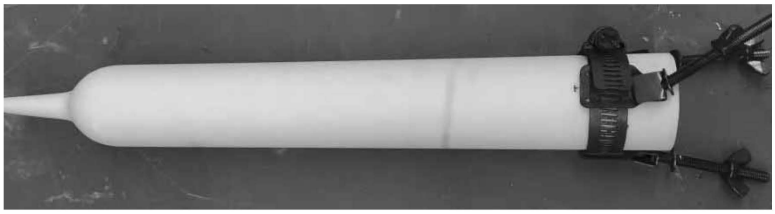

**Figure 41. Alumina tube used for steam saturation with silica wool**

**Figure 42. Silica wool inserted into the tube**

2. INSERT ALUMINA TUBE INTO PREHEATER

After the alumina tube has been filled with silica wool, insert it gently into the cylindrical opening in the preheaters as shown in **Figure 43**. The tube should slide through the preheaters, and the nose should rest inside the smaller diameter alumina tube on the test chamber side of the preheaters. The tube should not be fully inserted; approximately 5 cm (2 in) of the tube, including the metal collar, should extend from the preheater.

**Figure 43. Alumina tube filled with silica wool and inserted into the preheaters**

3. ATTACH STEAM GENERATOR TO ALUMINA TUBE

Place the circular piece of sheet insulation on the aft end of the silica tube, as shown in **Figure 44**. (Note: if needed, cut a new piece of insulation from the sheet. The outer diameter should be larger than the alumina tube, and the inner diameter should be large enough not to obstruct steam flow. Three slots should be cut in the insulation to allow the bolts to pass through.) Gently slide the steam generator into position directly behind the preheater. Rotate the alumina tube until the three bolts attached to the tube align with the three slots cut into the plate on the nose of the steam generator. Slide the bolts through the slots ensuring that the washers are on the steam generator side. Tighten the wingnuts to secure the steam generator to the tube. Check that the nose of the alumina tube is still in place on the other end of the preheaters; adjust alignment if necessary. **Figure 45** shows the nose of the steam generator and the alumina tube after they have been attached.

**Figure 44. Cut, round piece of sheet insulation in place prior to attachment of steam generator to alumina tube.**

**Figure 45. Nose of steam generator (right) secured to alumina tube which is inserted into preheaters (left).**

4. ATTACH THE DISTILLED WATER TUBE TO THE STEAM GENERATOR

The white tube that runs from the distilled water tank slips over the nipple of the blue water inlet tube on the aft end of the steam generator, as shown in **Figure 46**. Ensure that the tube is still firmly attached. Check the water level in the distilled water drum, and refill the drum from the reverse osmosis tank if necessary. (At a flow rate of 10 mL/min, a full drum should last for ~350 hours of steam generation.)

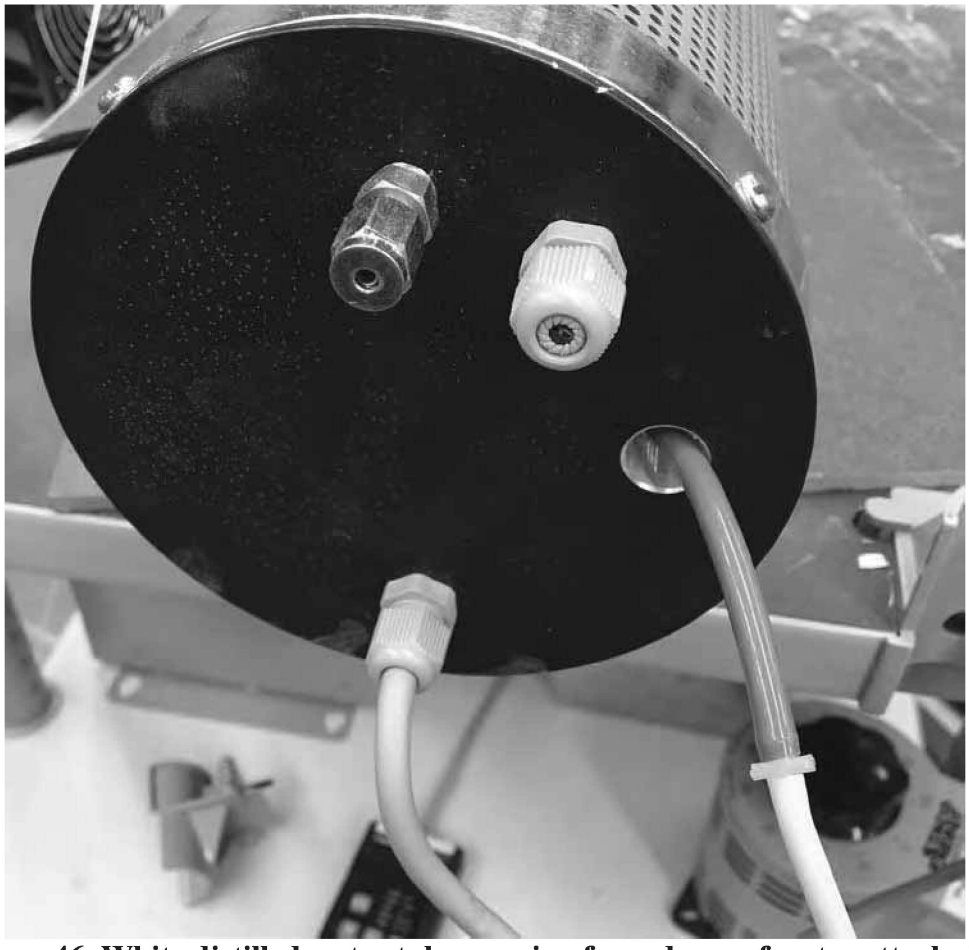

**Figure 46. White distilled water tube running from drum of water attached to blue water inlet tube on steam generator**

5. TURN ON STEAM GENERATOR AND PREHEATERS

Flip the switch on the left side of the BPAN-2010 to turn the system on. (Note: this switch can be left on between tests if not making adjustments to the preheaters.) Press the green button labeled "HEATER ON" to activate the preheaters. Use the Manual Command 40 Controller computer terminal to input the desired preheater temperature. Preheaters take several hours to heat up and can generally be left at temperature between tests unless adjustments to the equipment are required. The BPAN-2010 controller is shown in **Figure 47**. Turn on the steam generator power by flipping the switch on the voltage controller, shown in **Figure 48**, to ON. Adjust the voltage as necessary by turning the knob on the top of the voltage controller in order to regulate voltage between 0% and 100%.


**Figure 47. MHI BPAN-2010 control box. The switch on the left must be in the ON position and the HEATER ON light must be on in order for current to flow to the preheaters. As pictured, the switch is ON and the HEATER OFF list is on.**


**Figure 48. Voltage controller for steam generator. Steam generator power is controlled using the switch on the left side**

6. TURN ON WATER SUPPLY TO START FLOW OF STEAM

On the flow rate controller, pictured in **Figure 49**, press the red button labeled "RUN STOP." The same button is used to stop the water flow. As pictured, the flow rate is set to 10.0 mL/min. This flow rate can be adjusted using the vertical arrows on the left side of the controller. Steam should be produced within five minutes of turning on the steam generator and activating the distilled water pump.


**Figure 49. Flow rate controller. The red "RUN STOP" button is used to stop and start the flow of distilled water. Flow rate is adjusted using the vertical blue arrow buttons**

## Appendix B. SEM Images

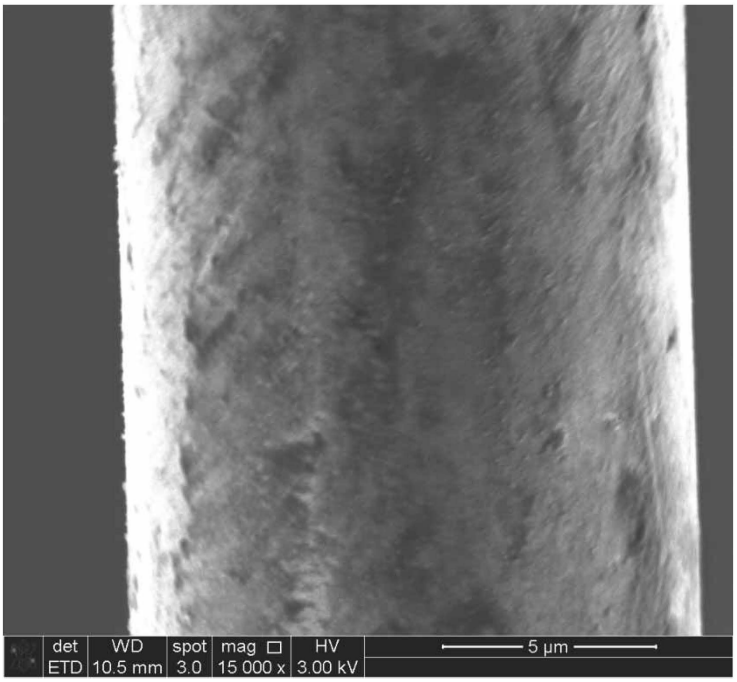


**Figure 50. SEM micrograph of the Hi-Nicalon™ S specimen "Air 8" examining fiber surface in lower portion of fiber ($\sigma_{cr}$ = 1023 MPa, $t_f$ > 100 h)**

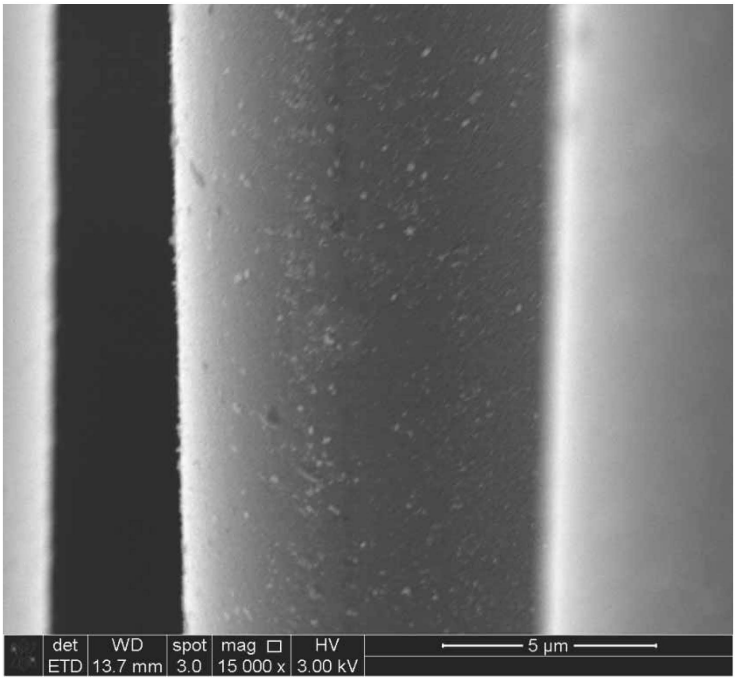


**Figure 51. SEM micrograph of the Hi-Nicalon™ S specimen "Air 8" examining fiber surface in lower portion of fiber ($\sigma_{cr}$ = 1023 MPa, $t_f$ > 100 h)**

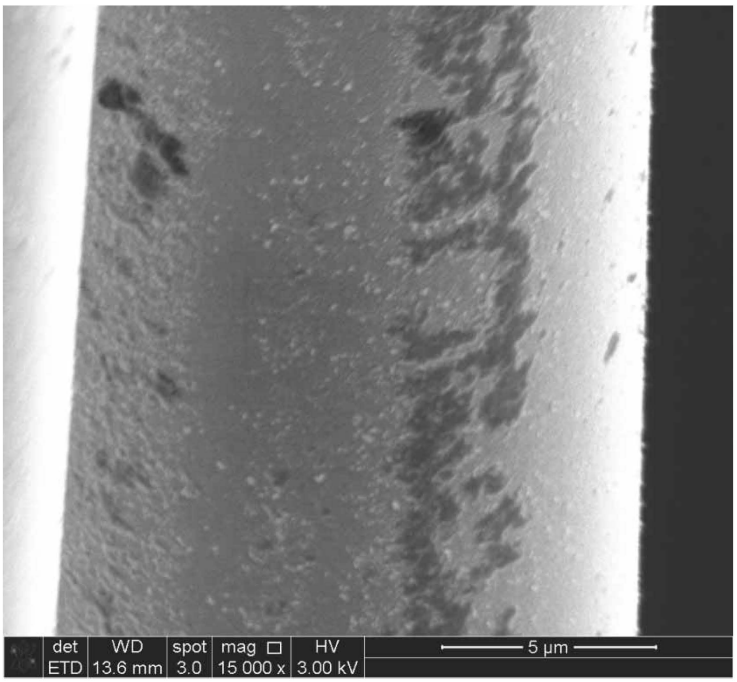


**Figure 52. SEM micrograph of the Hi-Nicalon™ S specimen "Air 8" examining fiber surface in lower portion of fiber ($\sigma_{cr}$ = 1023 MPa, $t_f$ > 100 h)**

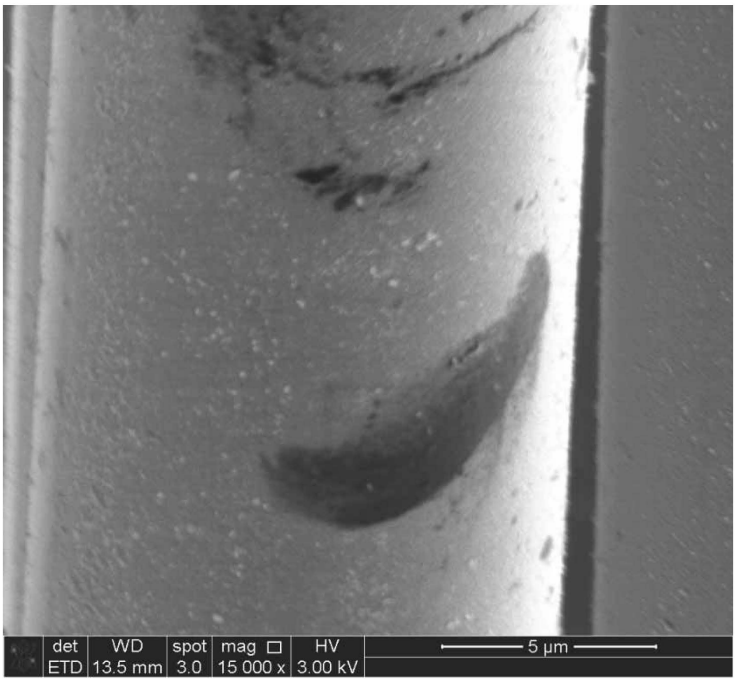


**Figure 53. SEM micrograph of the Hi-Nicalon™ S specimen "Air 8" examining fiber surface in lower portion of fiber ($\sigma_{cr}$ = 1023 MPa, $t_f$ > 100 h)**

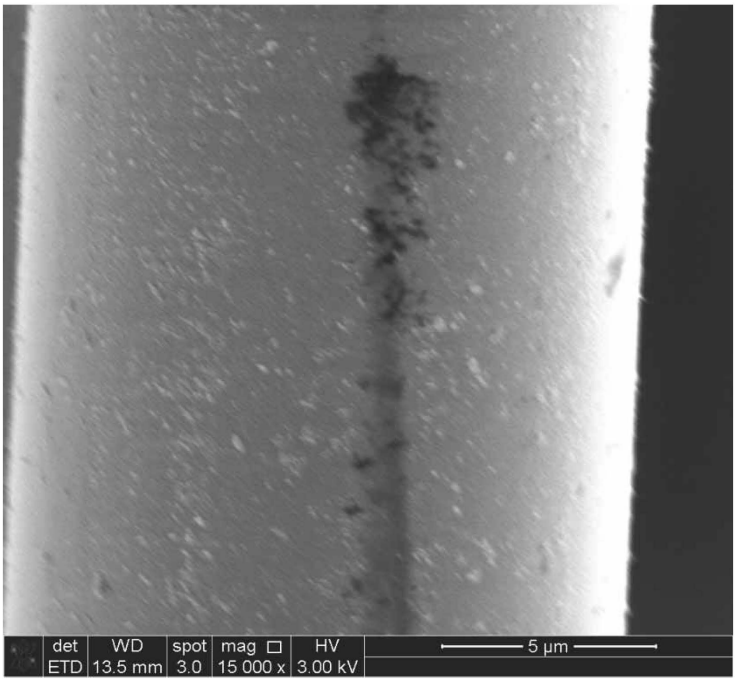


**Figure 54. SEM micrograph of the Hi-Nicalon™ S specimen "Air 8" examining fiber surface in lower portion of fiber ($\sigma_{cr}$ = 1023 MPa, $t_f$ > 100 h)**

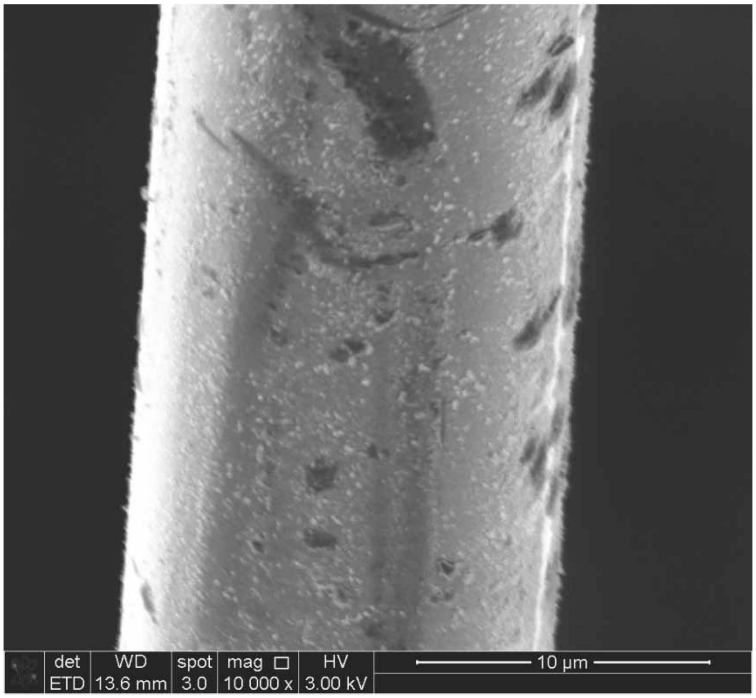


**Figure 55. SEM micrograph of the Hi-Nicalon™ S specimen "Air 8" examining fiber surface in lower portion of fiber ($\sigma_{cr}$ = 1023 MPa, $t_f$ > 100 h)**

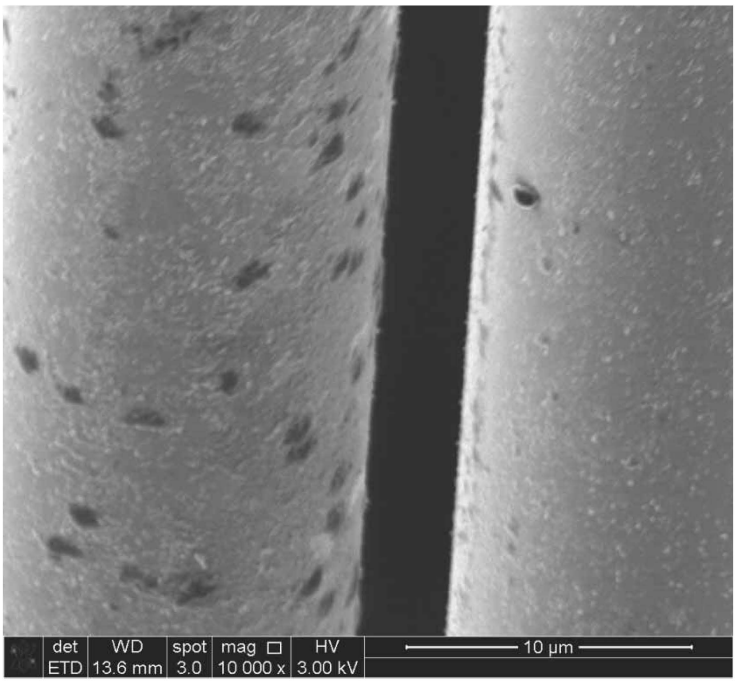


**Figure 56. SEM micrograph of the Hi-Nicalon™ S specimen "Air 8" examining fiber surface in lower portion of fiber ($\sigma_{cr}$ = 1023 MPa, $t_f$ > 100 h)**

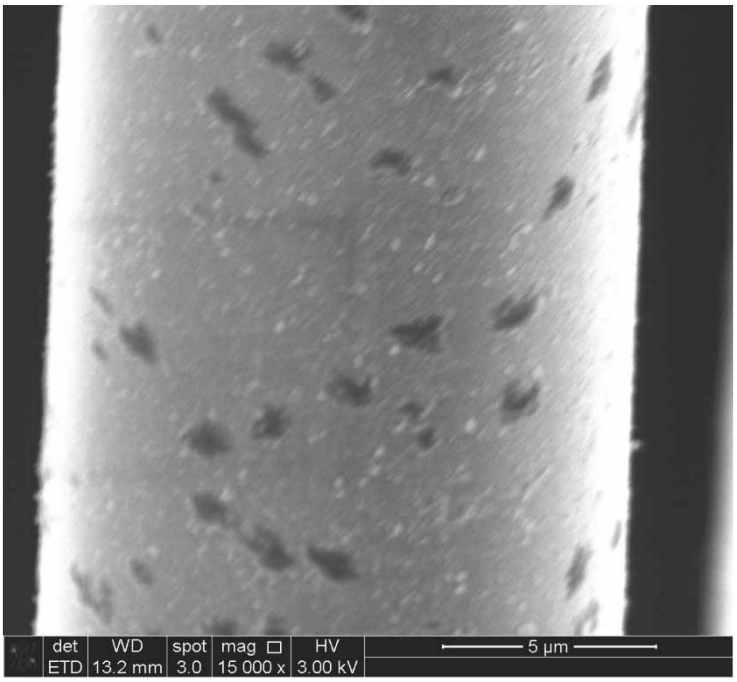


**Figure 57. SEM micrograph of the Hi-Nicalon™ S specimen "Air 8" examining fiber surface in lower portion of fiber ($\sigma_{cr}$ = 1023 MPa, $t_f$ > 100 h)**

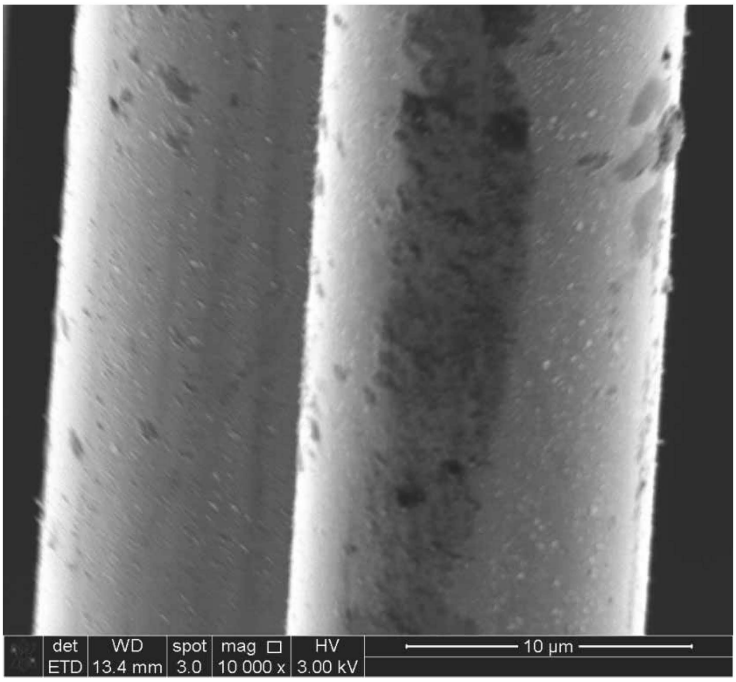


**Figure 58. SEM micrograph of the Hi-Nicalon™ S specimen "Air 8" examining fiber surface in lower portion of fiber ($\sigma_{cr}$ = 1023 MPa, $t_f$ > 100 h)**

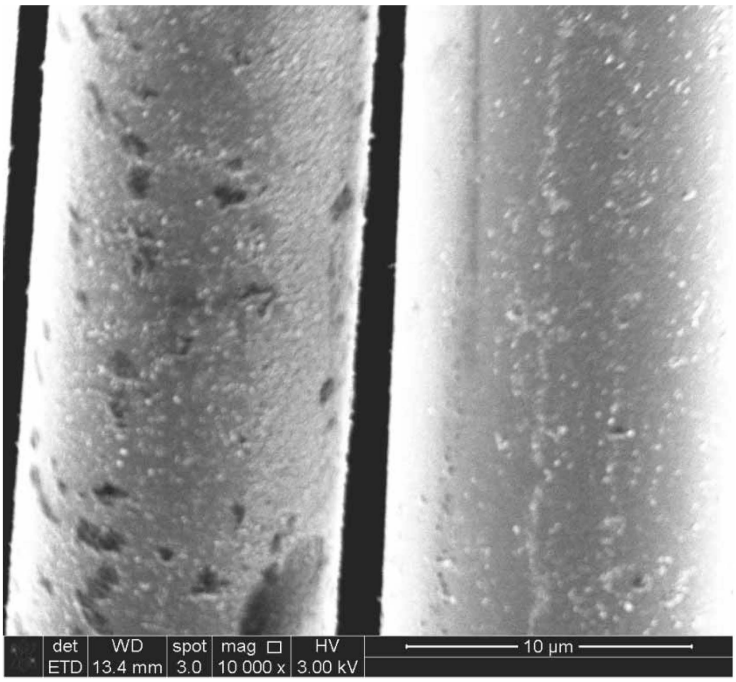


**Figure 59. SEM micrograph of the Hi-Nicalon™ S specimen "Air 8" examining fiber surface in lower portion of fiber ($\sigma_{cr}$ = 1023 MPa, $t_f$ > 100 h)**

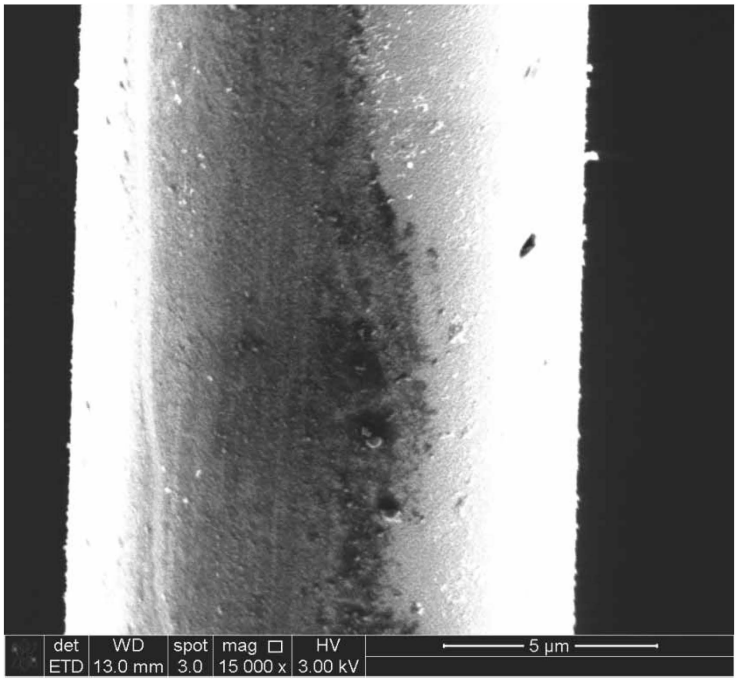


**Figure 60. SEM micrograph of the Hi-Nicalon™ S specimen "Air 8" examining fiber surface in lower portion of fiber ($\sigma_{cr}$ = 1023 MPa, $t_f$ > 100 h)**

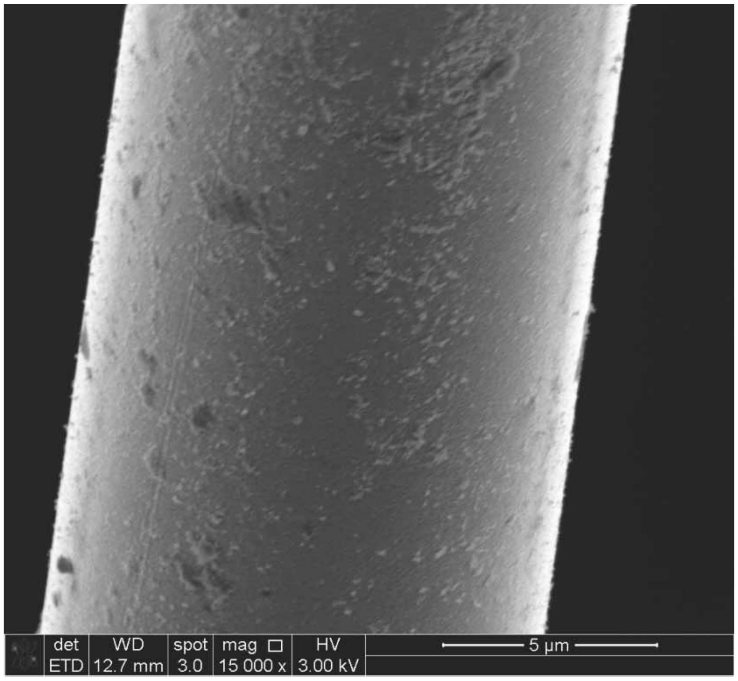


**Figure 61. SEM micrograph of the Hi-Nicalon™ S specimen "Air 8" examining fiber surface in lower portion of fiber ($\sigma_{cr}$ = 1023 MPa, $t_f$ > 100 h)**

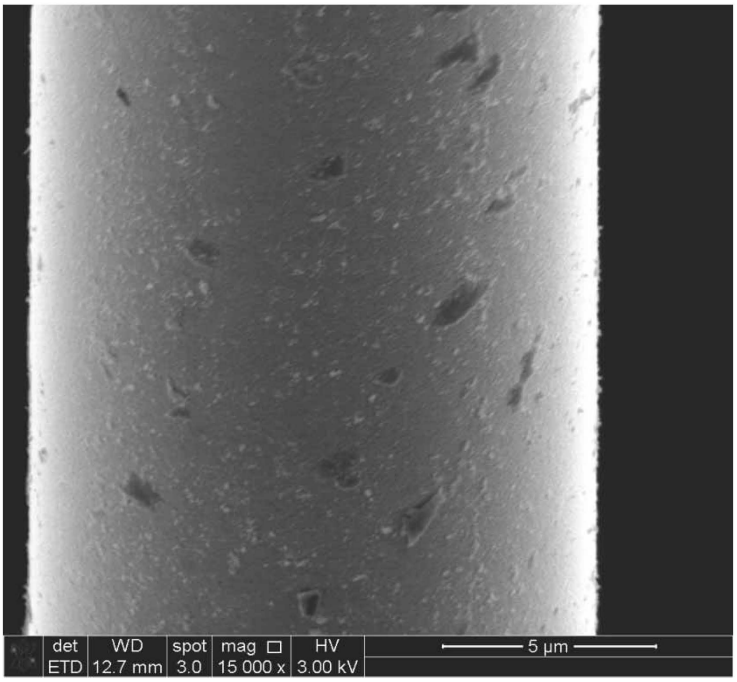


**Figure 62. SEM micrograph of the Hi-Nicalon™ S specimen "Air 8" examining fiber surface in lower portion of fiber ($\sigma_{cr}$ = 1023 MPa, $t_f$ > 100 h)**

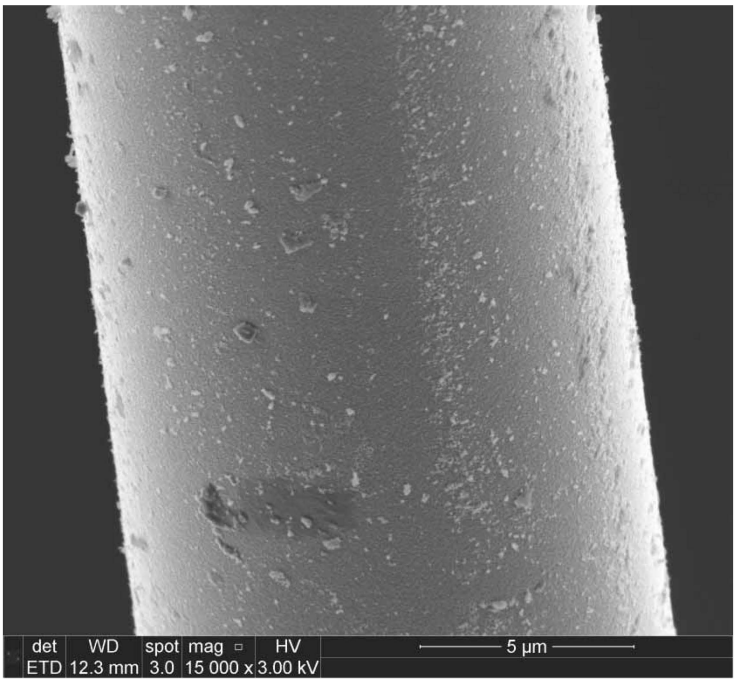


**Figure 63. SEM micrograph of the Hi-Nicalon™ S specimen "Air 8" examining fiber surface toward mid-fiber length ($\sigma_{cr}$ = 1023 MPa, $t_f$ > 100 h)**

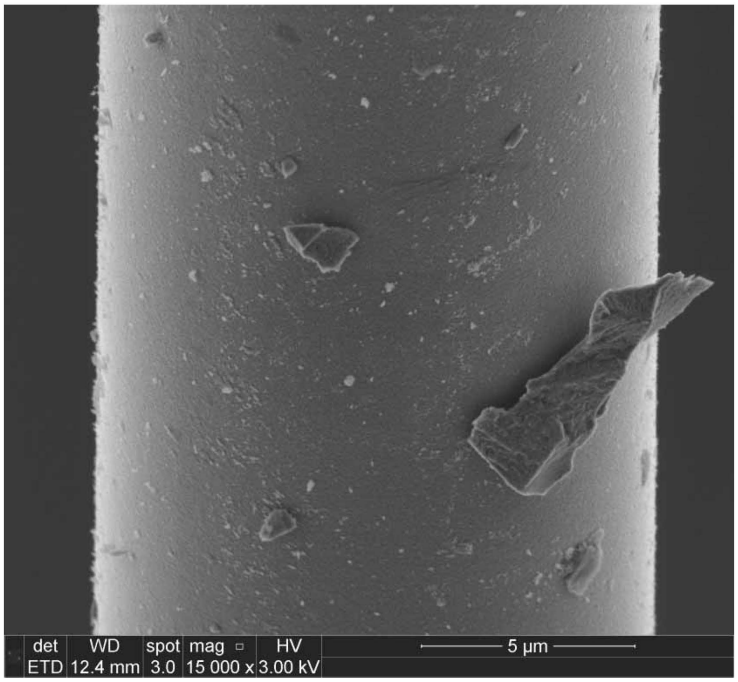


**Figure 64. SEM micrograph of the Hi-Nicalon™ S specimen "Air 8" examining fiber surface toward mid-fiber length ($\sigma_{cr}$ = 1023 MPa, $t_f$ > 100 h)**

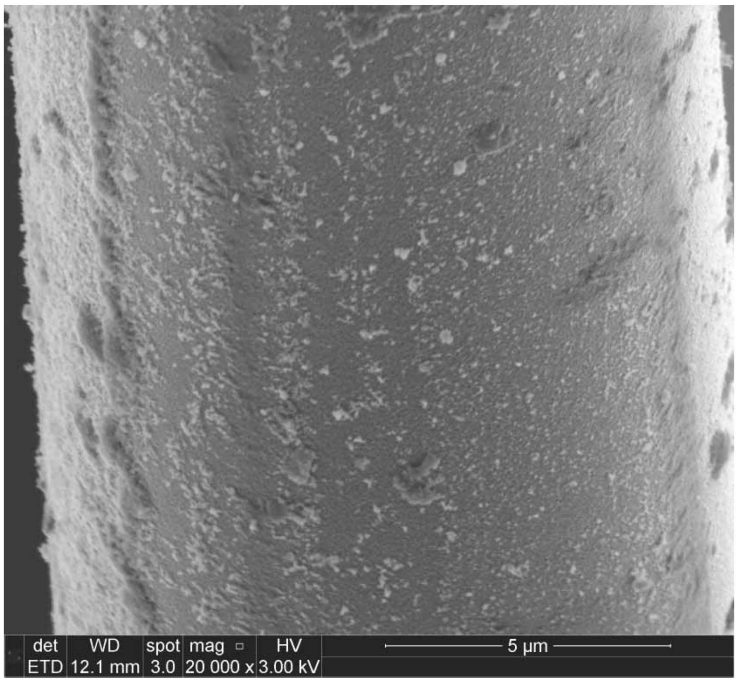


**Figure 65. SEM micrograph of the Hi-Nicalon™ S specimen "Air 8" examining fiber surface toward mid-fiber length ($\sigma_{cr}$ = 1023 MPa, $t_f$ > 100 h)**

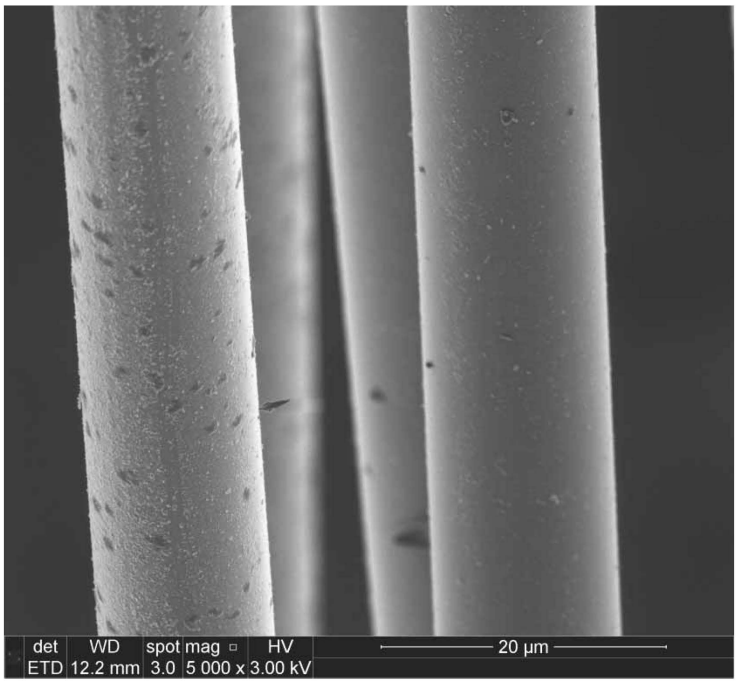


**Figure 66. SEM micrograph of the Hi-Nicalon™ S specimen "Air 8" examining fiber surface of multiple fibers toward mid-fiber length ($\sigma_{cr}$ = 1023 MPa, $t_f$ > 100 h)**

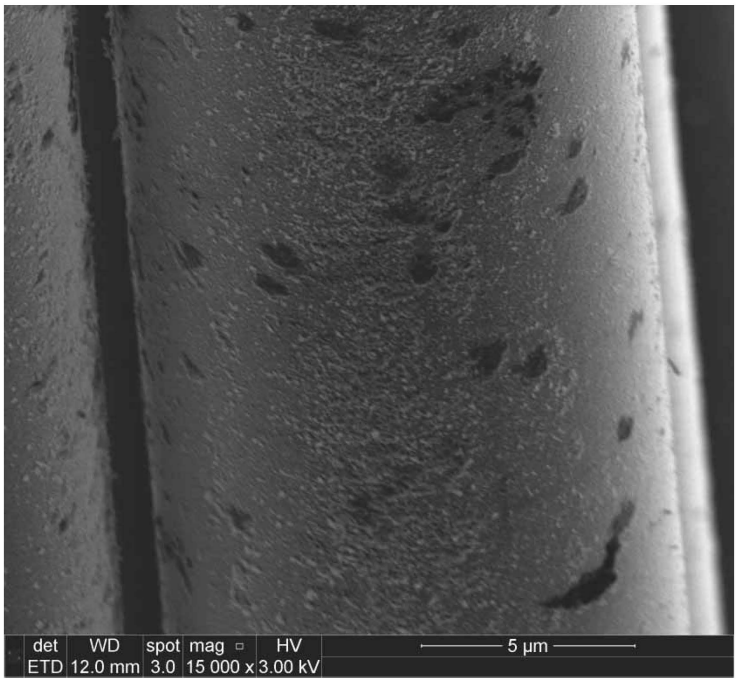


**Figure 67. SEM micrograph of the Hi-Nicalon™ S specimen "Air 8" examining fiber surface toward mid-fiber length ($\sigma_{cr}$ = 1023 MPa, $t_f$ > 100 h)**

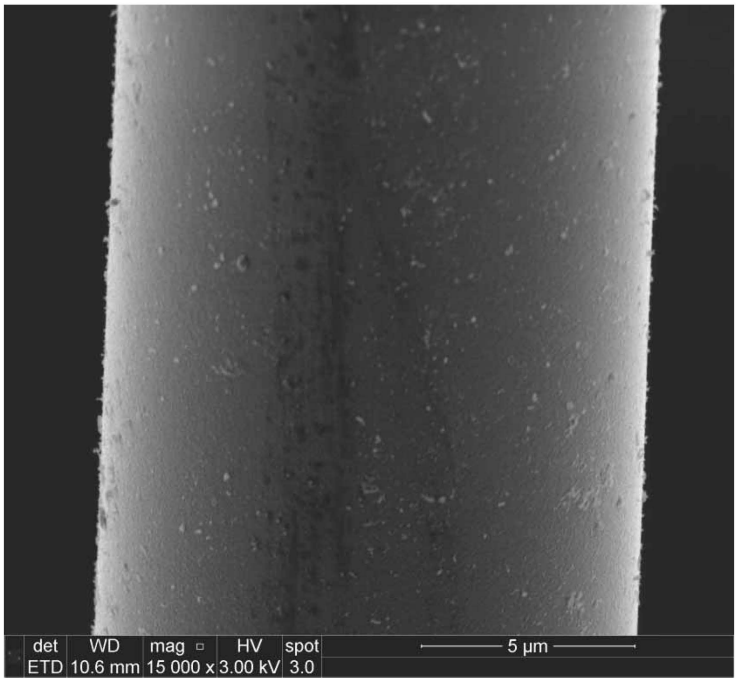


**Figure 68. SEM micrograph of the Hi-Nicalon™ S specimen "Air 9" examining fiber surface in the lower portion of the fiber, near the air inlet ($\sigma_{cr}$ = 2.96 MPa, $t_f$ > 100 h)**

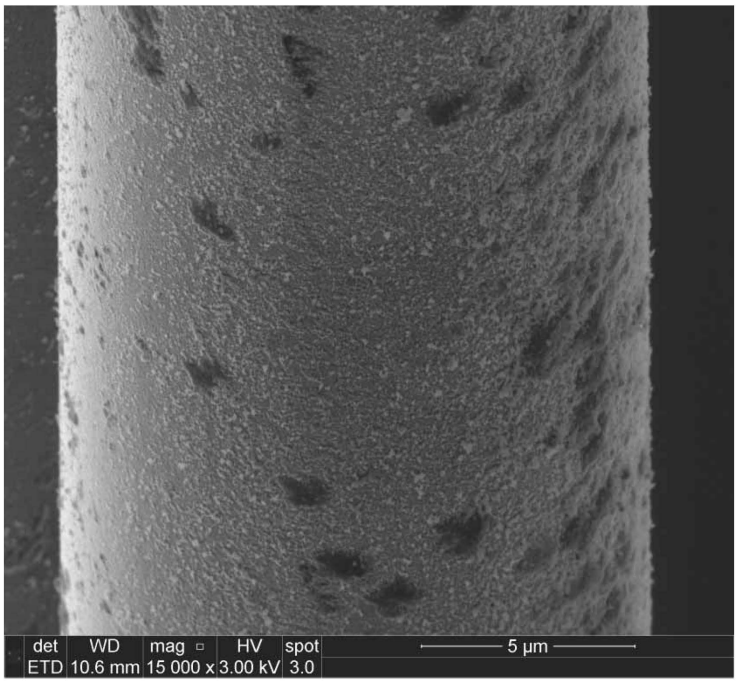


**Figure 69. SEM micrograph of the Hi-Nicalon™ S specimen "Air 9" examining fiber surface in the lower portion of the fiber, near the air inlet ($\sigma_{cr}$ = 2.96 MPa, $t_f$ > 100 h)**

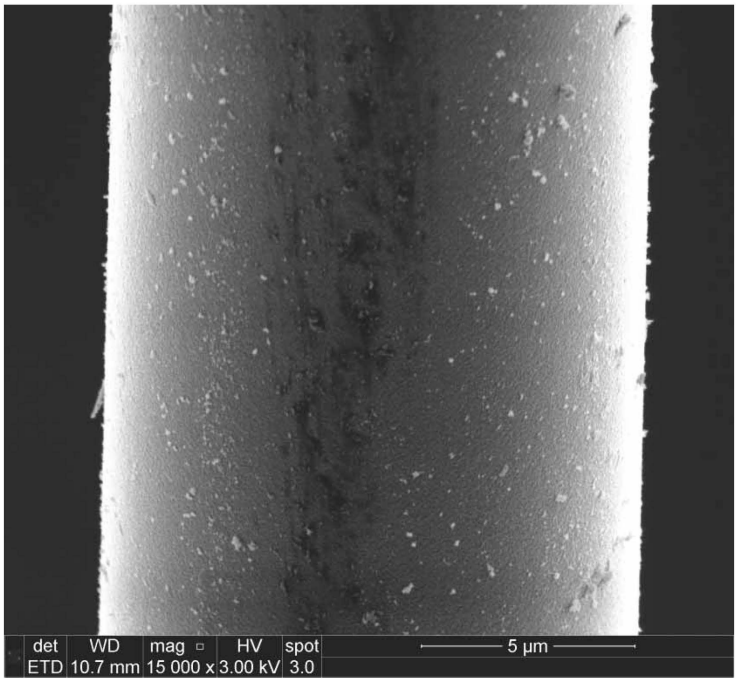


**Figure 70. SEM micrograph of the Hi-Nicalon™ S specimen "Air 9" examining fiber surface in the lower portion of the fiber, near the air inlet**

**($\sigma_{cr}$ = 2.96 MPa, $t_f$ > 100 h)**

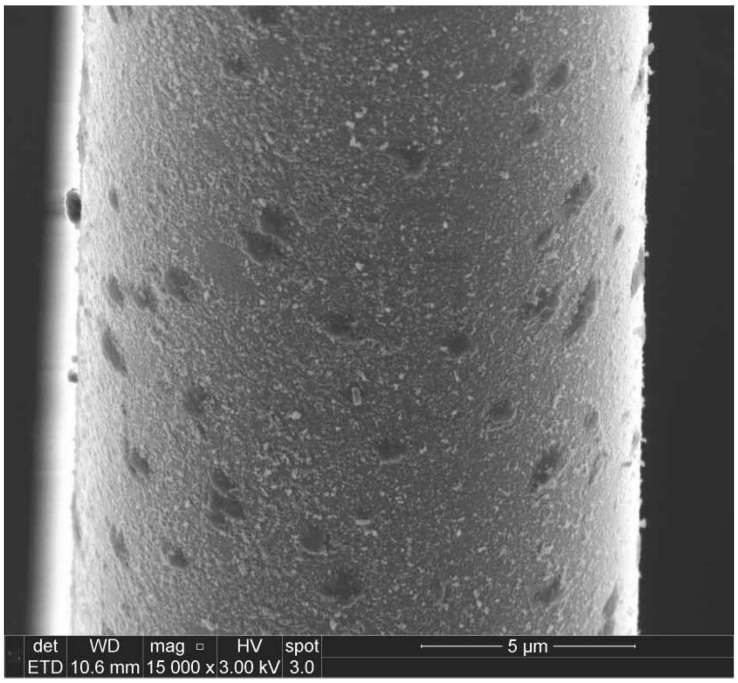


**Figure 71. SEM micrograph of the Hi-Nicalon™ S specimen "Air 9" examining fiber surface in the lower portion of the fiber, near the air inlet**

**($\sigma_{cr}$ = 2.96 MPa, $t_f$ > 100 h)**

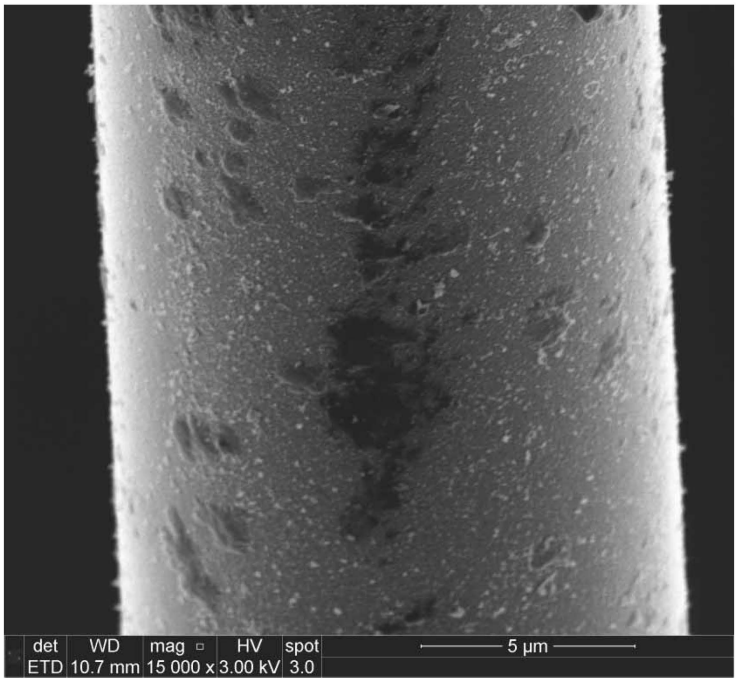


**Figure 72. SEM micrograph of the Hi-Nicalon™ S specimen "Air 9" examining fiber surface in the lower portion of the fiber, near the air inlet**

**($\sigma_{cr}$ = 2.96 MPa, $t_f$ > 100 h)**

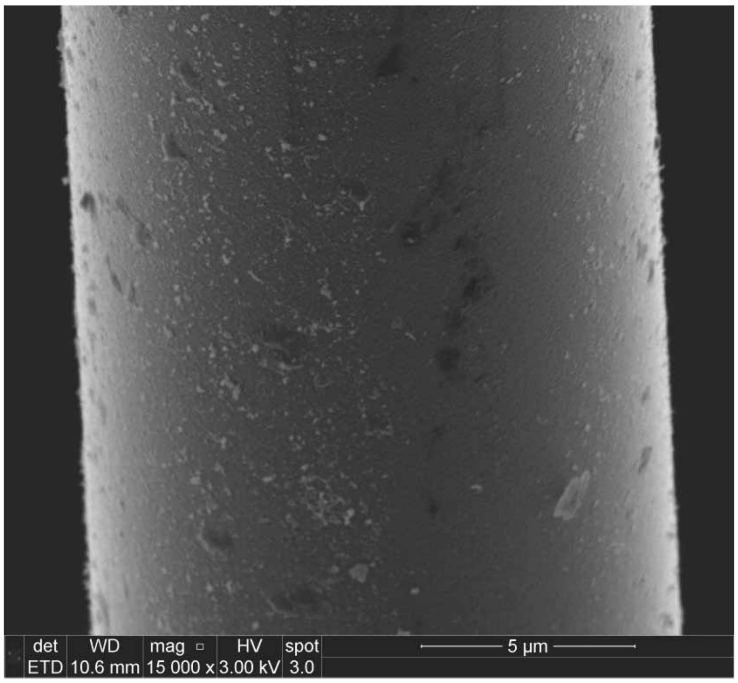


**Figure 73. SEM micrograph of the Hi-Nicalon™ S specimen "Air 9" examining fiber surface in the lower portion of the fiber, near the air inlet**

**($\sigma_{cr}$ = 2.96 MPa, $t_f$ > 100 h)**

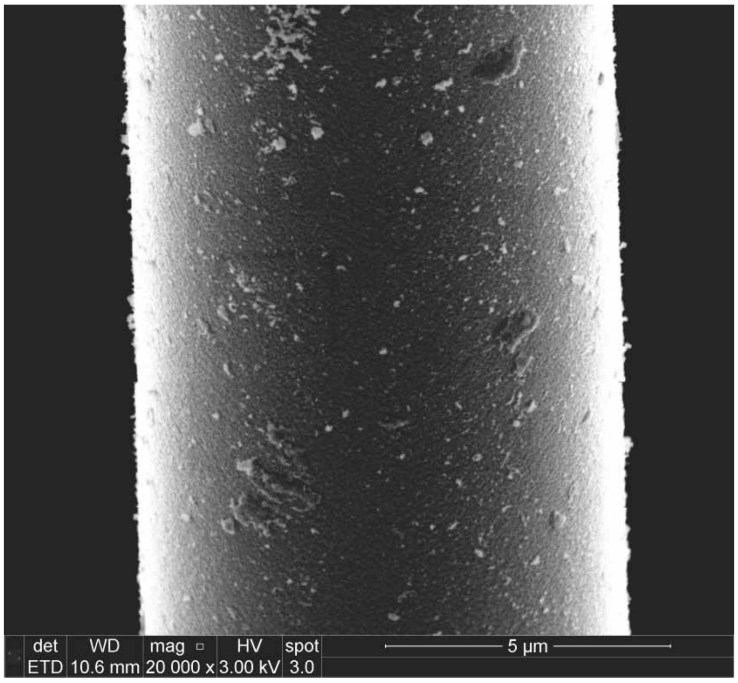


**Figure 74. SEM micrograph of the Hi-Nicalon™ S specimen "Air 9" examining fiber surface in the lower portion of the fiber, near the air inlet**

**($\sigma_{cr}$ = 2.96 MPa, $t_f$ > 100 h)**

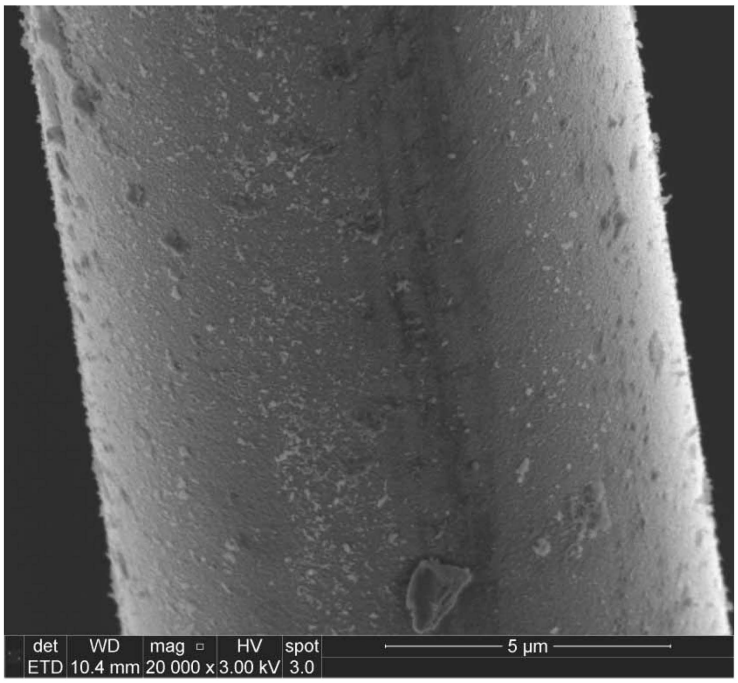


**Figure 75. SEM micrograph of the Hi-Nicalon™ S specimen "Air 9" examining fiber surface in the lower portion of the fiber, near the air inlet**

**($\sigma_{cr}$ = 2.96 MPa, $t_f$ > 100 h)**

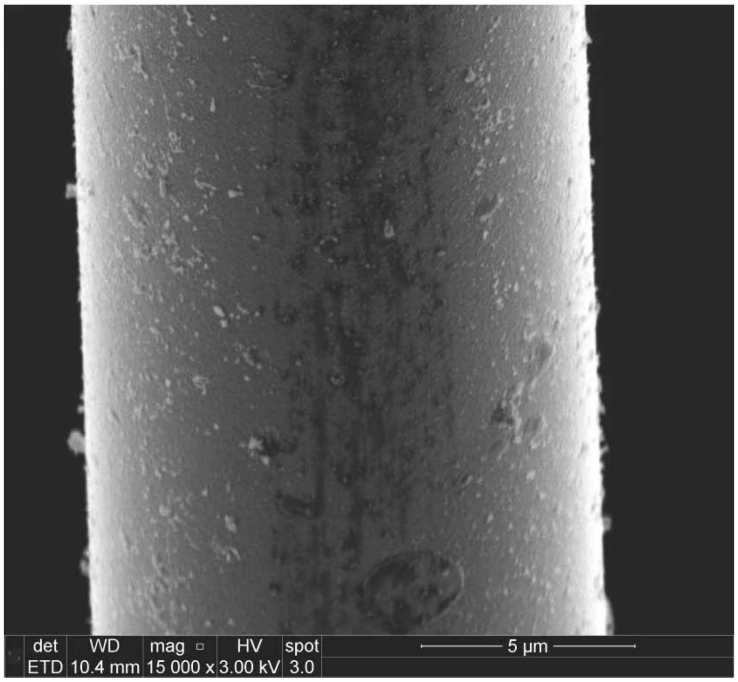


**Figure 76. SEM micrograph of the Hi-Nicalon™ S specimen "Air 9" examining fiber surface in the lower portion of the fiber, near the air inlet**

**($\sigma_{cr}$ = 2.96 MPa, $t_f$ > 100 h)**

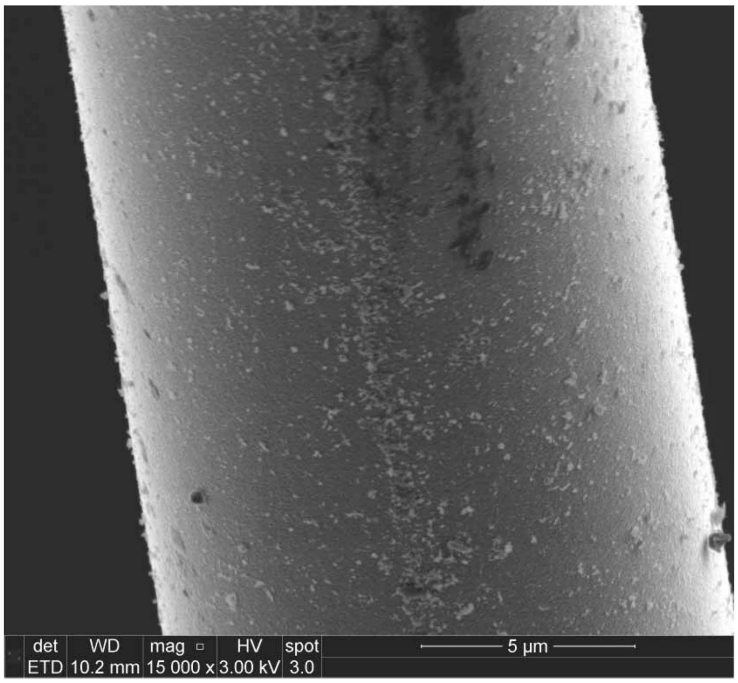


**Figure 77. SEM micrograph of the Hi-Nicalon™ S specimen "Air 9" examining fiber surface in the lower portion of the fiber, near the air inlet**

**($\sigma_{cr}$ = 2.96 MPa, $t_f$ > 100 h)**

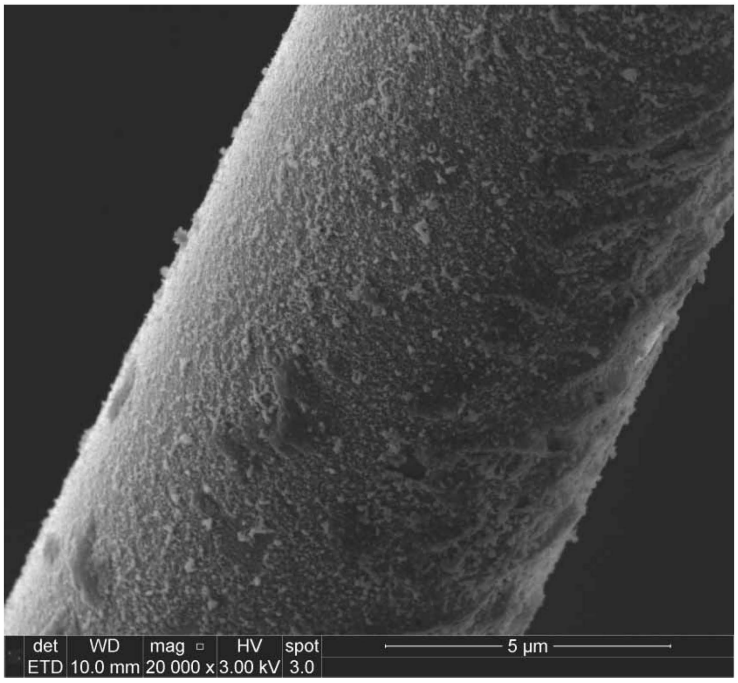


**Figure 78. SEM micrograph of the Hi-Nicalon™ S specimen "Air 9" examining fiber surface toward mid-fiber length ($\sigma_{cr}$ = 2.96 MPa, $t_f$ > 100 h)**

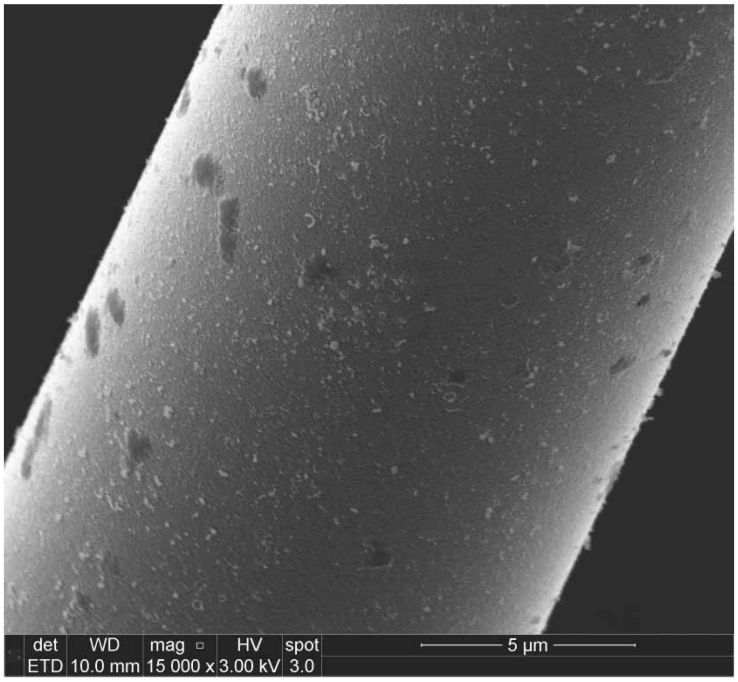


**Figure 79. SEM micrograph of the Hi-Nicalon™ S specimen "Air 9" examining fiber surface toward mid-fiber length ($\sigma_{cr}$ = 2.96 MPa, $t_f$ > 100 h)**

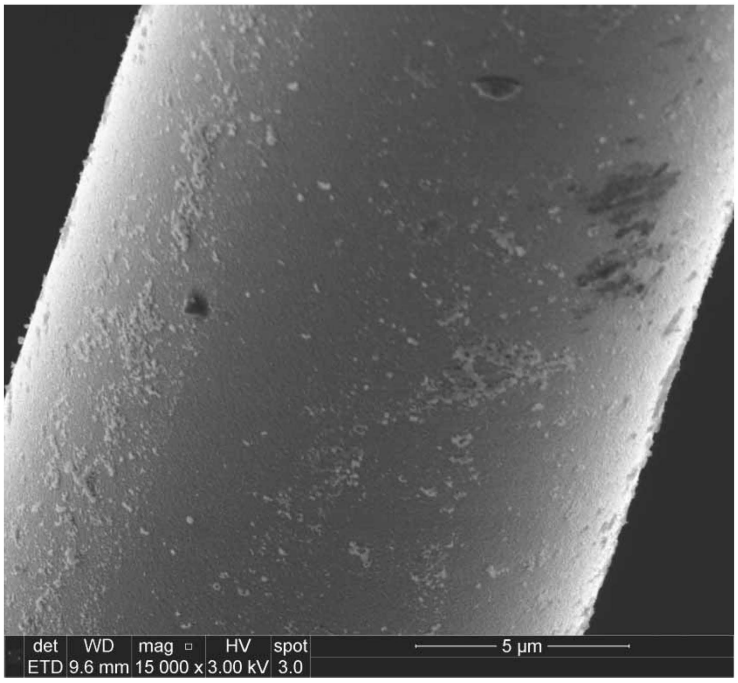


**Figure 80. SEM micrograph of the Hi-Nicalon™ S specimen "Air 9" examining fiber surface toward mid-fiber length ($\sigma_{cr}$ = 2.96 MPa, $t_f$ > 100 h)**

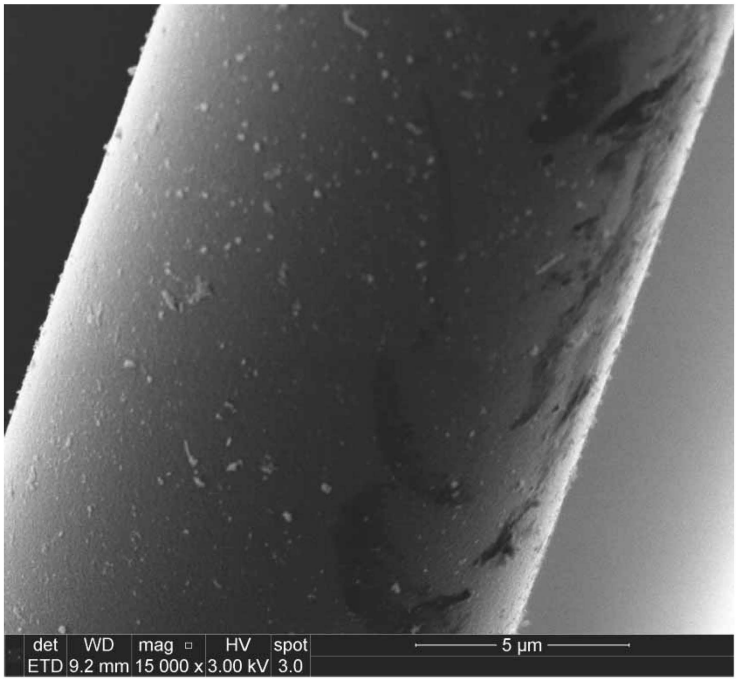


**Figure 81. SEM micrograph of the Hi-Nicalon™ S specimen "Air 9" examining fiber surface toward mid-fiber length ($\sigma_{cr}$ = 2.96 MPa, $t_f$ > 100 h)**

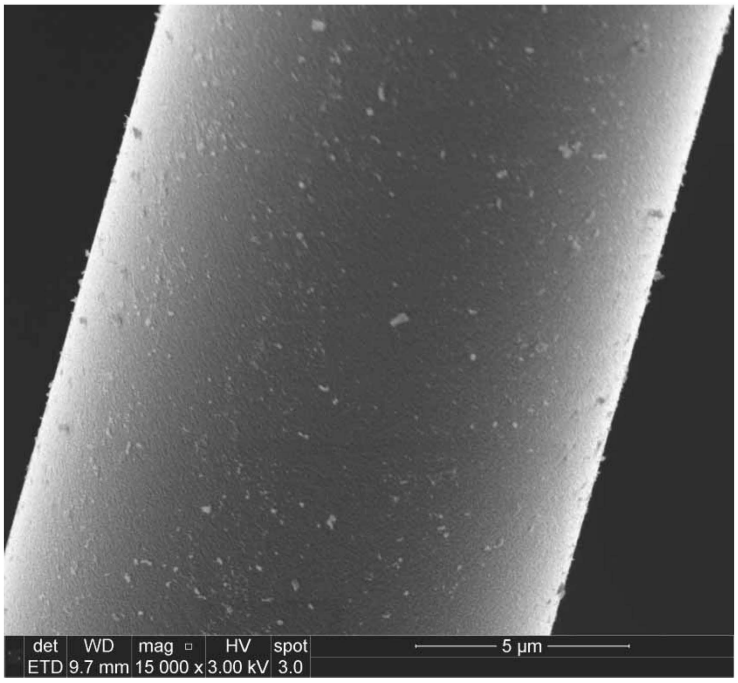


**Figure 82. SEM micrograph of the Hi-Nicalon™ S specimen "Air 9" examining fiber surface toward mid-fiber length ($\sigma_{cr}$ = 2.96 MPa, $t_f$ > 100 h)**

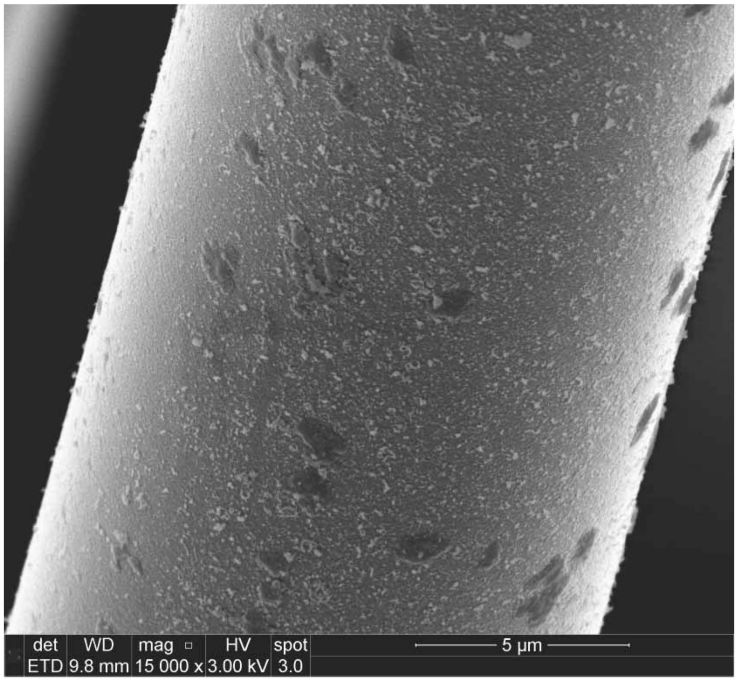


**Figure 83. SEM micrograph of the Hi-Nicalon™ S specimen "Air 9" examining fiber surface toward mid-fiber length ($\sigma_{cr}$ = 2.96 MPa, $t_f$ > 100 h)**

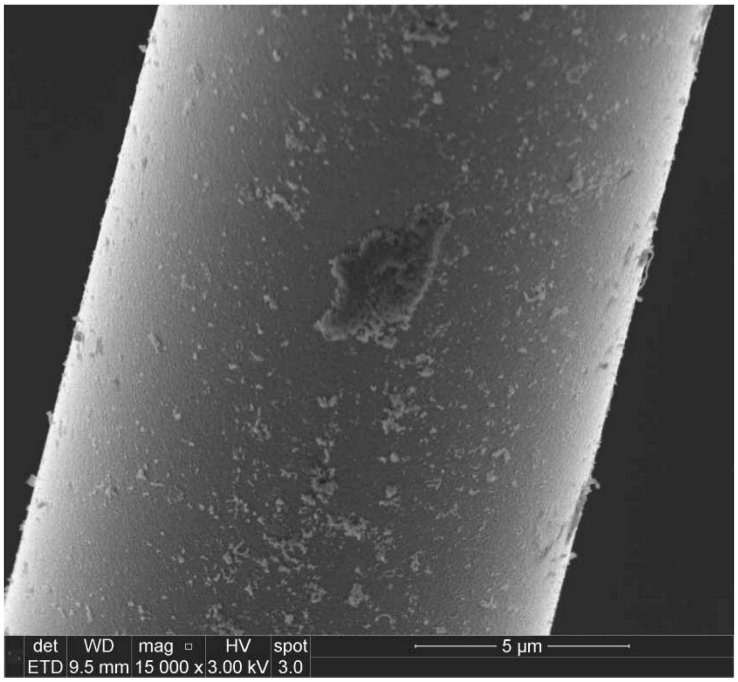


**Figure 84. SEM micrograph of the Hi-Nicalon™ S specimen "Air 9" examining fiber surface toward mid-fiber length ($\sigma_{cr}$ = 2.96 MPa, $t_f$ > 100 h)**

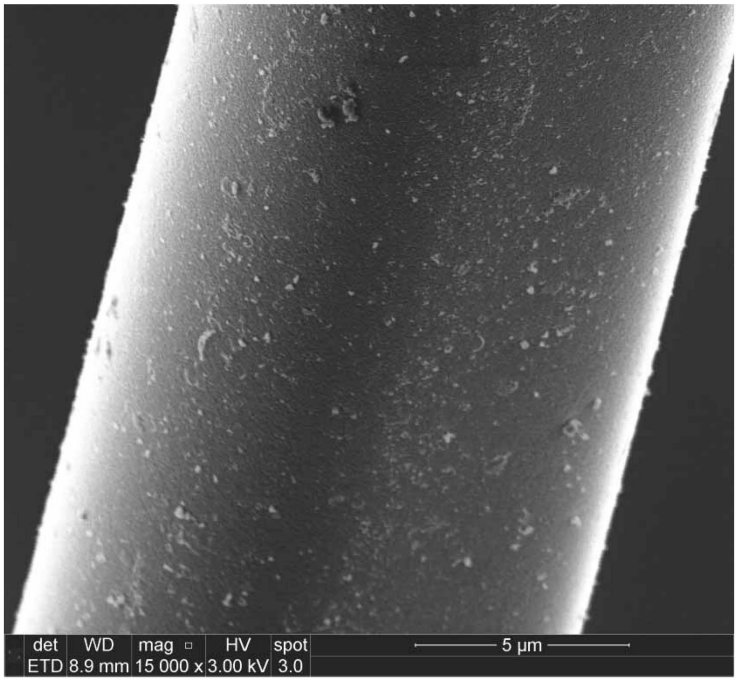


**Figure 85. SEM micrograph of the Hi-Nicalon™ S specimen "Air 9" examining fiber surface toward mid-fiber length ($\sigma_{cr}$ = 2.96 MPa, $t_f$ > 100 h)**

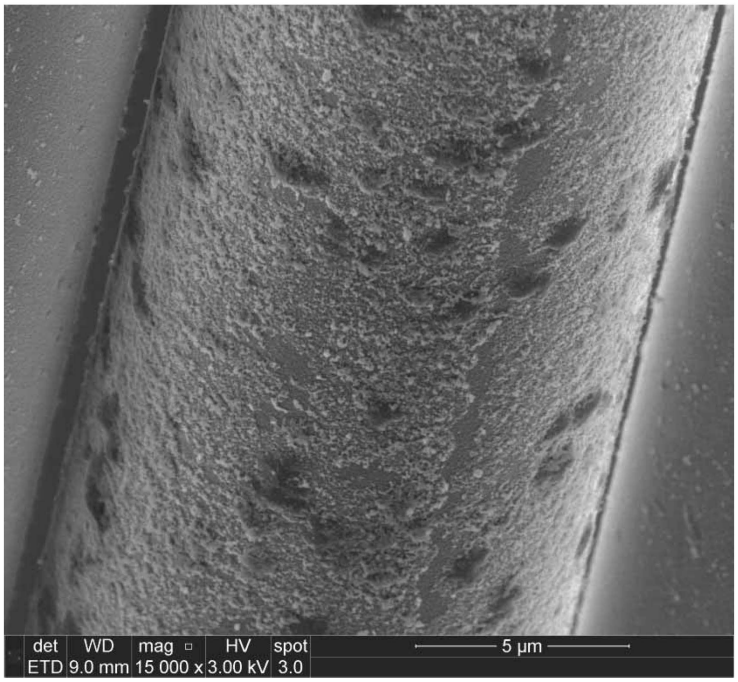


**Figure 86. SEM micrograph of the Hi-Nicalon™ S specimen "Air 9" examining fiber surface toward mid-fiber length ($\sigma_{cr}$ = 2.96 MPa, $t_f$ > 100 h)**

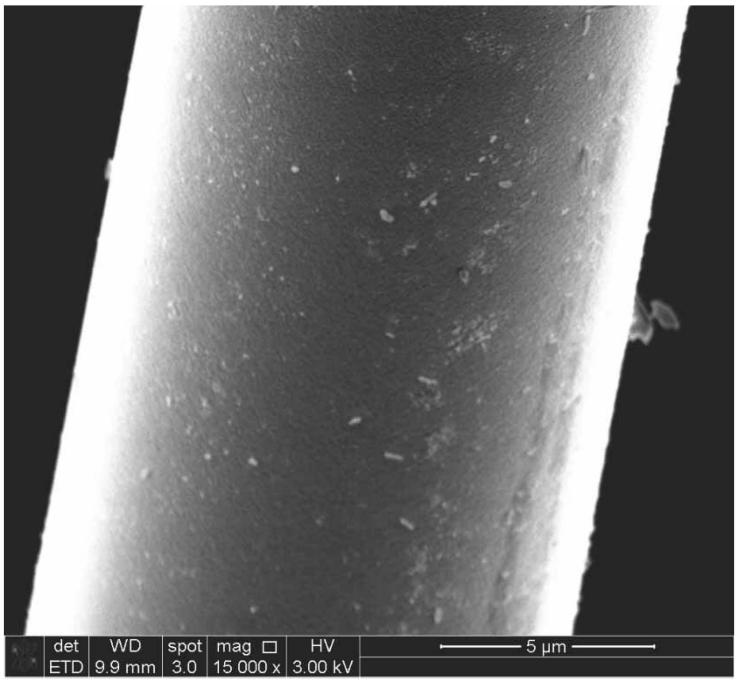


**Figure 87. SEM micrograph of the Hi-Nicalon™ S specimen "Air 16" examining fiber surface in the lower portion of the fiber, near the air inlet ($\sigma_{cr}$ = 1123 MPa, $t_f$ = 1.35 h)**

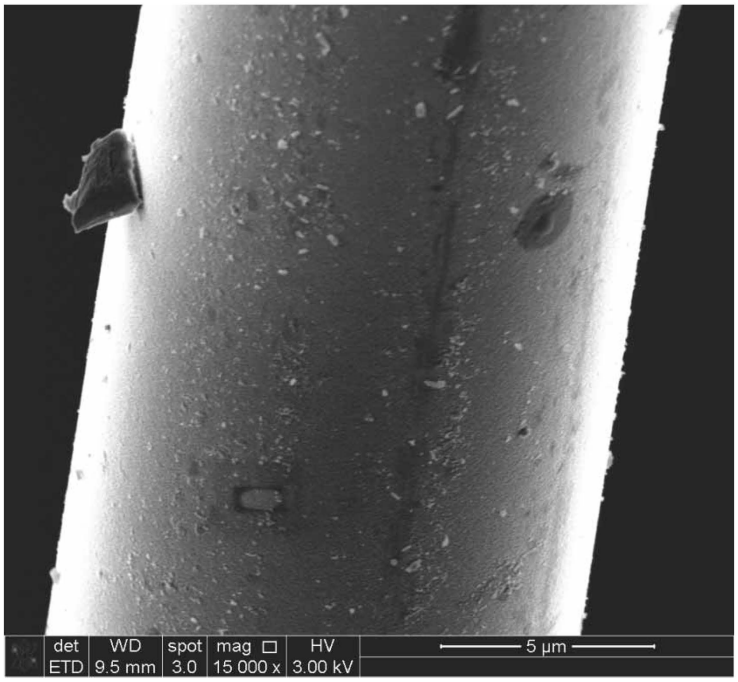


**Figure 88. SEM micrograph of the Hi-Nicalon™ S specimen "Air 16" examining fiber surface in the lower portion of the fiber, near the air inlet**

**($\sigma_{cr}$ = 1123 MPa, $t_f$ = 1.35 h)**

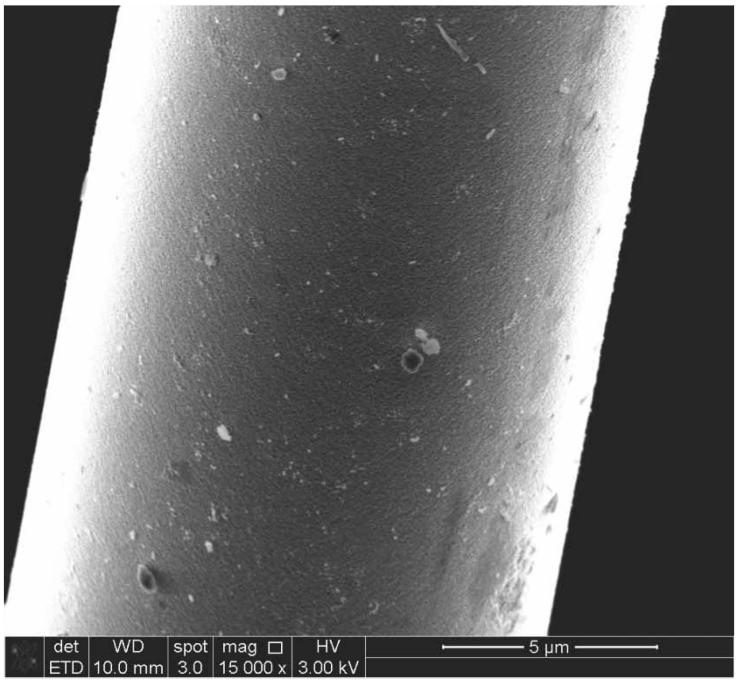


**Figure 89. SEM micrograph of the Hi-Nicalon™ S specimen "Air 16" examining fiber surface in the lower portion of the fiber, near the air inlet**

**($\sigma_{cr}$ = 1123 MPa, $t_f$ = 1.35 h)**

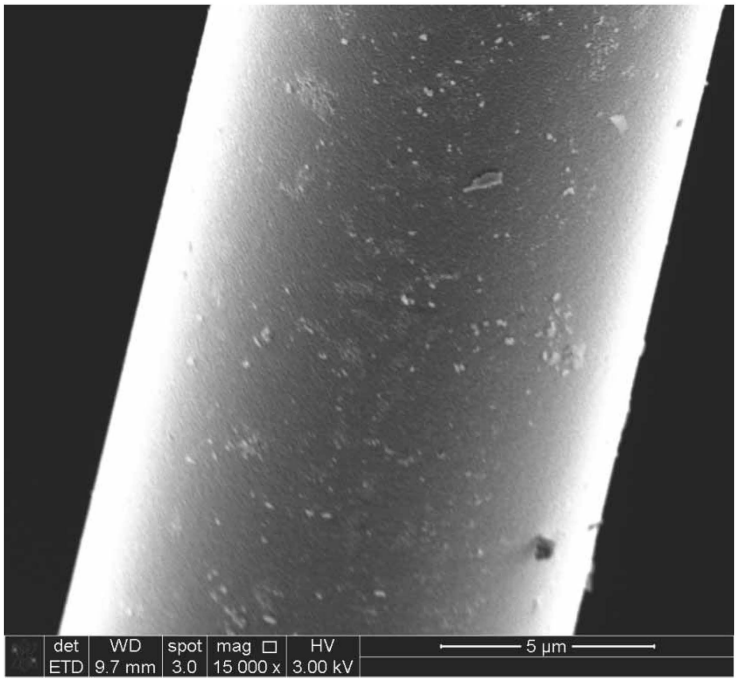


**Figure 90. SEM micrograph of the Hi-Nicalon™ S specimen "Air 16" examining fiber surface in the lower portion of the fiber, near the air inlet**

**($\sigma_{cr}$ = 1123 MPa, $t_f$ = 1.35 h)**

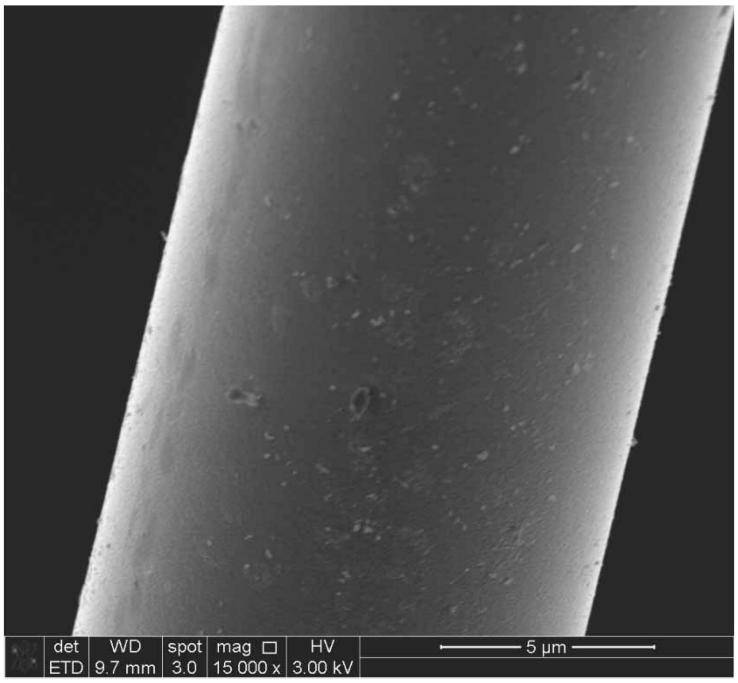


**Figure 91. SEM micrograph of the Hi-Nicalon™ S specimen "Air 16" examining fiber surface in the lower portion of the fiber, near the air inlet**

**$\sigma_{cr}$ = 1123 MPa, $t_f$ = 1.35 h)**

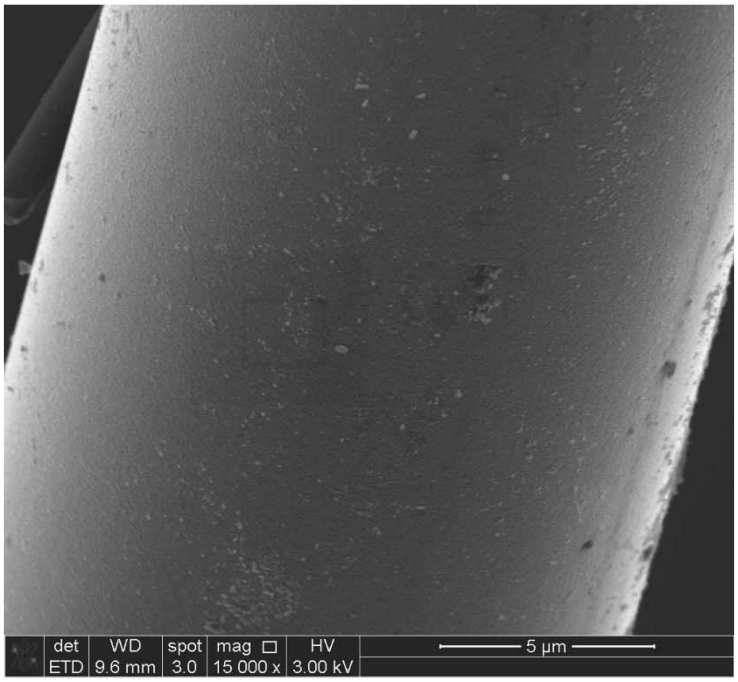


**Figure 92. SEM micrograph of the Hi-Nicalon™ S specimen "Air 16" examining fiber surface in the lower portion of the fiber, near the air inlet**

**($\sigma_{cr}$ = 1123 MPa, $t_f$ = 1.35 h)**

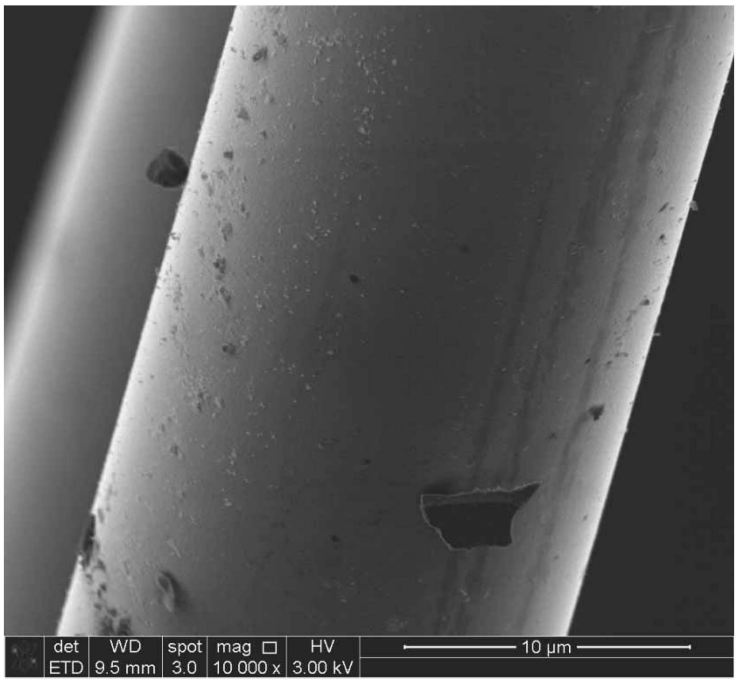


**Figure 93. SEM micrograph of the Hi-Nicalon™ S specimen "Air 16" examining fiber surface in the lower portion of the fiber, near the air inlet**

**($\sigma_{cr}$ = 1123 MPa, $t_f$ = 1.35 h)**

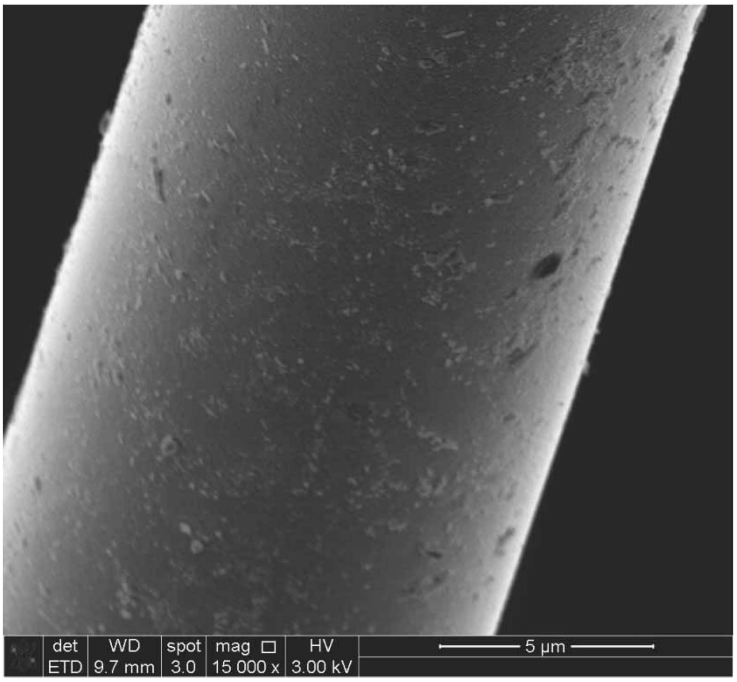


**Figure 94. SEM micrograph of the Hi-Nicalon™ S specimen "Air 16" examining fiber surface in the lower portion of the fiber, near the air inlet**

**($\sigma_{cr}$ = 1123 MPa, $t_f$ = 1.35 h)**

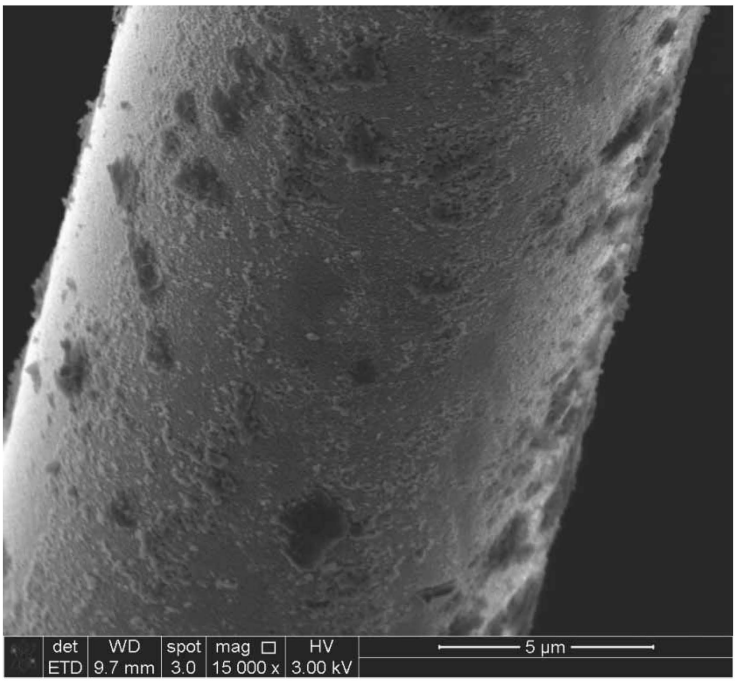


**Figure 95. SEM micrograph of the Hi-Nicalon™ S specimen "Air 16" examining fiber surface in the lower portion of the fiber, near the air inlet**

**($\sigma_{cr}$ = 1123 MPa, $t_f$ = 1.35 h)**

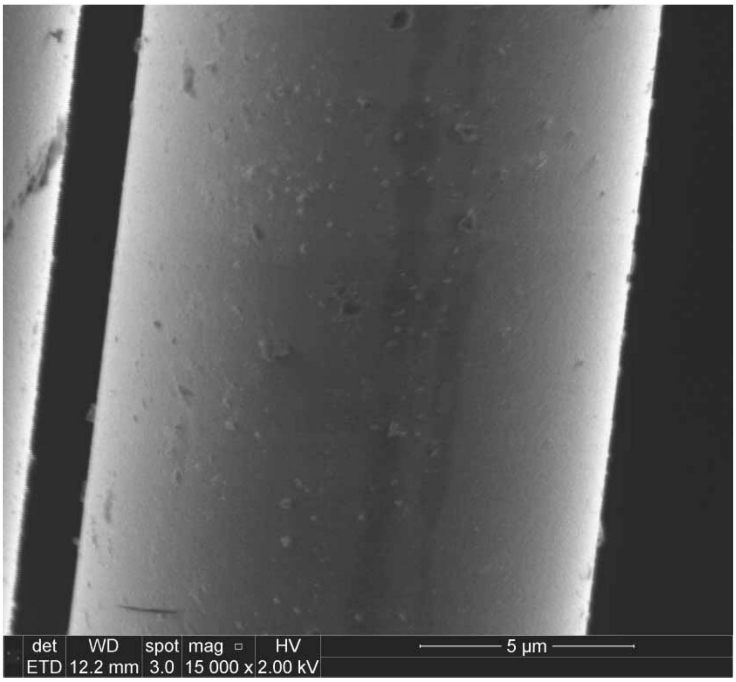


**Figure 96. SEM micrograph of the Hi-Nicalon™ S specimen "Air 16" examining fiber surface near the fracture surface ($\sigma_{cr}$ = 1123 MPa, $t_f$ = 1.35 h)**

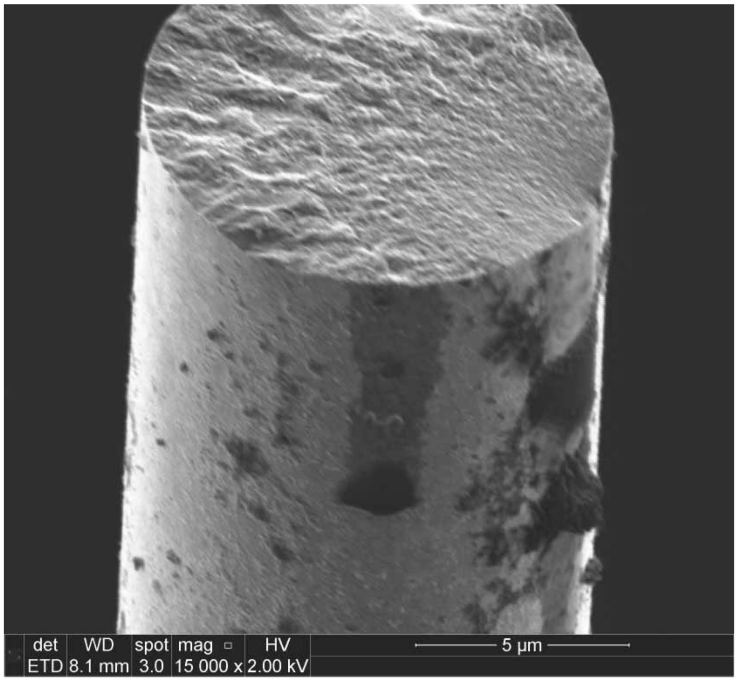


**Figure 97. SEM micrograph of the Hi-Nicalon™ S specimen "Air 16" examining the fracture surface of a fiber ($\sigma_{cr}$ = 1123 MPa, $t_f$ = 1.35 h)**

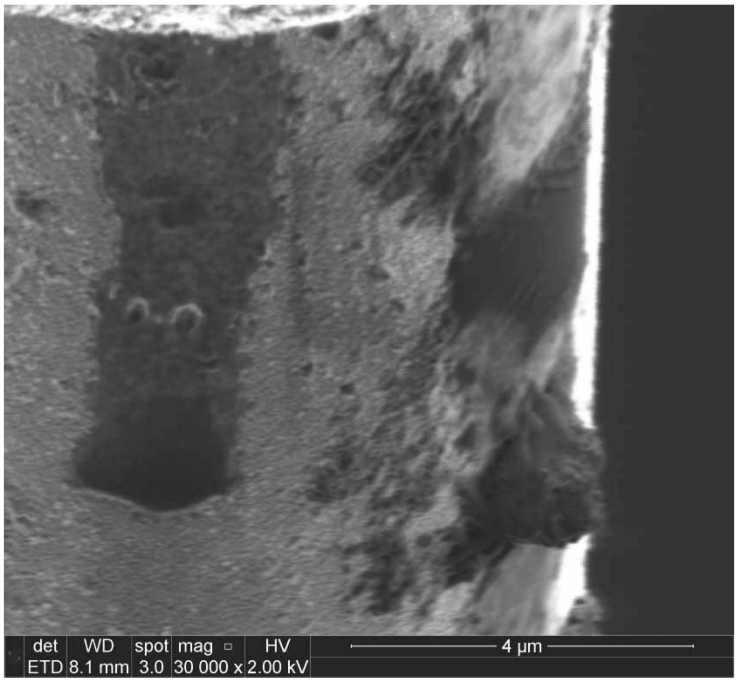


**Figure 98. SEM micrograph of the Hi-Nicalon™ S specimen "Air 16" examining fiber surface in the vicinity of the fracture surface. Note that the edge of the fracture surface is seen in the upper left corner of the image. This fiber is also seen in Figure 97 ($\sigma_{cr}$ = 1123 MPa, $t_f$ = 1.35 h)**

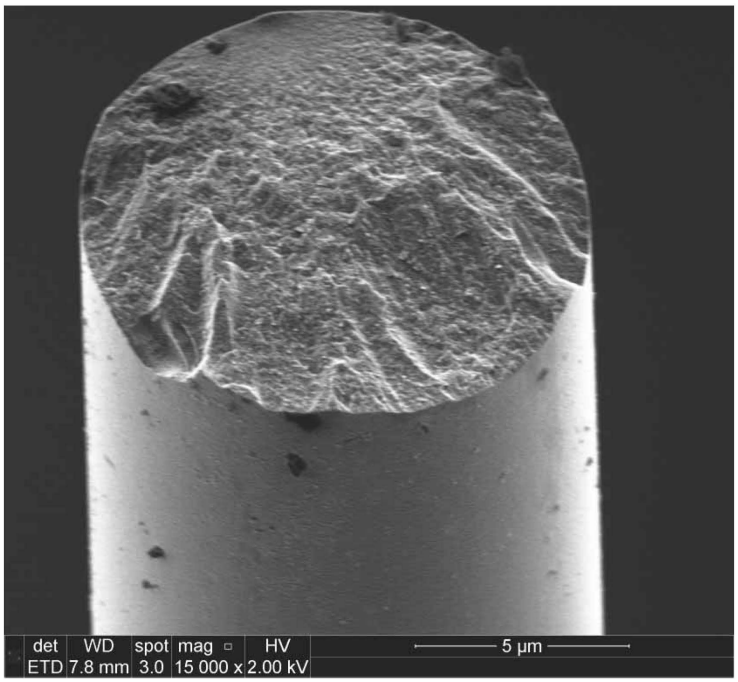


**Figure 99. SEM micrograph of the Hi-Nicalon™ S specimen "Air 16" examining the fracture surface of a fiber ($\sigma_{cr}$ = 1123 MPa, $t_f$ = 1.35 h)**

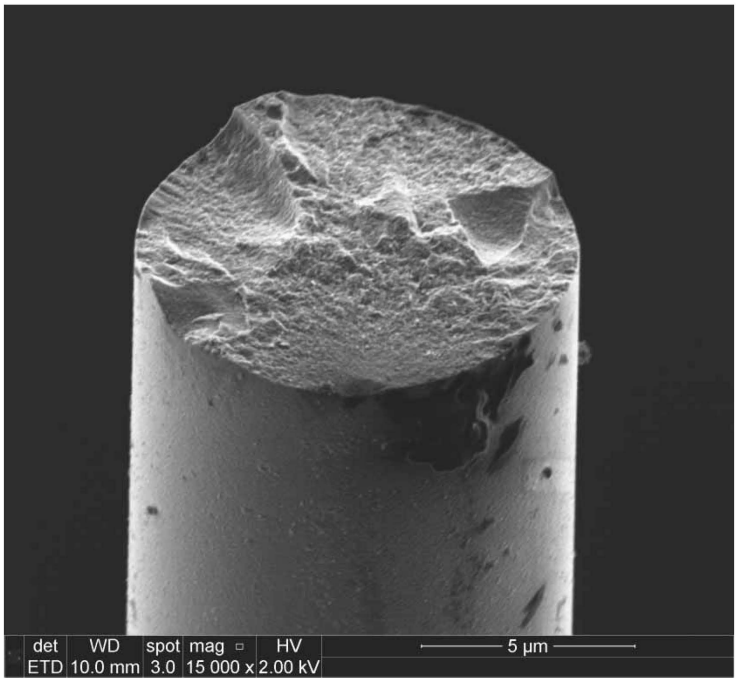


**Figure 100. SEM micrograph of the Hi-Nicalon™ S specimen "Air 16" examining the fracture surface of a fiber ($\sigma_{cr}$ = 1123 MPa, $t_f$ = 1.35 h)**

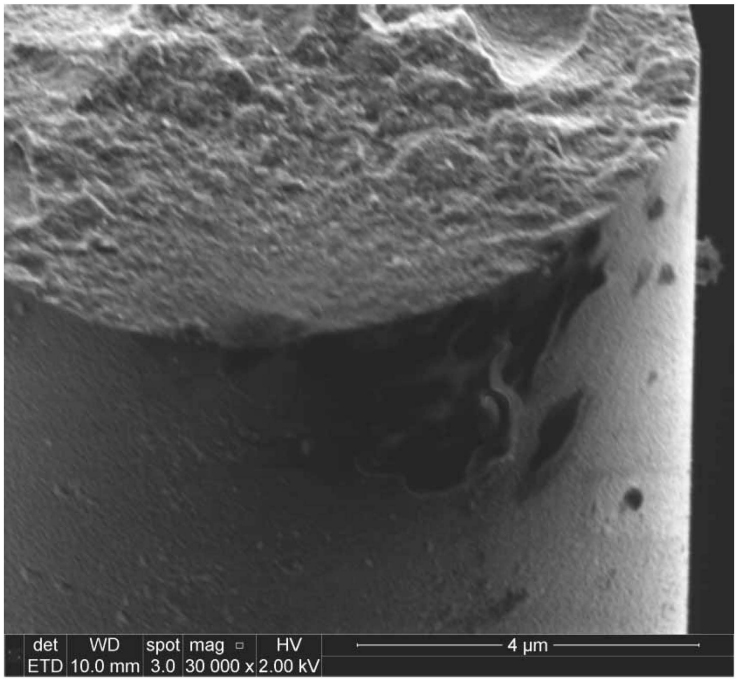


**Figure 101. SEM micrograph of the Hi-Nicalon™ S specimen "Air 16" examining the fracture surface of a fiber ($\sigma_{cr}$ = 1123 MPa, $t_f$ = 1.35 h)**

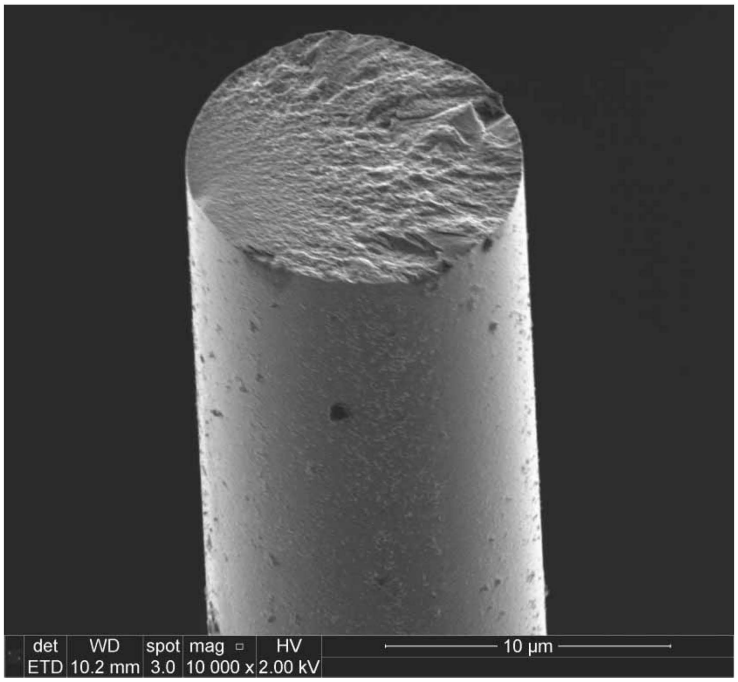


**Figure 102. SEM micrograph of the Hi-Nicalon™ S specimen "Air 16" examining the fracture surface of a fiber ($\sigma_{cr}$ = 1123 MPa, $t_f$ = 1.35 h)**

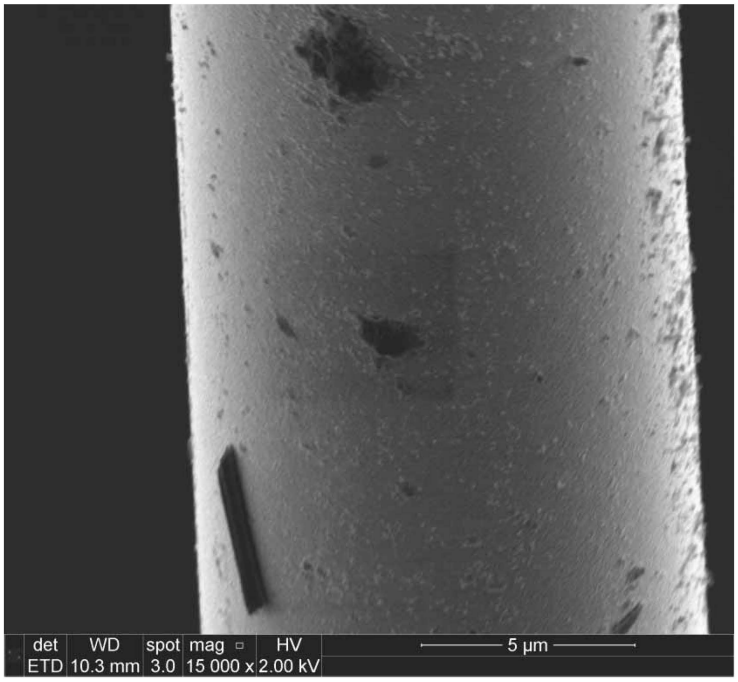


**Figure 103. SEM micrograph of the Hi-Nicalon™ S specimen "Air 16" examining a fiber surface near the fracture surface ($\sigma_{cr}$ = 1123 MPa, $t_f$ = 1.35 h)**

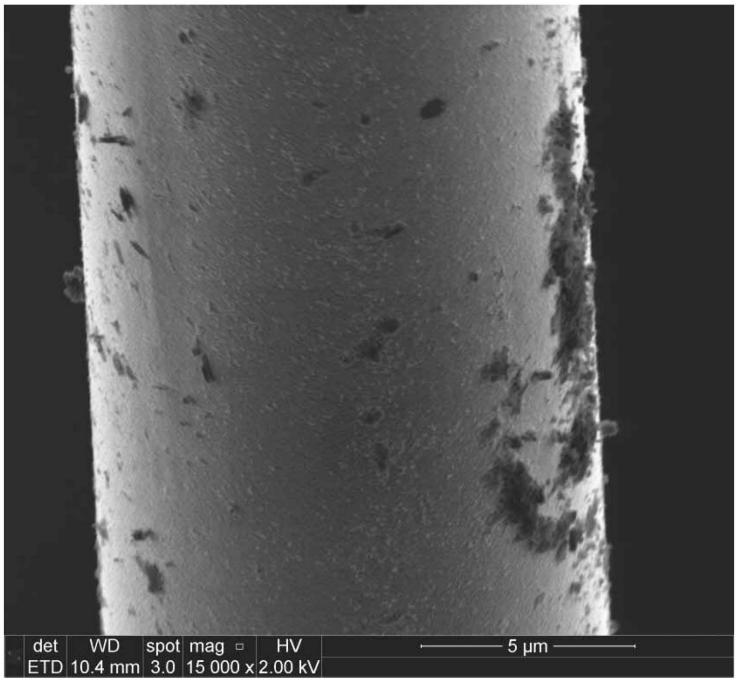


**Figure 104. SEM micrograph of the Hi-Nicalon™ S specimen "Air 16" examining a fiber surface near the fracture surface ($\sigma_{cr}$ = 1123 MPa, $t_f$ = 1.35 h)**

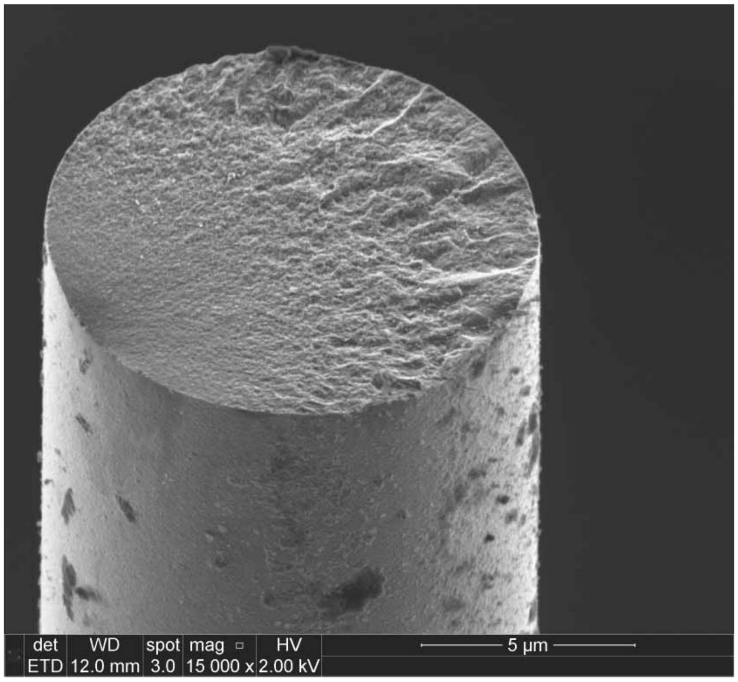


**Figure 105. SEM micrograph of the Hi-Nicalon™ S specimen "Air 16" examining a fiber surface near the fracture surface ($\sigma_{cr}$ = 1123 MPa, $t_f$ = 1.35 h)**

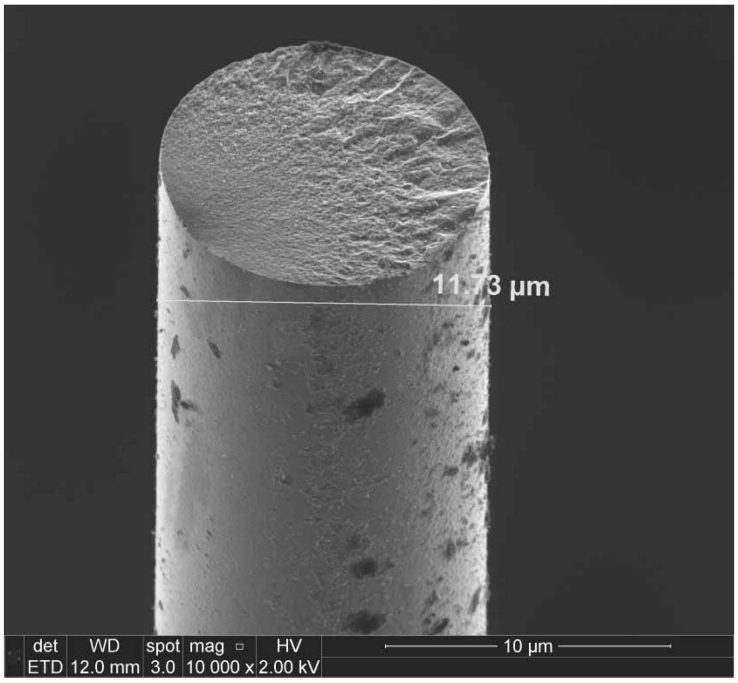


**Figure 106. SEM micrograph of the Hi-Nicalon™ S specimen "Air 16" examining a fiber surface near the fracture surface ($\sigma_{cr}$ = 1123 MPa, $t_f$ = 1.35 h)**

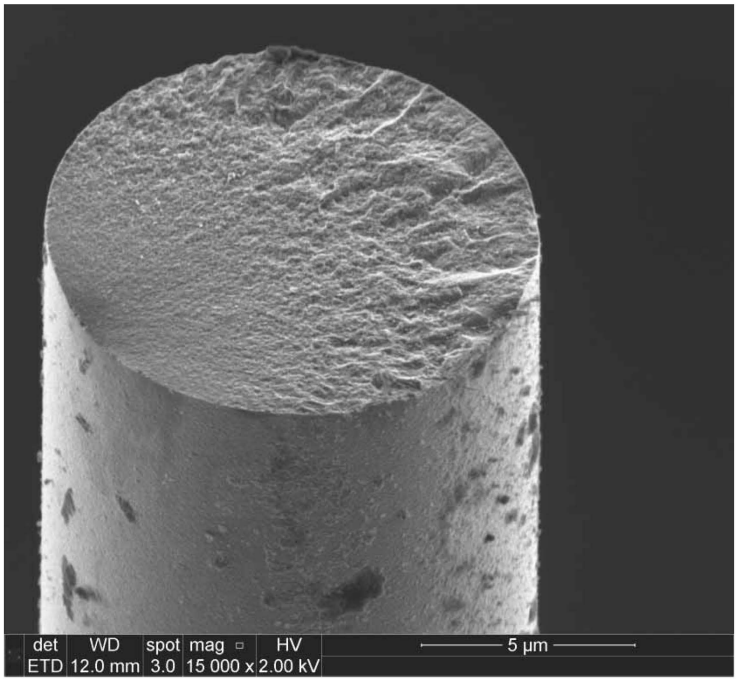


**Figure 107. SEM micrograph of the Hi-Nicalon™ S specimen "Air 16" examining the fracture surface of a fiber ($\sigma_{cr}$ = 1123 MPa, $t_f$ = 1.35 h)**

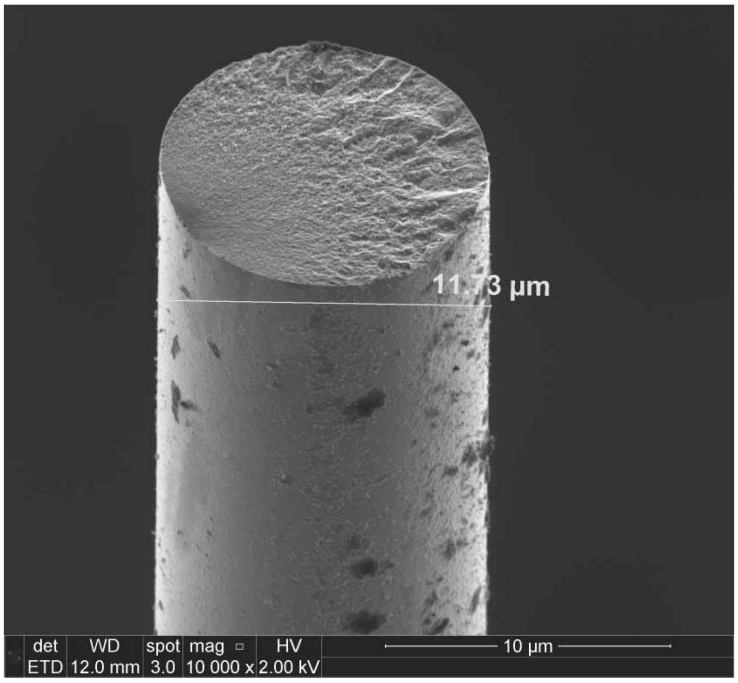


**Figure 108. SEM micrograph of the Hi-Nicalon™ S specimen "Air 16" examining the fracture surface of a fiber and the surface along the fiber length in the vicinity. This fiber is also shown in Figure 107 ($\sigma_{cr}$ = 1123 MPa, $t_f$ = 1.35 h)**

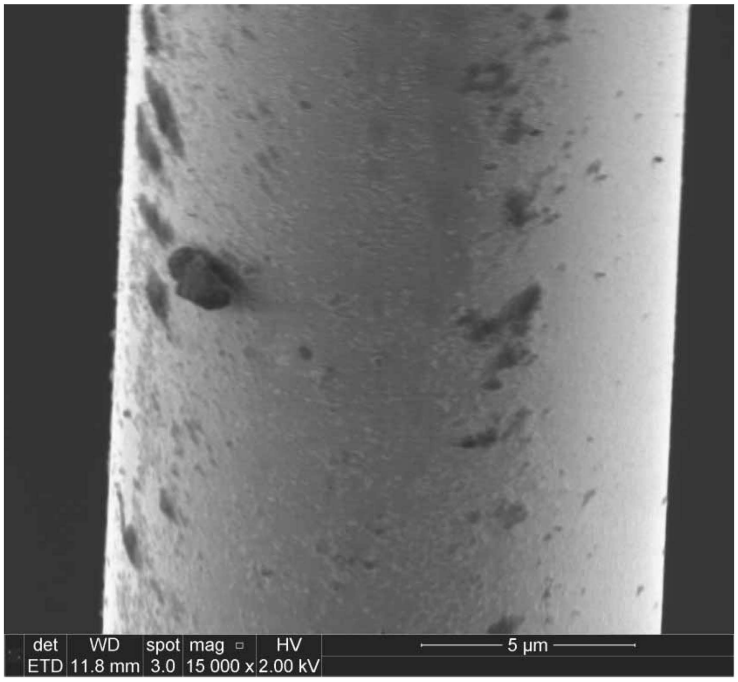


**Figure 109. SEM micrograph of the Hi-Nicalon™ S specimen "Air 16" examining a fiber surface near the fracture surface ($\sigma_{cr}$ = 1123 MPa, $t_f$ = 1.35 h)**

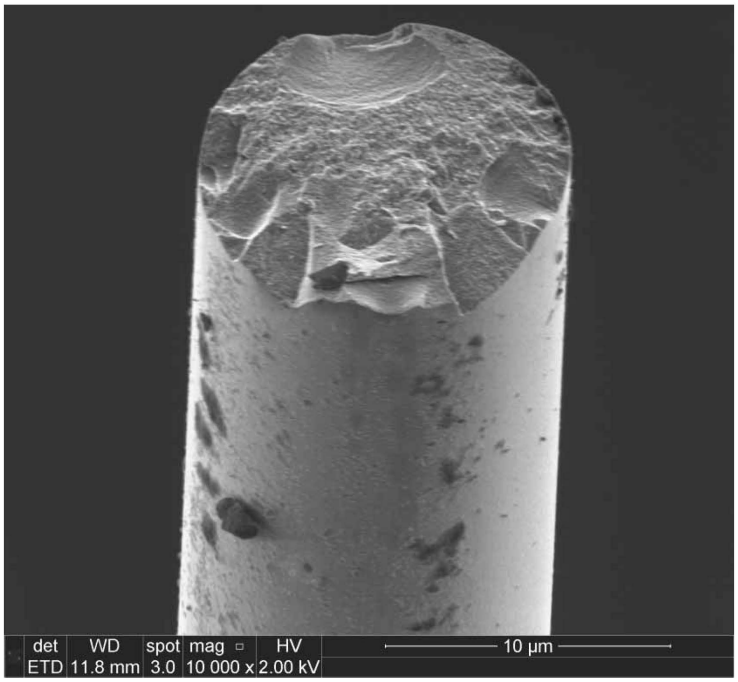


**Figure 110. SEM micrograph of the Hi-Nicalon™ S specimen "Air 16" examining the fracture surface of a fiber. This fiber is also shown in Figure 109**

**($\sigma_{cr}$ = 1123 MPa, $t_f$ = 1.35 h)**

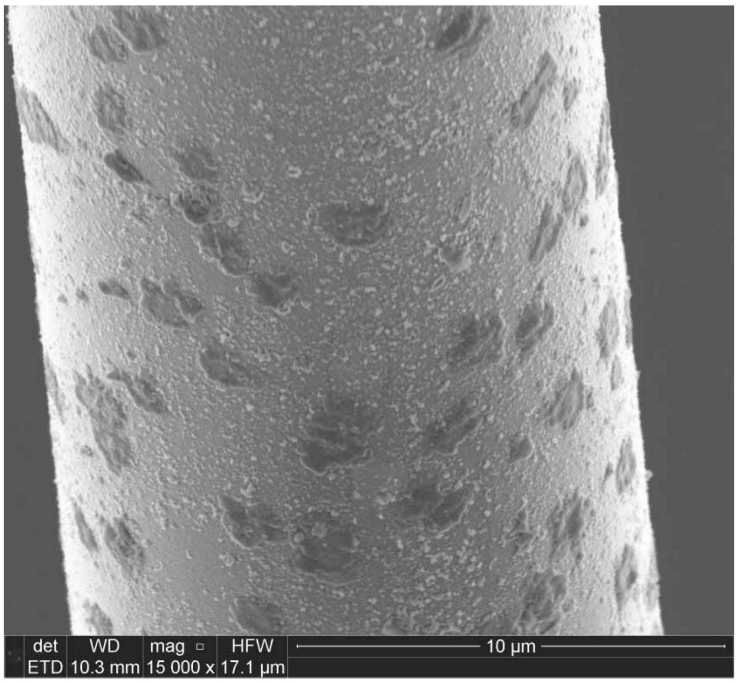


**Figure 111. SEM micrograph of the Hi-Nicalon™ S specimen "Steam 4" examining fiber surface in the lower portion of a fiber, near the steam inlet**

**($\sigma_{cr}$ = 2.96 MPa, $t_f$ > 100 h)**

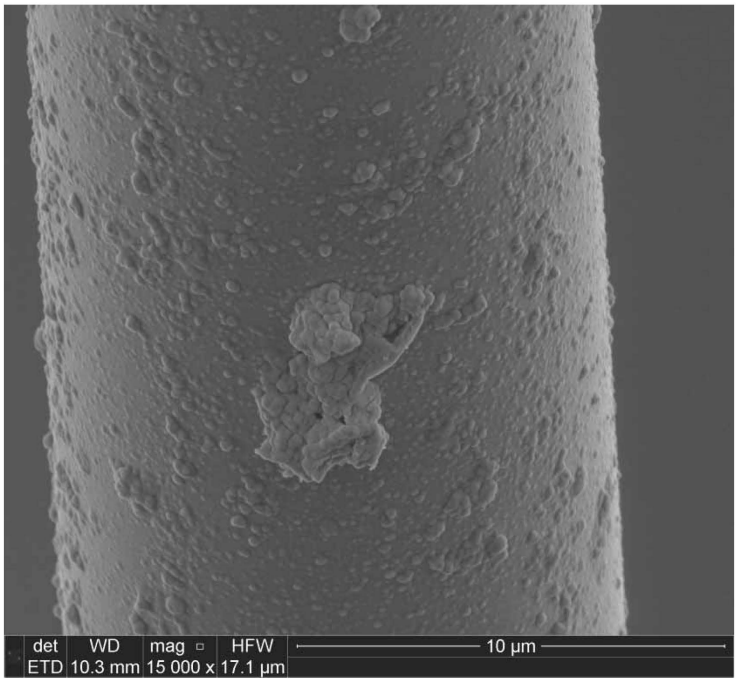


**Figure 112. SEM micrograph of the Hi-Nicalon™ S specimen "Steam 4" examining a fiber surface in the lower portion of a fiber, near the steam inlet ($\sigma_{cr}$ = 2.96 MPa, $t_f$ > 100 h)**

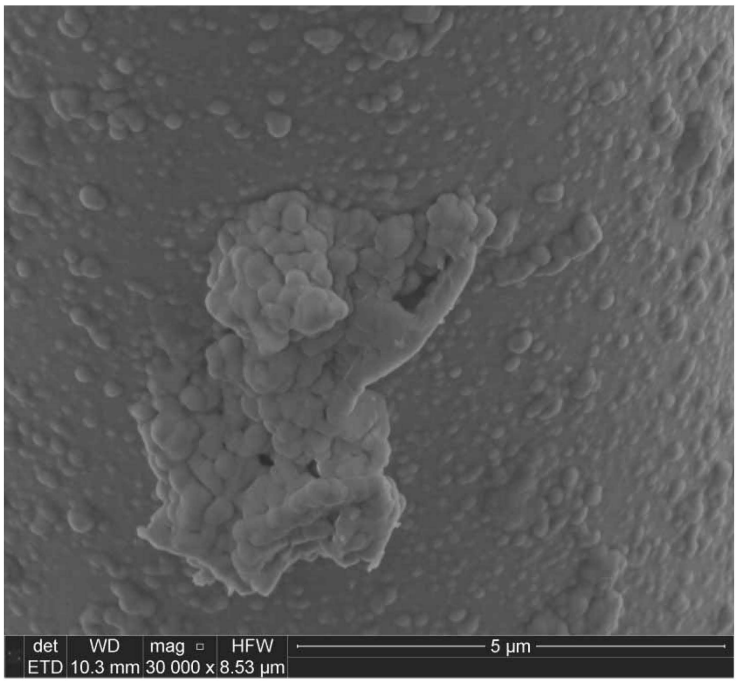


**Figure 113. SEM micrograph of the Hi-Nicalon™ S specimen "Steam 4" examining a deposit on the fiber surface in the lower portion of a fiber, near the steam inlet. This fiber is also shown in Figure 112 ($\sigma_{cr}$ = 2.96 MPa, $t_f$ > 100 h)**

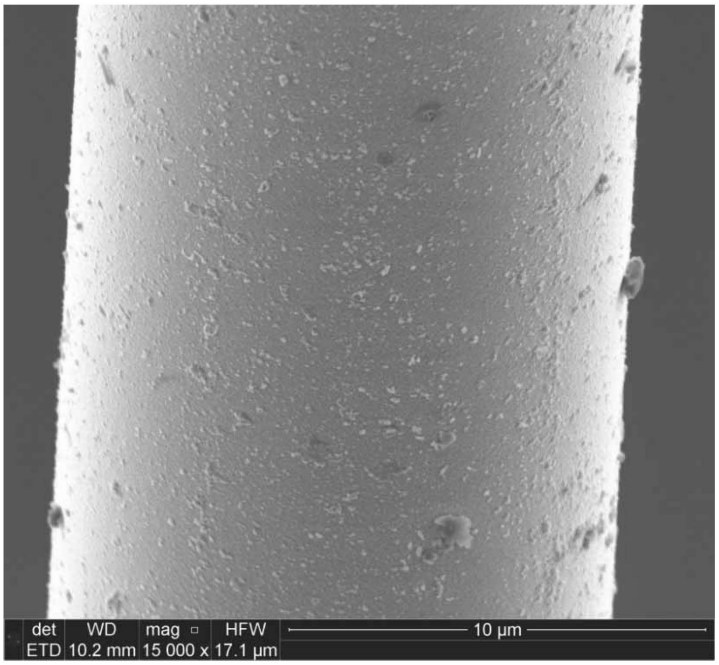


**Figure 114. SEM micrograph of the Hi-Nicalon™ S specimen "Steam 4" examining a fiber surface in the lower portion of a fiber, near the steam inlet**

**($\sigma_{cr}$ = 2.96 MPa, $t_f$ > 100 h)**

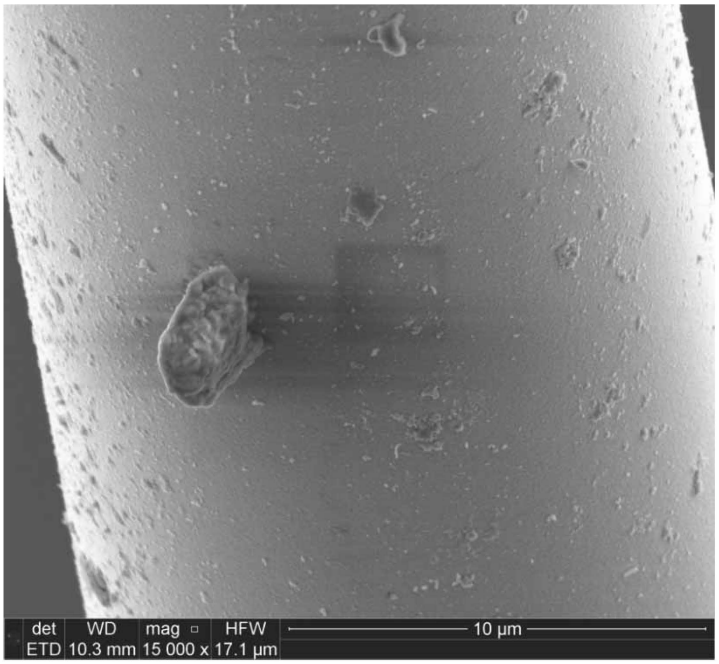


**Figure 115. SEM micrograph of the Hi-Nicalon™ S specimen "Steam 4" examining a fiber surface in the lower portion of a fiber, near the steam inlet. Note, the square seen in the center of the image is a product of the imaging process**

**($\sigma_{cr}$ = 2.96 MPa, $t_f$ > 100 h)**

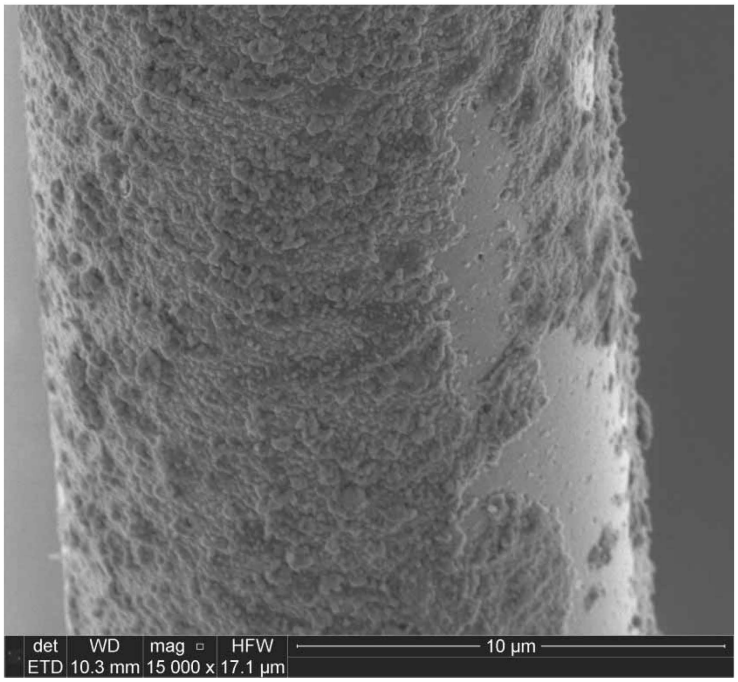


**Figure 116. SEM micrograph of the Hi-Nicalon™ S specimen "Steam 4" examining a fiber surface in the lower portion of a fiber, near the steam inlet. Note the deposits on the surface resulting from oxidation ($\sigma_{cr}$ = 2.96 MPa, $t_f$ > 100 h)**

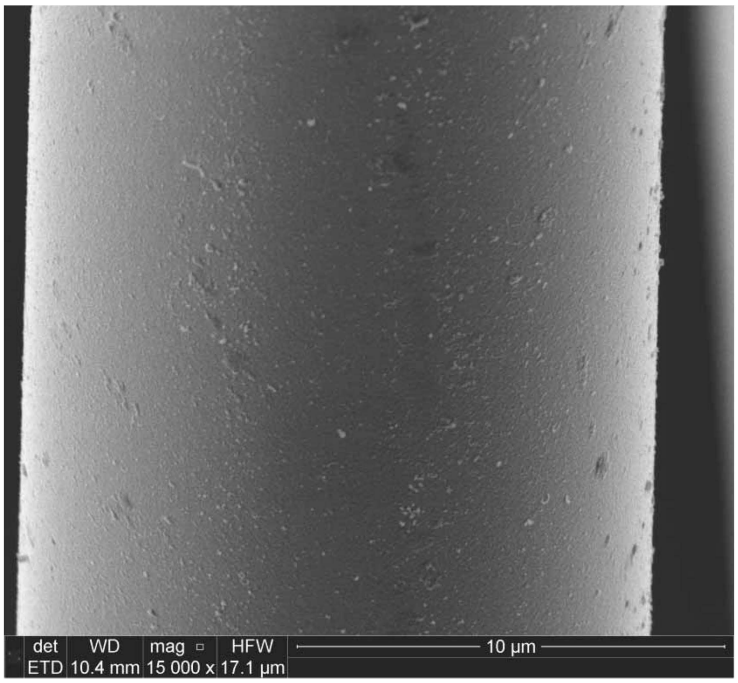


**Figure 117. SEM micrograph of the Hi-Nicalon™ S specimen "Steam 4" examining a fiber surface in the lower portion of a fiber, near the steam inlet ($\sigma_{cr}$ = 2.96 MPa, $t_f$ > 100 h)**

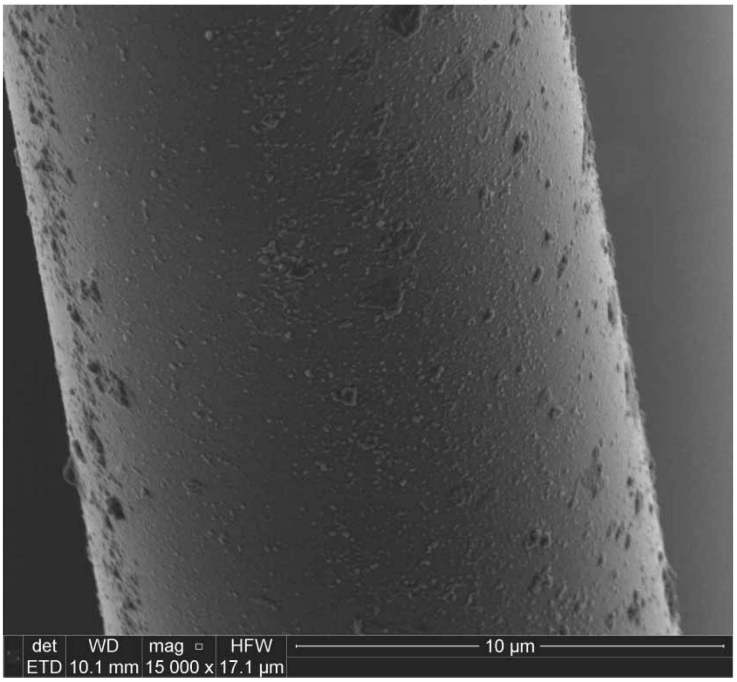


**Figure 118. SEM micrograph of the Hi-Nicalon™ S specimen "Steam 4" examining a fiber surface in the lower portion of a fiber, near the steam inlet ($\sigma_{cr}$ = 2.96 MPa, $t_f$ > 100 h)**

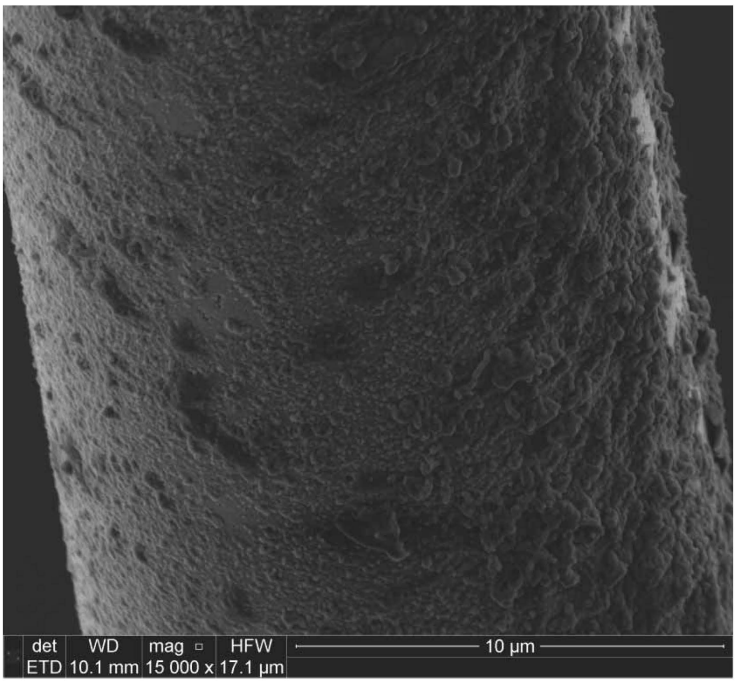


**Figure 119. SEM micrograph of the Hi-Nicalon™ S specimen "Steam 4" examining a fiber surface in the lower portion of a fiber, near the steam inlet. Note the deposits on the surface resulting from oxidation ($\sigma_{cr}$ = 2.96 MPa, $t_f$ > 100 h)**

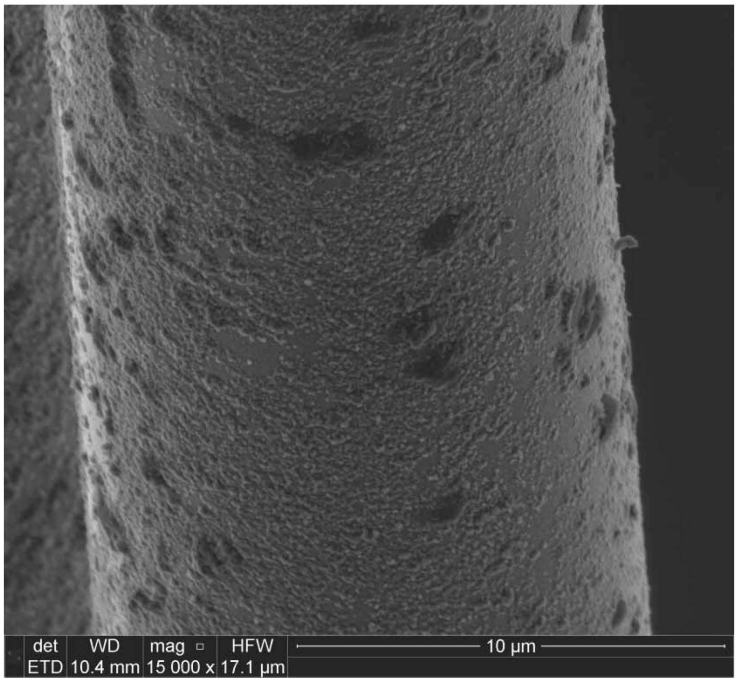


**Figure 120. SEM micrograph of the Hi-Nicalon™ S specimen "Steam 4" examining a fiber surface in the lower portion of a fiber, near the steam inlet ($\sigma_{cr}$ = 2.96 MPa, $t_f$ > 100 h)**

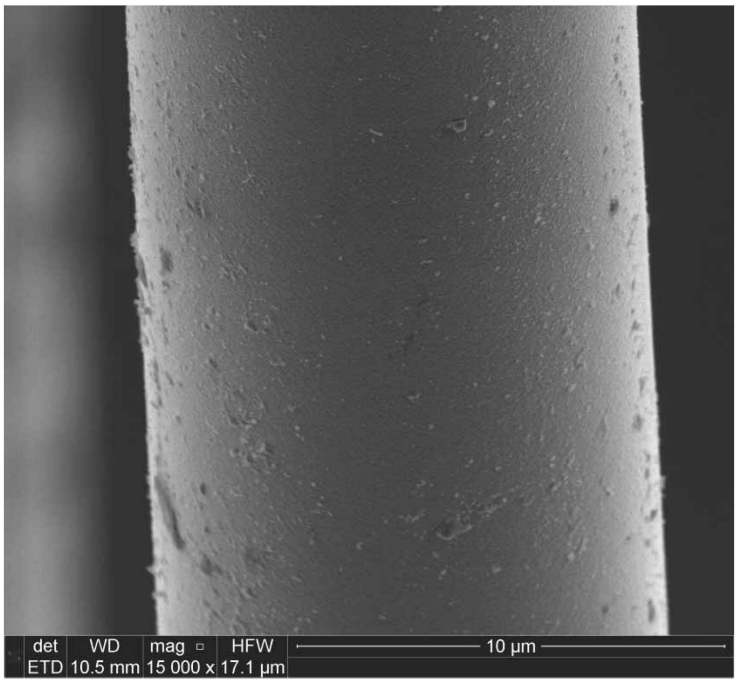


**Figure 121. SEM micrograph of the Hi-Nicalon™ S specimen "Steam 4" examining a fiber surface in the central portion of a fiber, near the midpoint of the effective length ($\sigma_{cr}$ = 2.96 MPa, $t_f$ > 100 h)**

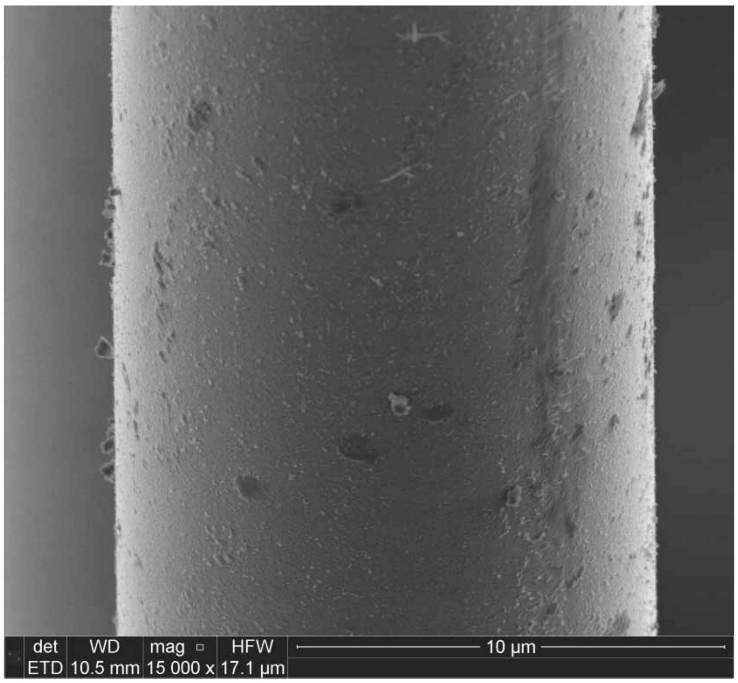


**Figure 122. SEM micrograph of the Hi-Nicalon™ S specimen "Steam 4" examining a fiber surface in the central portion of a fiber, near the midpoint of the effective length ($\sigma_{cr}$ = 2.96 MPa, $t_f$ > 100 h)**

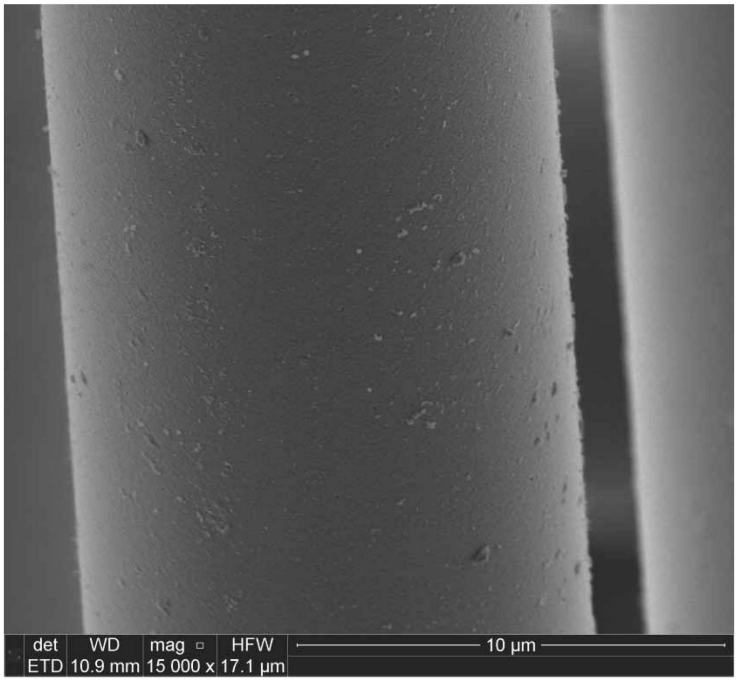


**Figure 123. SEM micrograph of the Hi-Nicalon™ S specimen "Steam 4" examining a fiber surface in the central portion of a fiber, near the midpoint of the effective length ($\sigma_{cr}$ = 2.96 MPa, $t_f$ > 100 h)**

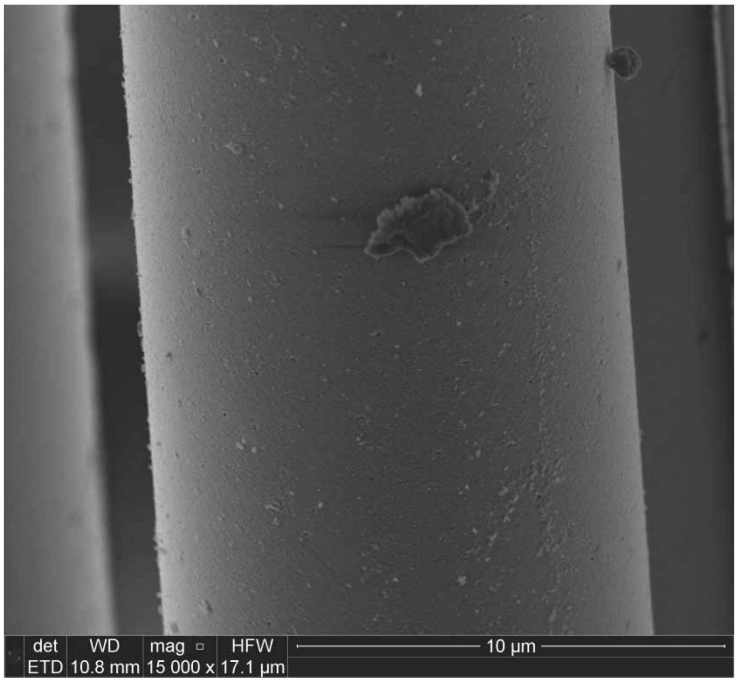


**Figure 124. SEM micrograph of the Hi-Nicalon™ S specimen "Steam 4" examining a fiber surface in the central portion of a fiber, near the midpoint of the effective length ($\sigma_{cr}$ = 2.96 MPa, $t_f$ > 100 h)**

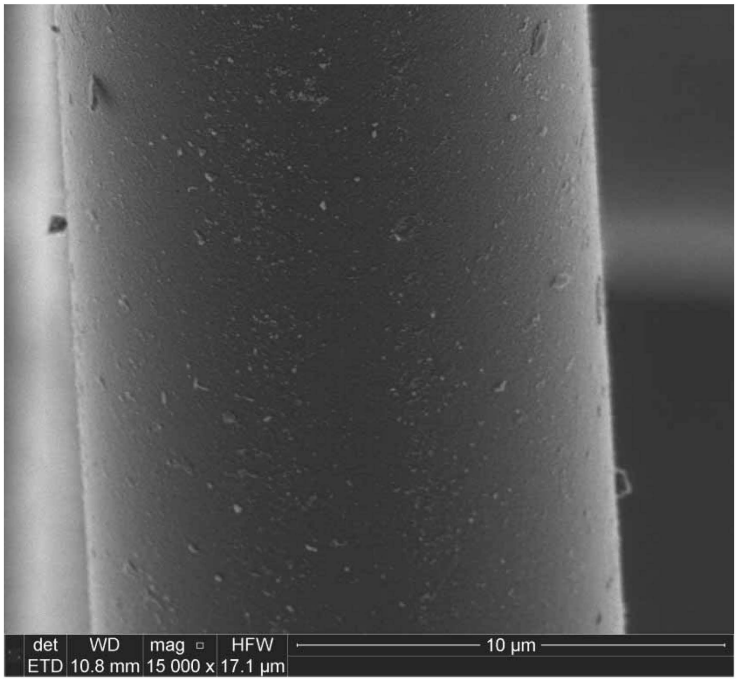


**Figure 125. SEM micrograph of the Hi-Nicalon™ S specimen "Steam 4" examining a fiber surface in the central portion of a fiber, near the midpoint of the effective length ($\sigma_{cr}$ = 2.96 MPa, $t_f$ > 100 h)**

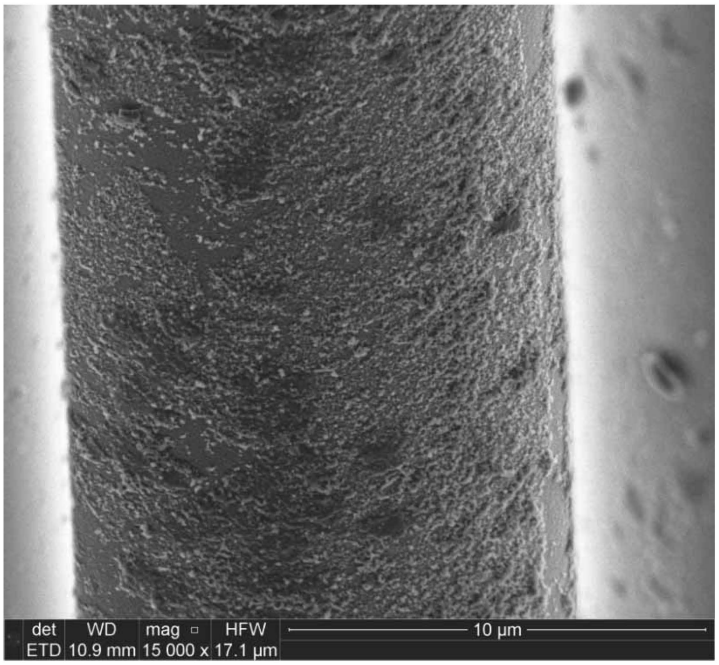


**Figure 126. SEM micrograph of the Hi-Nicalon™ S specimen "Steam 4" examining a fiber surface in the central portion of a fiber, near the midpoint of the effective length. Note the deposits on the surface resulting from oxidation**

**($\sigma_{cr}$ = 2.96 MPa, $t_f$ > 100 h)**

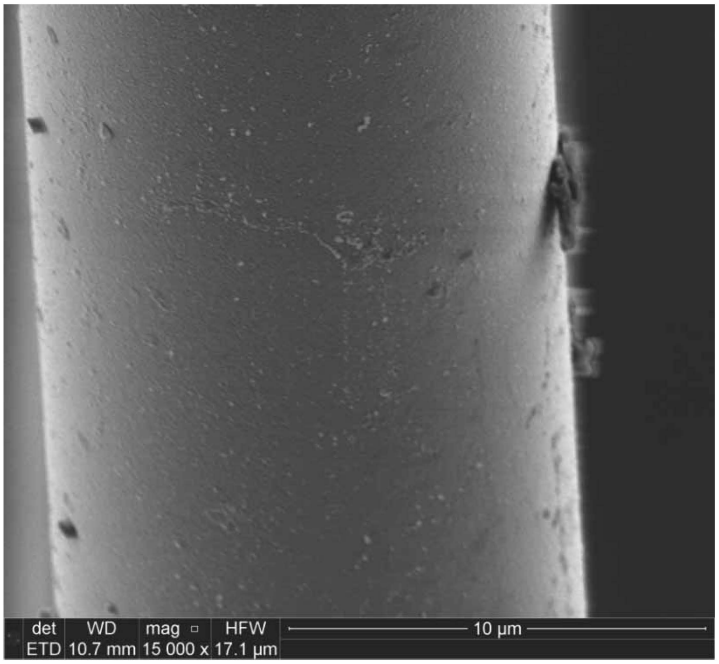


**Figure 127. SEM micrograph of the Hi-Nicalon™ S specimen "Steam 4" examining a fiber surface in the central portion of a fiber, near the midpoint of the effective length ($\sigma_{cr}$ = 2.96 MPa, $t_f$ > 100 h)**

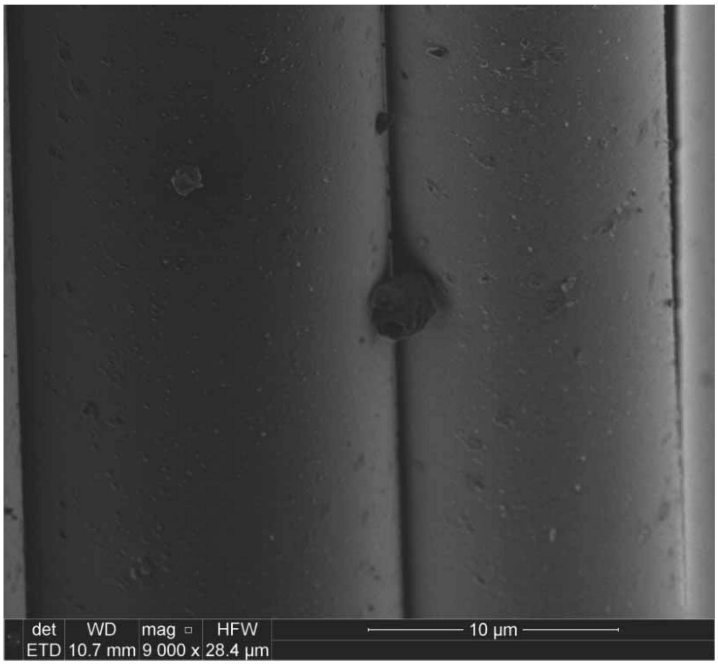


**Figure 128. SEM micrograph of the Hi-Nicalon™ S specimen "Steam 4" examining the surface of two fibers, near the midpoint of the effective length. The deposit in the center of the image appears connected to both fibers ($\sigma_{cr}$ = 2.96 MPa, $t_f$ > 100 h)**


**Figure 129. SEM micrograph of the Hi-Nicalon™ S specimen "Steam 4" examining a deposit that appears to be bound to two fibers, near the midpoint of the effective length. This deposit and these fibers are also shown in Figure 128**

**($\sigma_{cr}$ = 2.96 MPa, $t_f$ > 100 h)**

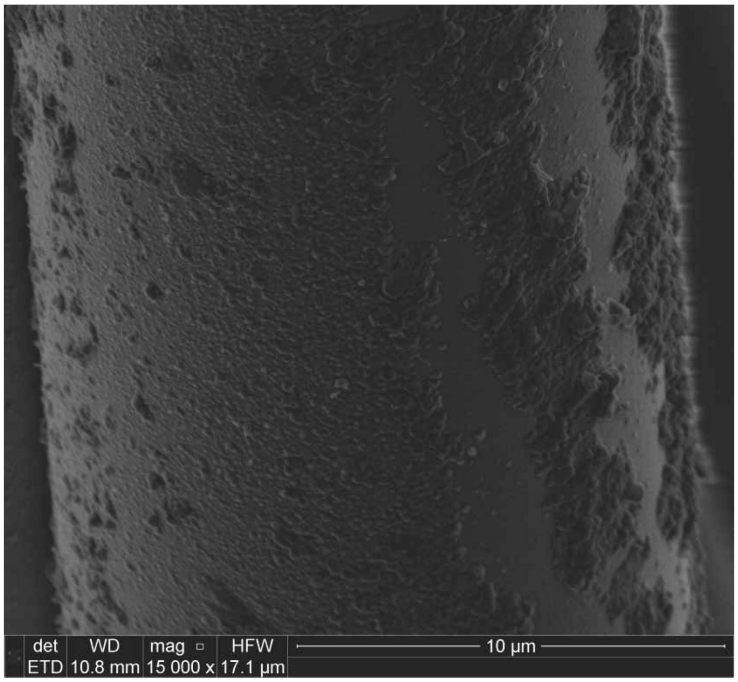


**Figure 130. SEM micrograph of the Hi-Nicalon™ S specimen "Steam 4" examining a fiber surface in the central portion of a fiber, near the midpoint of the effective length. Note the deposits on the fiber surface resulting from oxidation**

**($\sigma_{cr}$ = 2.96 MPa, $t_f$ > 100 h)**

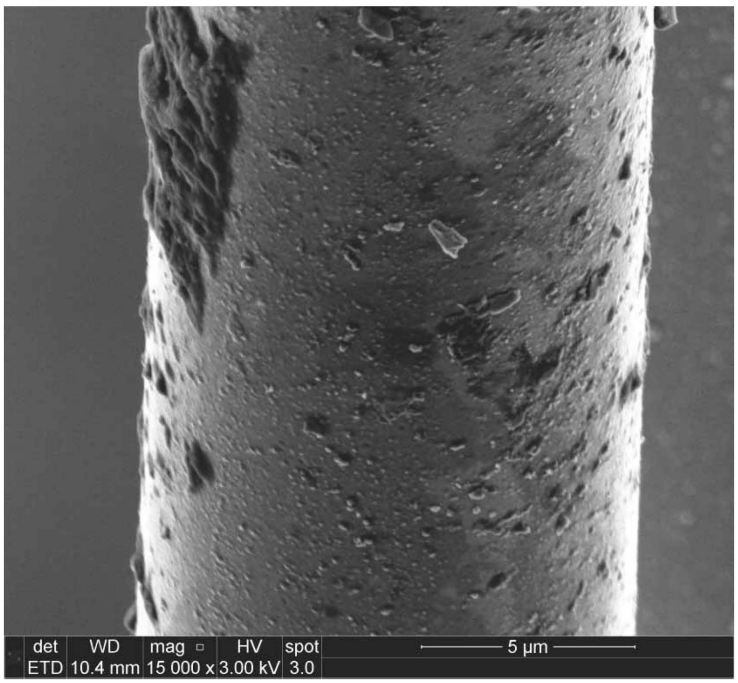


**Figure 131. SEM micrograph of the Hi-Nicalon™ S specimen "Steam 4" examining a fiber surface in the upper portion of a fiber ($\sigma_{cr}$ = 2.96 MPa, $t_f$ > 100 h)**

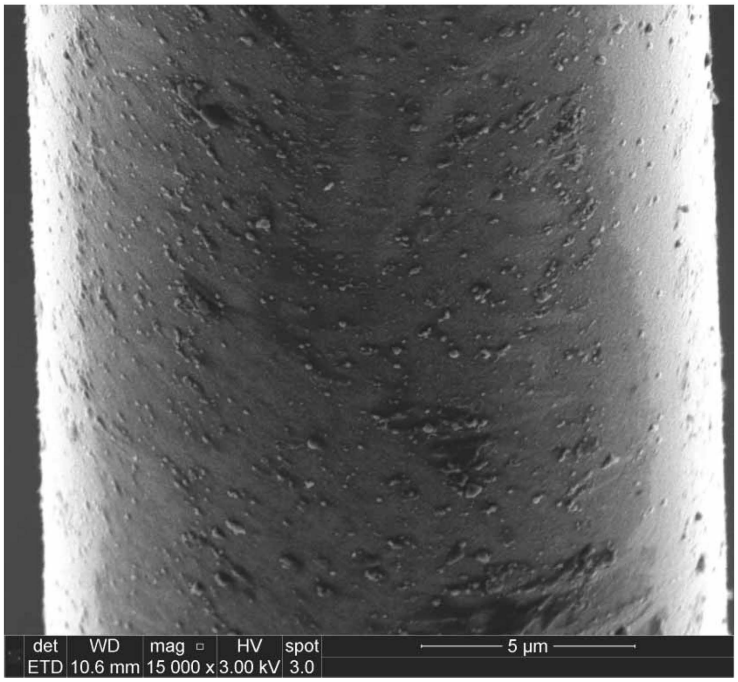


**Figure 132. SEM micrograph of the Hi-Nicalon™ S specimen "Steam 4" examining a fiber surface in the upper portion of a fiber ($\sigma_{cr}$ = 2.96 MPa, $t_f$ > 100 h)**

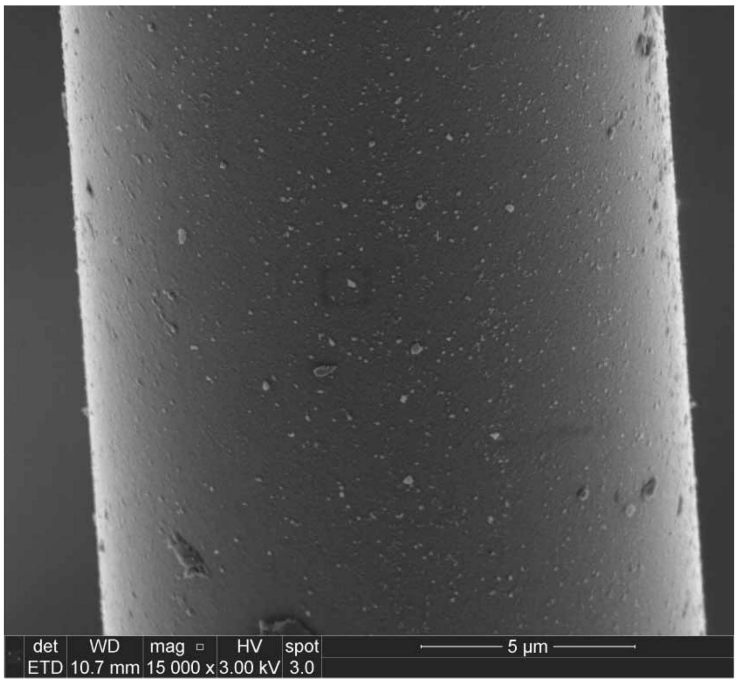


**Figure 133. SEM micrograph of the Hi-Nicalon™ S specimen "Steam 4" examining a fiber surface in the upper portion of a fiber. Note, the dark rectangle in the center of the image is a product of the imaging process ($\sigma_{cr}$ = 2.96 MPa, $t_f$ > 100 h)**

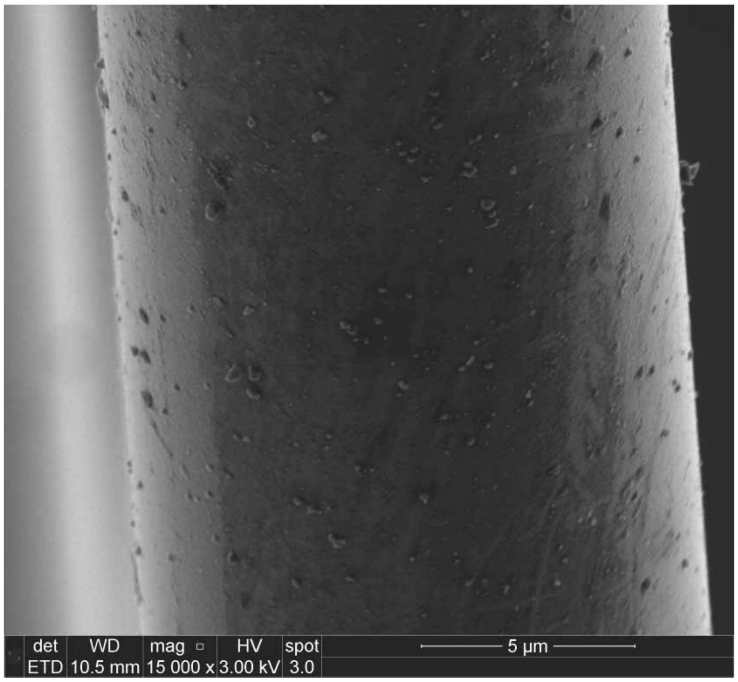


**Figure 134. SEM micrograph of the Hi-Nicalon™ S specimen "Steam 4" examining a fiber surface in the upper portion of a fiber ($\sigma_{cr}$ = 2.96 MPa, $t_f$ > 100 h)**

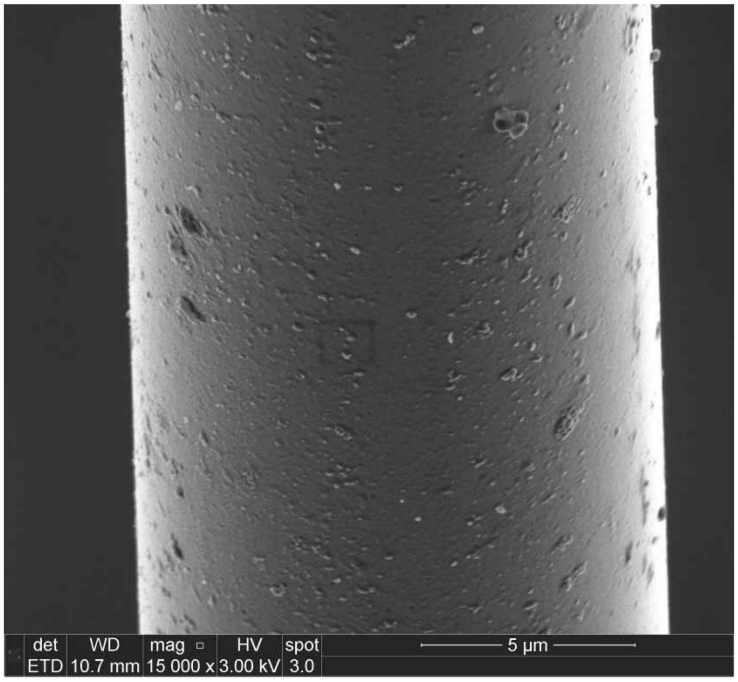


**Figure 135. SEM micrograph of the Hi-Nicalon™ S specimen "Steam 4" examining a fiber surface in the upper portion of a fiber. Note, the dark rectangle in the center of the image is a product of the imaging process ($\sigma_{cr}$ = 2.96 MPa, $t_f$ > 100 h)**

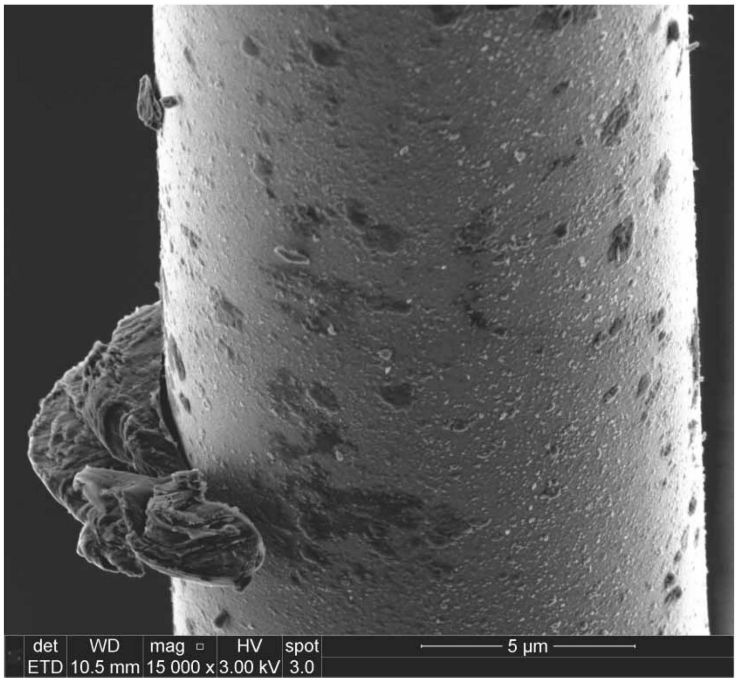


**Figure 136. SEM micrograph of the Hi-Nicalon™ S specimen "Steam 4" examining a fiber surface in the upper portion of a fiber ($\sigma_{cr}$ = 2.96 MPa, $t_f$ > 100 h)**

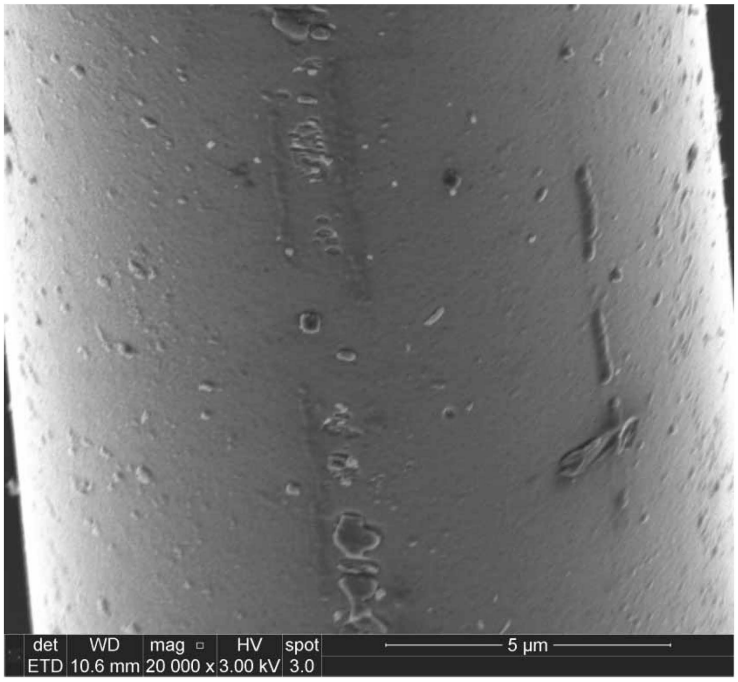


**Figure 137. SEM micrograph of the Hi-Nicalon™ S specimen "Steam 4" examining a fiber surface in the upper portion of a fiber ($\sigma_{cr}$ = 2.96 MPa, $t_f$ > 100 h)**

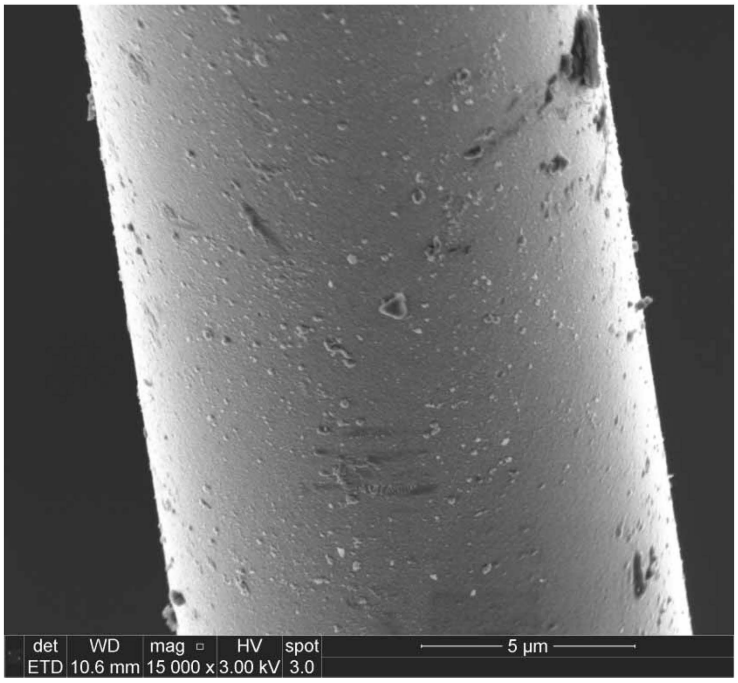


**Figure 138. SEM micrograph of the Hi-Nicalon™ S specimen "Steam 4" examining a fiber surface in the upper portion of a fiber ($\sigma_{cr}$ = 2.96 MPa, $t_f$ > 100 h)**

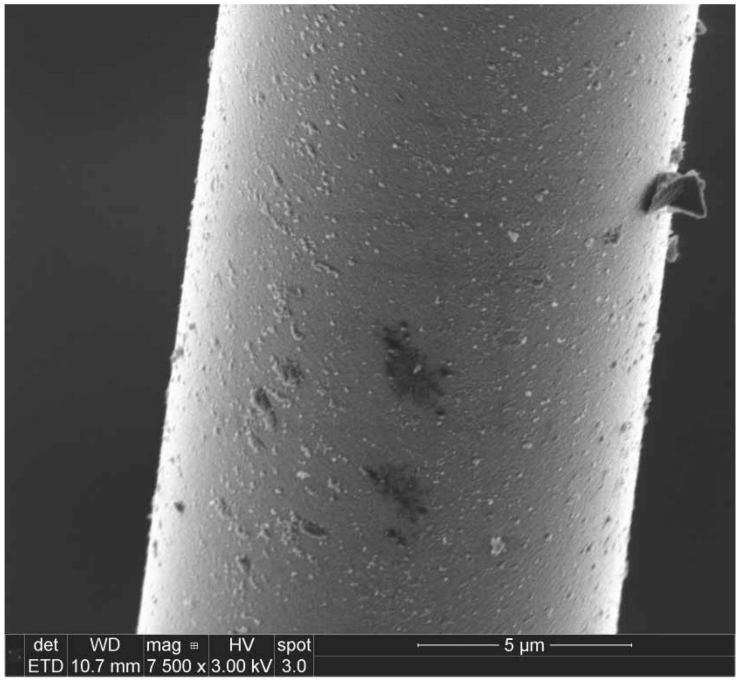


**Figure 139. SEM micrograph of the Hi-Nicalon™ S specimen "Steam 4" examining a fiber surface in the upper portion of a fiber ($\sigma_{cr}$ = 2.96 MPa, $t_f$ > 100 h)**

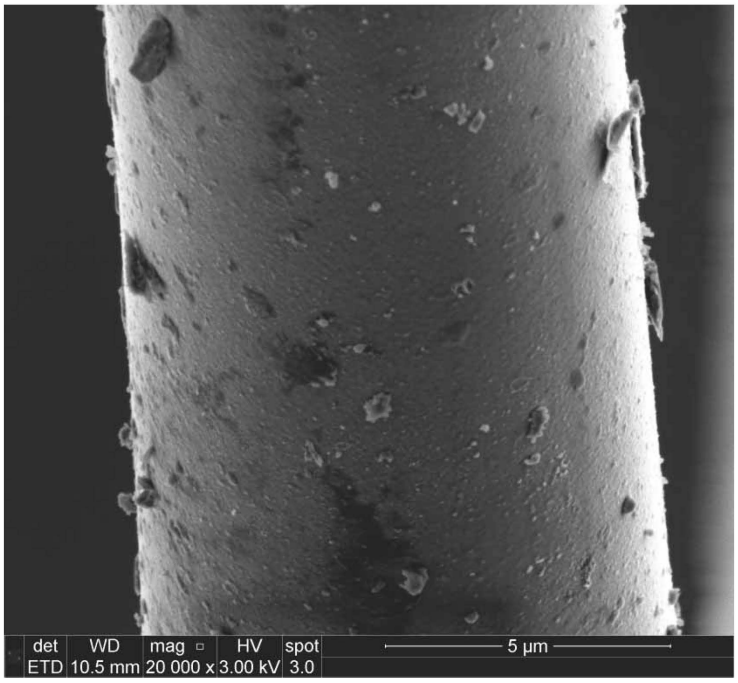


**Figure 140. SEM micrograph of the Hi-Nicalon™ S specimen "Steam 4" examining a fiber surface in the upper portion of a fiber ($\sigma_{cr}$ = 2.96 MPa, $t_f$ > 100 h)**

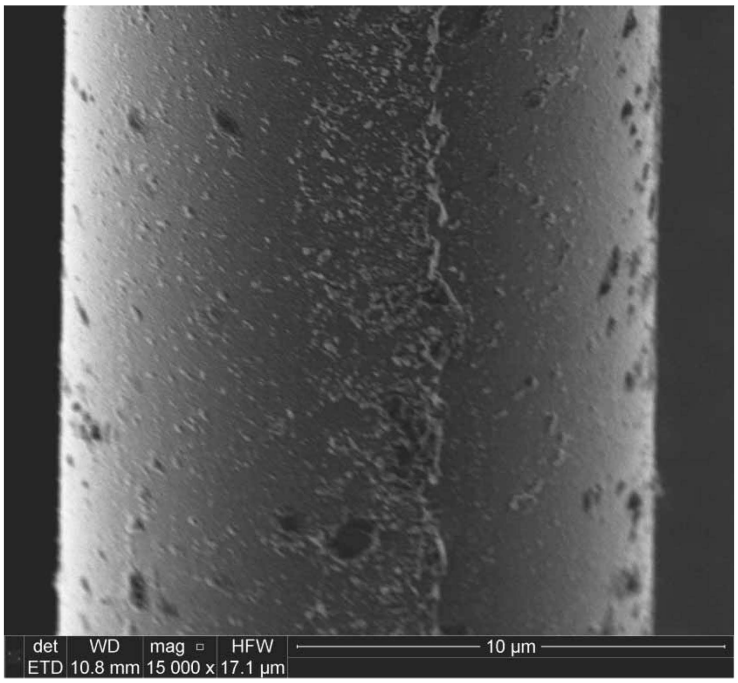


**Figure 141. SEM micrograph of the Hi-Nicalon™ S specimen "Steam 22" examining a fiber surface in the lower portion of a fiber, near the steam inlet ($\sigma_{cr}$ = 750 MPa, $t_f$ > 100 h)**

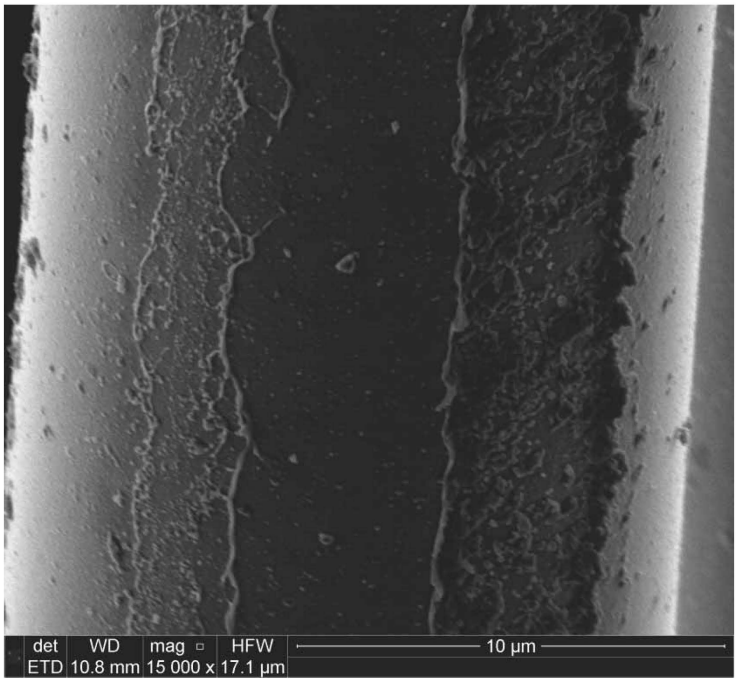


**Figure 142. SEM micrograph of the Hi-Nicalon™ S specimen "Steam 22" examining a fiber surface in the lower portion of a fiber, near the steam inlet**

**($\sigma_{cr}$ = 750 MPa, $t_f$ > 100 h)**

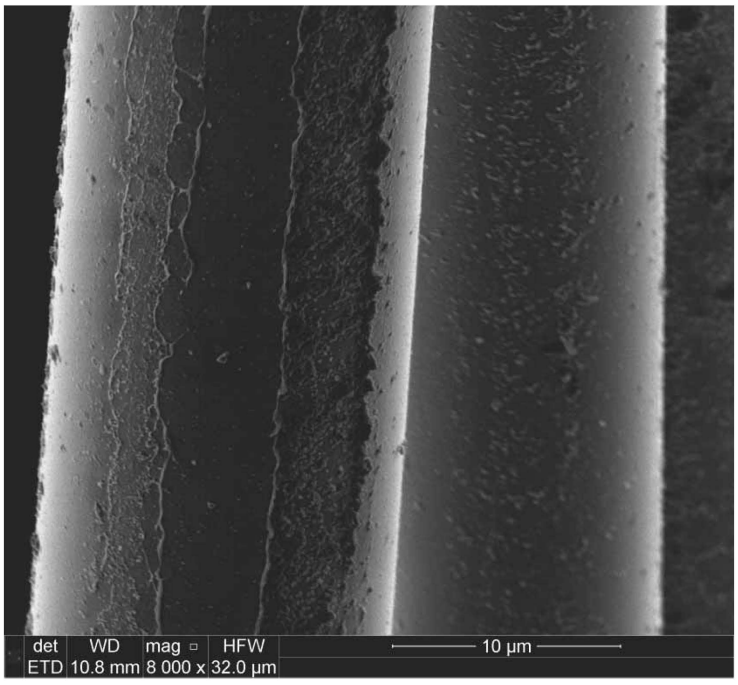


**Figure 143. SEM micrograph of the Hi-Nicalon™ S specimen "Steam 22" examining two fiber surfaces in the lower portion of the fiber tow, near the steam inlet**

**($\sigma_{cr}$ = 750 MPa, $t_f$ > 100 h)**

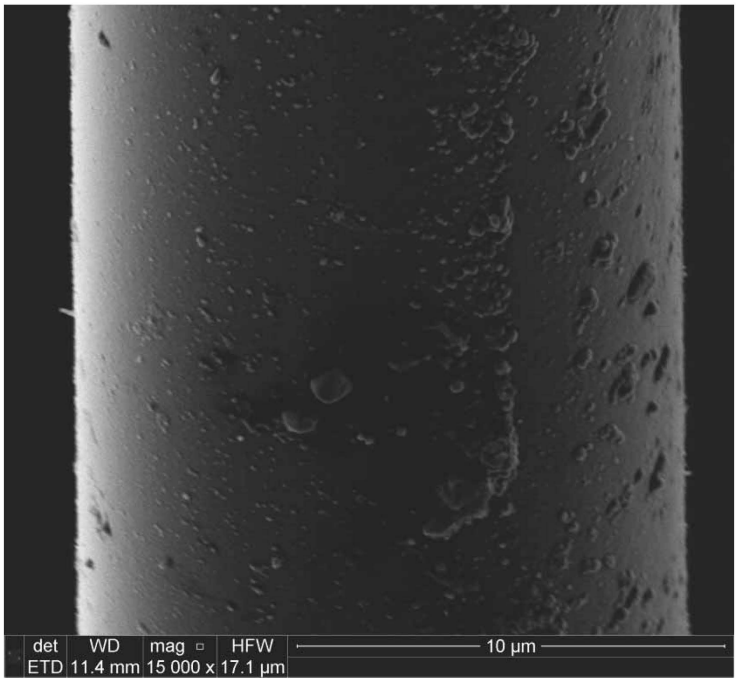


**Figure 144. SEM micrograph of the Hi-Nicalon™ S specimen "Steam 22" examining a fiber surface in the lower portion of a fiber, near the steam inlet**

**($\sigma_{cr}$ = 750 MPa, $t_f$ > 100 h)**

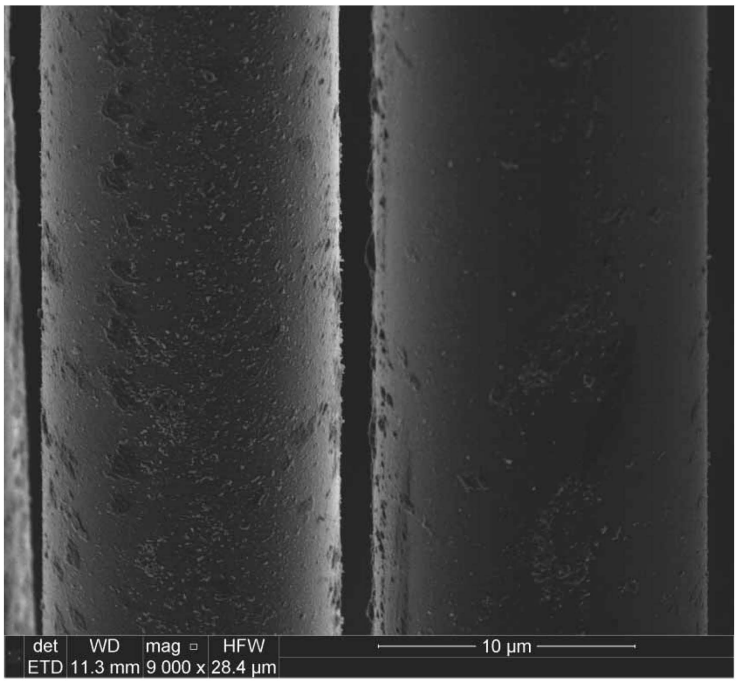


**Figure 145. SEM micrograph of the Hi-Nicalon™ S specimen "Steam 22" examining two fiber surfaces in the lower portion of the fiber tow, near the steam inlet**

**($\sigma_{cr}$ = 750 MPa, $t_f$ > 100 h)**

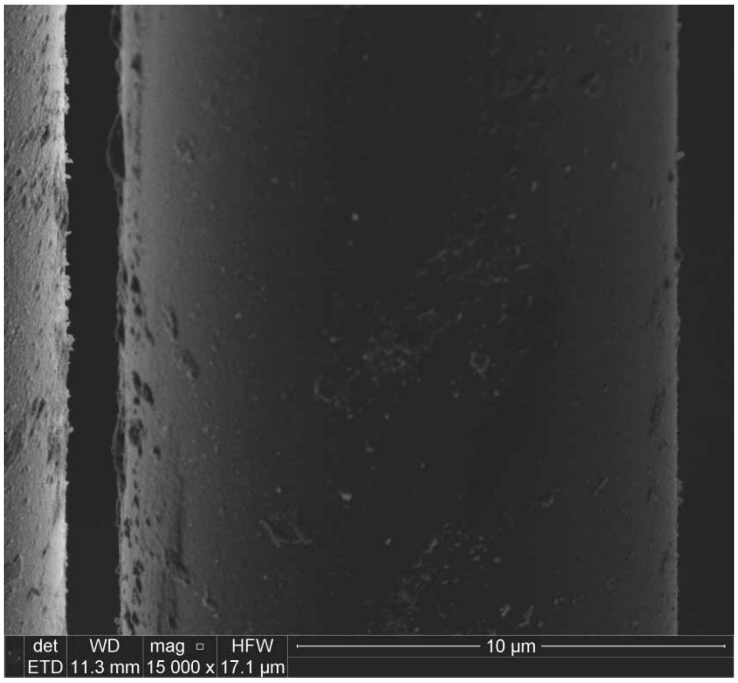


**Figure 146. SEM micrograph of the Hi-Nicalon™ S specimen "Steam 22" examining a fiber surface in the lower portion of a fiber, near the steam inlet**

**($\sigma_{cr}$ = 750 MPa, $t_f$ > 100 h)**

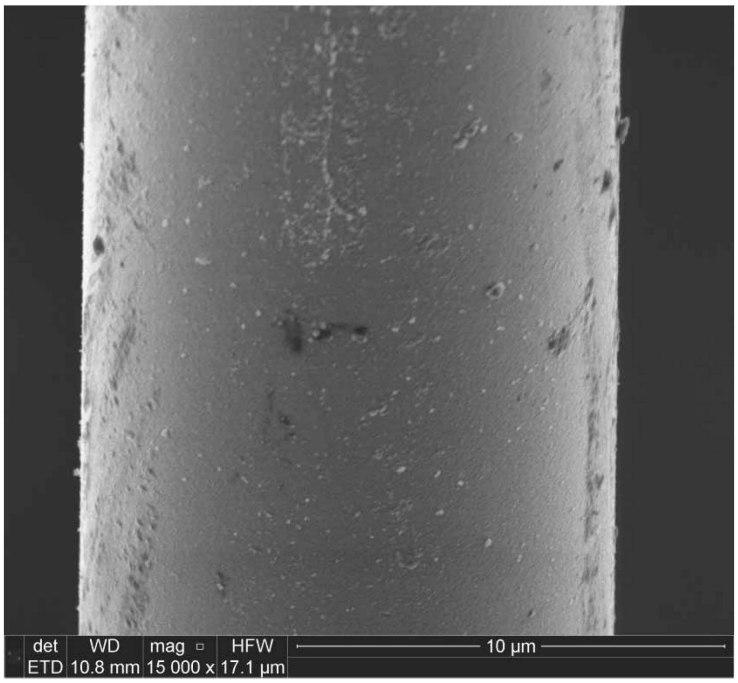


**Figure 147. SEM micrograph of the Hi-Nicalon™ S specimen "Steam 22" examining a fiber surface in the lower portion of a fiber, near the steam inlet**

**($\sigma_{cr}$ = 750 MPa, $t_f$ > 100 h)**

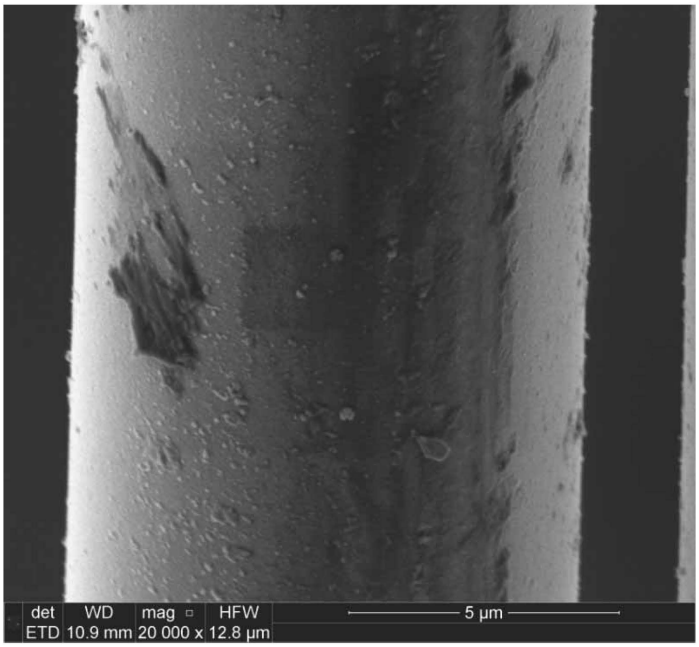


**Figure 148. SEM micrograph of the Hi-Nicalon™ S specimen "Steam 22" examining a fiber surface in the lower portion of a fiber, near the steam inlet. Note, the dark rectangular section in the center of the image is produced by the imaging process ($\sigma_{cr}$ = 750 MPa, $t_f$ > 100 h)**

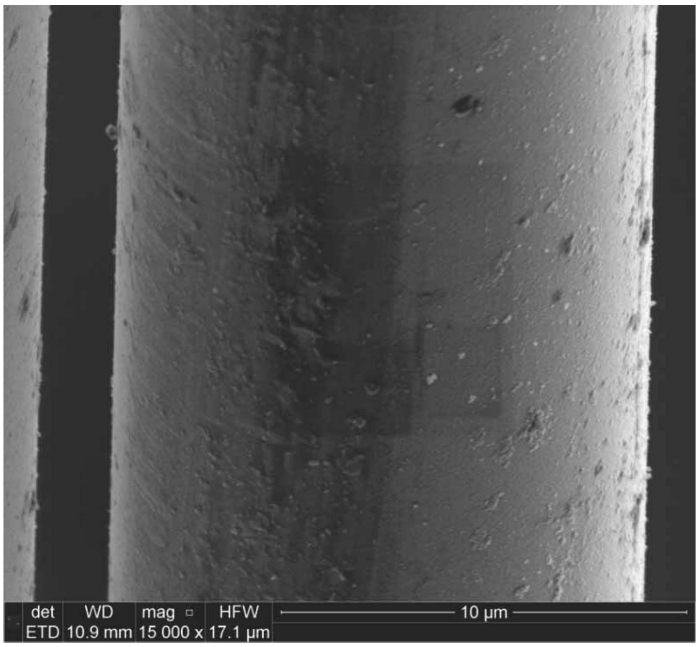


**Figure 149. SEM micrograph of the Hi-Nicalon™ S specimen "Steam 22" examining a fiber surface in the lower portion of a fiber, near the steam inlet. Note, the dark rectangular sections in the center of the image are produced by the imaging process ($\sigma_{cr}$ = 750 MPa, $t_f$ > 100 h)**

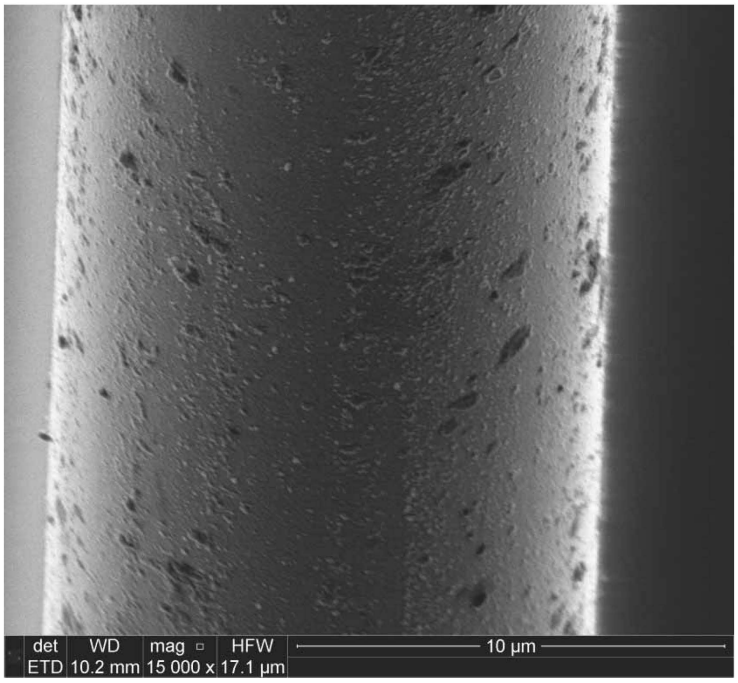


**Figure 150. SEM micrograph of the Hi-Nicalon™ S specimen "Steam 22" examining a fiber surface in the lower portion of a fiber, near the steam inlet ($\sigma_{cr}$ = 750 MPa, $t_f$ > 100 h)**

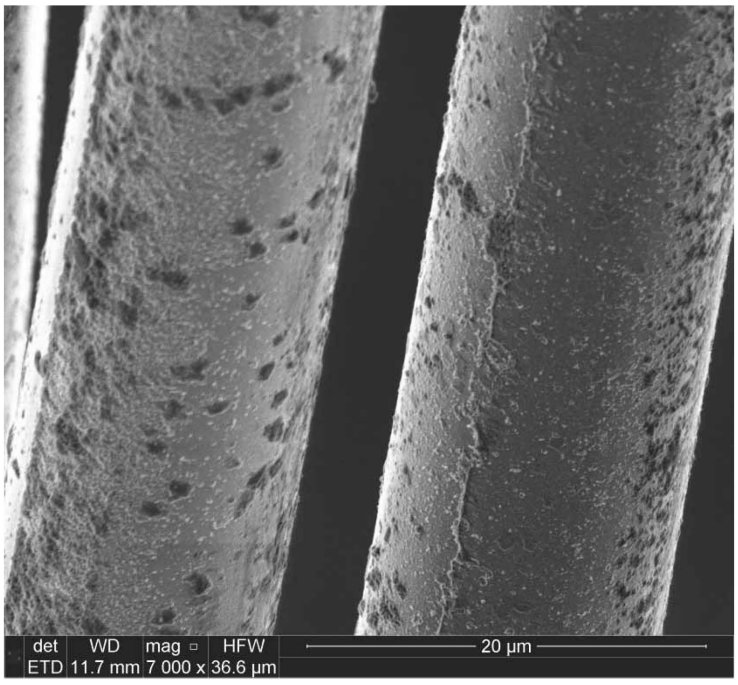


**Figure 151. SEM micrograph of the Hi-Nicalon™ S specimen "Steam 22" examining two fiber surfaces in the central portion of the fiber tow, near the midpoint of the effective length ($\sigma_{cr}$ = 750 MPa, $t_f$ > 100 h)**

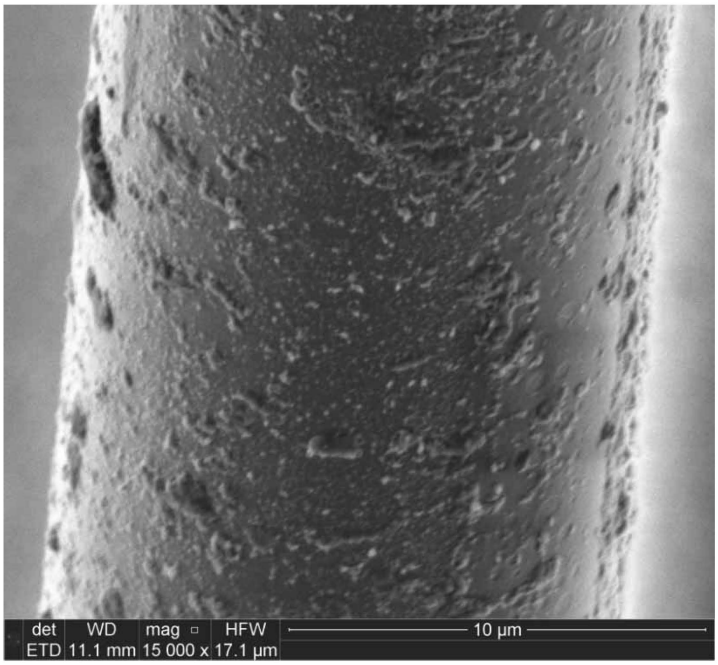


**Figure 152. SEM micrograph of the Hi-Nicalon™ S specimen "Steam 22" examining a surface in the central portion of the fiber, near the midpoint of the effective length. Note the deposits on the fiber surface resulting from oxidation**

**($\sigma_{cr}$ = 750 MPa, $t_f$ > 100 h)**

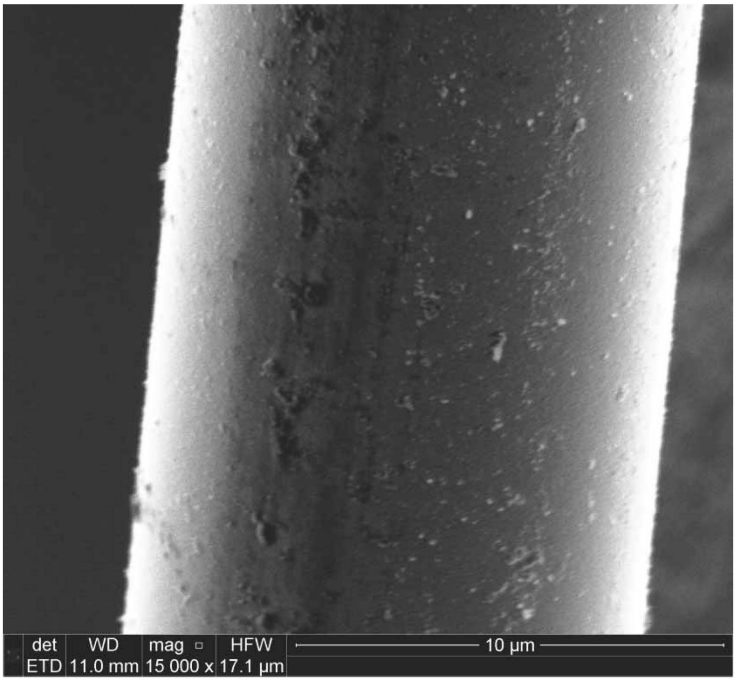


**Figure 153. SEM micrograph of the Hi-Nicalon™ S specimen "Steam 22" examining a surface in the central portion of the fiber, near the midpoint of the effective length ($\sigma_{cr}$ = 750 MPa, $t_f$ > 100 h)**

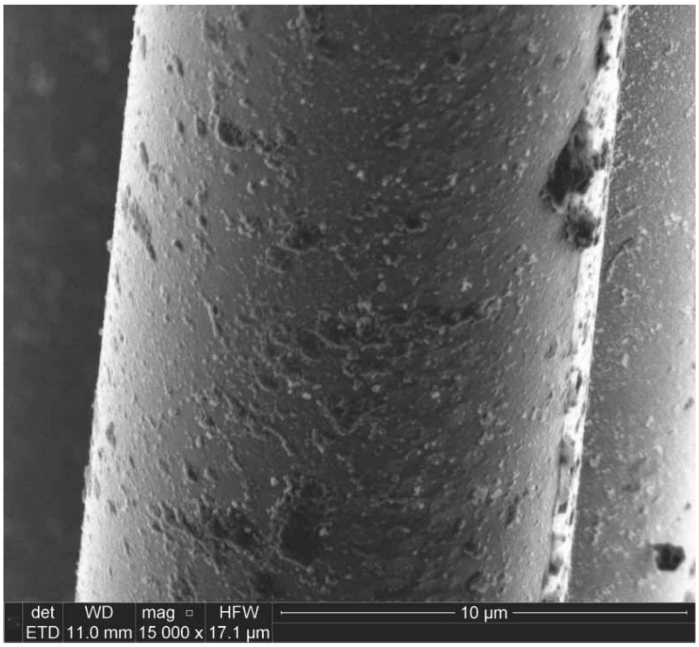


**Figure 154. SEM micrograph of the Hi-Nicalon™ S specimen "Steam 22" examining a surface in the central portion of the fiber, near the midpoint of the effective length. Note the deposits on the fiber surface resulting from oxidation**

**($\sigma_{cr}$ = 750 MPa, $t_f$ > 100 h)**

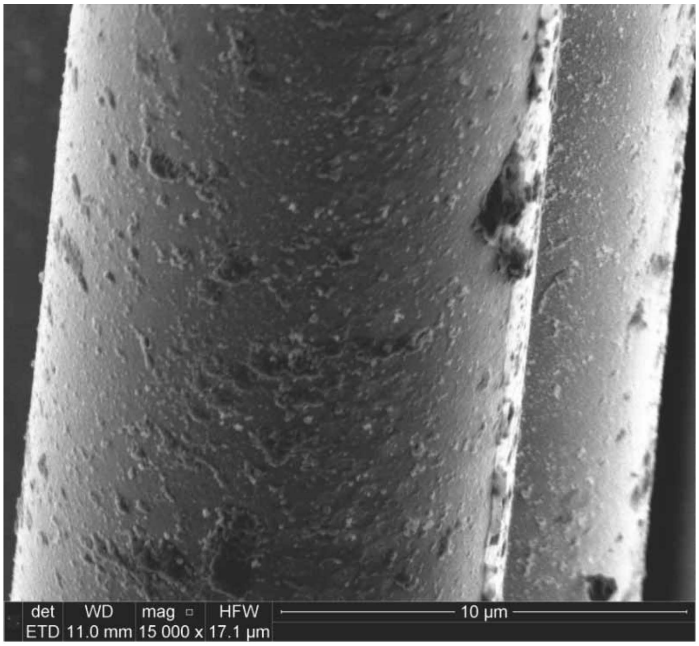


**Figure 155. SEM micrograph of the Hi-Nicalon™ S specimen "Steam 22" examining two fiber surfaces in the central portion of the fiber tow, near the midpoint of the effective length. Note the deposits on the fiber surfaces resulting from oxidation**

**($\sigma_{cr}$ = 750 MPa, $t_f$ > 100 h)**

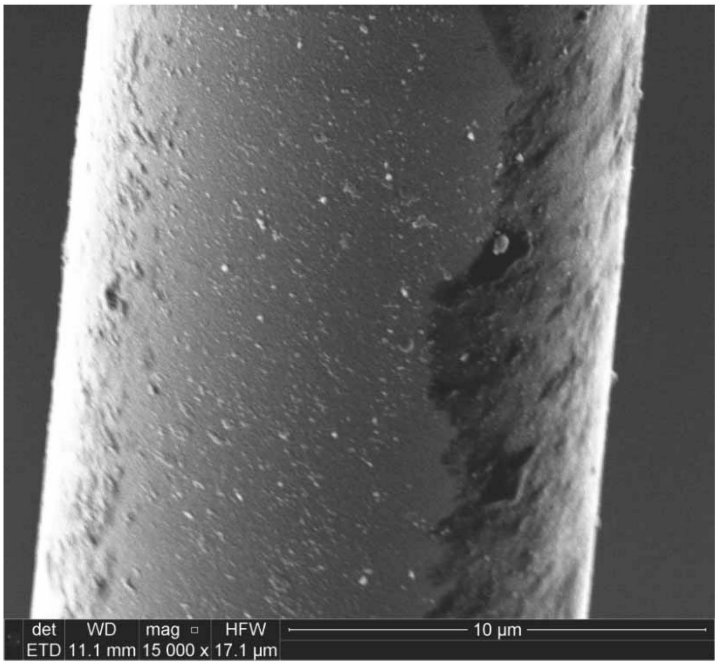


**Figure 156. SEM micrograph of the Hi-Nicalon™ S specimen "Steam 22" examining a surface in the central portion of the fiber, near the midpoint of the effective length ($\sigma_{cr}$ = 750 MPa, $t_f$ > 100 h)**

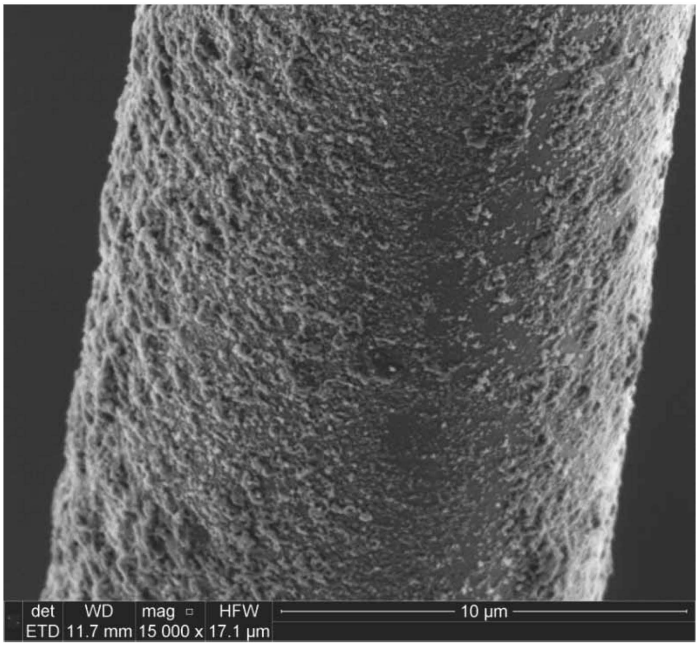


**Figure 157. SEM micrograph of the Hi-Nicalon™ S specimen "Steam 22" examining a surface in the central portion of the fiber, near the midpoint of the effective length. Note the deposits on the fiber surface resulting from oxidation ($\sigma_{cr}$ = 750 MPa, $t_f$ > 100 h)**

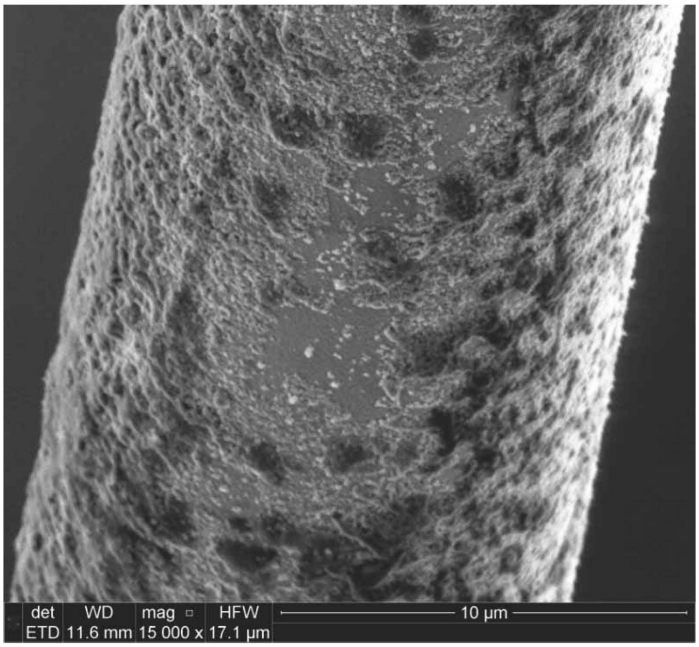


**Figure 158. SEM micrograph of the Hi-Nicalon™ S specimen "Steam 22" examining a surface in the central portion of the fiber, near the midpoint of the effective length. Note the deposits on the fiber surface resulting from oxidation**

**($\sigma_{cr}$ = 750 MPa, $t_f$ > 100 h)**

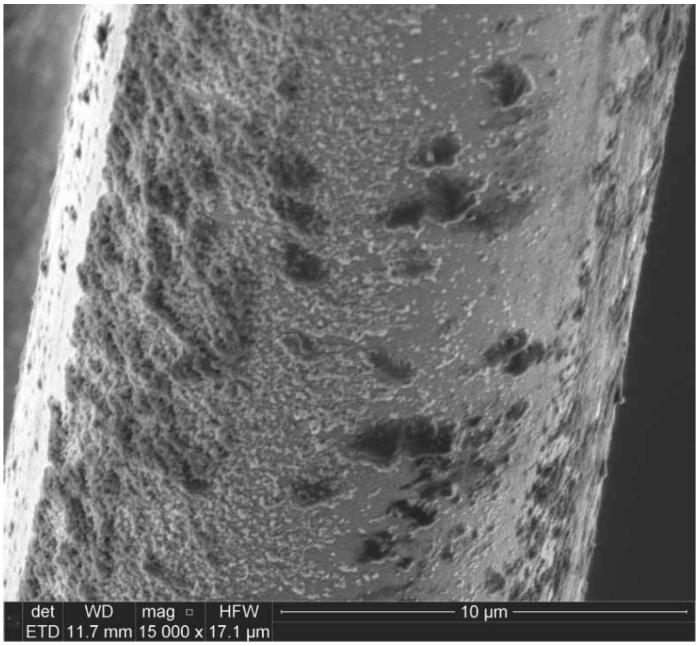


**Figure 159. SEM micrograph of the Hi-Nicalon™ S specimen "Steam 22" examining a surface in the central portion of the fiber, near the midpoint of the effective length. Note the deposits on the fiber surface resulting from oxidation**

**($\sigma_{cr}$ = 750 MPa, $t_f$ > 100 h)**

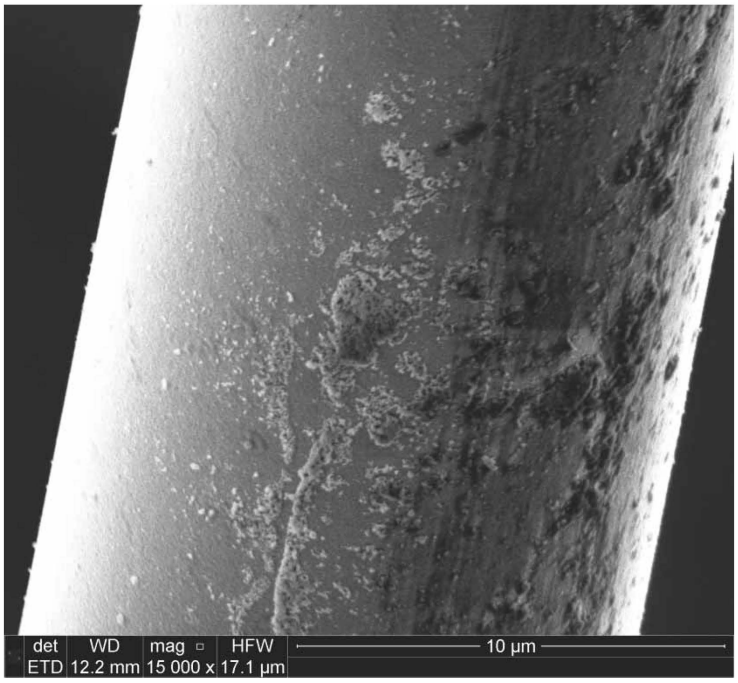


**Figure 160. SEM micrograph of the Hi-Nicalon™ S specimen "Steam 22" examining a surface in the central portion of the fiber, near the midpoint of the effective length ($\sigma_{cr}$ = 750 MPa, $t_f$ > 100 h)**

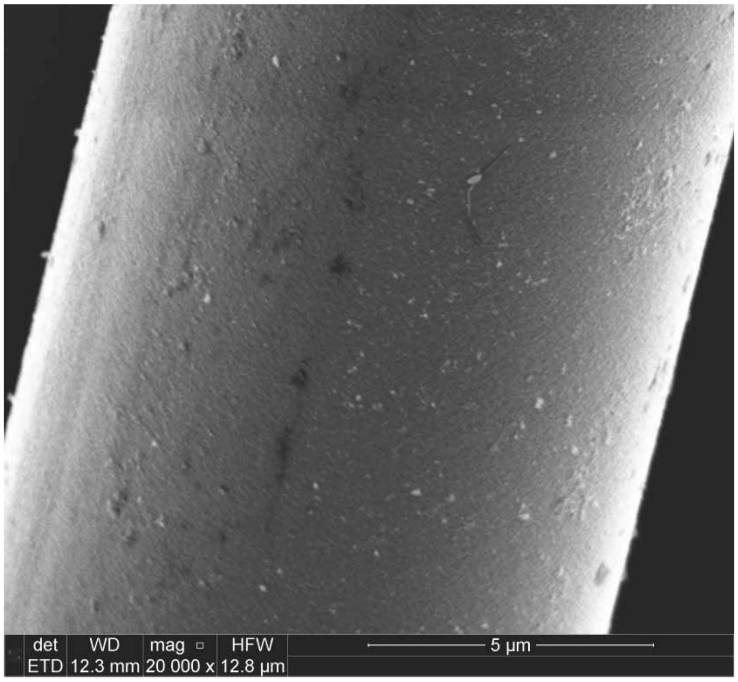


**Figure 161. SEM micrograph of the Hi-Nicalon™ S specimen "Steam 22" examining a fiber surface in the central portion of the fiber, near the midpoint of the effective length. ($\sigma_{cr}$ = 750 MPa, $t_f$ > 100 h)**

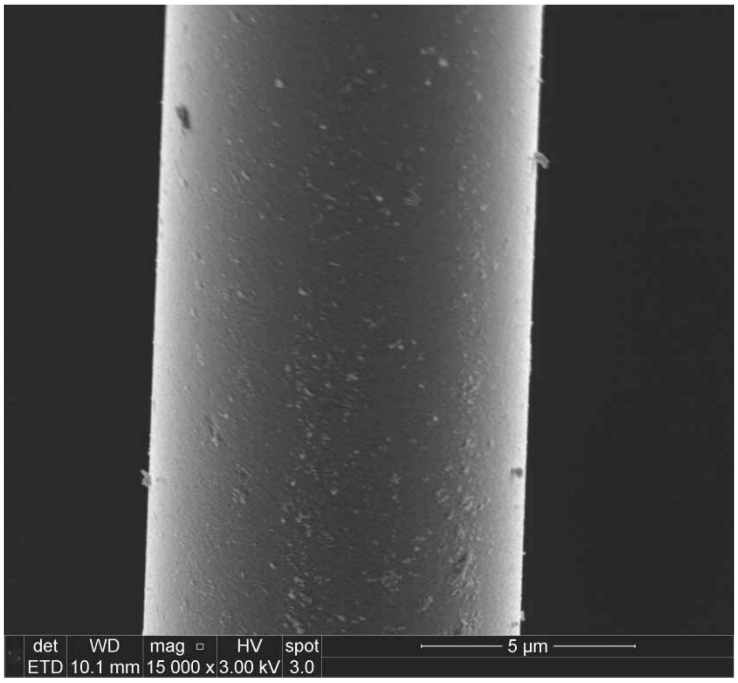


**Figure 162. SEM micrograph of the Hi-Nicalon™ S specimen "Steam 22" examining a surface in the upper portion of the fiber, near the highest point of the effective length ($\sigma_{cr}$ = 750 MPa, $t_f$ > 100 h)**

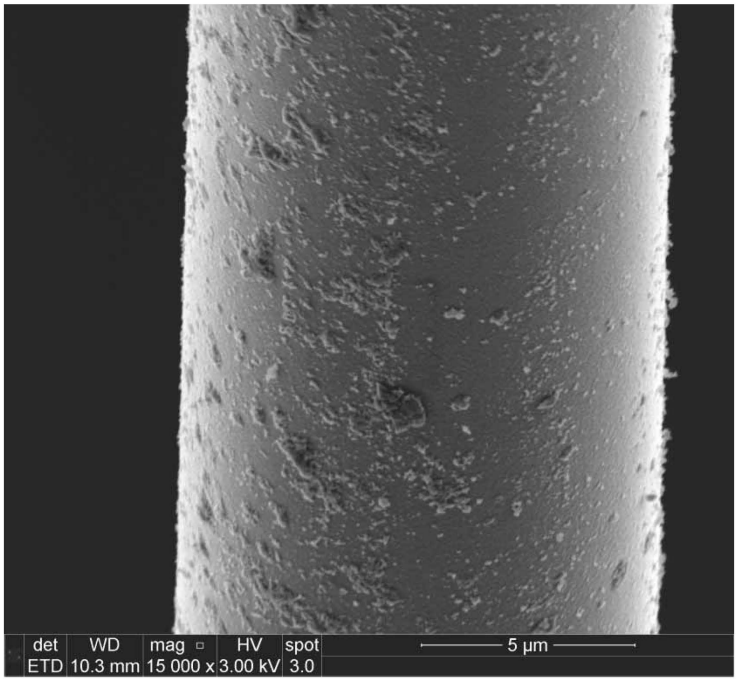


**Figure 163. SEM micrograph of the Hi-Nicalon™ S specimen "Steam 22" examining a surface in the upper portion of the fiber, near the highest point of the effective length ($\sigma_{cr}$ = 750 MPa, $t_f$ > 100 h)**

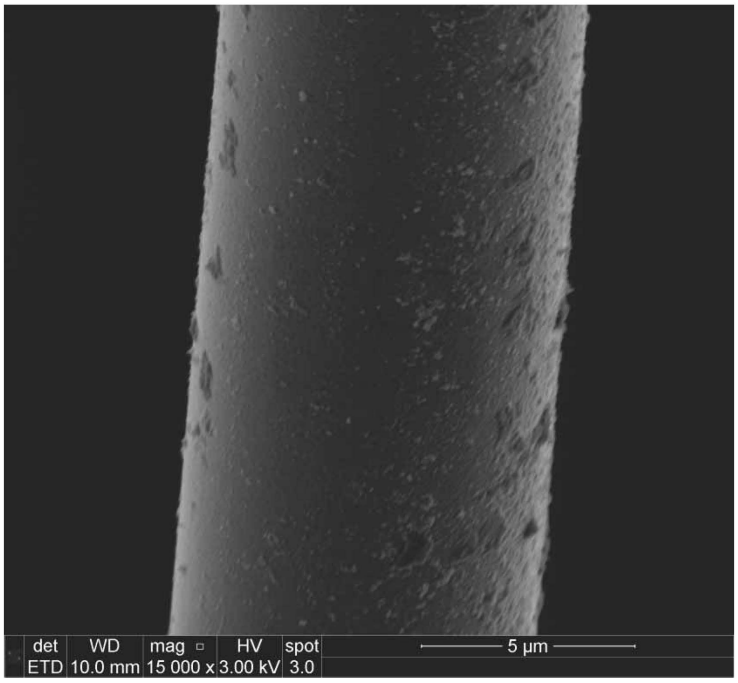


**Figure 164. SEM micrograph of the Hi-Nicalon™ S specimen "Steam 22" examining a surface in the upper portion of the fiber, near the highest point of the effective length ($\sigma_{cr}$ = 750 MPa, $t_f$ > 100 h)**

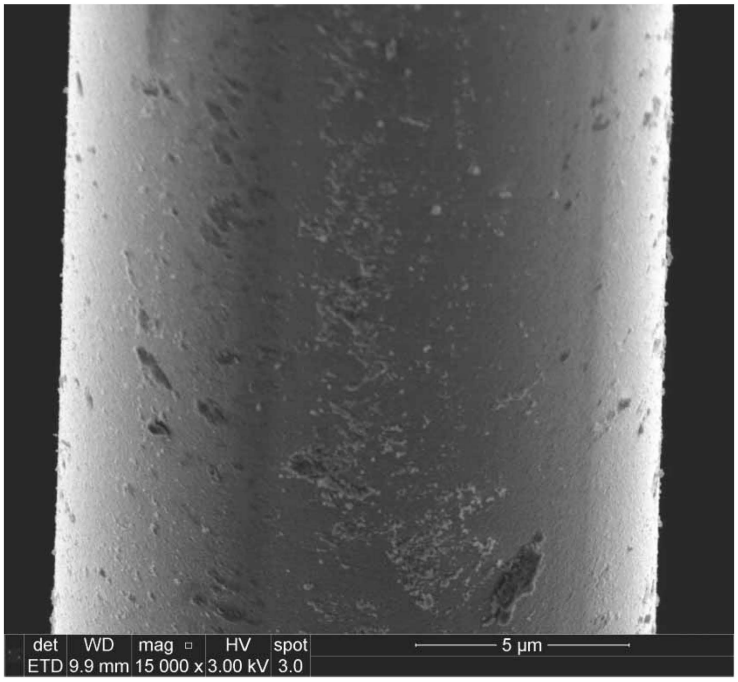


**Figure 165. SEM micrograph of the Hi-Nicalon™ S specimen "Steam 22" examining a surface in the upper portion of the fiber, near the highest point of the effective length ($\sigma_{cr}$ = 750 MPa, $t_f$ > 100 h)**

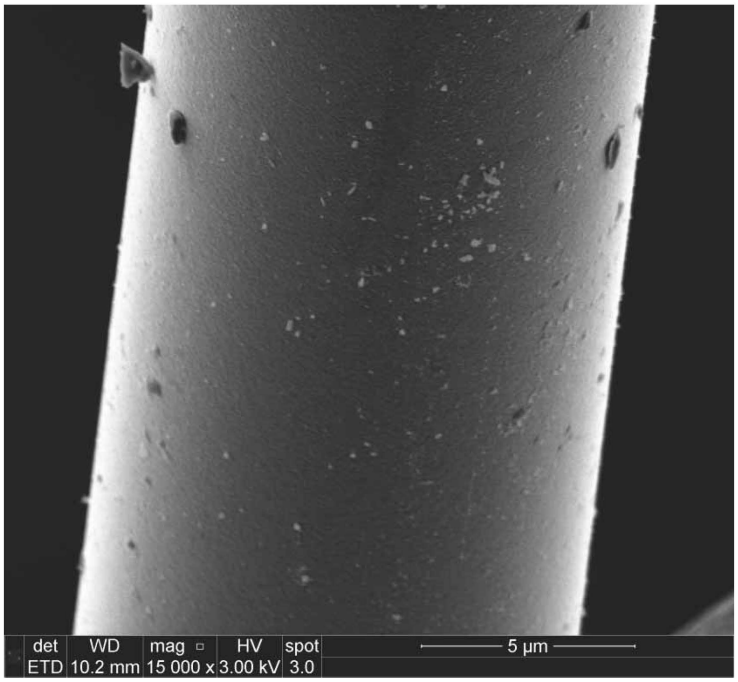


**Figure 166. SEM micrograph of the Hi-Nicalon™ S specimen "Steam 22" examining a surface in the upper portion of the fiber, near the highest point of the effective length ($\sigma_{cr}$ = 750 MPa, $t_f$ > 100 h)**

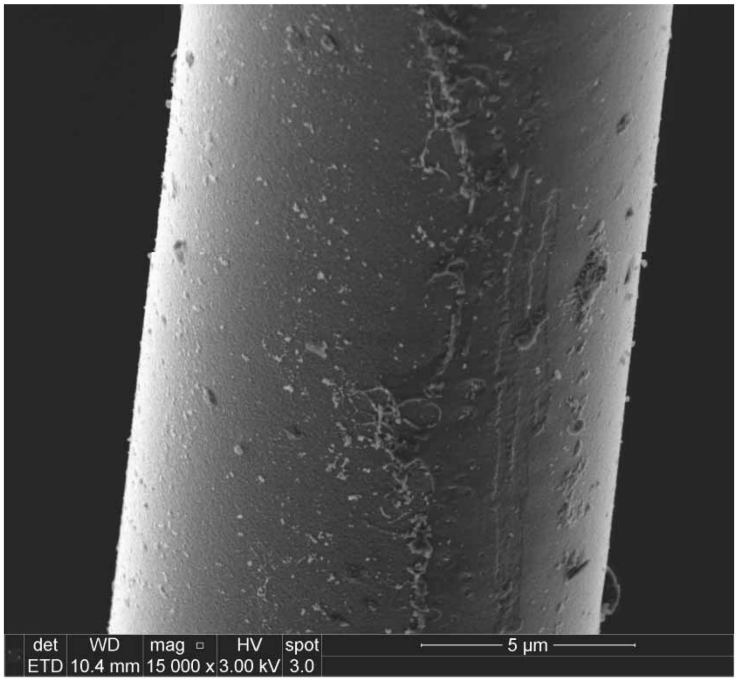


**Figure 167. SEM micrograph of the Hi-Nicalon™ S specimen "Steam 22" examining a surface in the upper portion of the fiber, near the highest point of the effective length ($\sigma_{cr}$ = 750 MPa, $t_f$ > 100 h)**

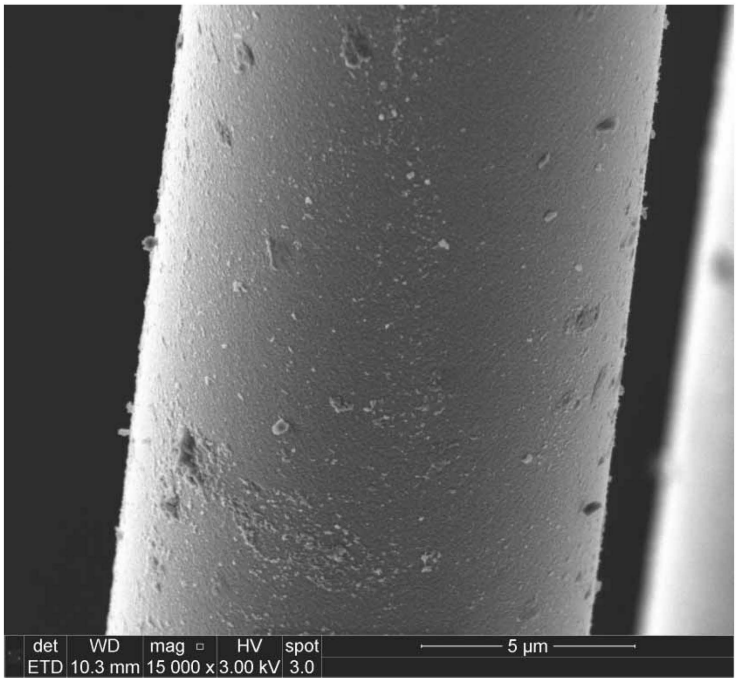


**Figure 168. SEM micrograph of the Hi-Nicalon™ S specimen "Steam 22" examining a surface in the upper portion of the fiber, near the highest point of the effective length ($\sigma_{cr}$ = 750 MPa, $t_f$ > 100 h)**

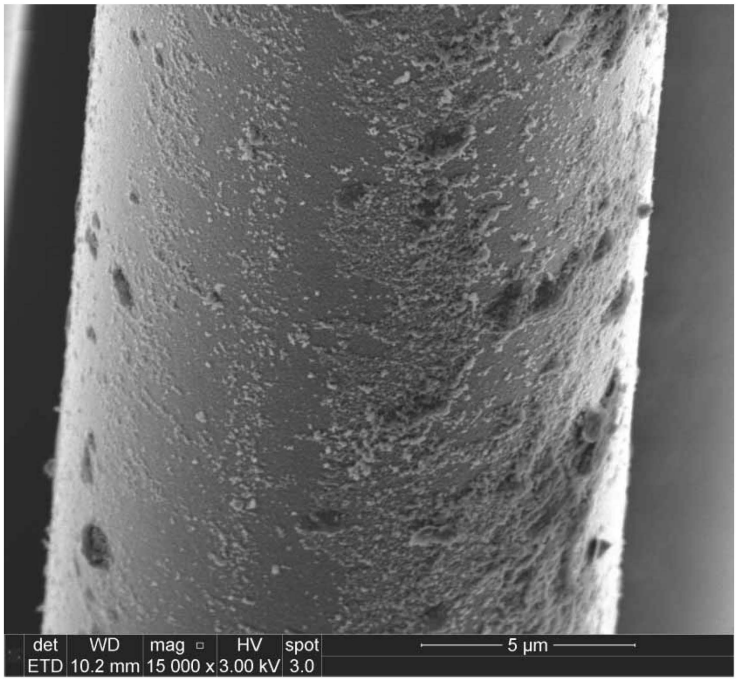


**Figure 169. SEM micrograph of the Hi-Nicalon™ S specimen "Steam 22" examining a surface in the upper portion of the fiber, near the highest point of the effective length ($\sigma_{cr}$ = 750 MPa, $t_f$ > 100 h)**

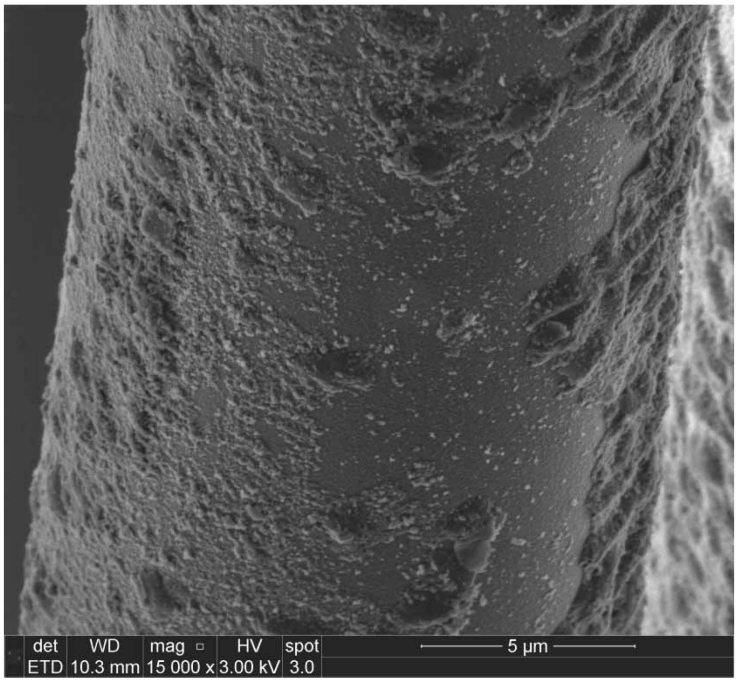


**Figure 170. SEM micrograph of the Hi-Nicalon™ S specimen "Steam 22" examining a surface in the upper portion of the fiber, near the highest point of the effective length ($\sigma_{cr}$ = 750 MPa, $t_f$ > 100 h)**

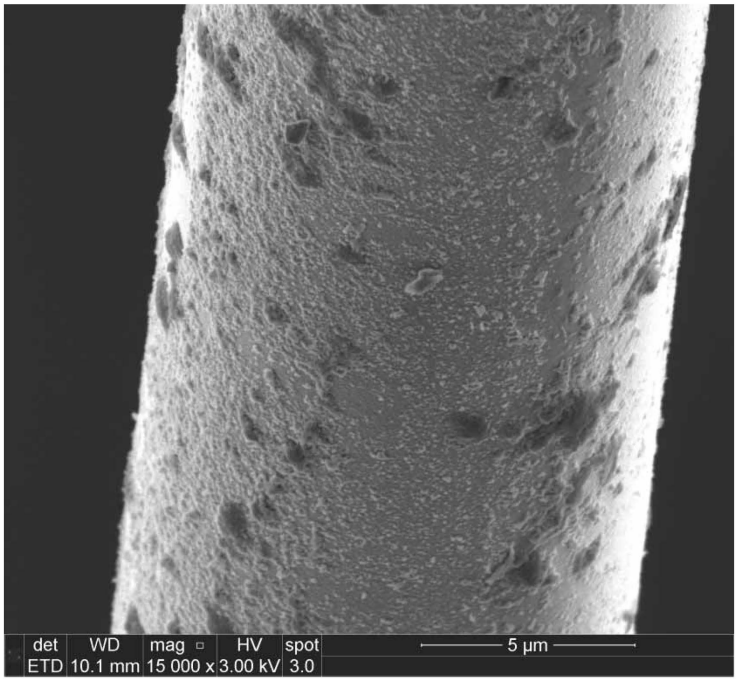


**Figure 171. SEM micrograph of the Hi-Nicalon™ S specimen "Steam 22" examining a surface in the upper portion of the fiber, near the highest point of the effective length ($\sigma_{cr}$ = 750 MPa, $t_f$ > 100 h)**

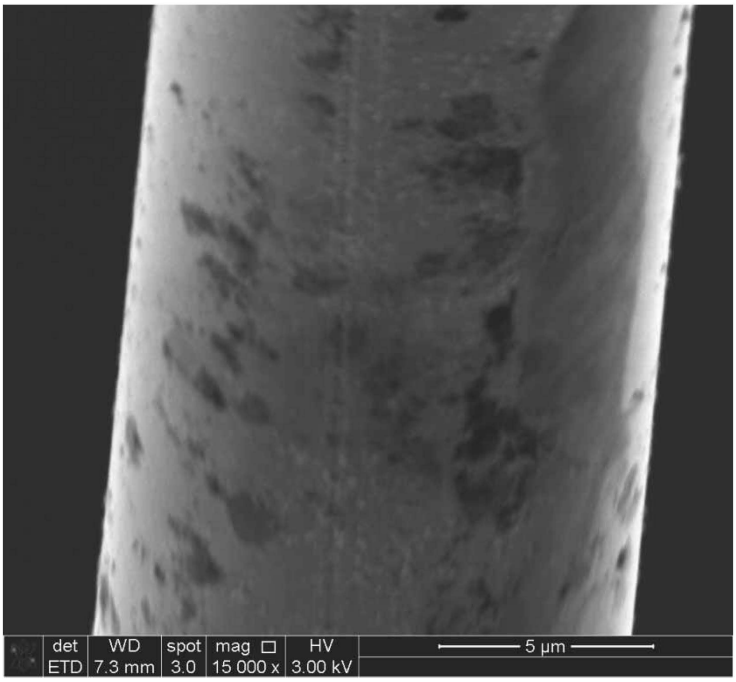


**Figure 172. SEM micrograph of the Hi-Nicalon™ S specimen "Steam 25" examining a fiber surface in the lower portion of a fiber, near the steam inlet**

**($\sigma_{cr}$ = 798 MPa, $t_f$ = 1.83 h)**

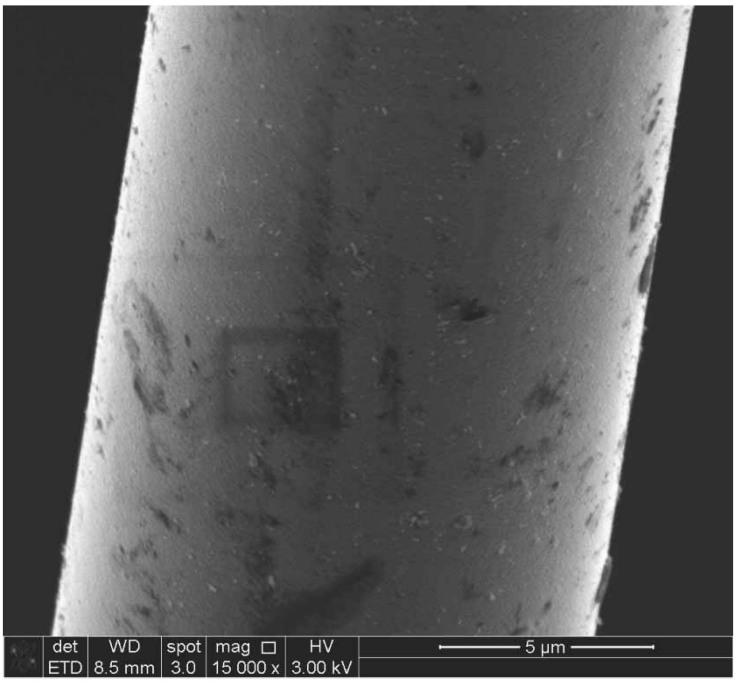


**Figure 173. SEM micrograph of the Hi-Nicalon™ S specimen "Steam 25" examining a fiber surface in the lower portion of a fiber, near the steam inlet. Note, the dark rectangular pattern is a product of the imaging process ($\sigma_{cr}$ = 798 MPa, $t_f$ = 1.83 h)**

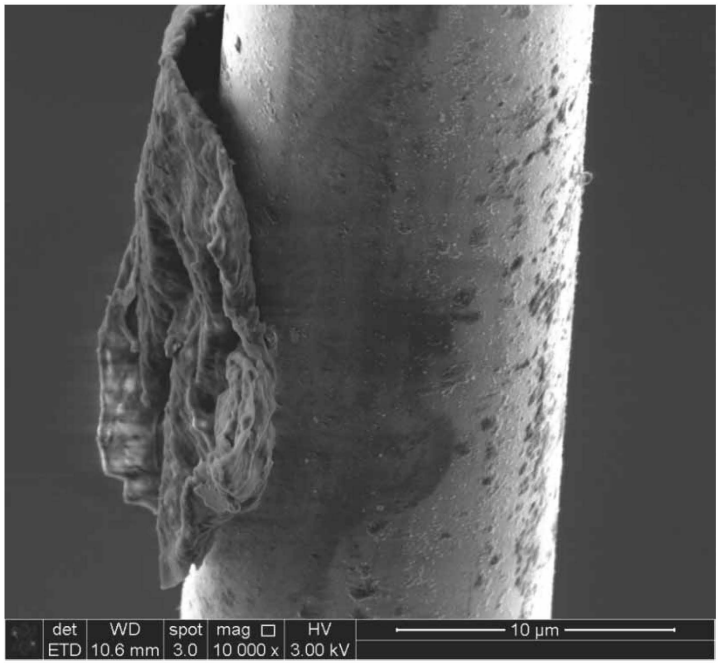


**Figure 174. SEM micrograph of the Hi-Nicalon™ S specimen "Steam 25" examining a fiber surface in the lower portion of a fiber, near the steam inlet. Note the large deposit of oxidized material ($\sigma_{cr}$ = 798 MPa, $t_f$ = 1.83 h)**

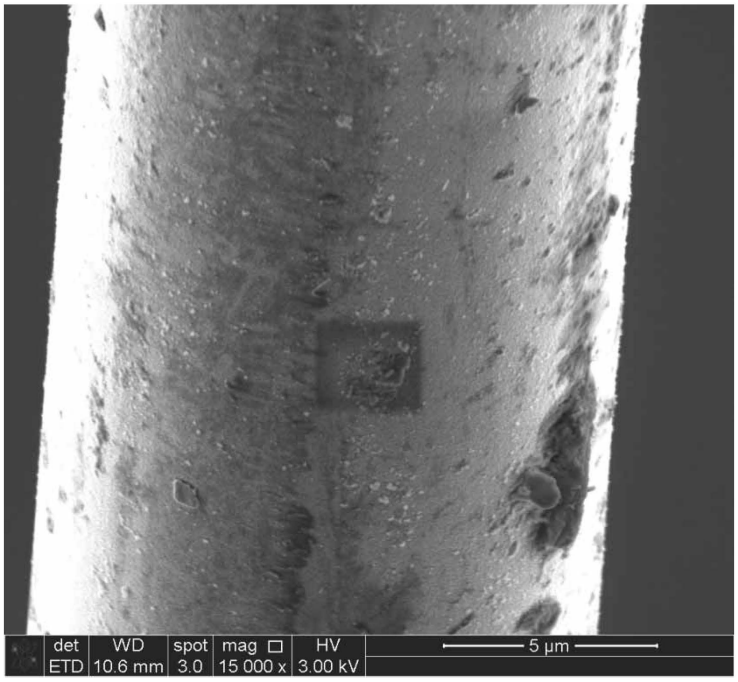


**Figure 175. SEM micrograph of the Hi-Nicalon™ S specimen "Steam 25" examining a fiber surface in the lower portion of a fiber, near the steam inlet. Note, the dark rectangular pattern at the center of the image is a product of the imaging process ($\sigma_{cr}$ = 798 MPa, $t_f$ = 1.83 h)**

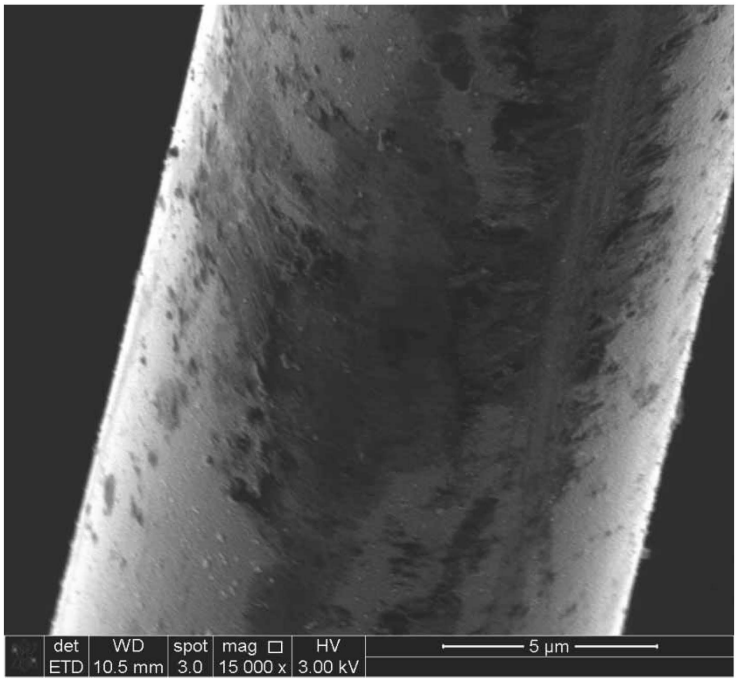


**Figure 176. SEM micrograph of the Hi-Nicalon™ S specimen "Steam 25" examining a fiber surface in the lower portion of a fiber, near the steam inlet**

**($\sigma_{cr}$ = 798 MPa, $t_f$ = 1.83 h)**

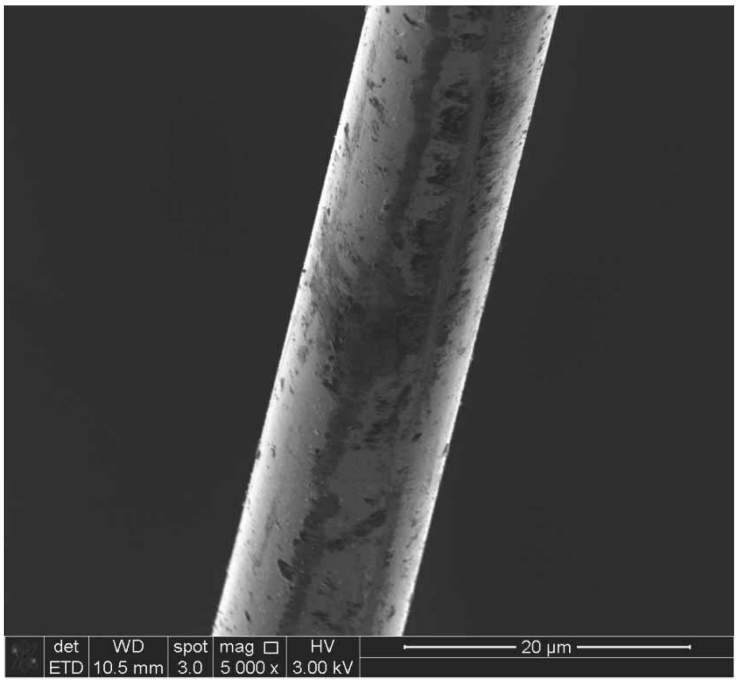


**Figure 177. SEM micrograph of the Hi-Nicalon™ S specimen "Steam 25" examining a fiber surface in the lower portion of a fiber, near the steam inlet**

**($\sigma_{cr}$ = 798 MPa, $t_f$ = 1.83 h)**

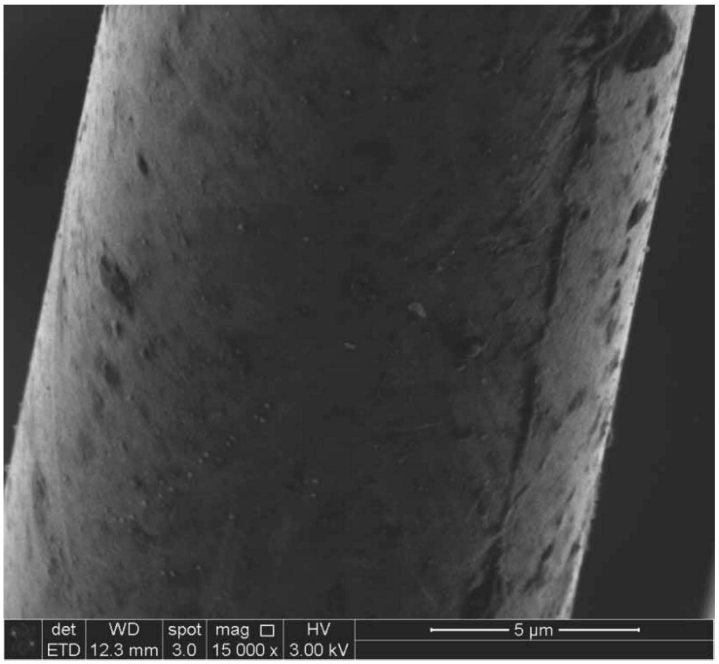


**Figure 178. SEM micrograph of the Hi-Nicalon™ S specimen "Steam 25" examining a fiber surface in the lower portion of a fiber, near the steam inlet**

**($\sigma_{cr}$ = 798 MPa, $t_f$ = 1.83 h)**

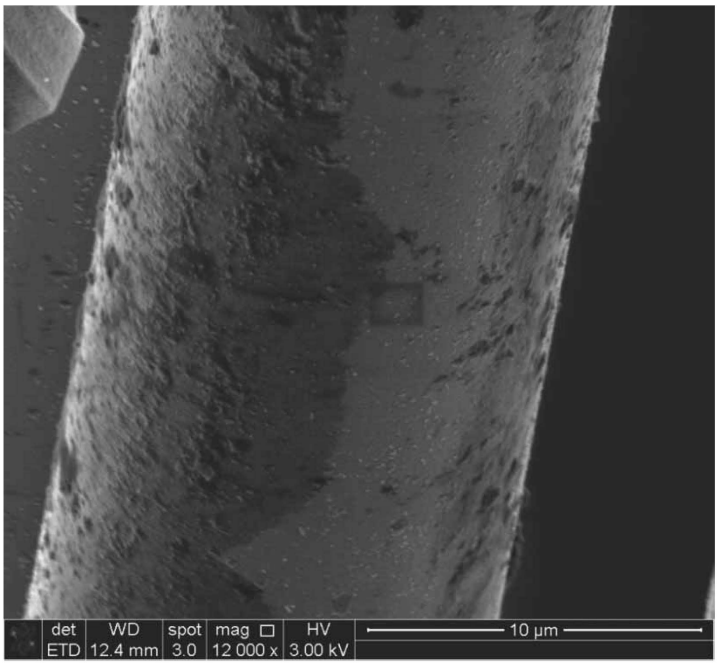


**Figure 179. SEM micrograph of the Hi-Nicalon™ S specimen "Steam 25" examining a fiber surface in the lower portion of a fiber, near the steam inlet. Note, the dark rectangular pattern at the center of the image is a product of the imaging process**

**($\sigma_{cr}$ = 798 MPa, $t_f$ = 1.83 h)**

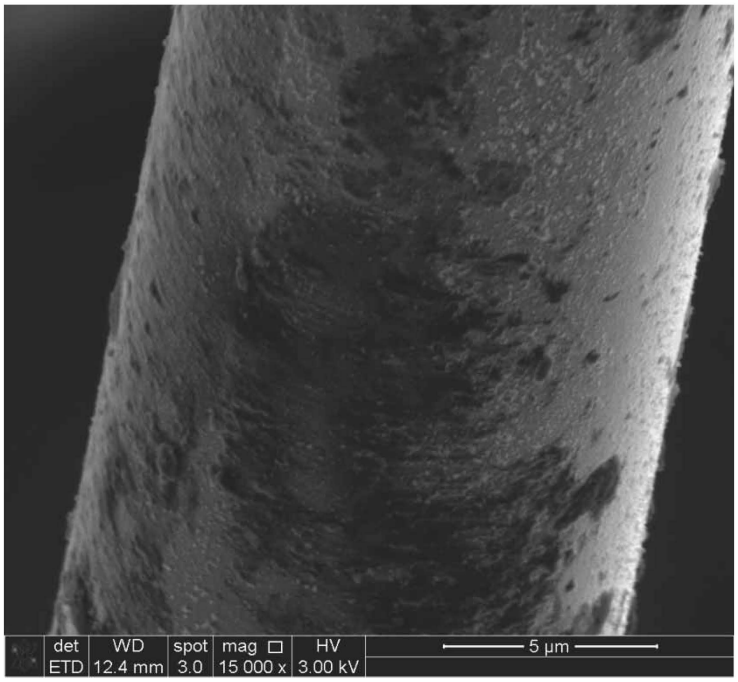


**Figure 180. SEM micrograph of the Hi-Nicalon™ S specimen "Steam 25" examining a fiber surface in the lower portion of a fiber, near the steam inlet ($\sigma_{cr}$ = 798 MPa, $t_f$ = 1.83 h)**

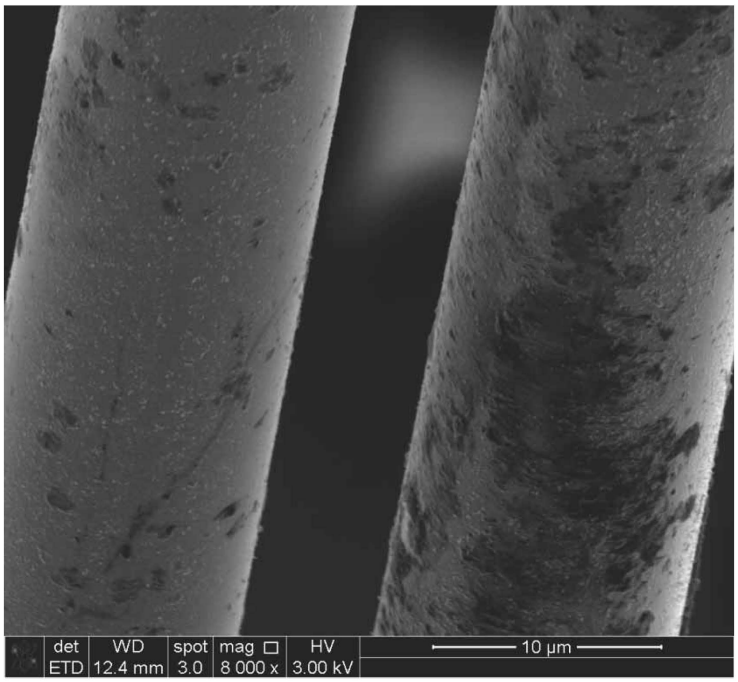


**Figure 181. SEM micrograph of the Hi-Nicalon™ S specimen "Steam 25" examining the surfaces of two fibers in the lower portion of the fiber tow, near the steam inlet ($\sigma_{cr}$ = 798 MPa, $t_f$ = 1.83 h)**

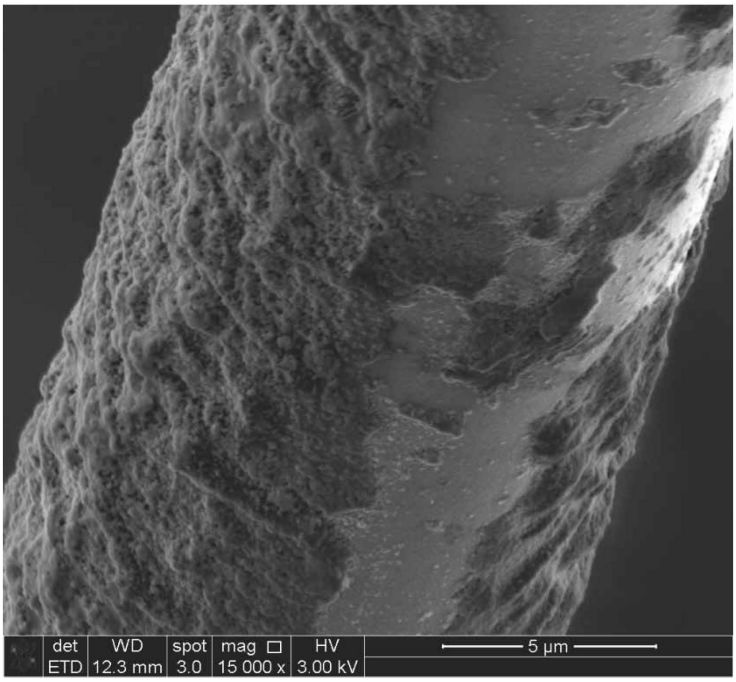


**Figure 182. SEM micrograph of the Hi-Nicalon™ S specimen "Steam 25" examining a fiber surface in the lower portion of a fiber, near the steam inlet. Note the deposits on the fiber surfaces resulting from oxidation ($\sigma_{cr}$ = 798 MPa, $t_f$ = 1.83 h)**

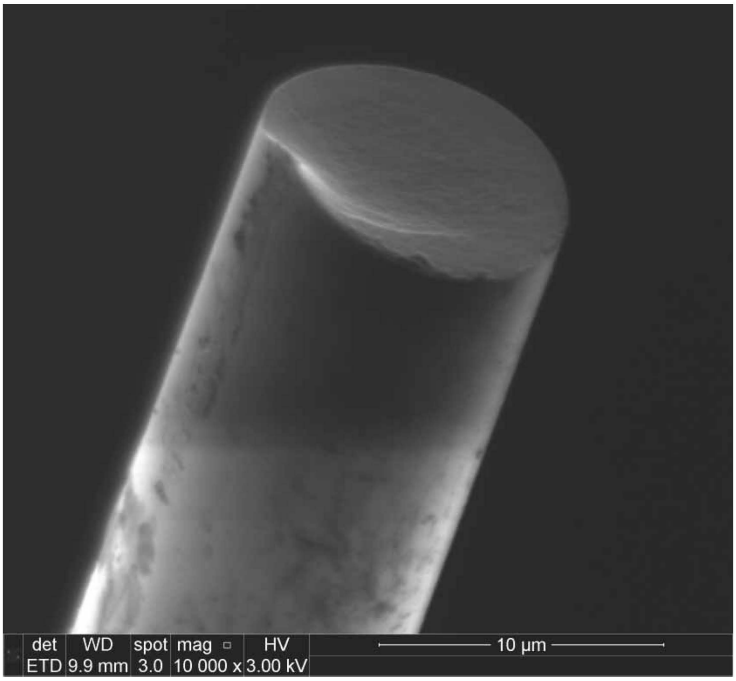


**Figure 183. SEM micrograph of the Hi-Nicalon™ S specimen "Steam 25" examining the fracture surface of a fiber ($\sigma_{cr}$ = 798 MPa, $t_f$ = 1.83 h)**

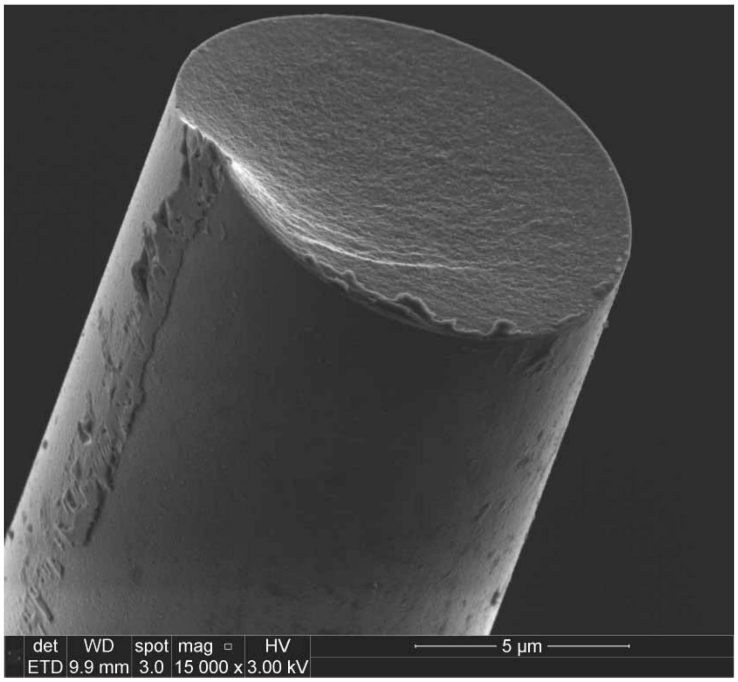


**Figure 184. SEM micrograph of the Hi-Nicalon™ S specimen "Steam 25" examining the fracture surface of a fiber ($\sigma_{cr}$ = 798 MPa, $t_f$ = 1.83 h)**

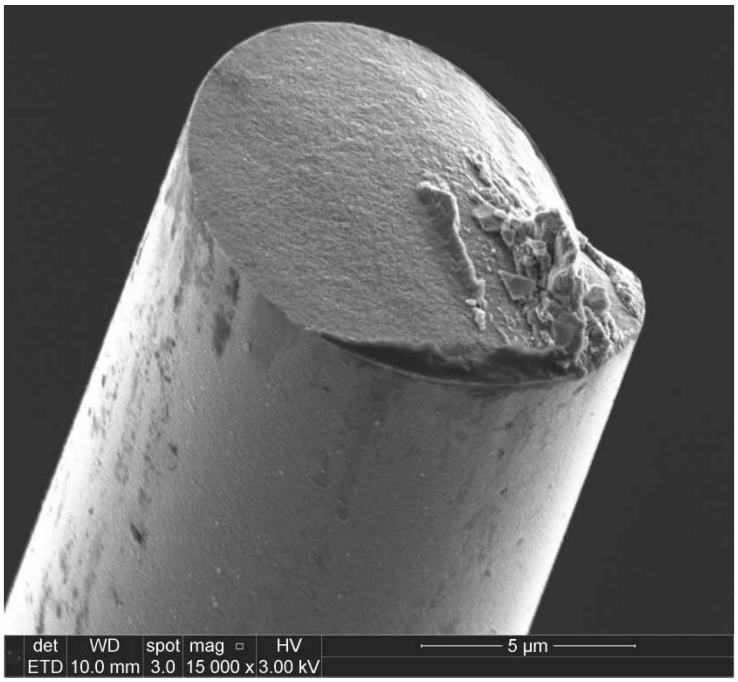


**Figure 185. SEM micrograph of the Hi-Nicalon™ S specimen "Steam 25" examining the fracture surface of a fiber ($\sigma_{cr}$ = 798 MPa, $t_f$ = 1.83 h)**

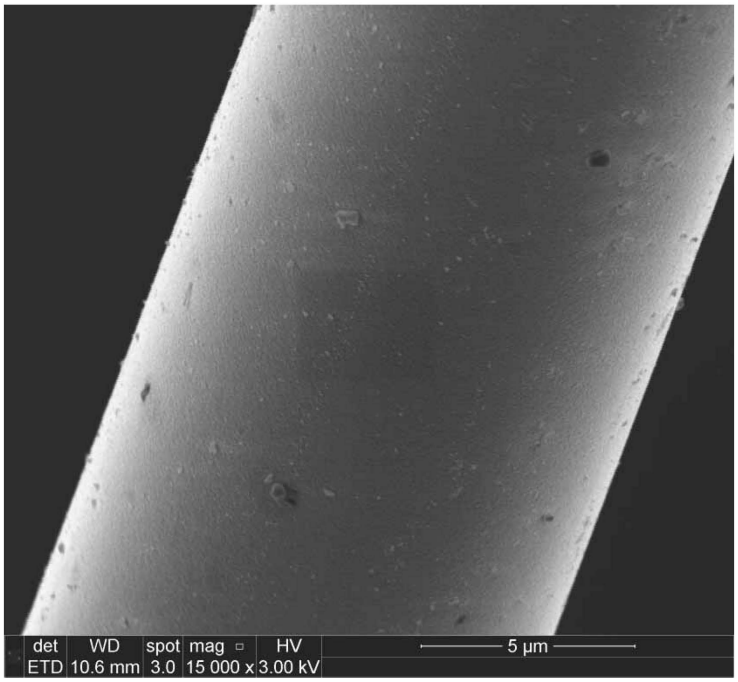


**Figure 186. SEM micrograph of the Hi-Nicalon™ S specimen "Steam 25" examining the surface along the length of a fiber near the fracture surface. Note, the dark rectangle near the center of the image is a product of the imaging process ($\sigma_{cr}$ = 798 MPa, $t_f$ = 1.83 h)**

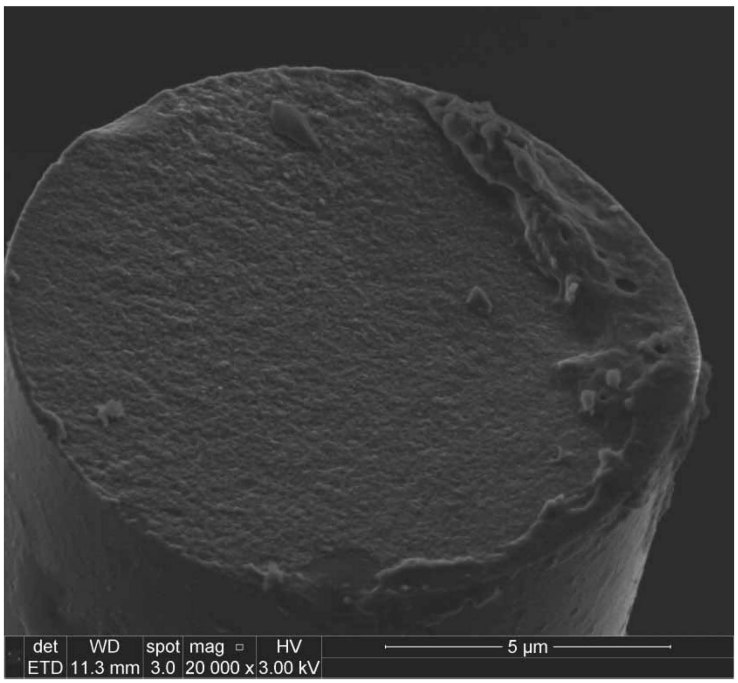


**Figure 187. SEM micrograph of the Hi-Nicalon™ S specimen "Steam 25" examining the fracture surface of a fiber ($\sigma_{cr}$ = 798 MPa, $t_f$ = 1.83 h)**

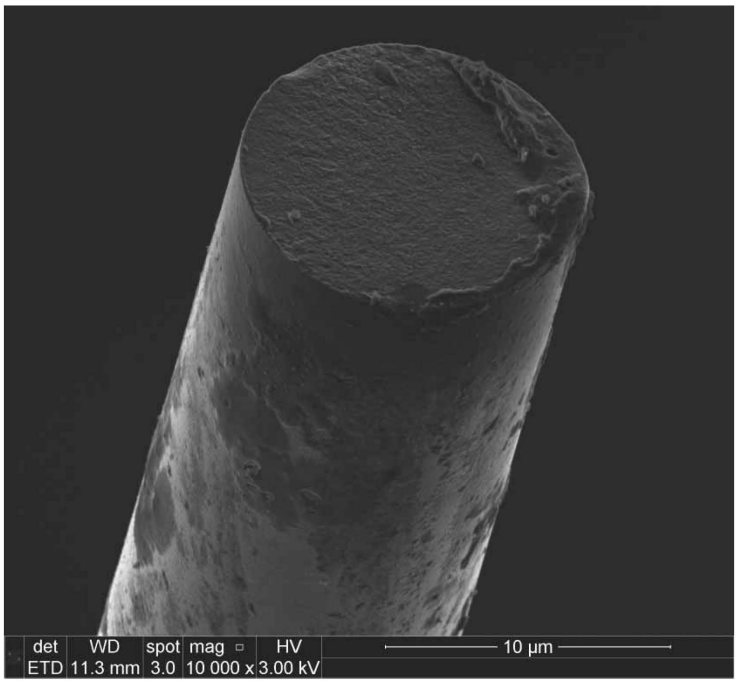


**Figure 188. SEM micrograph of the Hi-Nicalon™ S specimen "Steam 25" examining the fracture surface of a fiber ($\sigma_{cr}$ = 798 MPa, $t_f$ = 1.83 h)**

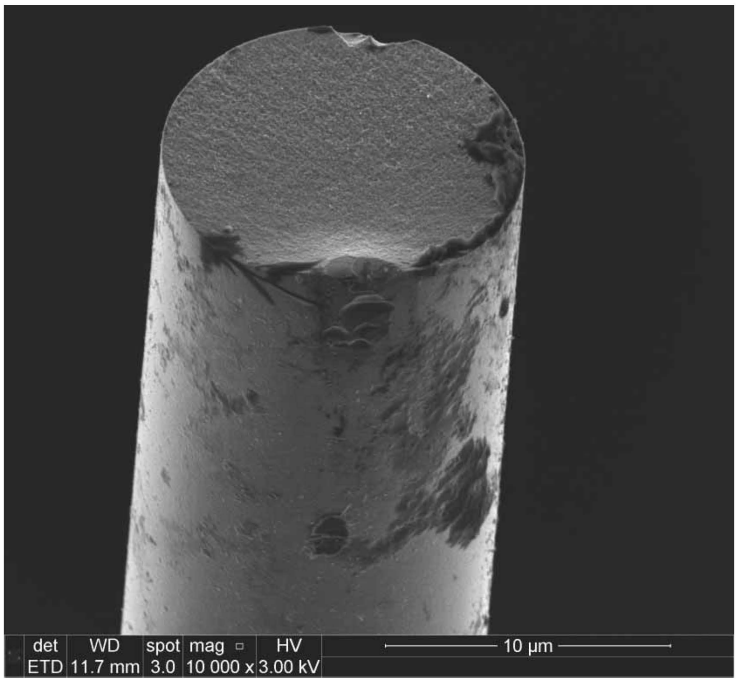


**Figure 189. SEM micrograph of the Hi-Nicalon™ S specimen "Steam 25" examining the fracture surface of a fiber ($\sigma_{cr}$ = 798 MPa, $t_f$ = 1.83 h)**

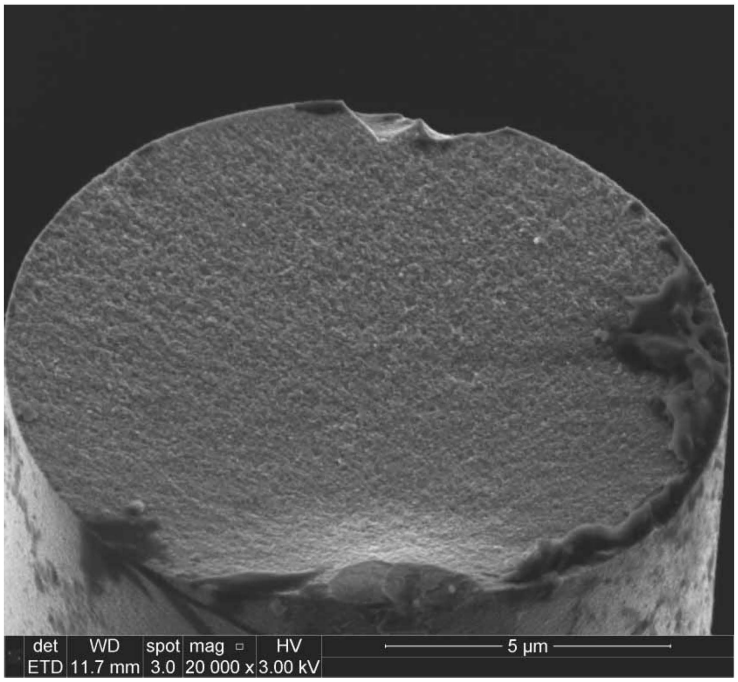


**Figure 190. SEM micrograph of the Hi-Nicalon™ S specimen "Steam 25" examining the fracture surface of a fiber ($\sigma_{cr}$ = 798 MPa, $t_f$ = 1.83 h)**

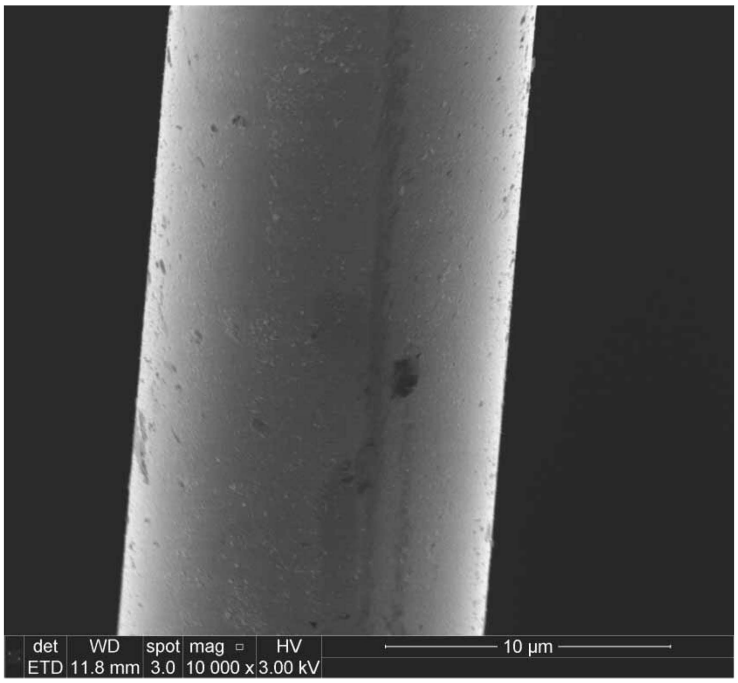


**Figure 191. SEM micrograph of the Hi-Nicalon™ S specimen "Steam 25" examining the surface along the length of a fiber near the fracture surface ($\sigma_{cr}$ = 798 MPa, $t_f$ = 1.83 h)**

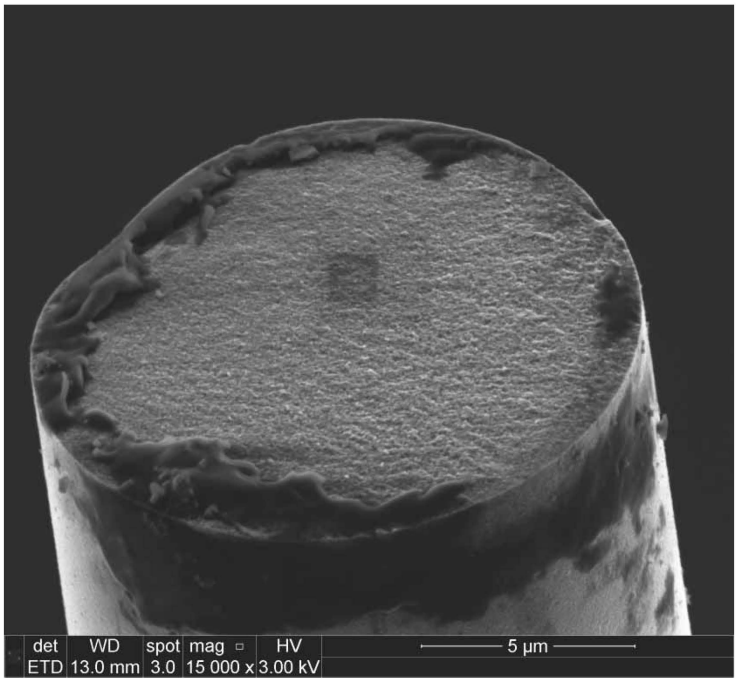


**Figure 192. SEM micrograph of the Hi-Nicalon™ S specimen "Steam 25" examining the fracture surface of a fiber. Note, the dark rectangle near the center of the image is a product of the imaging process ($\sigma_{cr}$ = 798 MPa, $t_f$ = 1.83 h)**

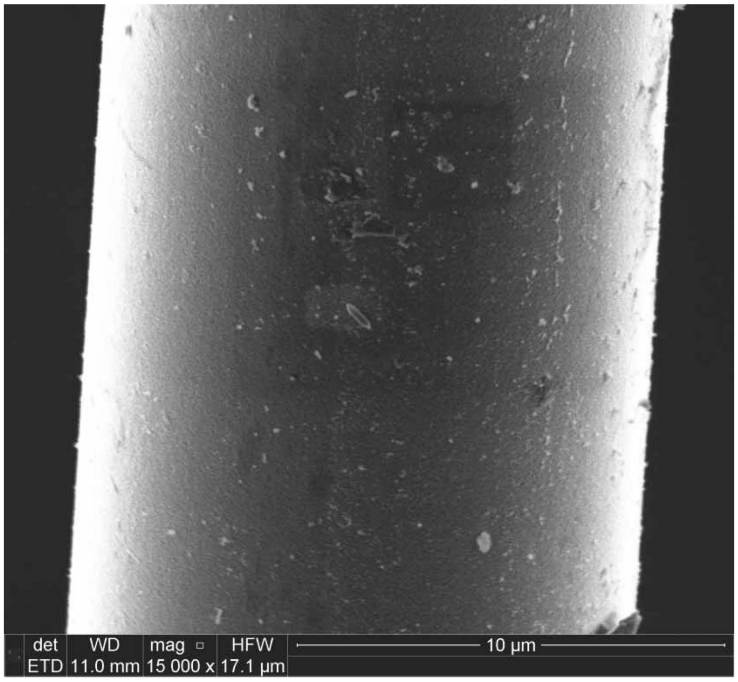


**Figure 193. SEM micrograph of the Hi-Nicalon™ S specimen "Steam 25" examining a fiber above the fracture surface. Note, the dark rectangle near the center of the image is a product of the imaging process ($\sigma_{cr}$ = 798 MPa, $t_f$ = 1.83 h)**

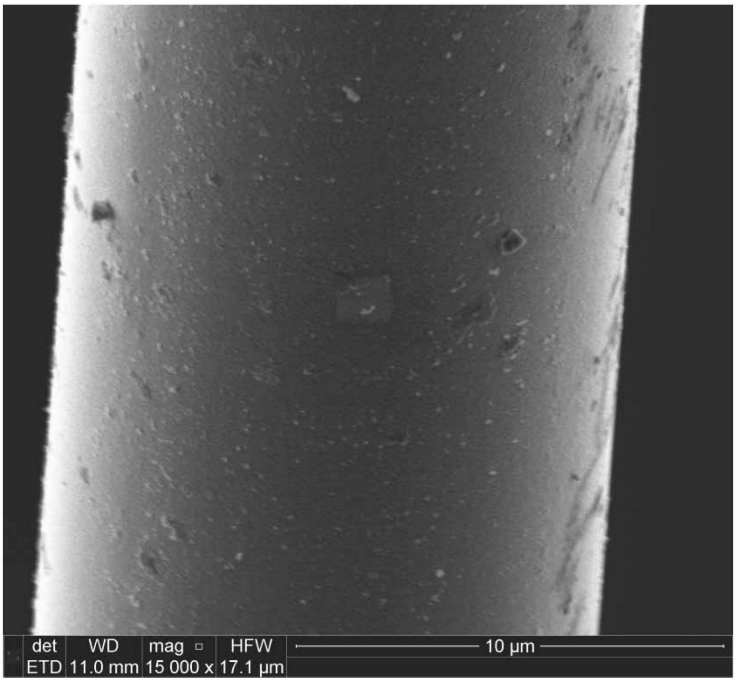


**Figure 194. SEM micrograph of the Hi-Nicalon™ S specimen "Steam 25" examining a fiber above the fracture surface ($\sigma_{cr}$ = 798 MPa, $t_f$ = 1.83 h)**

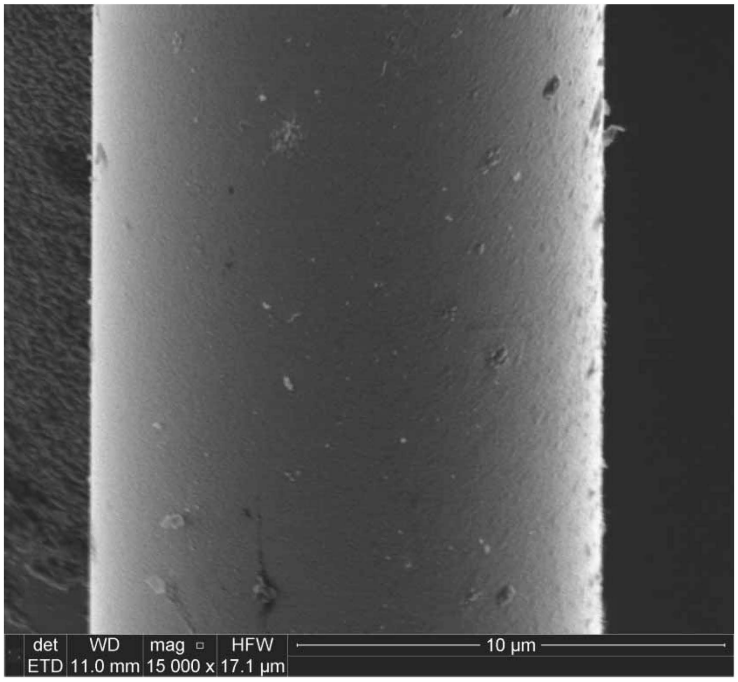


**Figure 195. SEM micrograph of the Hi-Nicalon™ S specimen "Steam 25" examining a fiber above the fracture surface ($\sigma_{cr}$ = 798 MPa, $t_f$ = 1.83 h)**

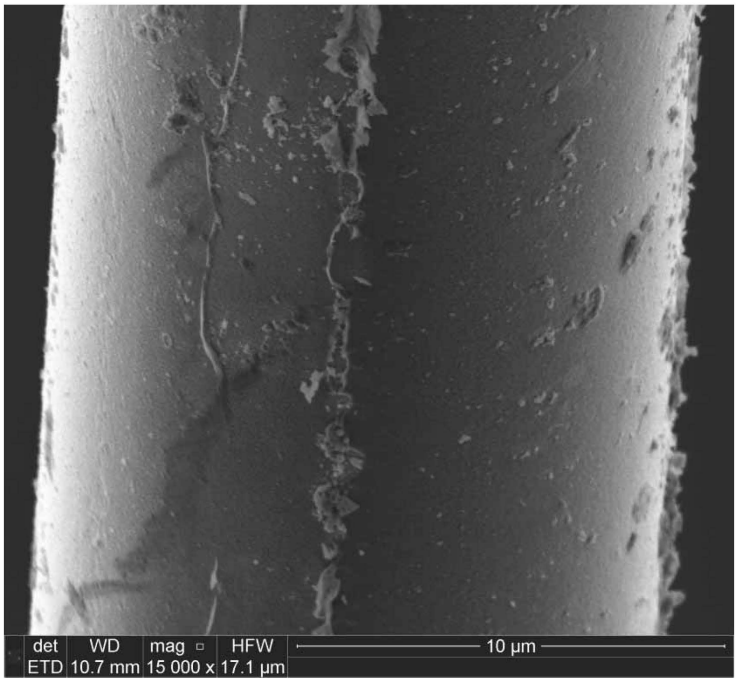


**Figure 196. SEM micrograph of the Hi-Nicalon™ S specimen "Steam 25" examining a fiber above the fracture surface ($\sigma_{cr}$ = 798 MPa, $t_f$ = 1.83 h)**

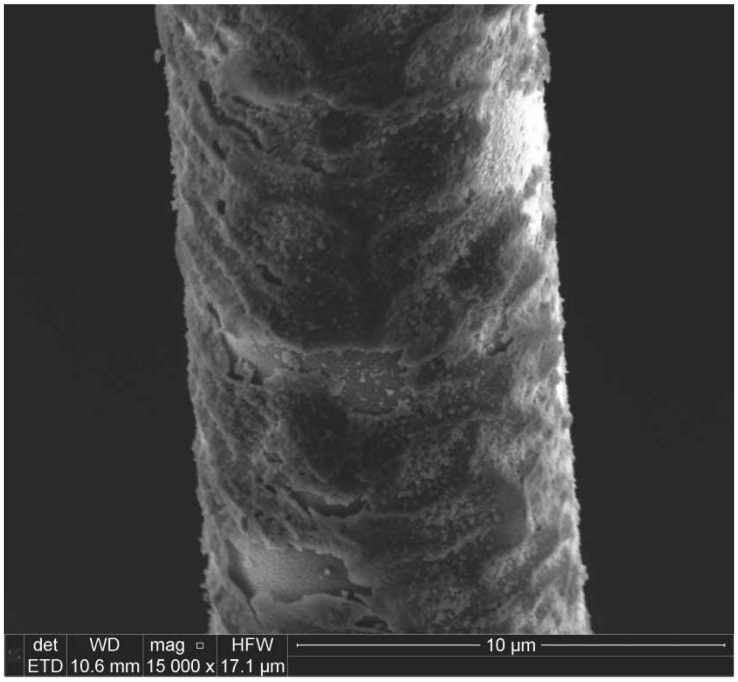


**Figure 197. SEM micrograph of the Hi-Nicalon™ S specimen "Steam 25" examining a fiber above the fracture surface. Note the deposits on the fiber surfaces resulting from oxidation ($\sigma_{cr}$ = 798 MPa, $t_f$ = 1.83 h)**

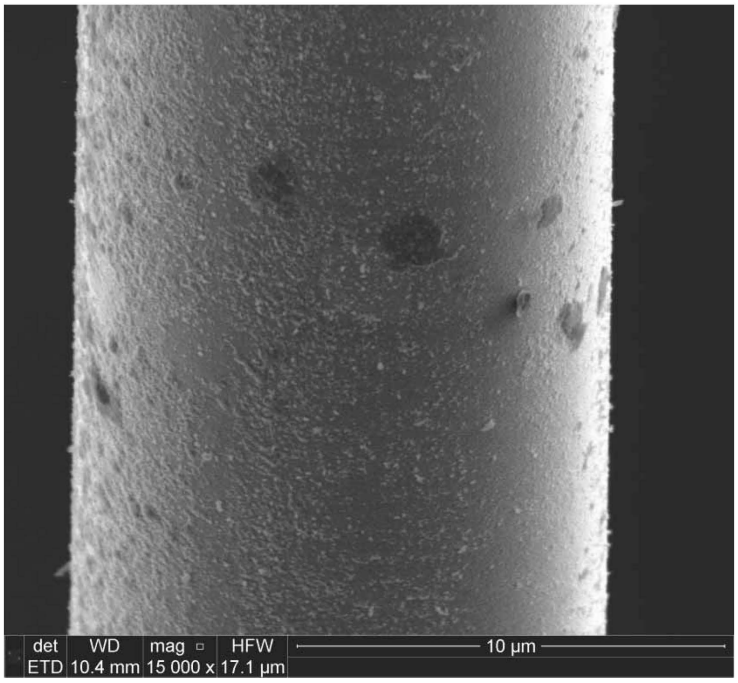


**Figure 198. SEM micrograph of the Hi-Nicalon™ S specimen "Steam 25" examining a fiber above the fracture surface ($\sigma_{cr}$ = 798 MPa, $t_f$ = 1.83 h)**

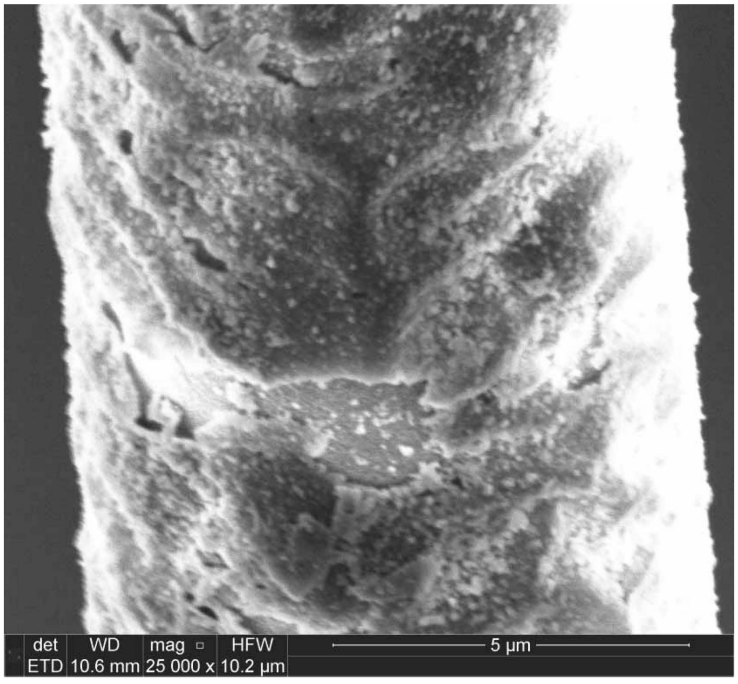


**Figure 199. SEM micrograph of the Hi-Nicalon™ S specimen "Steam 25" examining a fiber above the fracture surface. Note the deposits on the fiber surfaces resulting from oxidation ($\sigma_{cr}$ = 798 MPa, $t_f$ = 1.83 h)**

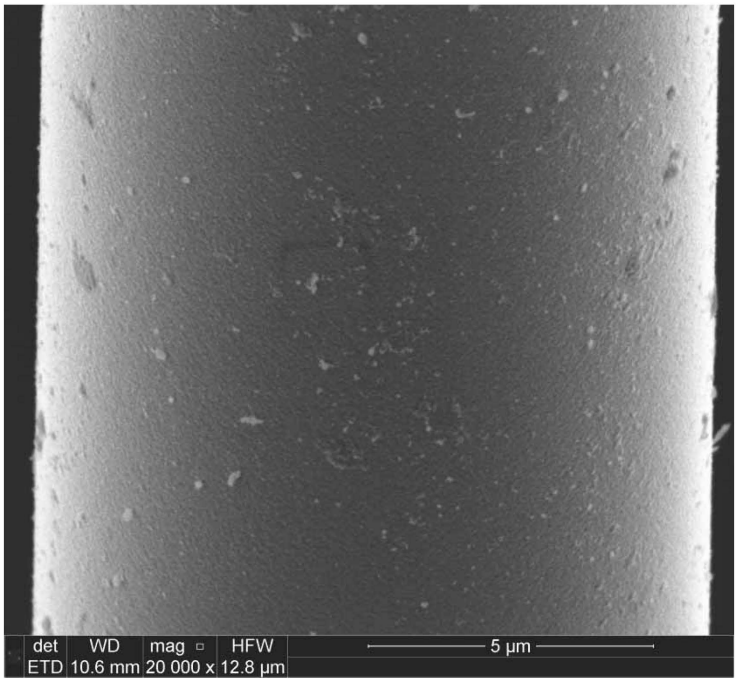


**Figure 200. SEM micrograph of the Hi-Nicalon™ S specimen "Steam 25" examining a fiber above the fracture surface ($\sigma_{cr}$ = 798 MPa, $t_f$ = 1.83 h)**

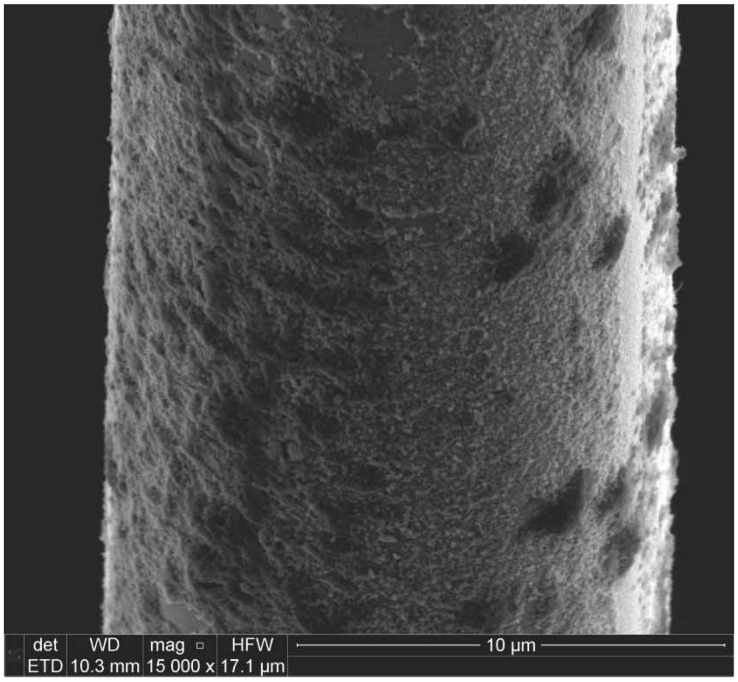


**Figure 201. SEM micrograph of the Hi-Nicalon™ S specimen "Steam 25" examining a fiber above the fracture surface. Note the deposits on the fiber surfaces resulting from oxidation ($\sigma_{cr}$ = 798 MPa, $t_f$ = 1.83 h)**

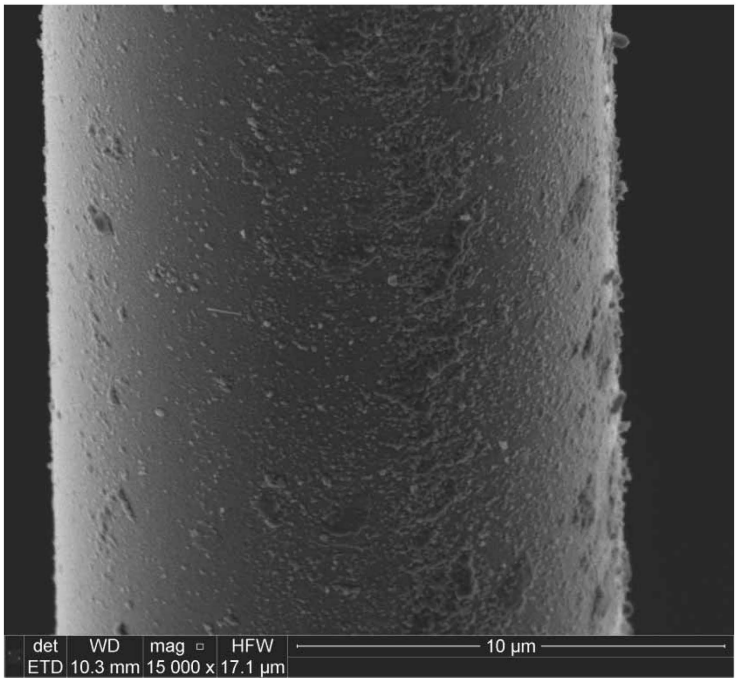


**Figure 202. SEM micrograph of the Hi-Nicalon™ S specimen "Steam 25" examining a fiber above the fracture surface ($\sigma_{cr}$ = 798 MPa, $t_f$ = 1.83 h)**

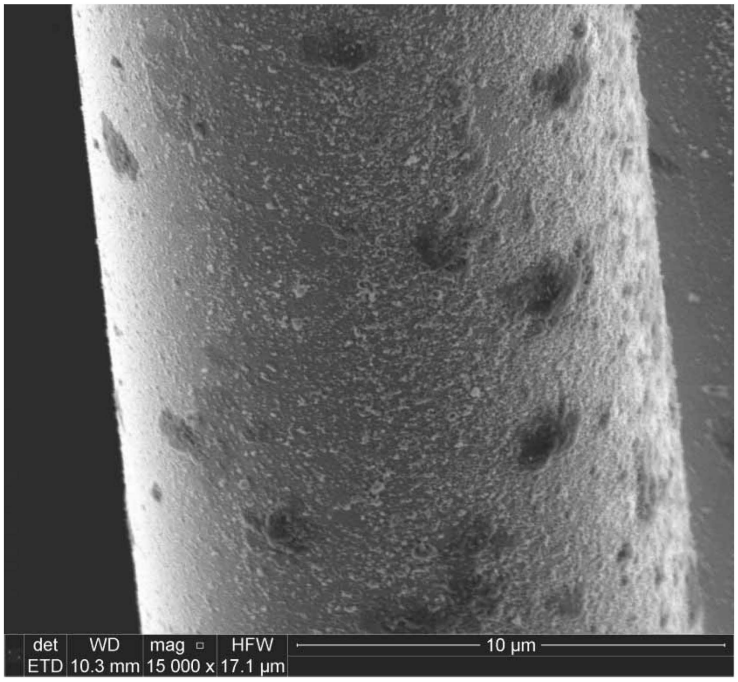


**Figure 203. SEM micrograph of the Hi-Nicalon™ S specimen "Steam 25" examining a fiber above the fracture surface. Note the deposits on the fiber surfaces resulting from oxidation ($\sigma_{cr}$ = 798 MPa, $t_f$ = 1.83 h)**

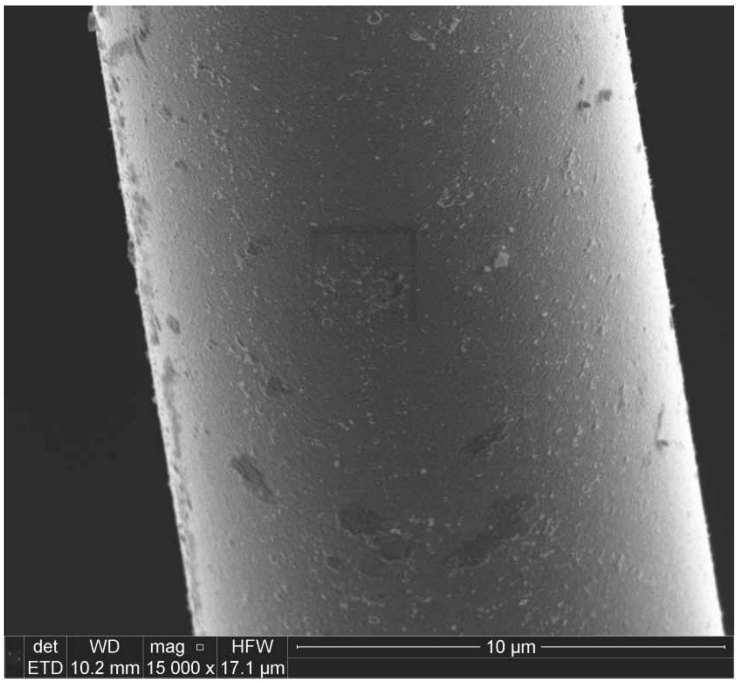


**Figure 204. SEM micrograph of the Hi-Nicalon™ S specimen "Steam 25" examining a fiber above the fracture. Note, the dark rectangle in the center of the image is a product of the imaging ($\sigma_{cr}$ = 798 MPa, $t_f$ = 1.83 h)**

## Bibliography


[1] I. M. Daniel and O. Ishai, *Engineering Mechanics of Composite Materials*, 2nd ed. Oxford: Oxford University Press, 2006.

[2] D. J. Vaughan, "Fiberglass Reinforcement," in *Handbook of Composites*, Second., G. Lubin and S. T. Peters, Eds. New York: Chapman & Hall, 1998.

[3] C. T. Herakovich, *Mechanics of Fibrous Composites*. John Wiley & Sons, 1998.

[4] H. R. Clauser, "Advanced composite materials," *Sci. Am.*, vol. 229, pp. 36–44, 1973.

[5] F. Smith, "The Use of Composites in Aerospace: Past, Present, and Future Challenges." 2013.

[6] R. Boyer, "Aircraft Materials," *Concise Encyclopedia of Composite Materials*. Elsevier, pp. 1–8, 2007.

[7] "Lockheed Martin extends Cytec contract for F-35 prepreg," *Composites World*, 2011. .

[8] W. Krenkel, Ed., *Ceramic Matrix Composites*. Wiley-VCH, 2008.

[9] K. K. Chawla, *Ceramic Matrix Composites*. Chapman & Hall, 1993.

[10] T. R. Shillig, "CREEP OF HI-NICALON S FIBER TOWS AT ELEVATED TEMPERATURE IN AIR AND IN STEAM," Air Force Institue of Tehnology, 2013.

[11] S. Schmidt, S. Beyer, H. Knabe, H. Immich, R. Meistring, and A. Gessler, "Advanced ceramic matrix composite materials for current and future propulsion technology applications," *Acta Astronaut.*, vol. 55, pp. 409–420, 2004.

[12] F. W. Zok and C. G. Levi, "Mechanical Properties of Porous-Matrix Ceramic

Composites," *Adv. Eng. Mater.*, vol. 3, no. 1–2, pp. 15–23, 2001.

[13] S. Robertson, "CREEP OF HI-NICALONTM S CERAMIC FIBER TOWS AT 800◦C IN AIR AND IN SILICIC ACID-SATURATED STEAM," 2015.

[14] R. J. Kerans and R. S. Hay, "Interface Design for Oxidation-Resistant Ceramic Composites," *J. Am. Ceram. Soc.*, vol. 85, pp. 2599–2632, 2002.

[15] J. B. Davis, J. P. A. Lofvander, A. G. Evans, E. Bischoff, and M. L. Emiliani, "Fiber Coating Concepts for Brittle-Matrix Composites," *J. Am. Ceram. Soc.*, vol. 76, no. 5, pp. 1249–1257, 1993.

[16] F. W. Zok, "Developments in Oxide Fiber Composites," *J. Am. Ceram. Soc.*, vol. 89, no. 11, pp. 3309–3324, 2006.

[17] I. H. A. Shames and F. A. A. Cozzarelli, *Elastic and Inelastic Stress Analysis*. Philadelphia, PA: Taylor & Francis Group, 1997.

[18] J. B. Wachtman, W. R. Cannon, and M. J. Matthewson, *Mechanical Properties of Ceramics*, 2nd ed. John Wiley & Sons, 2009.

[19] C. J. Armani, "Creep Performance of Oxide Ceramic Fiber Materials at Elevated Temperature in Air and in Steam," 2011.

[20] K. B. Sprinkle, "CREEP OF SYLRAMIC-iBN FIBER TOWS AT ELEVATED TEMPERATURE IN AIR AND IN SILICIC ACID-SATURATED STEAM," Air Force Institute of Technology (AU), 2015.

[21] J.-P. Poirier, *Creep of Crystals*. Cambridge, UK: Cambridge University Press, 1985.

[22] J. Lamon, S. Mazerat, and M. R'Mili, "No Title," in *Ceramic Matrix Composites: Materials, Modeling and Technology*, N. P. Bansal and J. Lamon, Eds. John Wiley

& Sons, 2015, pp. 3–5.

[23] A. R. Bunsell and A. Piant, “A review of the development of three generations of small diameter silicon carbide fibres,” *J. Mater. Sci.*, vol. 41, no. 3, pp. 823–839, 2006.

[24] T. Ishikawa, “Advances in Inorganic Fibers,” *Polym. Inorg. Fibers*, pp. 109–144, 2005.

[25] J. J. Sha, T. Nozawa, J. S. Park, Y. Katoh, and a. Kohyama, “Effect of heat treatment on the tensile strength and creep resistance of advanced SiC fibers,” *J. Nucl. Mater.*, vol. 329, no. A, pp. 592–596, 2004.

[26] J. J. Sha, J. S. Park, T. Hinoki, and a. Kohyama, “Heat treatment effects on creep behavior of polycrystalline SiC fibers,” *Mater. Charact.*, vol. 57, no. 1, pp. 6–11, 2006.

[27] C. Sauder and J. Lamon, “Tensile Creep Behavior of SiC-Based Fibers With a Low Oxygen Content,” *J. Am. Ceram. Soc.*, vol. 90, no. 4, pp. 1146–1156, 2007.

[28] H. M. Yun and J. A. DiCarlo, “Comparison of the Tensile , Creep , and Rupture Strength Properties of Stoichiometric SiC Fibers,” Glenn Research Center, 1999.

[29] B. R. Steffens, “CREEP OF HI-NICALON S CERAMIC FIBER TOWS AT ELEVATED TEMPERATURE IN AIR AND IN STEAM,” 2012.

[30] W. Gauthier and J. Lamon, “Delayed Failure of Hi-Nicalon and Hi-Nicalon S Multifilament Tows and Single Filaments at Intermediate Temperatures (500°-800°C),” *J. Am. Ceram. Soc.*, vol. 92, no. 3, pp. 702–709, 2009.

[31] J. A. DiCarlo, H.-M. Yun, G. N. Morscher, and R. T. Bhatt, “SiC/SiC Composites for 1200°C and Above,” in *Handbook of Ceramic Composites*, N. P. Bansal, Ed.

New York, NY, 2005, pp. 77–98.

[32] J. A. DiCarlo and H.-M. Yun, "Non-oxide (Silicon Carbide) Fibers," in *Handbook of Ceramic Composites2*, N. P. Bansal, Ed. New York, NY, 2005, pp. 33–52.

[33] R. S. Hay, G. Fair, E. Urban, J. Morow, J. Somerson, and M. Wilson, "Oxidation Kinetics and Strength Versus Scale Thickness for Hi-Nicalon$^{TM}$-S SiC Fiber," in *Design, Development, and Applications of Engineering Ceramics and Composites: A Collection of Papers Presented at the 8th Pacific Rim Conference on Ceramic and Glass Technology*, 2010, pp. 105–112.

[34] R. S. Hay, G. E. Fair, R. Bouffioux, E. Urban, J. Morrow, A. Hart, and M. Wilson, "Hi-NicalonTM-S SiC Fiber Oxidation and Scale Crystallization Kinetics," *J. Am. Ceram. Soc.*, vol. 94, no. 11, pp. 3983–3991, 2011.

[35] R. S. Hay, G. E. Fair, R. Bouffioux, E. Urban, J. Morrow, A. Hart, and M. Wilson, "Relationships Between Fiber Strength, Passive Oxidation and Scale Crystallization Kinetics of Hi-Nicalon$^{TM}$-S SiC Fibers," in *Mechanical Properties and Performance of Engineering Ceramics and Composites VI: Ceramic Engineering and Science Proceedings*, 2011, vol. 32, pp. 37–51.

[36] R. S. Hay, G. E. Fair, A. Hart, S. Potticary, and R. Bouffioux, "Kinetics of Passive Oxidation of Hi-Nicalon-S SiC Fibers in Wet Air: Relationships between SiO2 Scale Thickness, Crystallization, and Fiber Strength," in *Mechanical Properties and Performance of Engineering Ceramics and Composites VII*, 2012, vol. 33, no. 2, pp. 253–260.

[37] L. NGS Advanced Fibers Co., "No Title." [Online]. Available: http://www.ngs-advanced-fibers.com/eng/item/index.html. [Accessed: 23-Nov-2015].

[38] R. Morrell, “A tensile creep-testing apparatus for ceramic materials using simple knife-edge universal joints,” *J. Phys. E.*, vol. 5, no. 5, pp. 465–467, 1972.

[39] F. A. Kandil and B. F. Dyson, “Tensile Creep of Ceramics: the Development of a Testing Facility,” *Int. J. High Technol. Ceram.*, vol. 4, pp. 243–262, 1988.

[40] J. A. Dicarlo, “DiCarlo - Property Goals and Test Methods for High Temperature Ceramic Fiber Reinforcement,” *Ceram. Int.*, vol. 23, no. 4, pp. 283–289, 1995.

[41] V. H. Hammond, “Creep Rupture of an Oxide/Oxide Composite Fiber,” University of Virginia, 2001.

[42] H. M. Yun, J. C. Goldsby, and J. A. DiCarlo, “Tensile Creep and Stress-Rupture Behavior of Polymer Derived SiC Fibers,” 1994.

# REPORT DOCUMENTATION PAGE

*Form Approved*
*OMB No. 074-0188*



| 1. REPORT DATE *(DD-MM-YYYY)* | 2. REPORT TYPE | 3. DATES COVERED *(From – To)* |
|---|---|---|
| 04-03-2016 | Master's Thesis | August 2014 – March 2016 |

**TITLE AND SUBTITLE**

Creep of Hi-Nicalon™ S Ceramic Fiber Tows at 700°C in Air and in Silicic Acid-saturated Steam

**5a. CONTRACT NUMBER**

**5b. GRANT NUMBER**

**5c. PROGRAM ELEMENT NUMBER**

**6. AUTHOR(S)**

Piper, Matthew W., Captain, USAF

**5d. PROJECT NUMBER**

**5e. TASK NUMBER**

**5f. WORK UNIT NUMBER**

**7. PERFORMING ORGANIZATION NAMES(S) AND ADDRESS(S)**
Air Force Institute of Technology
Graduate School of Engineering and Management (AFIT/ENY)
2950 Hobson Way, Building 640
WPAFB OH 45433-8865

**8. PERFORMING ORGANIZATION REPORT NUMBER**

AFIT-ENY-16-M-234

**9. SPONSORING/MONITORING AGENCY NAME(S) AND ADDRESS(ES)**
Air Force Research Laboratory
Dustin Shaw
2977 Hobson Way, Building 652
Wright-Patterson AFB, OH 45433
dustin.shaw.1@us.af.mil

**10. SPONSOR/MONITOR'S ACRONYM(S)**

AFRL/RXSSR

**11. SPONSOR/MONITOR'S REPORT NUMBER(S)**

**12. DISTRIBUTION/AVAILABILITY STATEMENT**
**DISTRUBTION STATEMENT A.** APPROVED FOR PUBLIC RELEASE; DISTRIBUTION UNLIMITED.

**13. SUPPLEMENTARY NOTES**
This material is declared a work of the U.S. Government and is not subject to copyright protection in the United States.

**14. ABSTRACT**

Aircraft structural and engine components are subjected to elevated temperature and steam environments during operation. Ceramic matrix composites (CMCs) are prime candidates to replace superalloys as turbine blade materials. This research investigated a silicon carbide (SiC) fiber, Hi-Nicalon™ S, which is a candidate for reinforcement of CMCs with SiC-based matrices. Hi-Nicalon™ S fiber tows were creep tested at 700°C in air and in silicic acid-saturated steam. The steam was saturated with silicic acid in order to simulate the interaction that would occur in a SiC-SiC CMC as the steam environment enters through matrix cracks and leaches Si from the matrix while moving towards the fibers. Creep stresses ranged from 2.96 to 1256 MPa in air and from 2.96 to 798 MPa in silicic acid-saturated steam. Creep strains were measured and steady-state creep rates were determined. In air, creep runout was achieved at stresses as high as 1023 MPa, while in saturated steam creep runout was achieved only at 750 MPa. Creep rates were approximately an order of magnitude greater in saturated steam than in air. Post-test fiber microstructure analysis revealed the presence of a passive oxidation layer on the fibers tested in both environments but no evidence of active oxidation.

**15. SUBJECT TERMS**
Ceramic Matrix Composites, Composite Materials, Ceramic Fibers, Fiber Tows, Ceramic Materials, Fiber Reinforced Composites, Creep, Nicalon™ Fiber, Hi-Nicalon™ Fiber, Hi-Nicalon™ S Fiber, Steam, Air, Saturated Steam, Silicic Acid, Elevated Temperature

| 16. SECURITY CLASSIFICATION OF: | | | 17. LIMITATION OF ABSTRACT | 18. NUMBER OF PAGES | 19a. NAME OF RESPONSIBLE PERSON |
|---|---|---|---|---|---|
| a. REPORT | b. ABSTRACT | c. THIS PAGE | | | Dr. Marina B. Ruggles-Wrenn, AFIT/ENY |
| U | U | U | UU | 164 | 19b. TELEPHONE NUMBER *(Include area code)*<br>9372553636x4641<br>marina.ruggles-wrenn@afit.edu |